

UNIVERSITA' DEGLI STUDI DI MILANO – BICOCCA

Facoltà di Scienze Matematiche, Fisiche e Naturali

Dottorato di ricerca in Scienze Chimiche

XXIII ciclo – A.A. 2007-2008-2009-2010



**HETEROAROMATIC CONJUGATED MATERIALS**  
**WITH INNOVATIVE APPLICATIONS:**  
**FROM PHOTONICS TO TRANSISTORS**

Relatore: Chiar.mo Prof. Giorgio A. PAGANI

Coordinatore: Chiar.ma Prof.ssa Franca MORAZZONI

PhD Thesis of:

Alessandro SANGUINETI

Matr. 041028



---

## ACKNOWLEDGMENTS

This dissertation represents my personal contribution to the research field of organic functional systems for advanced materials. Besides being the result of a dense 3-year project, it can be properly defined as the final achievement of a longer educational cycle, which finds here its most elevated expression.

First of all I would like to thank my supervisor, Professor Giorgio A. Pagani: the man who primarily showed me the beauty of organic chemistry and instilled in me the curiosity about the unknown, from the very first lessons I attended during my academic studies. A true mentor, whose preeminent human and scientific presence guided me along the way, with continuous unforgettable teachings.

A very special thanks to Dr. Luca Beverina, for his irreplaceable scientific and human presence inside and outside the laboratory, for his constant teachings, support, helpfulness and his peculiar capacity of injecting enthusiasm and confidence, anytime you need it.

I would also like to thank Professor Tobin J. Marks and Professor Antonio Facchetti at Northwestern University for giving me the privilege of working in their outstanding research group, and for all the precious teachings and help during my stay in the USA.

I would like to thank very much Professor Antonio Papagni for his teachings, helpful suggestions and interesting discussions, and I sincerely thank all the people I have collaborated with during my PhD experience, especially: Dr. Rocio Ponce Ortiz and Dr. Massimiliano Delferro (at Northwestern University); Dr. Giorgio “Cioccio” Patriarca (Magneto), Dr. Norberto Manfredi, Mauro Sassi, Marco “Vetz” Vettigli, Gianluca Generali.

All this work could not obviously be accomplished without the presence and support of the many people who shared their time along with me during my PhD course.

A very special thank goes to my parents who believed in me from the very beginnings of my carrier and, last but not the least, to my sweet lovely princess Anna.

This PhD work was supported by the “Fondo Giovani 2006” grant for the development of “Broad band innovative telecommunication systems for security, prevention and intervention applications in case of natural calamities”.

---

# TABLE OF CONTENTS

## PART ONE

### “Heteroaromatic Conjugated Materials for Photonics”

<b><u>I. INTRODUCTION</u></b>	<b>7</b>
<b>I.1 NONLINEAR OPTIC IN ORGANIC MATERIALS</b>	<b>7</b>
1.1 Basic concepts of NLO	8
1.2 Second-order phenomena	12
1.3 Third-order phenomena	14
<b>I.2 ORGANIC MATERIALS FOR SECOND-ORDER NLO</b>	<b>16</b>
2.1 Approaches for enhancing $\beta$	19
2.1.1 Bond Length Alternation (BLA)	19
2.1.2 Auxiliary donor/acceptor strategy	22
2.1.3 Twisted zwitterionic systems	24
<b><u>II. RESULTS &amp; DISCUSSION</u></b>	<b>27</b>
<b>II.1 AUXILIARY DONOR/ACCEPTOR HETEROAROMATIC SYSTEMS</b>	<b>28</b>
1.1 Design & synthesis	28
1.2 Linear optical characterizations & modeling	33

---

<b>II.2 ZWITTERIONIC HETEROAROMATIC SYSTEMS</b>	<b>43</b>
2.1 Pyridonemethides & pyridoneimines	45
2.1.1 Design & synthesis	46
2.2 Tetrazolates	50
2.2.1 Design & synthesis	51
2.2.2 Characterizations	67
<b>II.3 TOWARD ELECTRO-OPTIC MATERIALS</b>	<b>76</b>
3.1 Host-Guest polymeric systems	83
3.2 Self-assembled structures	92
3.3 Vapor-deposited thin films	97
<b><u>III. CONCLUSIONS</u></b>	<b>105</b>
<b><u>EXPERIMENTAL SECTION</u></b>	<b>107</b>
<b><u>REFERENCES</u></b>	<b>125</b>

---

## PART TWO

### “Heteroaromatic Conjugated Materials for Transistor Applications”

<b><u>I. INTRODUCTION</u></b>	<b>133</b>
<b>I.1 FIELD EFFECT TRANSISTORS (FETs)</b>	<b>133</b>
1.1 Basic concepts & processes	134
1.2 Thin Film Transistors (TFTs)	140
1.2.1 Silicon	141
1.2.2 Metal oxides	142
1.2.3 Nanostructures	143
<b>I.2 ORGANIC THIN FILM TRANSISTORS (OTFTs)</b>	<b>145</b>
2.1 Device architectures & principles	146
<b>I.3 ORGANIC SEMICONDUCTORS</b>	<b>154</b>
3.1 <i>p</i> – type semiconductors	155
3.1.1 Small molecules	155
3.1.2 Polymeric systems	158
3.2 <i>n</i> – type semiconductors	160

---

<b>I.4 ENHANCING THE DEVICE PERFORMANCES</b>	<b>164</b>
4.1 The dielectric layer	165
4.2 The role of interfaces	170
<b><u>II. RESULTS &amp; DISCUSSION</u></b>	<b>174</b>
<b>II.1 SYNTHESIS OF THE ORGANIC SEMICONDUCTORS</b>	<b>174</b>
<b>II.2 OTFT DEVICES</b>	<b>178</b>
2.1 Semiconductor & contacts deposition	179
2.2 Device Characterization	181
<b><u>III. CONCLUSIONS</u></b>	<b>196</b>
<b><u>EXPERIMENTAL SECTION</u></b>	<b>198</b>
<b><u>REFERENCES</u></b>	<b>201</b>

---

# PART ONE

## HETEROAROMATIC CONJUGATED MATERIALS FOR PHOTONICS



## I. INTRODUCTION

### **I.1 NONLINEAR OPTIC IN ORGANIC MATERIALS**

Modern nanotechnologies find increasing applications in the development of contemporary telecommunication systems, enabling progressive device miniaturization and performance enhancements.

The field of organic materials has gained an extremely high attention in this regard, both in the scientific community and in industrial research programs, as a consequence of the fact that they offer several well suitable properties that inorganic ones cannot. The intrinsic tailory nature of organic molecules allows in fact a fine control of the material electrical and optical properties; furthermore their mechanical and chemical characteristics make possible a number of cheap, easily up-scalable and very flexible preparation techniques that result particularly attractive for a number of contemporary technical applications. There are clear signals that, with the help of organic chemistry, an information technology based on light can be achieved, breaking the limits imposed by electronic circuits on computation speeds and data storage capacities. Considering this issue, besides the great impact of molecular electronic (which constitutes the topic of the second part of this dissertation), the fundamental field of molecular photonic plays the role of an effective milestone for the realization of state-of-the-art advanced technological tools, such as: optical limiters, up-converted laser sources, 3D-imaging medical devices and innovative telecommunication systems for data acquisition, data transmission, data processing and data storage (i.e., digital logic gates, optical switchers, amplifiers, modulators, and electrical-to-optical signal transducers). To really exploit the potential of this technology, a deep knowledge of the optical processes involved in light-matter interactions at the molecular level is required.

Light-matter interactions can be divided into two main classes, namely linear and nonlinear, depending on their nature. The first class includes common physical-chemical phenomena, such as light refraction, diffraction, reflection, scattering and one-photon absorption; whilst nonlinear optic (NLO) is characterized by a non-conventional light-matter interaction that causes completely peculiar material responses, the most studied effects being: multiphoton absorption (TPA), second- and third- harmonic generation (SHG, THG), frequency mixing and radiation-induced change of the refractive index (Pockels and Kerr effects).

### 1.1 BASIC CONCEPTS OF NLO

The first investigations in nonlinear optic date back to 1875 with Kerr's publications concerning the change of the refraction index in CS<sub>2</sub> crystals induced by the quadratic component of the electric field. Successive developments in NLO obtained just few contributes during the decades until the '60s, when the introduction of proper laser sources enabled the investigation and rationalization of such phenomena, at the atomic and molecular level.<sup>1</sup> Whilst familiar linear processes occur for low intensity of the interacting radiation, nonlinear effects are in fact detectable only when the material undergoes an intense electromagnetic field, and this is commonly obtained from the availability of laser sources.

To explain this phenomenon, a qualitative chemically oriented description of the physic behind the NLO processes is reported in the following discussion, which considers the electrical component of the incident radiation only\*, while neglecting the magnetic one.<sup>2</sup>

---

\* The expression for the dependence on the radiation magnetic component is not reported here, being the latter strictly correlated to the electrical component through the well-known Maxwell's equations; furthermore, the magnetization effects on optical phenomena (characterized by rapid oscillations) are considered negligible for our purpose.

Generally speaking, an external applied oscillating electric field acts on a material causing a displacement of the electronic positions, which are stimulated to oscillate at the same imposed frequency. The induced perturbation determines a macroscopic medium polarization whose entity, for strong enough external electromagnetic radiation, can be expressed as reported in the expression below, where the nonlinear regime is characterized by the presence of the higher order terms (Eq. 1)

$$\text{Eq. 1} \quad \vec{P} = \chi^{(1)} \vec{E} + \chi^{(2)} \vec{E} \vec{E} + \chi^{(3)} \vec{E} \vec{E} \vec{E} + \dots$$

where  $\chi^{(1)}$  represent the linear and non linear optical susceptibilities.

Focusing on organic materials it is useful to trace back the polarization response, and thus the material optical behavior, at a molecular level; thus, starting from this consideration, it is possible to express this microscopic polarization as a power series of the electric field (Eq. 2), reported here up to the third term:<sup>5</sup>

$$\text{Eq. 2} \quad p_i = \sum_j \alpha_{ij}(-\omega_1; \omega_2) E_j(\omega_2) \\ + \sum_{j \leq k} \beta_{ijk}(-\omega_1; \omega_2, \omega_3) E_j(\omega_2) E_k(\omega_3) \\ + \sum_{j \leq k \leq l} \gamma_{ijkl}(-\omega_1; \omega_2, \omega_3, \omega_4) E_j(\omega_2) E_k(\omega_3) E_l(\omega_4) \\ + \dots$$

where the tensorial coefficients  $\alpha$ ,  $\beta$ ,  $\gamma$ , are the so-called linear polarizability and first-order (quadratic) and second-order (cubic) hyperpolarizability respectively and represent the microscopic analogous of the above reported macroscopic susceptibilities. It is worth noting in this equation the vectorial nature of the electric field and its frequency dependence.

By combining the above two equations for the macroscopic and microscopic polarization, it is possible to express the final polarization for an organic material of total  $N$  molecules as reported in Eq. 3.

$$\begin{aligned}
 \text{Eq. 3} \quad P_i &= \sum_J \chi_{ij}^{(1)} E_J \\
 &+ \frac{1}{2} \sum_{J,k} \chi_{ijk}^{(2)} E_J E_K \\
 &+ \frac{1}{6} \sum_{J,K,L} \chi_{ijkl}^{(3)} E_J E_K E_L \\
 &+ \dots
 \end{aligned}$$

Taking into account the correction of the external applied field due to the molecular local field (e.g. introducing a factor which considers the interaction due to the molecular vicinity), the macroscopic susceptibilities can be correlated to the microscopic polarizabilities as reported in the form of Eq. 4:

$$\begin{aligned}
 \text{Eq. 4} \quad \chi_{ij}^{(1)} &= N \sum_{ij} f_i \langle \cos \theta_{ii} \rangle f_j \langle \cos \theta_{jj} \rangle \alpha_{ij} \\
 \chi_{ijk}^{(2)} &= N \sum_{ijk} f_i \langle \cos \theta_{ii} \rangle f_j \langle \cos \theta_{jj} \rangle f_k \langle \cos \theta_{kk} \rangle \beta_{ijk} \\
 \chi_{ijkl}^{(3)} &= N \sum_{ijkl} f_i \langle \cos \theta_{ii} \rangle f_j \langle \cos \theta_{jj} \rangle f_k \langle \cos \theta_{kk} \rangle f_l \langle \cos \theta_{ll} \rangle \gamma_{ijkl}
 \end{aligned}$$

where  $f$  express the correction due to the presence of the local field and  $\theta$  is the angular factor which contemplate the relative orientation between couples of involved molecules.

Two kinds of NLO phenomena are possible. The first one involves energy exchange between the propagating waves and the material; as a consequence of that, the energy levels of the material change their population. Such processes are known as active, or non parametric, NLO phenomena. In the second type, the material acts simply as a "catalyst", which allows energy exchange between different propagating waves. In this case the population of material energy states is not affected. The latter are known as passive, or parametric, NLO processes. Active processes are restricted to odd orders, conversely parametric effects occur at any order of nonlinearity.<sup>4</sup> The most important NLO phenomena are reported, classified by susceptibility order, in Table. 1.

Following the usual convention, the frequency ( $\omega$ ) of the light waves involved in the process are presented as argument of the susceptibility. Frequencies of waves generated or amplified by the medium are reported with negative sign ( $-\omega$ ); static electric field are symbolized by a frequency value of 0.

Process	Susceptibility
Linear absorption/emission and refractive index	$\chi^{(1)}(-\omega; \omega)$
Optical rectification	$\chi^{(2)}(0; -\omega, \omega)$
Pockels effect	$\chi^{(2)}(-\omega; 0, \omega)$
Second-Harmonic Generation (SHG)	$\chi^{(2)}(-2\omega; \omega, \omega)$
Sum- and difference- frequency generation	$\chi^{(2)}(-\omega_3; \omega_1 \pm \omega_2)$
Kerr effect	$\chi^{(3)}(-\omega; 0, 0, \omega)$
Field Induced Second-Harmonic Generation	$\chi^{(3)}(-2\omega; 0, \omega, \omega)$
Third-Harmonic Generation (THG)	$\chi^{(3)}(-3\omega; \omega, \omega, \omega)$
Sum- and difference- frequency generation	$\chi^{(3)}(-\omega_3; \pm\omega_1, \omega_2, \omega_2)$
Two-Photon Absorption (TPA)	$\chi^{(3)}(-\omega; -\omega, \omega, \omega)$ OR $\chi^{(3)}(-\omega_1; -\omega_2, \omega_2, \omega_1)$

Table. 1: NLO phenomena classified by their susceptibility order

In the following a brief description of the various NLO phenomena reported above is summarized, together with their relative applications, considering the susceptibility order.<sup>5</sup>

## 1.2 SECOND-ORDER PHENOMENA

- Sum-frequency generation and difference-frequency generation

Two external radiations of frequency  $\omega_1$  and  $\omega_2$  interact inside a nonlinear material generating a light field of frequency  $\omega = \omega_1 + \omega_2$  (sum) or  $\omega = \omega_1 - \omega_2$  (difference). Usually the sum-frequency generation allows a UV-output whilst in the difference-frequency generation a photon with a longer wavelength than the two incident lasers is emitted, commonly a near-IR or mid-IR radiation. The laser radiations thus obtained find applications in all those fields where a tunable laser source is required, such as: telecommunications, environmental sensing and industrial-control processes.

- Optical rectification

This is the situation when in the previous case the interacting radiations possess the same frequency: a static electric field is created within the medium as a response to a light wave.

- Second-harmonic generation (SHG)

When the two interacting photons possess the same frequency, the sum-frequency process leads to the emission of a radiation of frequency  $2\omega$ ; the two incoming photons are destroyed and the produced one is emitted in a single quantum-mechanical step. This phenomenon is widely used to change the output of fixed-frequency lasers to a different spectral region. For example, with nonlinear crystals the near infrared radiation of a Nd:YAG laser with a wavelength of 1064 nm is routinely converted to a visible 532 nm laser beam.

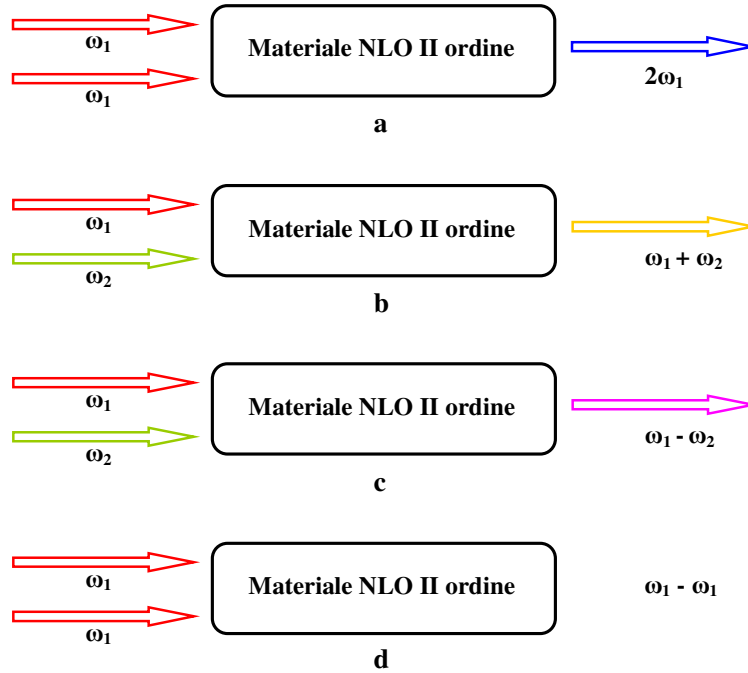


Figure. 1: Schematic diagram of the NLO second-order effects: (a) SHG, (b) sum-frequency generation, (c) difference-frequency generation, (d) optical rectification.

- Pockels (or linear electro-optic) effect

This effect consists in the change of the refractive index of the medium caused by the application of an external static electric field and a light field; the phenomenon behind this effect is the phase-shift of the incoming radiation inside the material. The refractive index changes according to the direction of the incident light (birefringence). The Pockels effect has been widely used to produce a variety of guided wave optical devices including electro-optical switches, modulators, filters and other components in telecommunications networking.

It is worth noting that in order to meet the compatibility requirements imposed by the above effects, the material must avoid detrimental phenomena such as absorption of the incoming and outgoing frequency, as well as occurrence of destructive interferences between these two radiations.

### 1.3 THIRD-ORDER PHENOMENA

Among the third-order NLO effects reported in Table. 1, the most relevant one is the two-photon absorption (TPA) phenomenon due to its important technological applications. TPA is the parametric process described by the imaginary part of the third-order susceptibility, by which a molecule or crystal can be promoted from its electronic ground state to an allowed excited state by the simultaneous absorption of two photons of the same or different energies. Depending on the time scale of the experiment and on the number and position of the energy levels of the absorbing materials, there are many different ways in which a material can absorb two photons in a very short period of time:

- Self TPA

The two photons arise from the same optical field and the energy jump is exactly twice the energy of the source.

- Pump and probe TPA

The two photons arise from two different optical fields in a typical pump and probe configuration.

- ESA

The two photons are absorbed along a two-step process where a first one-photon excitation to a real state (with possible subsequent relaxation to another excited level) is followed by the absorption of a second photon, of the same or different energy. This is not a true TPA process but is still a nonlinear phenomenon.

During all these processes the material absorbs two photons having lower energy than that possessed by the photon absorbed in a common linear one-photon excitation; the system can therefore absorb the external radiation in a region of the spectra where it should not (IR or near-IR) by a common linear process.



The most important applications of this phenomenon are reported.

- Optical limiting

TPA process does not follow the Lambert-Beer law, the probability of the TPA process being proportional to the square of the laser intensity. A consequence of this characteristic behavior is that at low input level the material is almost transparent because TPA is negligible and there are no linear absorption phenomena operating at the TPA frequency. When intensity becomes high enough, TPA starts very quickly to operate and output level deviate remarkably from linear transmission behavior. Optical limiters are very useful for the protection of human eyes or artificial light sensors, operating in the presence of very intense light sources.<sup>6</sup>

- Up-converted frequency lasing

Once promoted to its excited state by a TPA process, an organic molecule can show a one-photon fluorescence emission, arising from a further excited state in which the system relaxes after two-photon excitation (TPE). Being the emission frequency similar to (slightly lower than) that corresponding to linear absorption, it follows that the two-photon induced fluorescence frequency is consistently higher than that absorbed during TPA; for some specifically designed organic materials the fluorescence emission can be stimulated, giving rise to an up-converted lasing.

- 3D imaging, 3D fabrication, 3D optical data storage

Considering that the intensity of a focused laser beam decreases quadratically with the distance from the focus, TPA drops-off as the fourth power of the distance from the focus thus allowing an excitation confinement in very small volumes around it, conferring volumetric resolution.<sup>7</sup> Furthermore being the medium refractive index dependent on the radiation intensity, an auto-focusing behavior is observed.<sup>8</sup>

These features impart 3D character to the phenomenon, which can be exploited, in 3D high-resolution microscopy bio-imaging (two-photon laser scanning confocal microscopy), 3D micro-/nano- fabrications and photo-polymerizations for telecommunication applications, and finally 3D optical data storage for volume memory.

- Photo Dynamic Therapy (PDT)

It is possible to exploit the peculiar characteristics of the TPA process using laser sources possessing wavelength in the biological tissue transparency region (800-1100 nm), in order to excite opportune photo-sensitizers capable in turn of activating molecular oxygen to photo-generate singlet oxygen, which behaves as a reactive species toward cancer cells.

## I.1 ORGANIC MATERIALS FOR SECOND-ORDER NLO

A successful research on organic materials for photonics begins from an accurate design of the systems at the molecular level. During the last 10-15 years many hundreds of NLO-phores have been introduced in the literature with the target of enhancing the final nonlinear response, meeting at the same time the requests for chemical, thermal and environmental stability. Interdisciplinarity in this field of research is essential; collaboration between organic and organometallic chemists as well as with colleagues from other scientific disciplines resulted in multidisciplinary teams capable of producing substantial innovations in molecular and supramolecular systems, thus enabling significant progress in the material performances and in turn yielding major technological achievements. Although much research is still needed, current improvements have been so significant to meet some of the rigorous mass market criteria. Many classes of chromophores possessing specific properties applications have been realized to satisfy precise structural requisites, depending on the NLO phenomenon or the final application.<sup>5,9,10,11,12</sup>

Analyzing the various approaches reported in the literature, it is possible to obtain common general features to delineate molecular archetypes for NLO active molecules. First of all, the energy of the interacting radiation imposes a restriction on the molecular energy levels involved in the optical process: suitable energies are those typical of  $\pi$ -electrons, thus excluding the participation of the more deeply confined  $\sigma$ -electrons, characteristic of the molecular carbon-skeleton. To achieve substantial levels of interaction with the radiation beam, it is necessary for the incoming perturbation to induce a significant displacement of such  $\pi$ -electrons from their equilibrium positions; the fundamental design therefore implicates polar and polarizable systems.  $\pi$ -conjugated molecules, whose  $\pi$ -electrons are mobile and highly delocalizable, are the preferential candidates for satisfying this requisites. The enhancement of the molecular electron mobility is finally obtained by end-capping the  $\pi$ -conjugated framework with proper electron-donating (donor) and electron-withdrawing (acceptor) substituents, which in general act through their resonance effects. Chemists have designed and developed new donor and acceptor groups, more and more refined and efficient, and have combined them in new structural frames. Sometimes other functionalities have also been incorporated to add multifunctionality (e.g. the ability to strongly emit light or to initiate a polymerization reaction) and in other cases the design was not limited to all-organic systems, but used a synergic interaction with metals, ions and matrices of different nature to look for additional and enhanced material properties.

Besides the basic electronic properties of individual segments and their combination, structural symmetry is the other important feature to take into account for achieving high NLO responses; it is possible to recognize three fundamental geometries for NLO-phores: dipolar systems (push-pull), quadrupolar chromophores (centrosymmetric-based structures) and octupolar (branched chromophores showing complex 2D/3D dimensionality).

Second-order active molecules must satisfy further requisites besides the above mentioned: first of all, they must be non-centrosymmetric, for symmetry reason in fact the odd terms in the expansion for the microscopic polarization (Eq. 2) vanish for a centrosymmetric system; furthermore it is necessary to consider an asymmetric charge distribution between fundamental and excited states.<sup>13,14</sup> The most studied prototype for such NLO-phore is thus that of push-pull systems where an intramolecular charge transfer (ICT) takes place from the donor to the acceptor substituent, through the conjugated  $\pi$ -bridge. Such molecule can always be described in terms of a contribution between two resonance limiting structures: a neutral form and a charge-separated (zwitterionic) form (**Figure.2**).

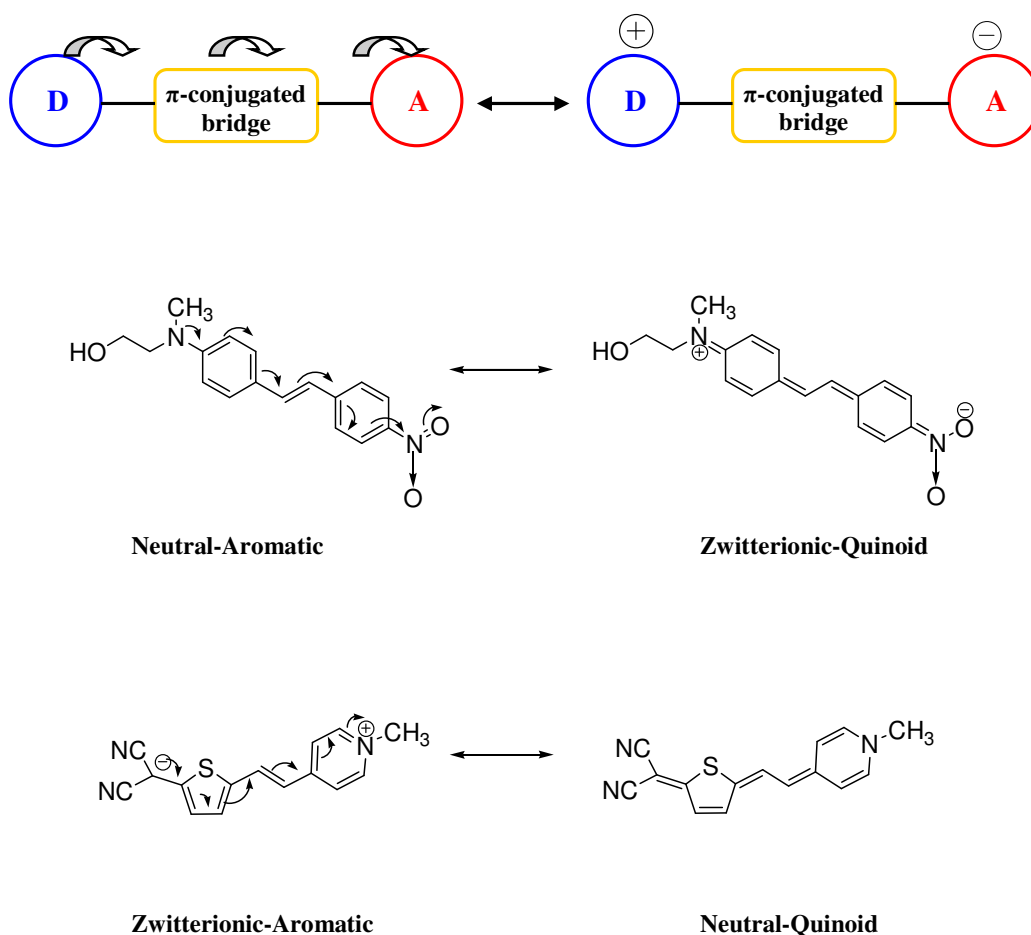


Figure. 2: Scheme of dipolar push-pull molecules

The relative contribute of the two limiting resonance forms, which determines the final molecular (as well as supramolecular) electronic property, optical behavior and structural geometry, originates from the presence of stabilizing factors due to aromaticity, intermolecular interactions and solvent effects. By considering the co-presence of all these aspects, and in the attempt of rationalizing a structure-property relationships, different approaches have been introduced in the literature to maximize the second-order NLO response  $\beta$ .

### 1.1 APPROACHES FOR ENHANCING $\beta$

In order to achieve NLO efficiency, organic design needs to be based on precise directions. Even though some of the guidance could seem obvious (in general molecular second-order NLO sensitivity is higher as the  $\pi$ -conjugated framework is longer and donor and acceptor substituents are stronger), this not always verified (stronger donor and acceptor groups may decrease the molecular hyperpolarizability, *vide infra*) and other factors, such as  $\pi$ -orbitals coupling or stability, must be taken into account. Concepts are therefore more complex than originally expected and accurate relationships are in demand.

#### 1.1.2 BOND LENGTH ALTERNATION (BLA)

In the early 70s it was suggested that a simple two-state model could be used to guide the design of second-order NLO chromophores, exploiting the correlation between  $\beta$  and various factors associated both to the electronic properties of the molecular ground and first excited states only, as well as to structural parameters.<sup>15</sup> In this model, with the hypothesis of unidirectional charge-transfer (as it is the case for linear dipolar systems), the  $\beta$  results proportional to the change in the dipole moment ( $\Delta\mu$ ) between the two aforementioned energy levels, as reported in the following expression (Eq. 5):

$$\text{Eq. 5 } \beta = \beta_0 \frac{1}{\left[1 - \left(\frac{2\omega}{\omega_{eg}}\right)^2\right] \left[1 - \left(\frac{\omega}{\omega_{eg}}\right)^2\right]} = \left[ \frac{3}{2\epsilon_0} \frac{\Delta\mu \cdot \mu_{eg}^2}{(\hbar\omega_{eg})^2} \right] \frac{1}{\left[1 - \left(\frac{2\omega}{\omega_{eg}}\right)^2\right] \left[1 - \left(\frac{\omega}{\omega_{eg}}\right)^2\right]}$$

where  $\beta_0$  represents the intrinsic second-order hyperpolarizability,  $\mu_{eg}$  is the transition dipole moment,  $\hbar\omega_{eg}$  the energy gap between the two involved energy levels and  $\omega$  the frequency of the interacting radiation.

Starting from this model, Marder and co-workers proposed an approach that correlates the hyperpolarizability  $\beta$  to the degree of molecular ground-state polarization, the latter in donor-acceptor polyenes being related to a geometrical parameter named Bond Length Alternation (BLA).<sup>16,17,18</sup> The BLA parameter can be defined as the average of the difference in length between adjacent carbon-carbon bonds in polymethine chain<sup>19</sup>, thus its magnitude changes according to bond order, which in turn depends on the relative contribution of the two limiting resonance forms discussed above in defining the fundamental state of NLO-phore (**Figure.3**).

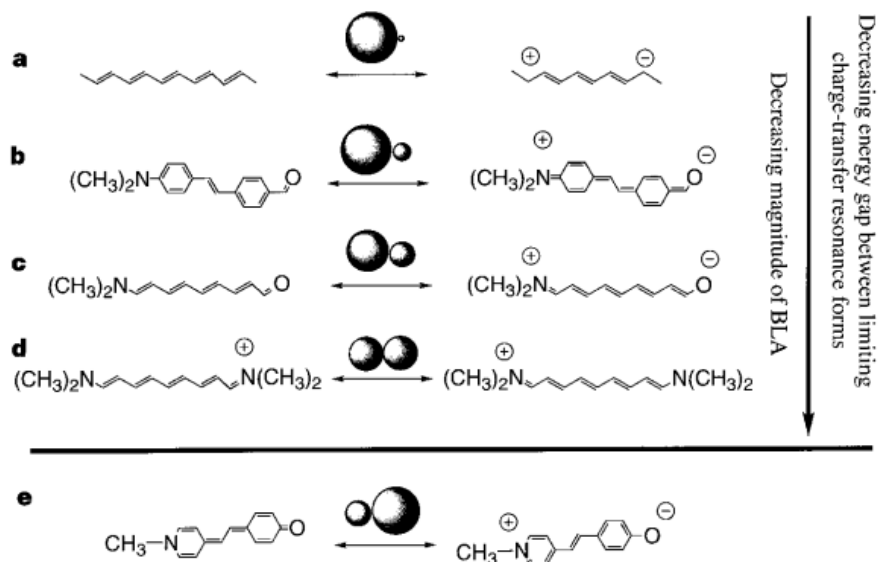


**Figure. 3:** Illustration of the decrease in BLA as the two resonance forms contribute more equally to the molecular ground state structure.

For substituted polyenes with weak donors and acceptors, the neutral resonance form dominates the ground-state wavefunction, and the molecule has a high degree of BLA. With stronger donors and acceptors, the contribution of the zwitterionic charge-separated resonance form increases, and BLA decreases. When the two resonance forms contribute equally to the ground-state structure the molecule exhibits essentially no BLA. This zero BLA limit is the so-called cyanine limit, which is represented by two degenerate resonance forms. Finally, if the charge-separated form dominates the ground-state wavefunction, the molecule acquires a reversed BLA pattern.<sup>20</sup>

It was found that it is possible to relate the second-order NLO parameter to the BLA: the discovered dependence varies in a sort of sinusoidal manner demonstrating that  $\beta$  does not monotonically increase with the strength of the donor and acceptor groups but on the contrary exists an optimal combination of donor, acceptor and conjugated bridge to gain higher NLO responses (**Figure.4**). The BLA approach provided the rigorous correlation existing between specific structural properties and NLO response, boosting a strong advancement in the field in the last decade.

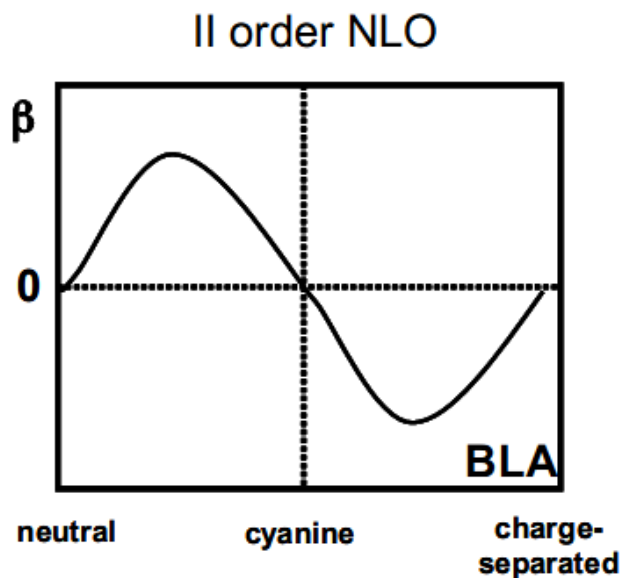


Figure. 4: Plot of  $\beta$  versus BLA

### 1.1.2 AUXILIARY DONOR/ACCEPTOR STRATEGY

Within the framework of classical "two-state model" another strategy has emerged for enhancing the molecular hyperpolarizability  $\beta$ , namely the auxiliary donors and acceptors model.<sup>21</sup> This approach basically correlates the molecular hyperpolarizability with the electron density of the  $\pi$ -conjugation, arguing that electron-excessive/deficient heterocycle bridges act as auxiliary donors/acceptors, and leads to substantial increases in  $\beta$  values by increasing the electronic transmission between the donor and the acceptor end groups, thus enhancing both the transition moment and the change in the molecular dipole moment.

In designing NLO-phores, several groups have developed systems containing easily delocalizable five-membered and six-membered heteroaromatic rings to overcome the problem of saturation of molecular nonlinearity in structure containing aromatic spacers.<sup>22,23</sup> The latter phenomenon originates from the barrier due to the aromatic delocalization energy of the benzene ring which can be successfully overcome exploiting the tunability of the electronic properties characteristic of heteroaromatic moieties.<sup>24,25,26</sup> Theoretical as well as experimental studies in fact evidence how the replacement of the homocyclic benzene ring on the donor/acceptor ends with heteroaromatic substituents results in clear  $\beta$  values increase.<sup>27,28,29</sup> Investigations on the origin of the second-order NLO response variation demonstrates the co-participation of two main effects: the lower delocalization energy of heteroaromatic rings on the one hand, and the augmented bridge electron density on the other hand.<sup>30</sup> An in-depth analysis of the phenomenon permits to distinguish aromaticity from electron density effects, demonstrating that the latter plays the major role in determining second-order NLO response properties; the computed  $\beta$  values in fact do not follow a simple increasing pattern expected from the decreasing order of aromaticity of the inserted rings. Furthermore the NLO response depends strongly not only on the nature but also on the location of the heterocyclic ring (i.e., connection



at the donor or at the acceptor end). Recently in the literature a few publications concerning thiazole<sup>31,32</sup> five-membered heterocycle substituents have emerged, which demonstrate also the critical issue of the regiochemistry of insertion. When the thiazole ring is in fact connected at the acceptor group through the electro-poor carbon C2 (or analogously at the donor group through the electron-rich carbon C5) a "matched" situation takes place which enables a molecular dipole moment reinforcement. In such a case the  $\beta$  value is higher than that characteristic of a "mismatched" situation. Further proves demonstrating the fact that the auxiliary donor/acceptor effect primarily influences the molecular dipole moments<sup>33</sup> come from the predicted stronger effect on the hyperpolarizability when thiazole is adjacent to the electron acceptor, rather than to the electron donor, both inserted in a "matched" configuration.

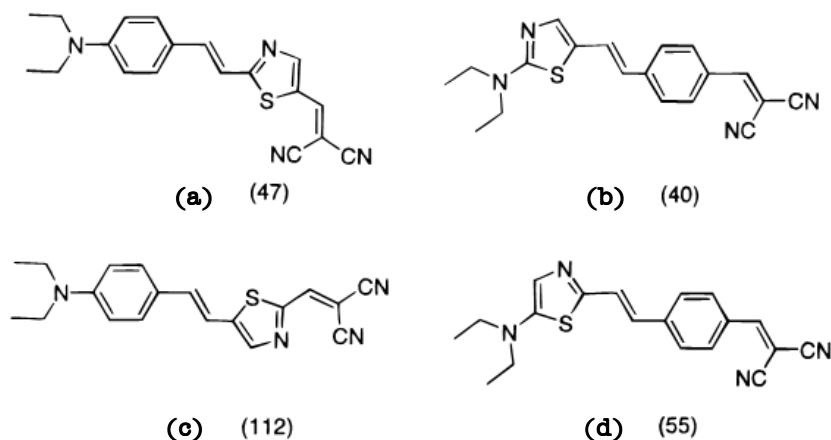


**Figure 5: The role of thiazole location and regiochemistry of insertion (a) mismatched on the acceptor, (b) mismatched on the donor, (c) matched on the donor, (d) matched on the acceptor.  $\beta$  values (1907 nm) are reported in parenthesis in units of  $10^{-30}$  esu.**

Therefore it is possible to infer that electron-excessive heterocycles act as auxiliary donors due to the exhibition of a lesser tendency to deplete charge from end donor substituents, hence increasing the donor ability. Similarly, electron-deficient heterocycles act as auxiliary acceptors, withdrawing electron density from end acceptor substituents, and hence increasing the acceptor ability.

### 1.1.2 TWISTED ZWITTERIONIC SYSTEMS

The two strategies reported so far focus primarily on extensive planar  $\pi$ -conjugation. Such kind of molecules presents evident limitations: they are inherently structurally complex, complicating synthetic access and introducing potential chemical, thermal and photochemical frailties. Extended conjugated systems usually show bathochromic shifts in optical excitation, thus eroding transparency at the near-IR working wavelengths of many photonic applications (1300 nm and 1500 nm) and, above all, not significant enhancements in hyperpolarizability have recently been obtained exploiting the above mentioned approaches. Interestingly, it has been argued by Kuzyk<sup>34</sup> that the  $\beta$  responses of all organic NLO-phores prepared to date fall far short of the theoretical fundamental quantum limits by a factor of  $\sim 10^{-3/2}$ . Therefore, alternative paradigms for very large  $\beta$  chromophores would clearly be desirable, and there is growing evidence that simple two-state model systems are inadequate.<sup>35</sup> In this regard, computational investigation has proven extremely valuable in suggesting new candidate species and in understanding the nature of their nonlinear response; recent theoretical works by Marks and Ratner suggest that unconventional chromophores with twisted  $\pi$ -electron systems bridging donor and acceptor substituents (TICTOID = twisted intramolecular charge-transfer) may exhibit unprecedented hyperpolarizabilities through non-classical mechanisms.<sup>36,37,38</sup> In the TICT response mechanism, rotation about a bond connecting the conjugated substituents can reduce the overlap between the orbitals of the donor/acceptor groups; as a consequence, such twist-induced reduction in D- $\pi$ -A conjugation leads to aromatic stabilization and formal charge-separated zwitterionic ground-state, relatively low-energy optical excitation, and large dipole moment changes from the ground to the first excited state.

One fundamental characteristic of such systems is that the optical response (linear and nonlinear) is sterically tunable via modification of the interplanar dihedral angle  $\theta$  between twisting moieties (**Figure.6**).<sup>35</sup>

Model exact hyperpolarizabilities of push-pull polyenes reveal in this regard maximization of the SHG coefficient at twist angle between  $65^\circ$  and  $85^\circ$ , and between  $95^\circ$  and  $135^\circ$ , while near-vanishing SHG coefficients at  $90^\circ$ . The latter effect is explicable, within a simple Hückel picture if one considers that the transfer integral, which scales as the cosine of the twist angle, vanish near  $90^\circ$ .

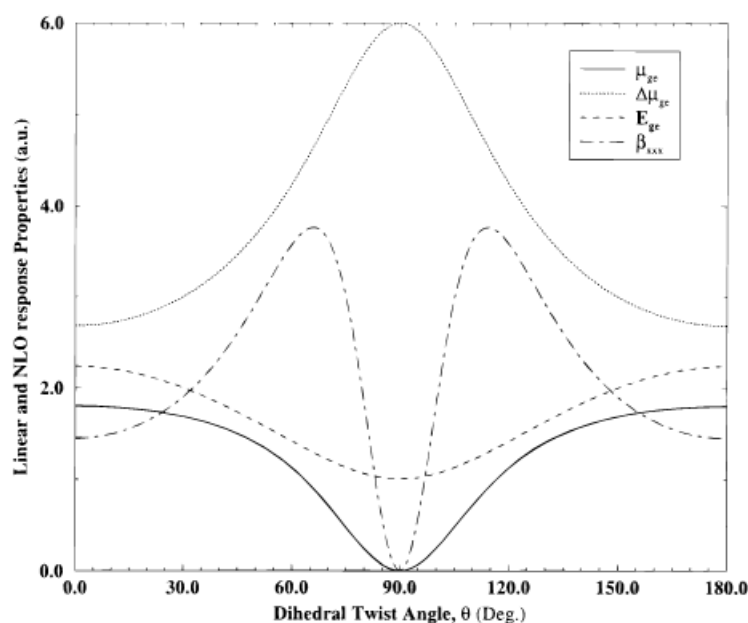
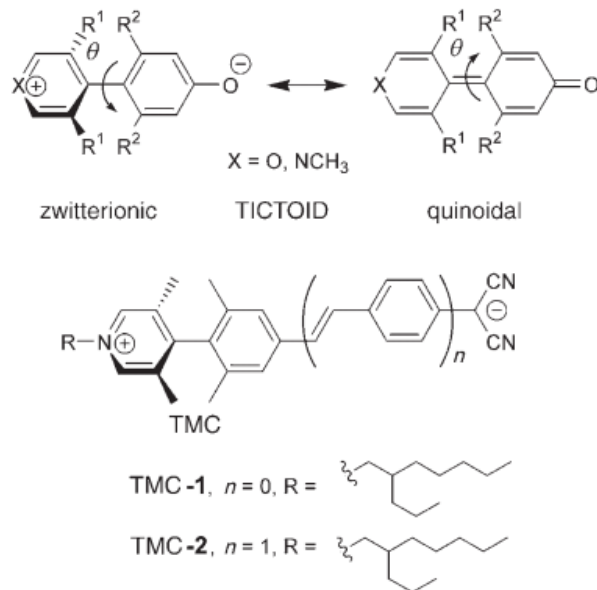


Figure. 6: Variation of the linear optical parameters  $\mu_{eg}$ ,  $\Delta\mu_{eg}$ ,  $E_{eg}$  and the dominant component of the first hyperpolarizability as a function of the dihedral twist angle

In addition to the aforementioned, twist-angle dependent variation of linear and nonlinear response properties in twisted  $\pi$ -conjugated systems, there are other optical features in these structure at angle of  $90^\circ$ ; at such angle the disruption of conjugation also implies that these systems can be ideally represented by two disjoint molecular subfragments and that the linear absorption of the individual subfragments (intra-subfragment excitation) should be observable, in addition to a weak charge-transfer excitation (inter-subfragment).

Experimental studies have demonstrated efficient synthesis and exceptional ultralarge molecular hyperpolarizabilities in zwitterionic twisted  $\pi$ -electron system heteroaromatic biaryls (**Figure.7**).



**Figure. 7: Structures of TICTOID and TMC (twisted  $\pi$ -electron system molecular chromophore)**

Facchetti and co-workers<sup>39,40</sup> recently reported the first realization of such TICTOID chromophores which shows unprecedented hyperpolarizabilities on the order of 10-20x larger than previously observed ( $9800 \times 10^{-30}$  esu), thus reaching nonresonant  $\mu\beta$  values as high as  $-488000 \times 10^{-48}$  esu; these are to our knowledge the largest values ever achieved for any molecules reported in the literature.

In summary, unconventional theory-inspired twisted  $\pi$ -electron system chromophores have been introduced and developed which present peculiar linear and nonlinear features, enabling optical responses far larger than those of conventional organic  $\pi$ -conjugated NLO-phores; analyzing the structure-properties relation it is possible to infer that the principal factor that affects the linear and NLO response in such TICTOID chromophores is in the ease with which charge separation can be affected and how the charge separation is stabilized.

## II. RESULTS & DISCUSSION

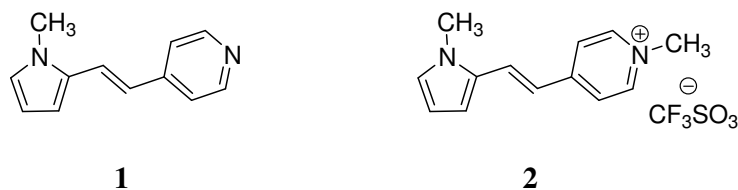
It is herein introduced a broad class of heteroaromatic  $\pi$ -conjugated systems for application in the telecommunications, the following section represents our latest contribute to the field of second-order NLO organic materials, with particular interest for electro-optics devices. Basic starting point for the realization of such molecular materials has been the deep expertise of our research group in the field of heteroaromatic NLO dyes and their supramolecular assemblies for advanced photonics. In designing such systems at the molecular level, the three previously reported theoretical approaches have been followed in this work, exploiting the potentiality of their combination with the peculiar electrical and optical features of heteroaromatic rings. At the supramolecular level the most important literature strategies were used for achieving active electro-optic functional materials, namely: poled host-guest polymers, self-assembled monolayers (SAMs), physical-vapor deposited thin films.

It is possible to recognize in the strategy reported here a continuing evolution of our systems, which have been finely tailored to match the requests for enhanced performance-stability tradeoffs. The investigation starts from our well-known literature push-pull benchmark chromophores, with the introduction of the auxiliary donor/acceptor concept in order to examine the effect of such secondary groups on the NLO molecular response. The second molecular approach consists of zwitterionic charge-separated derivatives in which either carbanions or nitranions constitute the electron-donating moieties, while different azines behave as the acceptor; particular interest is devoted in this contest to the heteroaromatic tetrazole ring, inserted as possible donor group. The final and most challenging development of this last class of compound was focused on the attainment of fully heteroaromatic twisted  $\pi$ -conjugated systems.

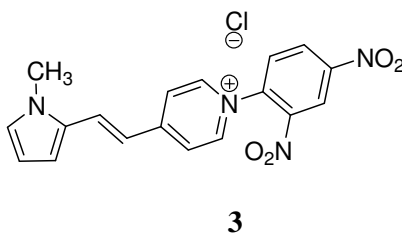
## II.1 AUXILIARY DONOR/ACCEPTOR HETEROAROMATIC SYSTEMS

### 1.1 DESIGN & SYNTHESIS

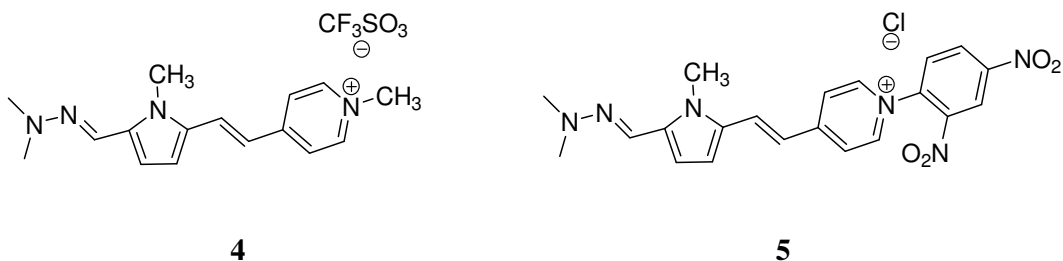
In order to properly exploit heterocycles, and thus tune the intramolecular charge transfer (ICT) in  $\pi$ -acceptor/ $\pi$ -donating systems, a detailed knowledge of their properties is required. In the past years our research group have undergone a systematic study aimed at elucidating and quantitatively rank the electron-acceptor properties of  $\pi$ -deficient six-membered (e.g. azines, 1,3-azoles, triazoles, and purines) and  $\pi$ -excessive five-membered (furan, thiophene, pyrrole) heteroaromatic rings.<sup>41,42,43,44</sup> In this way it has been experimentally ascertained that heterocyclic azines behaves as strong acceptor groups whose electron-withdrawing power has been proved ranking on the same scale of primary  $\pi$ -deficient organic functionalities;<sup>45,46</sup> on the other hand, the electron richness of  $\pi$ -excessive five-membered heterocycles makes these latter systems particularly suitable as tunable donor moieties. Therefore our design strategy for auxiliary donor/acceptor molecules starts from heteroaromatic NLO-phores previously introduced by us and widely studied for their peculiar features and NLO response at the second and third order;<sup>6,47</sup> the basic reference system embodying our dipolar NLO prototype is the highly conjugated push-pull chromophore **1** in which the donor moiety (D) is represented by the five-membered  $\pi$ -excessive pyrrole, whilst the acceptor group (A) is the  $\pi$ -deficient heterocyclic pyridine. Alkylation of the pyridyl nitrogen atom further increase the electron-withdrawal of the six-membered ring, thus favoring the push-pull characteristics of the system. The methylated chromophore **2** represents an easy entry into the class of unsymmetrical cyanine dyes that, together with merocyanines and hemicyanines, exhibit considerable interest for NLO properties.



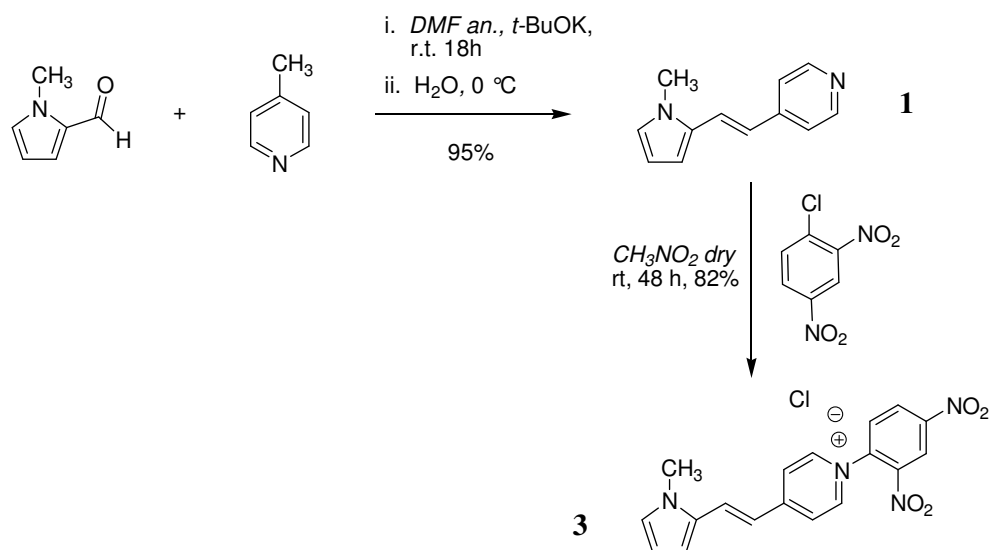
The effect of auxiliary acceptor groups has been pioneered with the introduction of molecule **3** in which the electron-withdrawing power of the parental pyridine ring has been enforced throughout alkylation with the additional acceptor (A') 2,4-dinitrophenyl, leading to the chemical structure sequence DAA'.



In derivatives **4** and **5** the insertion of a supplemental donor component was studied through the introduction of the strong hydrazono group ( $R_2N-N=$ ), capable of efficiently delocalizing an electron pair residing on the terminal nitrogen atom, onto the molecule  $\pi$ -conjugated system. It is surprisingly in this regard the absence in literature, with very few exceptions,<sup>48,49,50</sup> of such important donor organic functionality. In the reported structures (DD'A for **4** and DD'AA' for **5**) of the examined chromophores, the pyrrole ring acts as the auxiliary donating moiety.

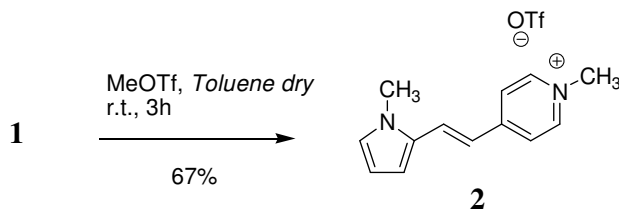


Compound **1** was obtained through a slight modification of the original methodology already reported in the literature by us<sup>47</sup>: in anhydrous DMF 4-picoline was deprotonated with potassium *t*-butylate and then condensed with *N*-methylpyrrole-2-carboxyaldehyde, giving the desired product in nearly quantitative yield after a 18-hours time reaction. Molecule **3** was synthesized from this precursor through nucleophilic aromatic substitution on 1-chloro-2,4-dinitrobenzene; the reaction was easily conducted in dry nitromethane to give the final adduct in high yield as a dark-red solid, after reacting 2 days at room temperature (**Scheme.1**).



Scheme. 1

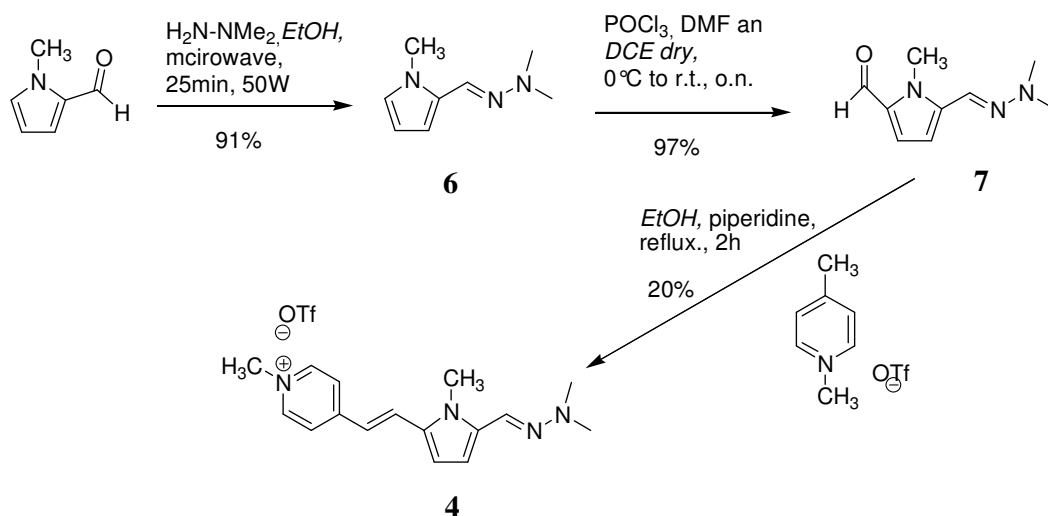
The methylated derivative **2** of the prototype push-pull parental dye was formed according to literature by alkylation in toluene under dry conditions with methyl trifluoromethanesulfonate (**Scheme.2**).



Scheme. 2

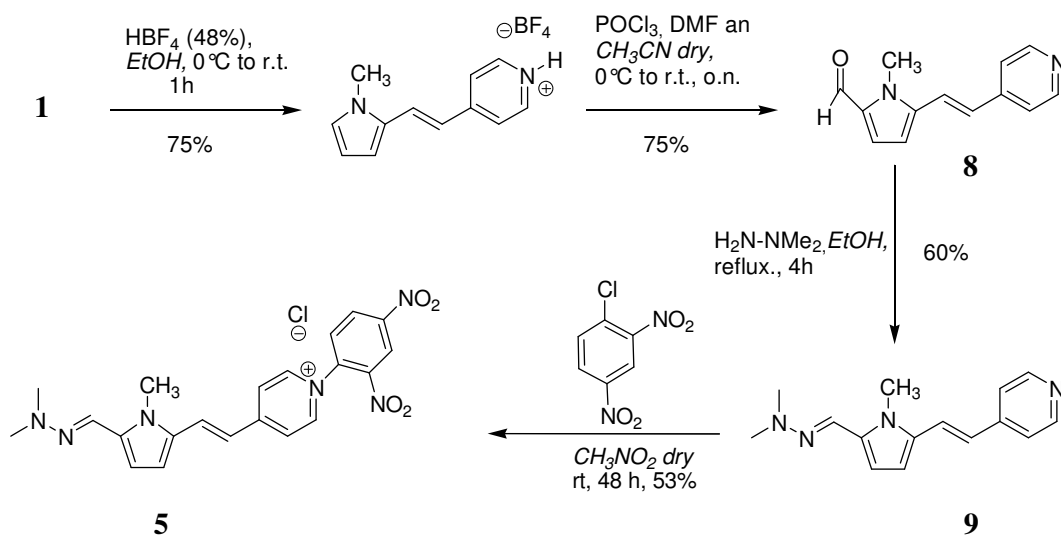


DD'A chromophore **4** was prepared following the synthetic procedure recently reported by our group in the literature<sup>51</sup>; here the acceptor group is inserted on the pyrrole ring after the insertion of the donor moieties, in order not to depress the reactivity of the heterocyclic aldehyde toward nucleophiles due to the electron-withdrawing effect of the acceptor substituent. *N*-methylpyrrole-2-carboxyaldehyde therefore was firstly converted under microwave irradiation to the corresponding hydrazone **6** by reaction with dimethylhydrazine. Formylation at the pyrrole 5-position was then achieved following Vilsmeier-Haak protocol with DMF/POCl<sub>3</sub> in dry dichloroethane; the reaction proceeds toward the desired product **7** very easily in quantitative yield, thanks to the enhanced reactivity of the activated  $\alpha$  position of the 5-membered ring. In the final step, condensation with 4-methylpicolinium triflate performed in Knoevenagel conditions (catalytic piperidine in refluxing ethanol) introduces the acceptor group. The reaction mixture is treated with CH<sub>2</sub>Cl<sub>2</sub> and washed with water affording the crude product which is purified through crystallization in EtOH (**Scheme.3**).



Scheme. 3

The synthetic pathway to obtain compound **5** starts from system **1** and involves Vilsmeier-Haak formylation at the electron-rich position of pyrrole. According to literature,<sup>51</sup> it was in fact possible in this case to perform the donor insertion directly on the acceptor-containing precursor **8**; this procedure evidences the lower electron-withdrawing capacity of the non-alkylated pyridine comparing to the methylated ring, reducing to a minimum the reactivity depression of the aldehydic functionality in system **8**. It is worth noting that direct formylation of **1** is not possible to achieve anyway because of interactions with the POCl<sub>3</sub>/DMF adduct giving rise to partial decomposition of the formylating species and to the formation of a number of byproducts;<sup>52</sup> precursor **1** is therefore primarily protected at the pyridic nitrogen with tetrafluoroboric acid. Condensation of the obtained formylated species **8** with dimethylhydrazine in refluxing ethanol, leads to the insertion of the hydrazono donor moiety in good yields (**Scheme.4**) to give push-pull molecule **9**. The latter is let react 48 hours in dry nitromethane with 1-chloro-2,4-dinitrobenzene following the same reaction procedure reported for compound **3**. The reaction mixture in the final reaction step is then poured into Et<sub>2</sub>O leading to the pure product **5** which precipitates as a dark solid.



Scheme. 4

### 1.2 LINEAR OPTICAL CHARACTERIZATIONS & MODELING\*

A summary of the linear optical experimental responses for the studied systems DAA' (**3**) and DD'AA' (**5**) is reported in **Figure.8**, compared to the well-known parental dye DA (**2**).

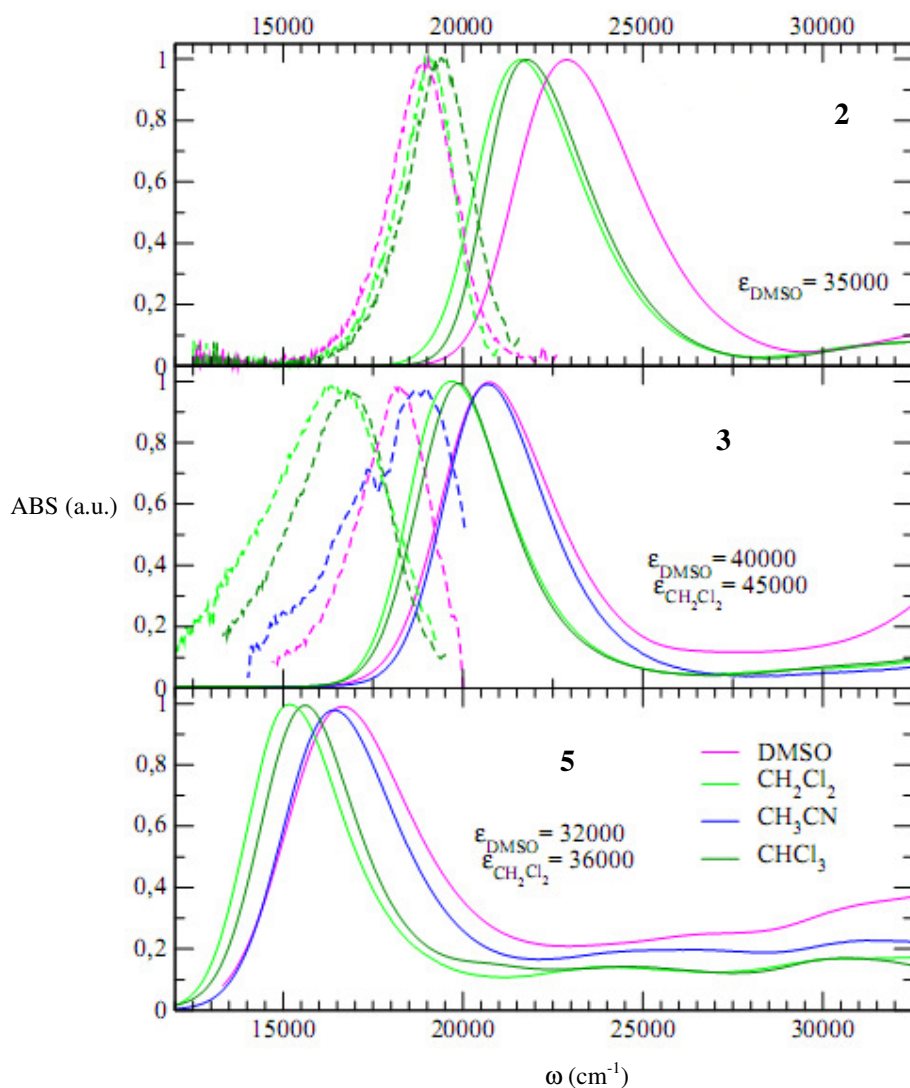


**Figure. 8:** Linear absorption (full lines, right scale) and emission (dotted lines, left scale) spectra for the studied systems **2, 3, 5**

\* The reported modeling was computed by Prof. Anna Painelli and co-workers at the University of Parma, Department of Chemistry GIAF.

Absorption and emission spectra in organic solvents of different polarities were registered for all the compounds, which resulted substantially insoluble in the most common non-polar solvent (including toluene and  $\text{CCl}_4$ ), as expected due to their saline nature, while exhibiting different levels of solubility in increasing polar medium ( $\text{CH}_2\text{Cl}_2$ ,  $\text{CHCl}_3$ ,  $\text{CH}_3\text{CN}$ , DMSO). In the spectral range between 310 – 850 nm a single absorption ICT broad band was registered for all the systems (**2**: 437 nm, **3**: 483 nm, **5**: 598 nm), compound **5** indeed shows two higher energy transitions at 385 nm and 327 nm. Fluorescence responses resulted very weak for compound **3** (quantum yields < 1%), whilst no linear emission was detectable for chromophore **5** in the spectral region accessible to our spectrofluorimeter (no intense fluorescence emission is in any case expected for this compound considering the complete absence of any emission tail in the registered spectral range); fluorescence obtained for dye **2** confirms the emitting behavior reported in the literature, in our previous works.<sup>6,53</sup>

A significant solvatochromic effect is clearly detectable for all the systems, which follows the medium polarity: a substantial red-shift of the absorption band maximum is registered for all the chromophores moving from dichloromethane to dimethylsulfoxide. Analogous trend is detected for the fluorescence emission of **3**, whilst inverted behavior is observed for **2**. It is worth noting both for compound **3** and **5**, the presence of an absorption band peak shift in dichloromethane, depending on the solution concentration; it has been detected in fact an asymptotic red-shift of the absorption maximum with decreasing solution concentration in the range  $5 \times 10^{-5}$  –  $1 \times 10^{-6}$  M. This behavior is explicable with the occurrence of blue-shifted absorbing aggregates in such a solvent; in **Figure.9** a deconvolution of compound **5** absorption band is reported, where the extrapolated absorption for the aggregated species is also shown. Unfortunately it was not possible to gain further spectroscopic data concerning the aggregate (e.g. stoichiometry, emission spectra, molar extinction coefficient), thus its reported molar extinction coefficient value represents only an indicative estimation.

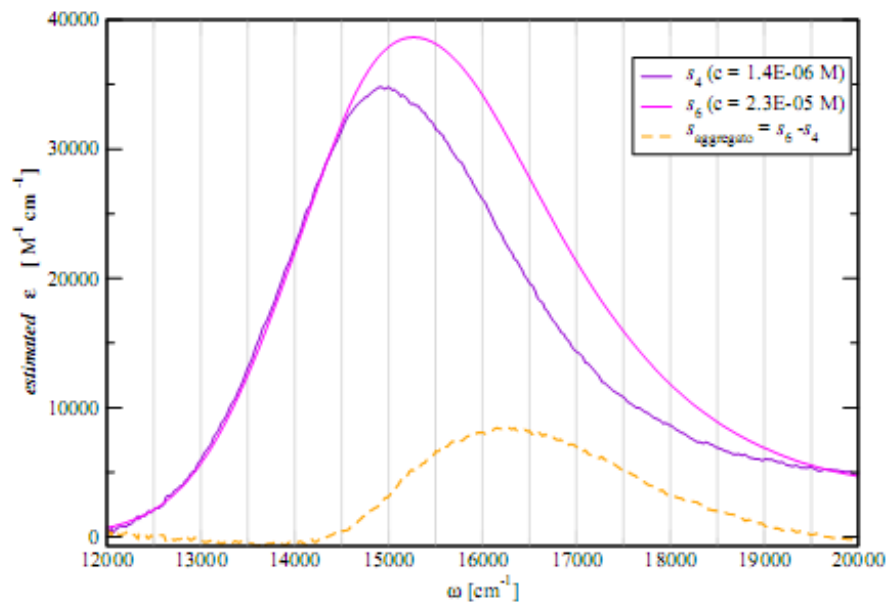


**Figure. 9:** Estimated linear absorption spectrum for the aggregate (dotted line) of system **5** in  $\text{CH}_2\text{Cl}_2$  obtained by subtraction of two spectra of **5** at different concentrations

Fundamental cause of the above reported behaviors is the intrinsic charged nature of the systems, which gives rise to strong intermolecular as well as molecule-solvent interactions.

Photochemical stability in solution was explored for compound **3** and **5** in DMSO. The former system results instable in solution when exposed to the light radiation, especially for dilute solution, as observed during fluorescence emission analysis. Linear absorption measurements conducted during such experiments show a progressive reduction of the ICT transition at 483 nm and the simultaneous appearance of a band centered at 365 nm. In the same solvent, chromophore **5** resulted even more instable: the absorbing behavior changes dramatically when exposed to light, with the appearance of three new absorption bands at 420 nm, 375 nm, 320 nm, which rapidly become more intense than the fundamental ICT one. In this latter case, the formed species results fluorescent (intense emission at 565 nm), thus its fluorescence emission spectra was detected experimentally, as reported in **Figure.10**.

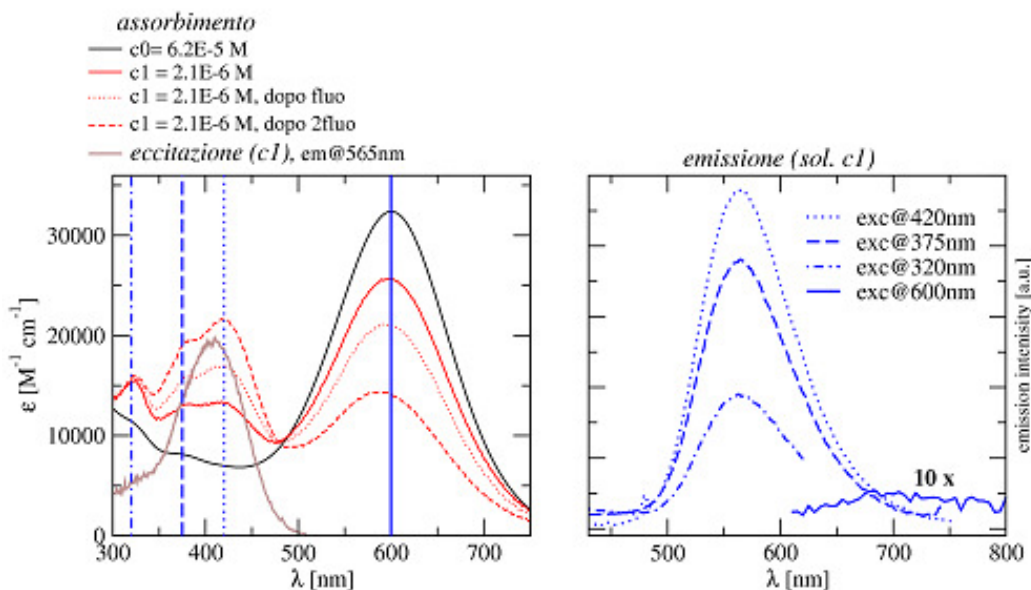


**Figure. 10: Photostability of system 5. Linear absorption spectra with increasing light-exposure and excitation fluorescence spectra gained collecting radiation at the emission maximum (for the decomposition by-product) as detected during fluorescence emission experiments (left); emission spectra for the decomposition by-product obtained varying the excitation position (right)**

In the absence of reliable theoretical models for describing solvation of charged molecular systems, it was not possible to properly simulate solvatochromism, fluorescence emission, and correct absorption band structure for the above introduced saline chromophores; modeling of such systems is therefore quite simplified and as a result it was possible to reproduce only the transition position and its intensity (oscillator strength). The development of such simple model started from the experimental data obtained in DMSO, summarized in **Table.2**. Following the common approach used for analyzing donor-acceptor systems, the electronic structure of this molecular series was modeled throughout an opportune combination of fundamental states resulting from the possible resonance limiting forms. The basic idea here was to use a bottom-up approach: the description of the simplest parental dye **2** is transferred into the more complex systems, adding supplemental terms which take into account the donor and acceptor subunits introduced in the fundamental DA unit.

Chromophore	Abs Band	$\omega_{\text{Abs}}$ (cm <sup>-1</sup> )	$\epsilon$ (M <sup>-1</sup> cm <sup>-1</sup> )	Oscillator strength
<b>2</b>	CT	22900	35000	0.65
<b>3</b>	CT	20800	40000	0.73
	CT <sub>1</sub>	-	<3000	0
<b>5</b>	CT	16700	32000	0.65
	CT <sub>1</sub>	26000	<8000	<0.1
	CT <sub>2</sub>	30600	<11000	<0.2

Table. 2: Experimental data for the three systems, obtained from spectra in DMSO

- Two-state model for describing **2**

The two state model has already been used by us for modeling the chromophoric prototype **2** in a previously reported publication:<sup>54</sup> the two basic resonance forms  $|DA\rangle$  and  $|D^+A^-\rangle$ , which differ in energy for a quantity  $2z$  ( $z = 1$  eV) and whose combination is described by the element  $\tau$  ( $\tau = 1$  eV), define the ground and first excited electronic molecular states; whilst  $\mu_0$  and 0 represent the dipolar moment associated to the zwitterionic and the neutral state respectively.

- Three-state model for describing **3**

For chromophore DAA' **3** it is possible to conceive three main structures:  $|DAA'\rangle$  (at energy 0),  $|D^+A^-A'\rangle$  (at energy  $2z$ ) and  $|D^+AA'^-\rangle$  (at energy  $2x$ ). The mixing element between the neutral state  $|DAA'\rangle$  and the first zwitterionic state  $|D^+A^-A'\rangle$  being  $\tau$ , and that relative to the hopping between the acceptors of the two zwitterionic states  $|D^+A^-A'\rangle$  and  $|D^+AA'^-\rangle$  being  $\tau_A = \tau'$ . The dipole moment introduced for the second zwitterionic state  $|D^+AA'^-\rangle$  is  $\alpha\mu_0$  ( $\alpha = 1.5$ ) while the others are inherited unchanged from the two-state model above.

The Hamiltonian and the dipole moment operator for system **3** can therefore be expressed as follows:

$$\mathcal{H} = \begin{pmatrix} 0 & -\tau & 0 \\ -\tau & 2z & -\tau' \\ 0 & -\tau' & 2x \end{pmatrix} \quad \mu_0 = \begin{pmatrix} 0 & 0 & 0 \\ 0 & \mu_0 & 0 \\ 0 & 0 & \frac{3}{2}\mu_0 \end{pmatrix}$$

- Five-state model for describing **5**

For chromophore DD'AA' **5**, it is possible to conceive at least five different states, the neutral one  $|DD'AA'\rangle$  (at energy 0) plus four different mono-zwitterionic forms\*:  $|DD'^+A^-A'\rangle$  (at energy  $2z$ ),  $|D^+D'A^-A'\rangle$  (at energy  $2x$ ),  $|DD'^+AA'^-\rangle$  (at energy  $2y$ ) and  $|D^+D'A^-A'\rangle$  (at energy  $2z'$ ). Considering the significance of the on-site energy it is possible to assume immediately that  $2z' = 2x + 2y - 2z$ . It is then possible to define at least three different mixing integral:  $\tau$  between the neutral state and  $|DD'^+A^-A'\rangle$  state, and two more  $\tau_A$  and  $\tau_D$  relative to the hopping between the acceptors and the donors respectively; for simplicity it is possible to assume that  $\tau_D = \tau_A = \tau'$  of the DAA' system. The dipole moment is once again  $\mu_0$  for the  $|DD'^+A^-A'\rangle$  state,  $\alpha\mu_0$  for the mono-zwitterionic states  $|D^+D'A^-A'\rangle$  and  $|DD'^+AA'^-\rangle$ , while for  $|D^+D'A^-A'\rangle$  it is defined as  $\alpha'\mu_0$ , where  $\alpha' > \alpha$  (with  $\alpha = 1.5$  &  $\alpha' = 2$ ).

The Hamiltonian and the dipole moment operator for system **5** can therefore be expressed as follows:

$$\mathcal{H} = \begin{pmatrix} 0 & -\tau & 0 & 0 & 0 \\ -\tau & 2z & -\tau' & -\tau' & 0 \\ 0 & -\tau' & 2x & 0 & -\tau' \\ 0 & -\tau' & 0 & 2y & -\tau' \\ 0 & 0 & -\tau' & -\tau' & 2x + 2y - 2z \end{pmatrix} \quad \mu_0 = \begin{pmatrix} 0 & 0 & 0 & 0 & 0 \\ 0 & \mu_0 & 0 & 0 & 0 \\ 0 & 0 & \frac{3}{2}\mu_0 & 0 & 0 \\ 0 & 0 & 0 & \frac{3}{2}\mu_0 & 0 \\ 0 & 0 & 0 & 0 & 2\mu_0 \end{pmatrix}$$

---

\* The bi-zwitterionic state is located at high energy and thus it is not been taken into account here.



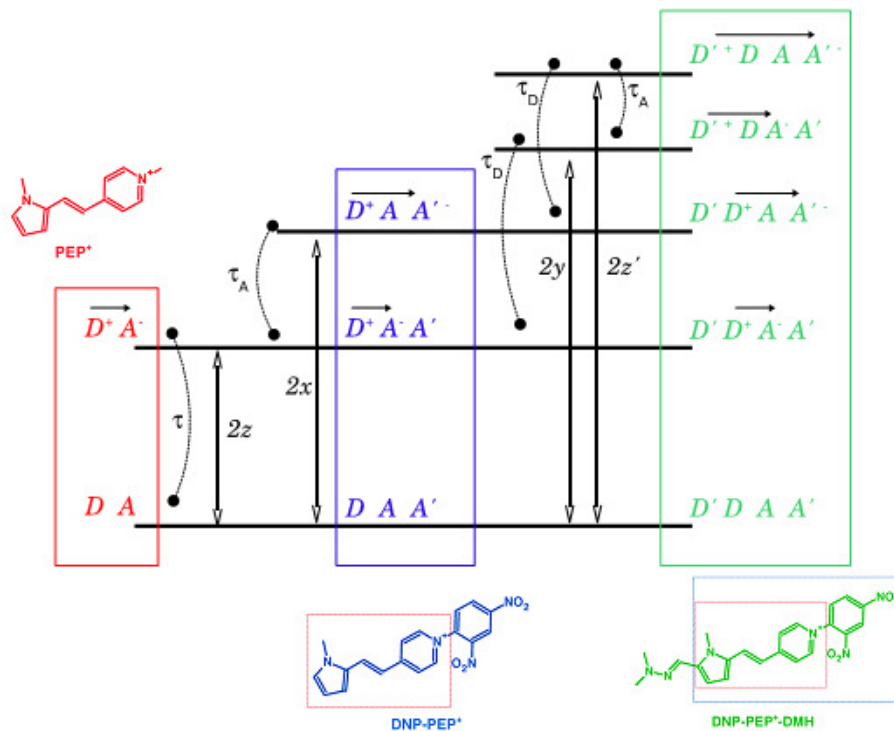


Figure. 11: General scheme of the molecular energy states as reported in the bottom-up approach

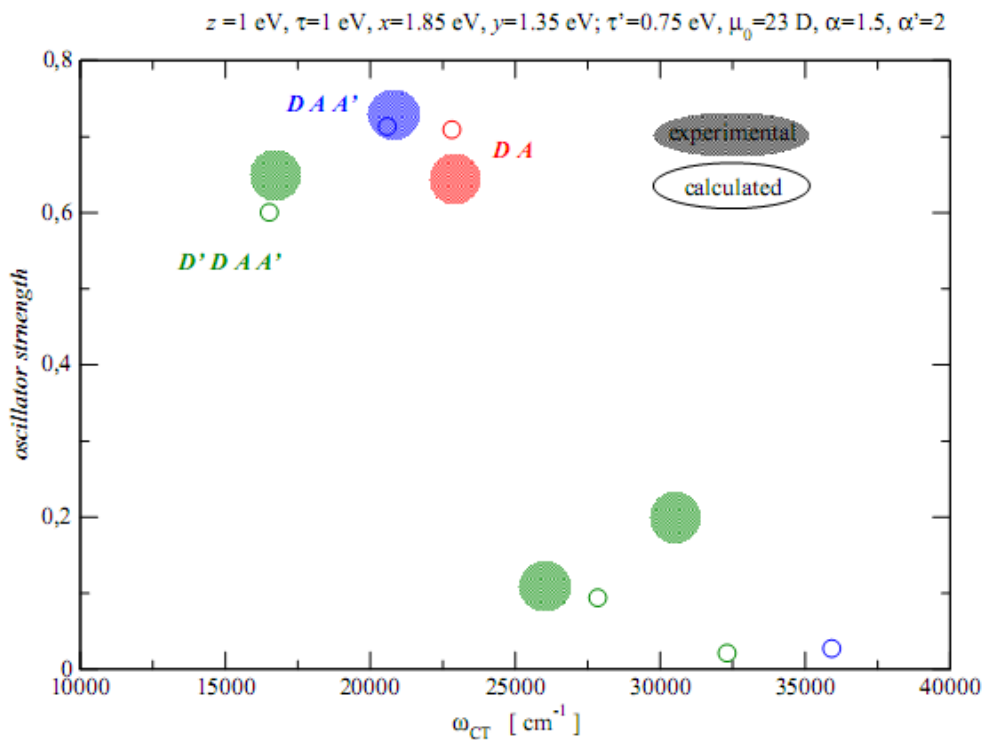
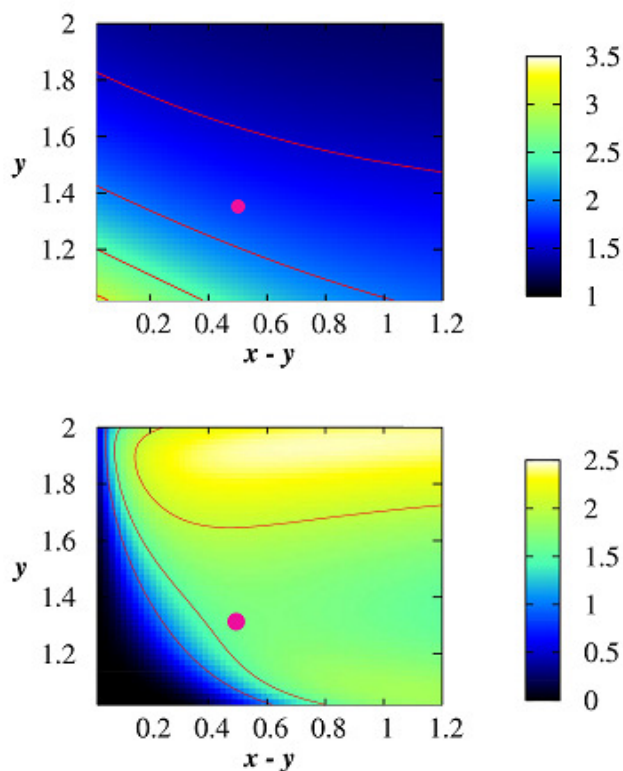


Figure. 12: Comparison between experimental and calculated data for the studied systems

The goodness of the introduced models can be verified by calculating the experimental parameters previously reported in **Table.2**; the comparison is expressed in **Figure.12** where the parameters set used in the model is reported. Once verified the reliability of the above calculations, it has been possible to exploit the introduced modeling to predict the NLO responses (mainly TPA and  $\beta$ ) for the reported system **5**, containing both auxiliary donor and acceptor moieties, focusing on the importance of both polarity effects and excited states energies.

In this regard it was studied the effect of the energies of the two fundamental zwitterionic states ( $2x$  and  $2y$ ) on the TPA response of the first two excited states. By using modeling parameters sets located in the region of the previously introduced ones, a two-fold increase of the two-photon absorption response with respect to system **2** has been calculated for these excited states, as reported in **Figure.13**.



**Figure. 13:** TPA response enhancement for compound DD'AA' with respect to system 2, for the first (up) and second (down) excited states, as calculated by the 5-state model. The pink spot indicates the position in the x and y region using the same parameters set reported in figure. 12. The energy values are in eV.

With the same approach the first hyperpolarizability was also predicted for system **5**; in this case both the intrinsic static hyperpolarizability ( $\omega \rightarrow 0$ ) and the  $\beta$  response at fixed wavelength (commonly  $\beta$  @ 1064 nm) were predicted. The obtained results reported in **Figure.14**, highlight a very good second order response, showing at least a basic three-fold enhancement of both the static and wavelength-dependent hyperpolarizability with respect to the  $\beta$  response characteristic of the molecular archetype **2**.

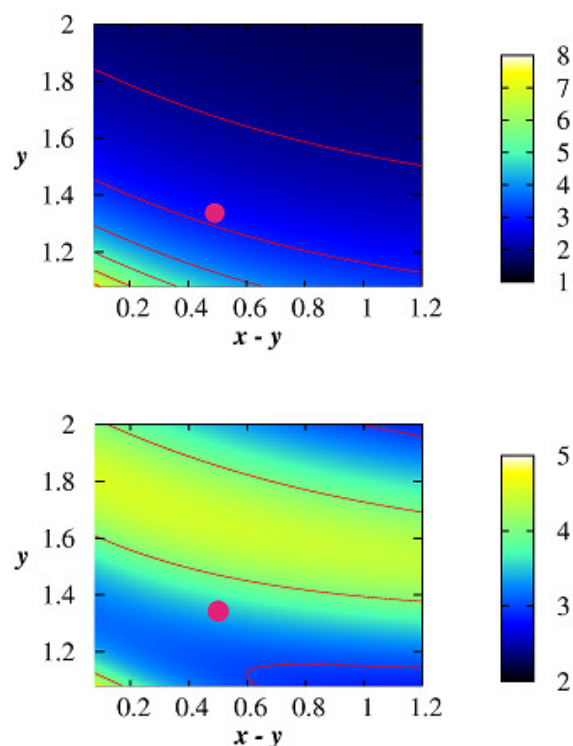


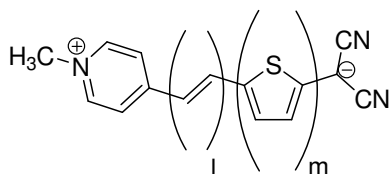
**Figure. 14:**  $\beta$  response enhancement for compound DD'AA' with respect to system **2**, as calculated by the 5-state model: static  $\beta$  (up) and  $\beta$ @1064 (down). The pink spot indicates the position in the  $x$  and  $y$  region using the same parameters set reported in figure. 12. The energy values are in eV.

The data obtained from the reported modeling evidence how the DD'AA' chromophoric system **5** represents a valid breakthrough in the field of auxiliary donor/acceptor containing push-pull dyes to gain enhanced molecular NLO features. This new system is the results of a valuable method to increase the optical response of simple DA systems, such as the parental dye **2**, through a facile and *ad oc* functionalization.

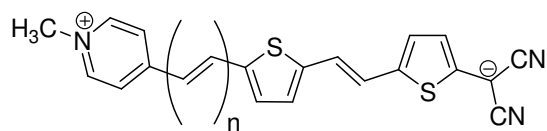
In summary, a combination of organic design and synthesis, linear optical absorption and emission spectroscopy, photostability measurements, structure modeling and NLO properties computations has been applied to the investigation of a new family of dipolar donor-acceptor compounds based on co-donors and co-acceptors end groups. The insertion of supplemental acceptor and donor groups, as well as the role played by heterocyclic  $\pi$ -excessive and  $\pi$ -deficient rings, have been taken into account to study their effect on linear and nonlinear optical properties. Despite the huge number of dipolar compounds showing NLO activity reported in the literature, the concept of combining the donor properties of the hydrazono group and the auxiliary donor effects of electron-rich heteroaromatic rings represents a completely new peculiar approach of our research group; also the idea of enforcing the accepting characteristic of the pyridine ring through alkylation of the heteroaromatic nitrogen with a strong acceptor moiety (such as the 2,4-dinitrophenyl) represents an uncommon answer to the request for enhancing the molecular NLO response. This multidisciplinary study has demonstrated, through a computational approach, that this class of chromophores is endowed with good second-order molecular NLO activity; the computed first hyperpolarizability and TPA response of compound **5** demonstrating more than a three-fold and two-fold increment respectively, compared to the simple push-pull archetype **2**. The linear optical analysis shows a substantial red-shift in the absorption and emission spectra, accompanied by aggregation effects at high solution concentration, as expected due to the insertion of stronger donor/acceptor moieties and to the presence of charged sites on the molecules. The major drawback for these systems is the relative low photostability threshold imputable to the low optical gap, which makes the molecules prone to photodamages in the visible region of the spectra, and once again to their fundamental ionic nature. Investigation of the experimental NLO properties in solution as well as in the bulk of host-guest and side-chain materials is currently in progress.

## II.2 ZWITTERIONIC HETEROAROMATIC SYSTEMS

Considering the various examples reported in the literature and keeping in mind the two-state model, it has been shown previously that the generation of highly efficient NLO-phores with a large quadratic hyperpolarizability requires extensive molecular polarization of the  $\pi$ -electron structure, usually provided by means of a strong interaction between end-capped donor and acceptor groups, this situation giving rise to a dominant intramolecular charge-transfer (ICT) transition from the ground state to the first excited state. Furthermore, both the sign and value of  $\beta$  have been correlated with the molecular structure by means of the BLA parameter: in the plot of  $\beta$  against BLA, for push-pull polyenes, the hyperpolarizability moves in fact from positive (BLA > 0, neutral ground state) to negative (BLA < 0, dipolar ground state), with values passing through zero (BLA = 0, cyanine limit) depending on the energy gap between the two resonance limiting forms and thus on their relative contribution in defining the molecular ground state. In contrast to the most common methodology reported in the literature, in the last years our group pioneered the un-conventional approach of designing NLO molecules which present a dipolar zwitterionic aromatic ground state retaining a quinoid structure in the neutral resonance limiting formula.<sup>55</sup> The archetypal NLO-phores of such alternative approach are mainly represented by our thiophene-spaced *N*-alkylpyridinium dicyanomethanides **10**.



- a:  $l = 0; m = 1$   
 b:  $l = 0; m = 2$   
 c:  $l = 1; m = 1$

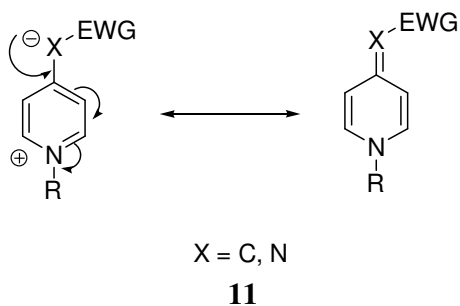


- d:  $n = 0$   
 e:  $n = 1$

In these molecules proper combination of various optimization strategies led to the exploitation of an *N*-alkylpyridium  $\pi$ -deficient ring as the acceptor moiety, a negatively charged dicyanomethanide carbanion as the donor group, and a  $\pi$ -excessive thiophene ring as the  $\pi$ -conjugated spacer group. The zwitterionic nature of this class of heteroaromatic system has been widely investigated and confirmed by us through a vast set of experimental analysis as well as calculations, demonstrating the strict connection between occurrence of high dipole moment in the ground state, large negative solvatochromism, and first hyperpolarizability. Accordingly to the two-states model, dyes **10** exhibit in fact large negative  $\beta$  values, mainly due to the very high molecular dipole moment of the ground state (preferentially described by the charge-separated aromatic resonance limiting form), and in turn to the large difference between dipole moments in the neutral-quinoid and zwitterionic-aromatic structures. The electro-optic figure of merit  $\mu\beta_0$ , which enables to take into account the above mentioned structural features, reaches for system **10c** the notable value of  $-6990 \times 10^{-48}$  esu (in  $\text{CHCl}_3$ ) which is among the highest ones ever reported in the literature for this kind of systems. These results clearly illustrates the reliability of the reported novel approach toward high-performance NLO-phores; we realized, however, for the above mentioned zwitterions, the solvent polarity to have a great influence on ICT and thus on  $\beta$ . Structure-stabilizing effects due to solvent-dye intermolecular interactions, in fact, have been proven to strongly impinge on the relative weights of the two limiting forms in describing the molecular ground and excited states, thus affecting the linear and nonlinear optical responses. In short, the large second-order molecular NLO activities of these structures can only be reached if medium polarity effects are carefully taken into consideration, this results particularly important when moving toward chromophore-containing bulk functional materials: an excellent NLO response in solution in fact might vanish when the active chromophore is dispersed in a matrix with unsuitable dielectric properties.

## 2.1 PYRIDONEMETHIDES & PYRIDONEIMINES

The above reported findings prompted us to investigate further the solvent response of the zwitterionic systems. In this regard, our research group developed a new class of pyridine-based push-pull derivatives having the general formula **11**, demonstrating the possibility of finely tuning the intramolecular charge-transfer and the  $\pi$ -electron distribution by varying the nature of the electron-withdrawing groups (EWG), the bridging site (X), and the solvent polarity.<sup>56</sup> On the basis of multinuclear NMR analysis and exploitation of shift/ $\pi$ -electron density relationships, accompanied by solvatochromic data, it was provided evidence of how such systems could experiment a whole range of push-pull electron structures, from fully aromatic-zwitterionic to quinoid-neutral forms, going through all the intermediate situations along the path.

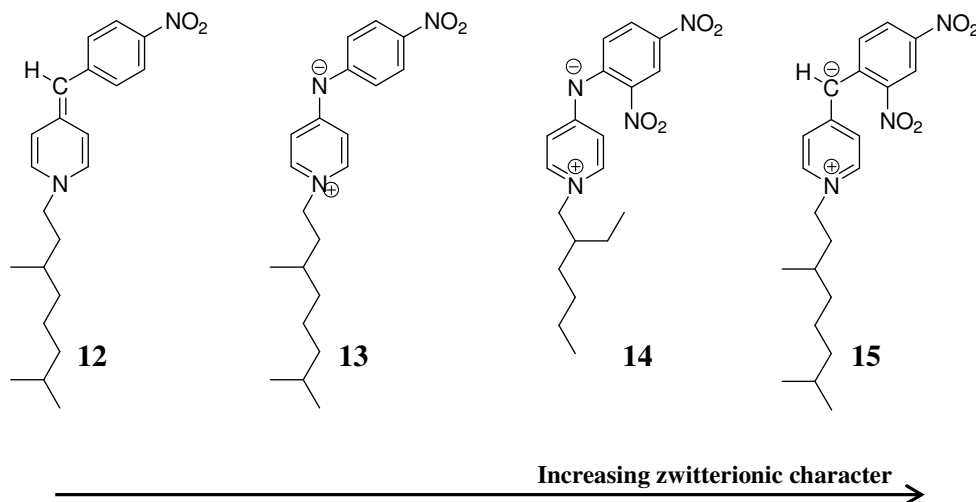


In these systems the donor moiety is represented by alternatively a carbanion or a nitranion center, whose activity is regulated by the strength of the EWG group directly connected to it. Consequently, when the EWG group is a stronger acceptor than the pyridinium ring, the negative charge is preferentially delocalized on the former, with the heteroaromatic ring being in the aromatic form (zwitterionic-aromatic resonance form for **11**); conversely, when the EWG group is weaker than the heterocycle acceptor, charge transfer takes place from the negative center to the ring, leading to a quinoid structure.<sup>57,58</sup>

Focusing on the role played by the different donor atoms, it emerges that the nitranionic bridges stabilizes the charge-separated form with respect to the carbanionic, due to the higher ability of the nitrogen atom to support negative charge because of its higher electronegativity. As a result, if the other substituents effects are taken as constant, it was proven that pyridoneimines exist prevalently as aromatic-zwitterions but the corresponding pyridonemethides have a clear quinoid character. The other main consequence due mainly to the presence of the nitranionic center, is the increased stability, both thermal, chemical, photochemical and temporal of the NLO-phores.

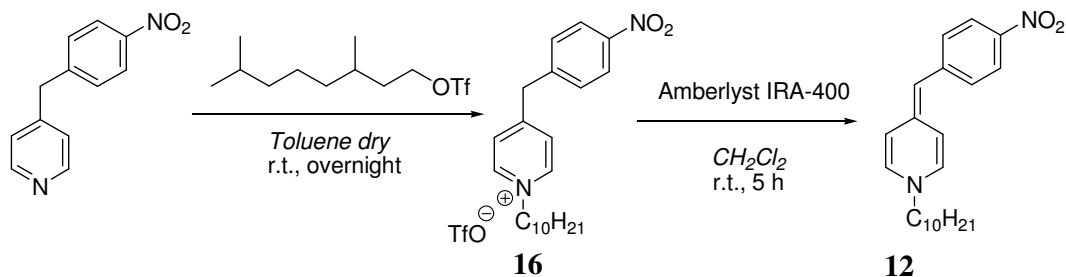
### 1.2.1 DESIGN & SYNTHESIS

The present contribution to the above reported strategy regard the design and synthesis of pyridoneimines and pyridonemethides derivatives for their introduction in polymeric matrix, in order to achieve advanced host-guest materials for electro-optic. The study was focused on the functionalization of the pyridic nitrogen with opportune terminal groups capable of enhanced compatibility with the polymeric matrix, thus enabling the incorporation of such charge-separated active dyes and preventing their segregation. In the following, systems are ordered from neutral-quinoid to zwitterionic-aromatic character, drawn according to the most relevant limit formula descriptor.<sup>56</sup>





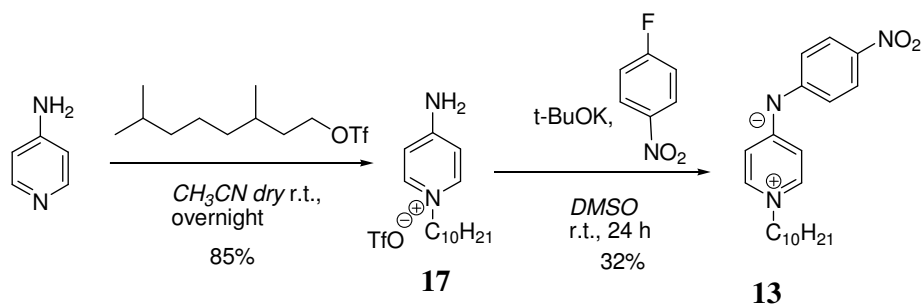
Pyridonemethide **12** presenting a nitrobenzene substituent as EWG group, was prepared according to literature method<sup>59</sup> with slight modifications, as reported in **Scheme.5**.



**Scheme. 5**

4-(4-nitrobenzyl)pyridine is alkylated in anhydrous conditions with 3,7-dimethyloctyl trifluoromethanesulfonate; the reaction is conducted at room temperature overnight, leading to the protonated form of the desired product **16** in quantitative yield as a light yellow oil. Product **12** is obtained after treatment of the precursor with a basic ionic exchange resin in dichloromethane: Amberlyst IRA-400 basic resin is dispersed in the lightly colored dichloromethane solution of the precursor which immediately changes its color turning deep blue-violet, after few hours at room temperature under stirring the deprotonation is complete. This last step represents the central modification of the original synthetic procedure which allows to conduct the reaction in a very clean and simple way; the final product is simply recovered from the mixture through filtration of the polymeric resin.

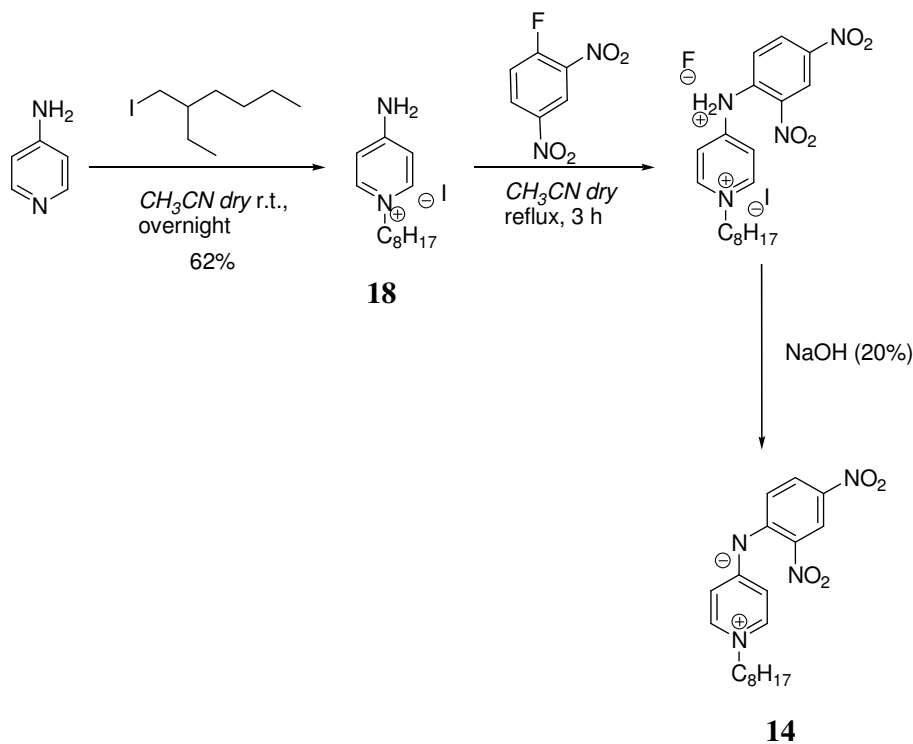
The corresponding *N*-nitrobenzyl substituted pyridoneimine **13** was obtained in a two-step reaction as reported in **Scheme.6**.



**Scheme. 6**

Pyridin-4-amine is easily alkylated with 3,7-dimethyloctyl triflate in dry acetonitrile reacting overnight at room temperature; the alkylated derivative **17** is deprotonated with potassium *tert*-butoxide in DMSO forming the reactive nitranionic species for the successive nucleophilic aromatic substitution reaction on 1-fluoro-4-nitrobenzene. After 24 hours at room temperature a reddish mixture is formed which is poured into ice, the final crude product is collected as an orange sticky solid which is purified by trituration with petroleum ether. It is immediately possible to notice here the effect of the bridging heteroatom in stabilizing the negative charge, which is retained on the site rather than delocalized on the pyridinium ring, thus favoring the zwitterionic limiting resonance form.

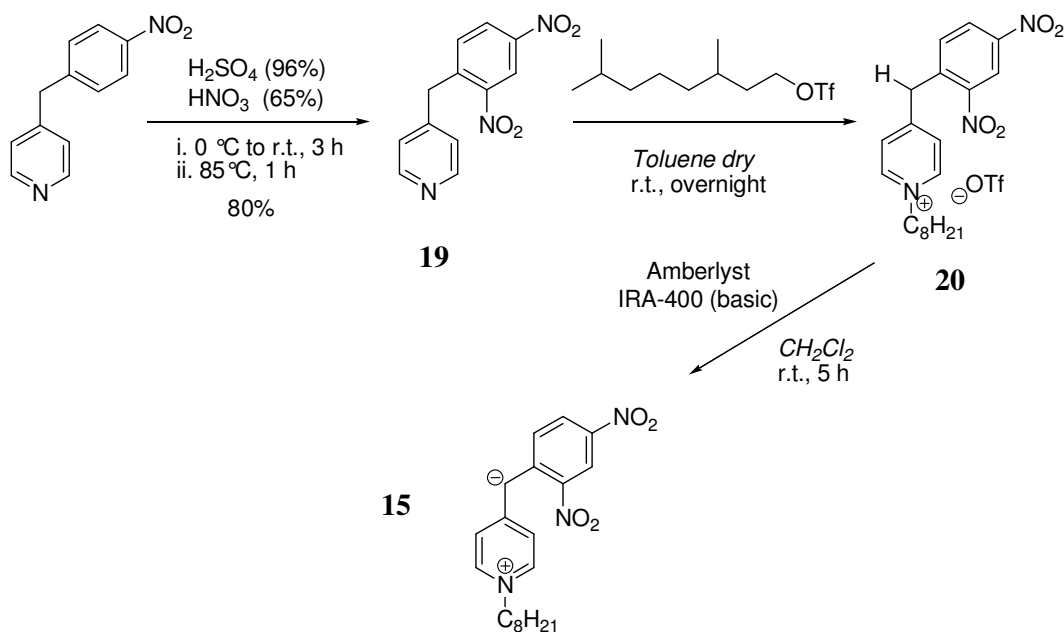
Nucleophilic substitution of 4-amino-1-(2-ethylhexyl)pyridinium iodide with 2,4-dinitrofluorobenzene led to the dinitro-compound **14** as reported in **Scheme.7**. The reaction followed a different procedure compared to that previously reported in the literature by us.<sup>56</sup>



Scheme. 7

In the published paper the use of potassium carbonate in acetone was reported. This method led to the formation of the desired product in pretty low yield only due to the formation of the di-substituted byproduct because of the high reactivity and low selectivity of the nitranionic species toward substitution on the dinitro-functionalized aromatic ring. To circumnavigate this problem, in the present methodology no base was used to deprotonate the substitution adduct, optimization of the synthetic pathway was instead achieved by using a higher boiling point solvent (acetonitrile vs acetone) and favoring the nucleophilic attack by increasing the reaction temperature. The desired product **14** was then obtained in good yield, after treatment of the reaction crude product with a NaOH solution, by filtration through a short alumina plug in dichloromethane.

Corresponding *CH*-analogue **15** was obtained through nitration of precursor 4-(4-nitrobenzyl)pyridine according to literature.<sup>60</sup> The obtained adduct 4-(2,4-dinitrobenzyl)pyridine **20** was alkylated as already stated for the other reported systems leading to the protonated adduct **21** as a yellow oil (**Scheme.8**) which was deprotonated with ion exchange resin obtaining the desired final product in quantitative yield.



Scheme. 8

## 2.2 TETRAZOLATES

The major drawback of the zwitterionic systems reported so far is their relatively low stability in ambient conditions; this is especially true for carbanionic structures, where the negative charge is located on a carbon atom which thus becomes highly reactive. The main reason of this instability is that, generally speaking, all the electron rich portions of the chromophores are attacked by oxygen, either oxidatively or by cycloadditions with singlet oxygen  $^1O_2$ ; thus all such systems undergo bleaching, unless embedded in a compact solid state.

Our strategy to solve this problem at the molecular level started from noting the increased stability of the pyridoneimines derivatives, introduced in the previous paragraph, compared to their *CH*-analogues. As previously stated, in fact, the more electronegative nitrogen atom of the bridging segment is capable of better sustain the negative charge with respect to the carbon atom. The obvious strategy to pursue, in order to preserve the peculiar electronic and optical features of these systems and contemporaneously enhance their environmental stability, was therefore that of designing zwitterionic NLO-phores based on innovative nitranionic donor centers. Theoretical as well as experimental works on highly dipolar heterocyclic betaines<sup>61,62,63</sup> suggested in this regard the possibility of gaining unusually high dipole moments and extremely large first hyperpolarizabilities from a proper design of unconventional extended  $\pi$ -systems containing azinium and azolates subunits.<sup>64,65,66</sup> The resulting approach chosen by us in order to match the requests in terms of chemical, photochemical, thermal and temporal stability, together with a higher NLO response, thus involved zwitterionic dipolar NLO-phores based on tetrazolates as donor heterocycle embedded nitranionic centers, and well-known azinium salts as acceptor segments.

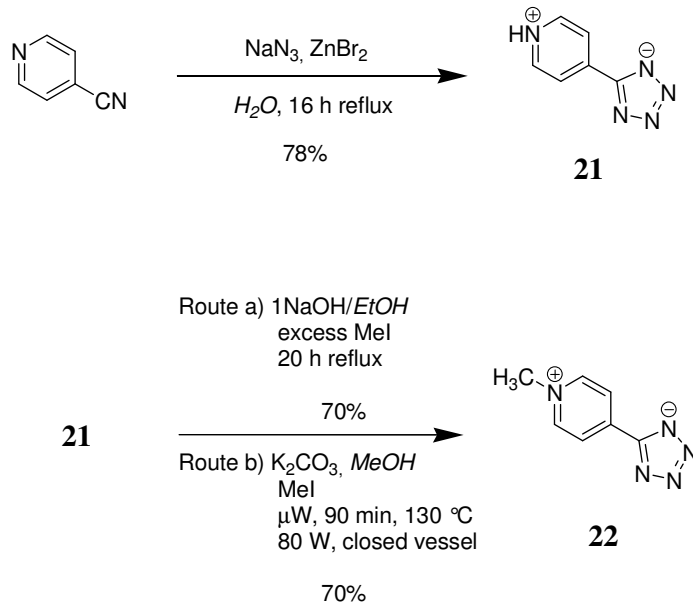
### 2.2.1 DESIGN & SYNTHESIS

Tetrazoles occupy a special place among five-membered nitrogen-containing heterocycles. Tetrazoles contain in fact the maximally possible number of nitrogen atoms (four) and have partial aromatic character. As compared with other nitrogen-containing heterocycles, higher delocalization energies are characteristic for these compounds. The charge distributions in tetrazoles and their closest heterocyclic analogs, triazoles, also differ substantially. Appreciable differences are observed in the dipole moments, heats of formation, and acid-base properties. These peculiarities have a substantial effect on the chemical and physical properties of tetrazoles: the tetrazole ring results resistant to the action of acids, bases and oxidizing as well as reducing agents, tetrazoles form stable complexes with metals and halogens and some of them are stable up to 300°C. Tetrazolate anions moreover have dual reactivity, and this expands the possibilities of the application of these compounds in organic synthesis significantly.

The number of publications devoted to the study of tetrazoles increases each year; significant advances and developments in the chemistry of tetrazoles during the last decades has been largely associated with the wide-scale employment of these compounds in medicine (substituted tetrazoles have been largely studied because of their pharmacologic activity as analeptic and respiratory stimulants)<sup>67</sup>, biology, agriculture, in the manufacture of polymeric materials, in specialty explosives, photography, and also as components in advanced systems for the recording of informations.<sup>68,69</sup>

The new class of zwitterionic nitranions here introduced by us, which represents our third generation of NLO-phores for electro-optic applications, consists of two main groups of tetrazolates derivatives characterized by different heteroaromatic acceptor centers, namely: pyridyl tetrazolates and acridinyl tetrazolates.

The archetypal systems of our pyridyl tetrazolates family are compound **21** and its methylated analogue **22**, whose synthesis are reported in the following scheme.



Scheme. 9

Pyridyl tetrazolate **21** was synthesized according to literature<sup>70</sup> from 4-cyanopyridine and sodium azide using zinc bromide as the catalyst, the reaction pathway consisting in a concerted and highly regioselective [2+3] cycloaddition between the azide and the organic nitrile, activated by the electron-withdrawing pyridyl moiety. Computational as well as experimental approaches reported by Sharpless et al.<sup>71</sup> strongly support the hypothesis that coordination of the nitrile substrate to the Lewis acidic zinc is the source of the catalytic activity exerts by  $\text{ZnBr}_2$  in the formation of 1H-tetrazoles.

Derivative **22** synthetic access is exceedingly simple: we optimized the original procedure<sup>72</sup> introducing the microwave methodology by reacting the potassium salt of **21** with  $\text{CH}_3\text{I}$  in MeOH at 130°C into a pressurized vessel. The product, obtained in the same yield as for the standard procedure, precipitates already as analytical sample.



When applied to our system, the first method consisting in the common literature approach by Koguro et al.<sup>73</sup>, resulted in the formation of two different isomers of the desired product. NMR analysis in fact demonstrated the presence of both *cis*- and *trans*- forms of tetrazole **25**. To circumnavigate this major drawback and in the attempt to increase the overall reaction yield, pathway b) was followed which exploits the solvent-free synthetic approach used with various aromatic and heteroaromatic nitrile by Amantini et al.<sup>74</sup> In this method, with the hypothesis that fluoride anion could be an efficacious basic activator for the cycloaddition of trimethylsilyl azide (TMSN<sub>3</sub>) to organic nitriles, tetrabutylammonium fluoride (TBAF) was introduced as the optimum candidate as the fluoride ion source. By this route it was possible to obtain the desired product **25** in appreciable yield and in shorter time with respect to the previous approach.

One of the most important topic to take into account when considering the applications of NLO-phores-based active materials in electro-optic devices, is that of optical loss. There are several sources of optical loss in the final active material, including absorption, scattering, polarization dependence, reflections, radiation, and fiber coupling; addressing this topic is thus one of the fundamental challenge for developing successful optical material for the telecommunications. From the molecular point of view, it is found that the main cause of optical loss comes from absorption due to electronic and vibrational molecular excitations. Severe requests at the molecular level must therefore be satisfied in order to reduce such detrimental effects: beside avoiding any absorption in the visible region of the spectra, NLO-phores should provide transparency primarily in correspondence of the major telecom (1.31  $\mu\text{m}$  and 1.55  $\mu\text{m}$ ) and datacom (840 nm) wavelengths. Considering in this regard the major telecommunications windows, in the 1300-1600 nm range, absorption coming from the overtones of fundamental molecular vibrations are dominant.<sup>75</sup> Since the strength of the absorption tends to decrease by approximately an order of magnitude between each harmonic order, higher harmonics are



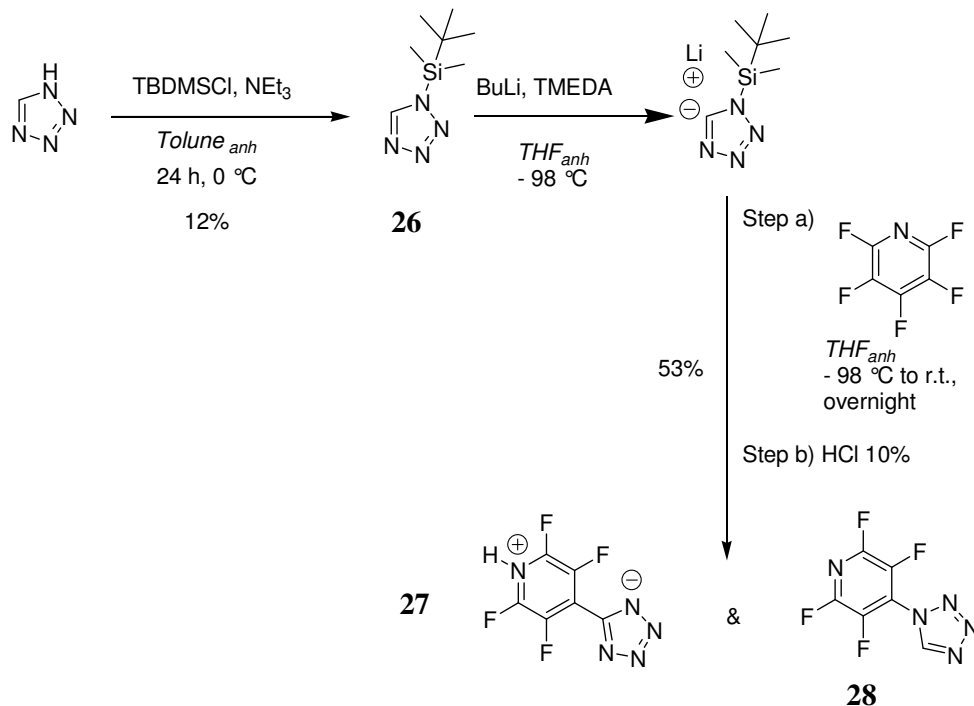
generally weak enough to not be of concern.<sup>76</sup> Clearly, the highest energy vibrations will be those that have high spring constant (stiff bonds, such as double bonds) and/or small reduced mass. The smallest reduced mass occurs when one of the atoms is hydrogen, and the *C-H* aliphatic bond is typically used as the benchmark for infrared absorptions. Considering (**Table.3**) the positions and intensities of various vibrational overtone absorptions of interest, both *C-H* and *O-H* overtones are seen to be highly absorptive in the telecommunications windows, whereas *C-F* overtones show extremely low absorption throughout the range of interest, owing to their higher harmonic order.

Bond	Overtone Order	Wavelength (nm)	Intensity (relative)
C-H	1	3390	1
C-H	2	1729	$7.2 \times 10^{-2}$
C-H	3	1176	$6.8 \times 10^{-3}$
C-F	5	1626	$6.4 \times 10^{-6}$
C-F	6	1361	$1.9 \times 10^{-7}$
C-F	7	1171	$6.4 \times 10^{-9}$
C=O	3	1836	$1.2 \times 10^{-2}$
C=O	4	1382	$4.3 \times 10^{-4}$
C=O	5	1113	$1.8 \times 10^{-5}$
O-H	2	1438	$7.2 \times 10^{-2}$

Table. 3: Wavelengths and intensities of some important vibrational overtones

Therefore, as hydrogens are removed through partial fluorination, the absorption of the active molecules reduces significantly.

Starting from the above considerations we introduced the specifically tailor-designed nitranionic zwitterion **27** synthesized from pentafluoropyridine and *N*-silyl-protected tetrazole **26** as reported in the following **Scheme.11**.

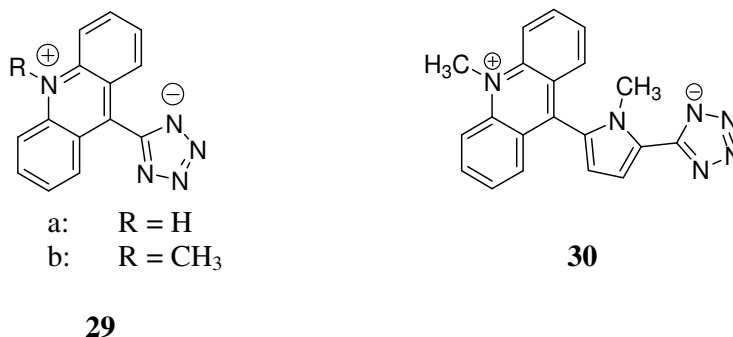


Scheme. 11

*N*-H position of 1H-tetrazole was protected according to literature,<sup>77</sup> with *tert*-Butyldimethylsilyl chloride in anhydrous conditions, leading to the desired compound **26**. It is worth noting the low yield of this step, due to the intrinsic instability of the silyl functionality toward humidity and temperature. Once protected the nitranionic position, the reactive tetrazole carbanionic species is generated through deprotonation with *n*-Butyllithium at -98 °C in anhydrous THF, and then coupled *in situ* with pentafluoropyridine in the same conditions.<sup>78</sup> The particularity of this approach is the last synthetic step which can be properly defined as a *domino* reaction. The *tert*-Butyldimethylsilyl protective group, in fact, results removable by the action of fluoride anions,<sup>79</sup> the latter being released from the *para* position of pentafluoropyridine during the nucleophilic substitution exerted by **26**.

Nucleophilic attack therefore automatically leads to the desired deprotected final product **27**. Unfortunately, as experimentally confirmed through the combination of diverse orthogonal analytical techniques such as  $^1\text{H}$  NMR,  $^{19}\text{F}$  NMR,  $^{13}\text{C}$  NMR and IR, the fluoride anions also deprotected reagent **26**, which is thus free to react as a nitranionic species, leading to the undesired by-product **28**. The molar ratio of the two final compounds in the reaction mixture resulted around 1:1; anyway, by serendipity we were able to remove the undesired isomer through sublimation.

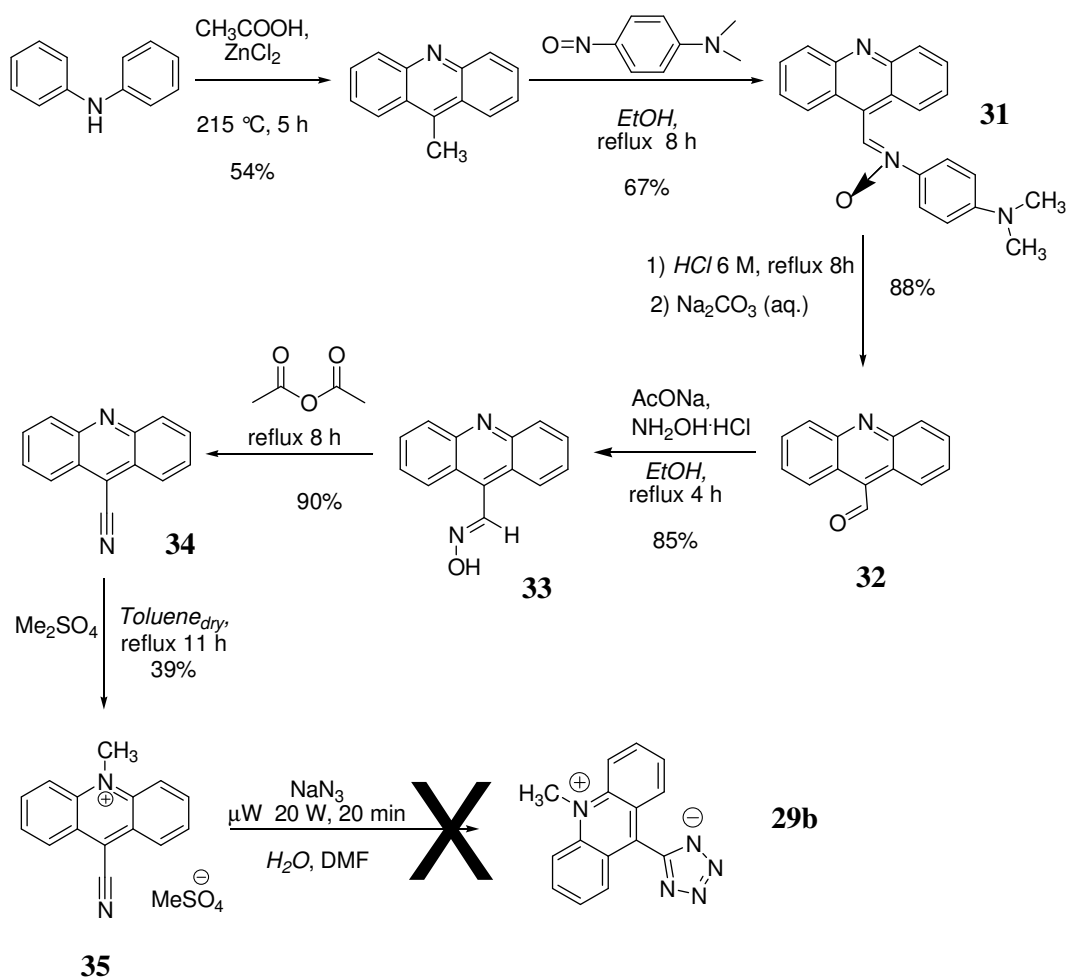
As anticipated at the beginning of this section, we further proceeded in the investigation of NLO zwitterionic nitranions by introducing the innovative class of acridinyl tetrazolates **29** and **30**.



The fundamental purpose in this case was to examine the effect of benzofusion on the accepting behavior of the pyridinium moiety, establishing in turn the consequent change in the molecular, electronic as well as optical, characteristics. Our group previously reported a similar study on the cooperative interplay of structure and environment in tuning of intramolecular charge transfer in dicyanomethanide zwitterionic NLO-phores.<sup>80</sup> For the first time in the literature it was exploited the *annelation effect* as a regulator of  $\pi$ -delocalization, demonstrating the possibility of influencing the relative importance of the aromatic/quinoid character of the azinium ring thus effecting the entire conjugated framework. By means of experimental as well as computational approaches it was shown how, moving from the pyridine ring toward the acridine heterocycles, the molecular ground

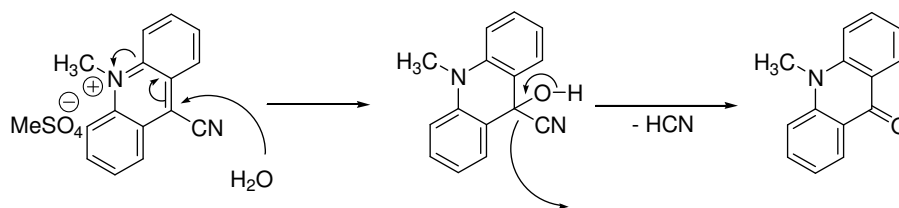
state was better describe by the neutral limiting form. This phenomenon originated from the intrinsic capacity of the acridinium ring to better sustain a quinoid character, thanks to the restored full aromaticity of the two benzene side rings. As a consequence, by choosing the opportune environmental polarity in order not to saturate the effect of benzocondensation, the second order NLO response was established to change its sign from negative to positive moving from the pyridyl compound to the acridinyl derivative.

The first acridinyl tetrazolate **29** was conceived as the benzocondesated analogue of pyridyl zwitterion **21**. The first synthetic approach (**Scheme.12**) followed the same common literature procedure used for pyridyl tetrazolate and, surprisingly, resulted to fail.



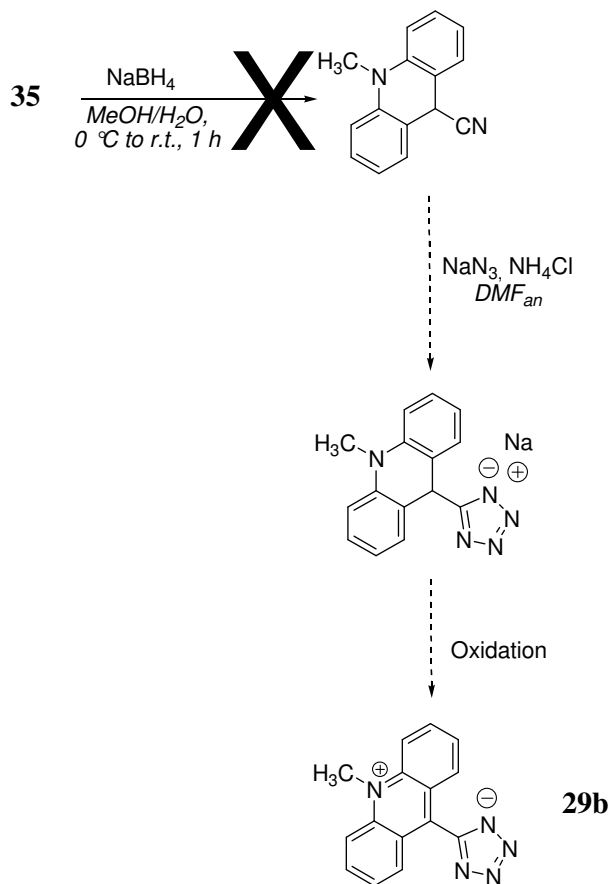
Scheme. 12

9-Methylacridine, obtained through the well-known Berntsen reaction method,<sup>81</sup> was easily converted to the nitron **31** derivate by reaction with 4-Nitroso-*N,N*-dimethylaniline in refluxing ethanol. Acidic hydrolysis in refluxing HCl 6M led to a yellow precipitate, that treated with a basic  $\text{Na}_2\text{CO}_3$  aqueous solution afforded the corresponding aldehyde **32**. Oxime **33** was also obtained as a yellow solid, treating acridine-9-carbaldehyde with sodium acetate and hydroxylamine hydrochloride in EtOH, refluxing 4 hours; conversion to nitrile **34** was achieved in quantitative yield through dehydration in acetic anhydride. In the last step, after alkylating the acridinic nitrogen with dimethyl sulfate, 9-cyano-10-methylacridinium **35** was reacted under microwave irradiation<sup>82,83</sup> with sodium azide in water and DMF. Analysis conducted on the isolated highly fluorescent product excluded the presence of the desired product **29b**, the obtained solid being instead 9-methylacridone. The possible rationalization for the above result is reported in **Scheme.13** where it is shown the high reactivity of the position 9 of the acridinium ring toward nucleophilic agents; even very weak nucleophiles as water can in fact easily attack such position leading to addition and, eventually, substitution.



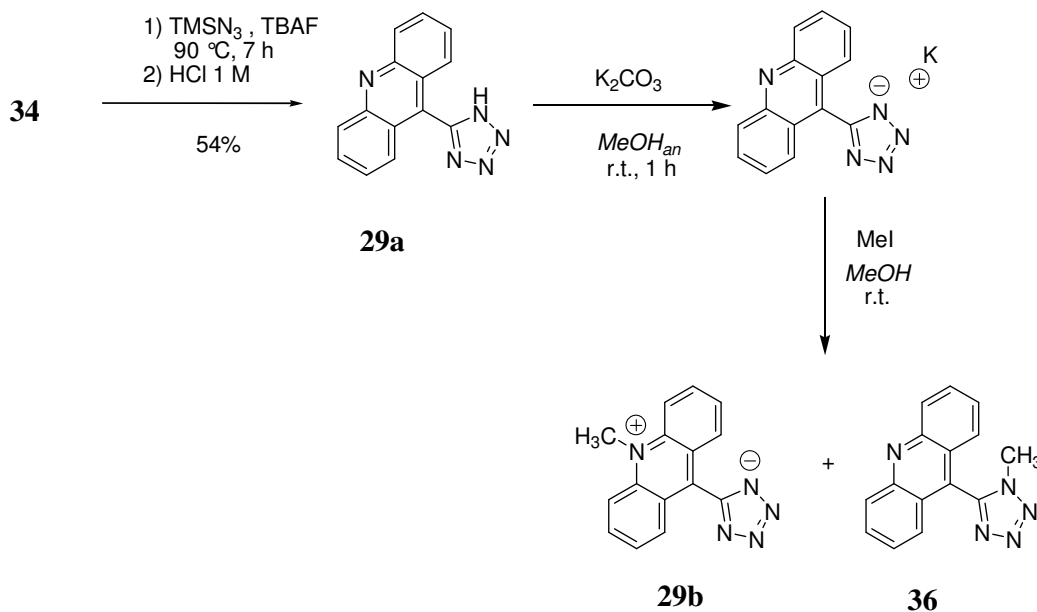
Scheme. 13

Another approach was proposed to bypass this major drawback (**Scheme.14**); the main step consisting in the reduction with  $\text{NaBH}_4$  of the acridinium nitrile **35** to the corresponding acridanic compound, inert toward nucleophilic attack at ring position 9. Very few attempts were conducted following this synthetic pathway which was soon abandoned due to the tedious separation procedure required to isolate the desired product from the reaction mixture.



Scheme. 14

The successive synthetic procedure elegantly circumnavigated the characteristic reactivity of the acridinium salt by simply delaying its formation to the final reaction step (**Scheme.15**); 9-substituted acridines in fact do not present the pronounced reactivity toward nucleophiles characteristic of the corresponding salts. Therefore, following the already mentioned Amantini protocol,<sup>74</sup> the desired acridinyl tetrazole **29a** was easily obtained in good yields by reaction with  $\text{TMSN}_3$  and TBAF at  $90^\circ\text{C}$  for 7 hours in a screw-capped Schlenk flask. The crude reaction mixture was treated with HCl 1M and extracted with  $\text{CH}_2\text{Cl}_2$  leading to the precipitation of the yellow product at the interlayer between the organic and aqueous phase, the pure analytical product was therefore collected by filtration.

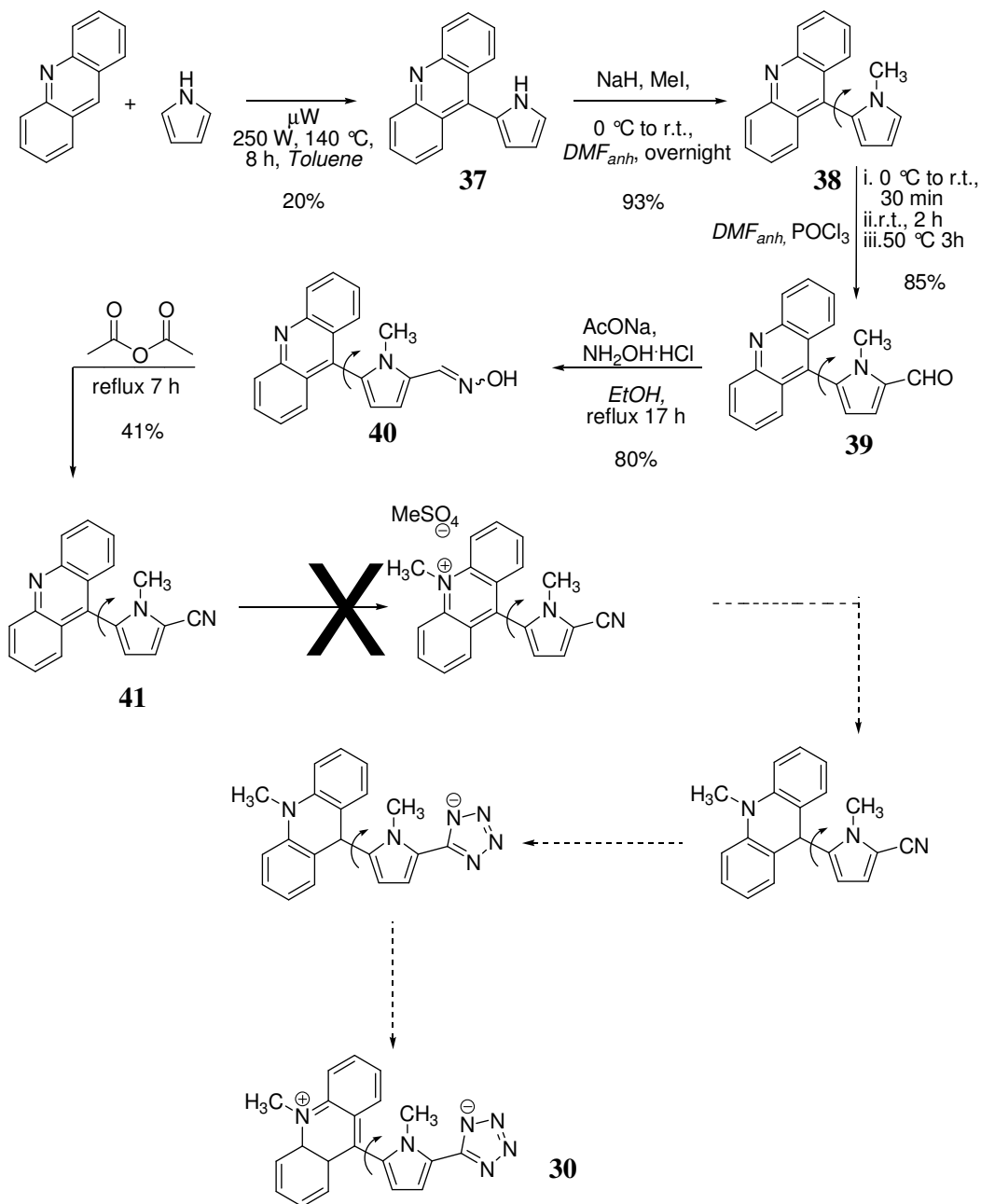


Scheme. 15

Addition of a  $\text{K}_2\text{CO}_3$  solution to a light yellow solution of **29a** in MeOH, led to a colorless solution of the deprotonated saline derivative which was alkylated *in situ* with excess MeI at room temperature. The final step led to a non-completely regioselective methylation of the bidentate nucleophilic precursor, which resulted alkylated at the pyridinic nitrogen and at the tetrazolic position as well, the major reaction being anyway the desired product **29b**. The mixture was separated in an agile manner thanks to the different solubility of the two compounds, the desired one being mainly soluble only in water.

Acridinyl tetrazolate **30** represent our personal effort to combine together all the design strategies for obtaining efficacious NLO-phores so far reported. A deep analysis of its structural features, in fact, permits one to recognize: a  $\pi$ -conjugated framework end-capped with a nitranionic donor (the tetrazolate group) and an heteroaromatic acceptor (the benzofused acridinium ring), an auxiliary heterocyclic donor (the pyrrolyl subunit) moiety connected in a "matched" fashion to the primary donor, a global molecular zwitterionic/aromatic configuration, and finally the possibility of gaining a twisted structure by tilting the bond between the acridine and the pyrrole subunit.

The synthesis of such an ambitious compound resulted rather complicated, thus various approaches were developed to bypass the obstacles encountered along the synthetic pathway; in the following, the final successful methodology which led to the desired product is reported (**Scheme.18**), after rapidly showing the two most significant synthetic attempts among the diverse prior experimental trials.



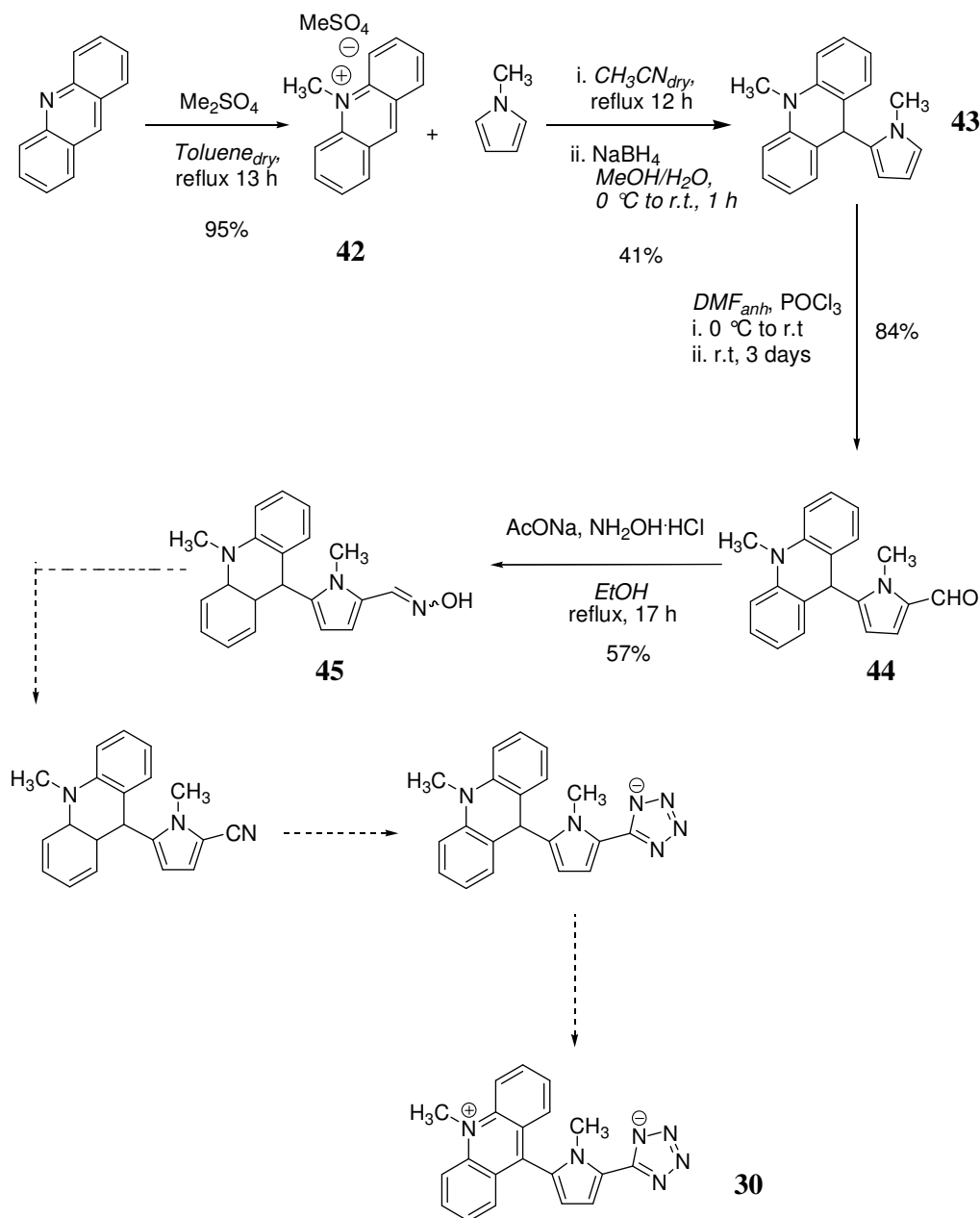
Scheme. 16



The first synthetic trial is reported in **Scheme.16**. The initial step consisted in a microwave-assisted modification of the original method reported in the literature by Treibs and Fligge<sup>84</sup>: pyrrole and acridine react in toluene into a pressurized vessel at 140 °C for 8 hours leading to the precipitation of the pure product **37** in low yield (<15%). Additional amount of the desired product (5%) was obtained from the final reaction mixture, containing residual acridine, di-substituted adduct and 9,10-dihydroacridine, throughout fractional sublimation technique. Methylation of **37** was easily achieved in quantitative yield using MeI after deprotonation of the pyrrolyl nitrogen with NaH in anhydrous DMF. Conversion of the obtained product **38** in the corresponding aldehydic derivative **39** was achieved throughout common Vilsmeier-Hack formulation using POCl<sub>3</sub> in anhydrous DMF. Aldehyde **39** reacted with hydroxylamine hydrochloride and sodium acetate in refluxing ethanol for 17 hours leading to desired product. The obtained oxime was dehydrated in refluxing acetic anhydride leading to a yellow solid which was purified by chromatography to yield the desired nitrile **41**. Methylation of **41** resulted very difficult to achieve due to the depressed nucleophilic activity of the acridinic nitrogen, attempts conducted with different alkylating agents failed. Using strong methylating reagents, such as methyl triflate, in fact led mainly to the protonated by-product, whilst milder reactive, like dimethyl sulfate, necessitated drastic conditions to force the reaction course leading to a non-separable mixture of desired product, protonated form, residual reagent and degraded by-products.

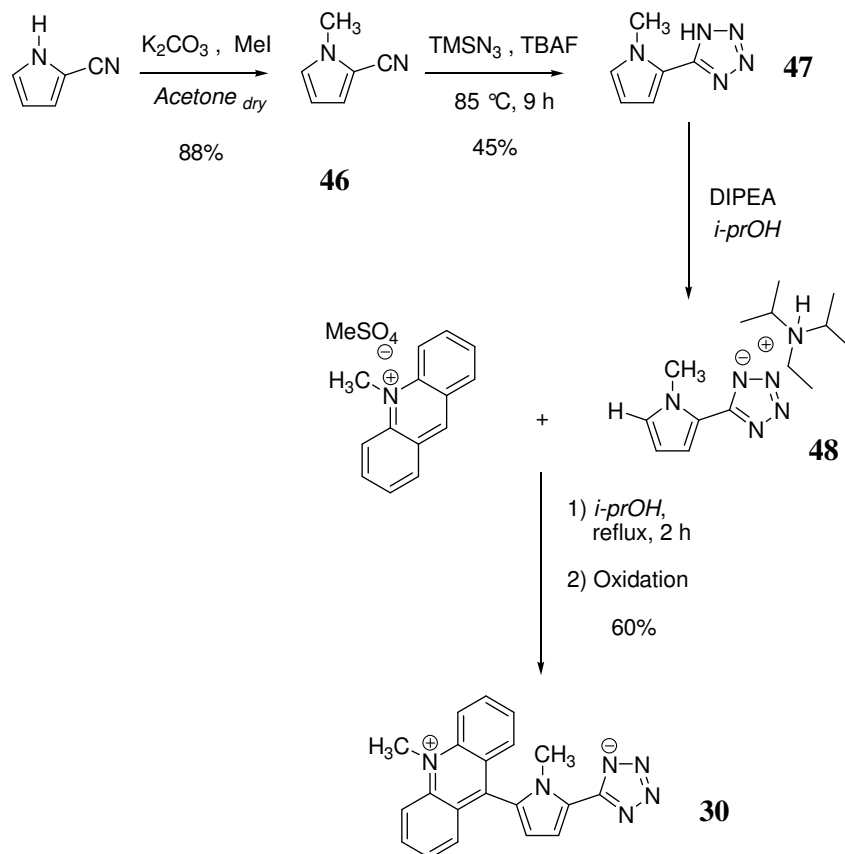
The above discussed reaction method was discarded in favor of a second approach, reported in **Scheme.17**. Exploiting the characteristic reactivity of acridinium salts at position 9, 10-methylacridinium methosulfate **42** was reacted with pyrrole, in anhydrous acetonitrile. After 12 hours refluxing the reaction mixture was poured into diethyl ether leading to the precipitation of the desired addition product only, which was purified by trituration with petroleum ether and AcOEt.

The obtained product was reduced with  $\text{NaBH}_4$  leading to derivative **43** as a dark orange solid. Formylation was achieved once again under Vilsmeier-Hack conditions in a 3-days reaction, leading to the desired pure product **44** as a light-brown solid which precipitated after treatment of the reaction mixture with a basic  $\text{Na}_2\text{CO}_3$  solution.



Scheme. 17

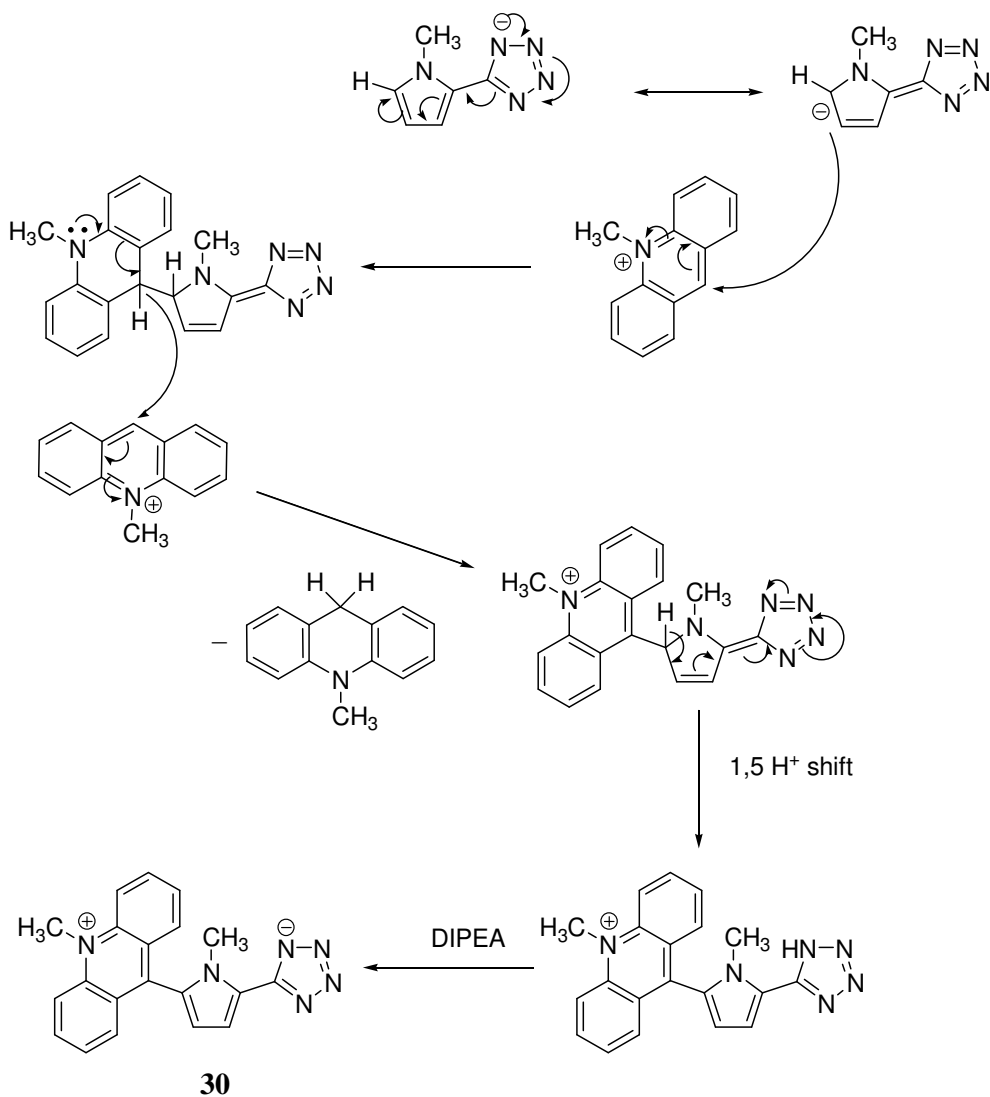
Conversion of the aldehydic product **44** into the corresponding oxime **45** led, as expected, to the two non-separable isomers. At this point such a promising synthetic method was abandoned thanks to a serendipity discover which enabled us to gain the desired final product **30** following the simpler and less time-consuming procedure reported in the following scheme.



Scheme. 18

*N*-methylpyrrole-2-carbonitrile **46** was easily obtained following a general synthetic procedure reported in the literature by us;<sup>56</sup> exploiting the already mentioned protocol by Amantini et al.<sup>74</sup> once again, the tetrazole derivative **47** was easily synthesized and collected by filtration as the pure product, after acidifying the reaction mixture with HCl 1M. Pyrrolyltetrazole was suspended in 2-propanol and deprotonated with DIPEA at room temperature.

The following reaction step deserves special attentions as it represents an unexpected reacting behavior toward electrophiles for the nitranionic tetrazolate **48**. While in fact one would expect the negatively charged tetrazole nitrogen atom to act as the nucleophilic agent, it appears the poorly charged carbon at the  $\alpha$  position of the electron-rich pyrrole ring to be the effective nucleophilic species. Deprotonated compound **48** thus behaves more as a carbanionic species than as a nitranionic one. The proposed reaction mechanism for the addition at position 9 of 10-methylacridinium salt is reported in **Scheme.19**.



Scheme. 19

### 2.2.2 CHARACTERIZATIONS

In the following the various characterizations of our final pyridinium and acridinium tetrazolates NLO-phores are reported.

Pyridinium tetrazolate **22** was deeply investigated in its crystal structure, linear and nonlinear optical responses, thermal and electrochemical behavior demonstrating the outstanding properties of such a system. Considering the structural features first, the single crystal analysis for NLO-phores **21** and **22** are reported in **Figure. 16** and **Figure. 17** respectively.

Crystallographic results for **21** confirms the occurrence of the zwitterionic charge-separated structure in the solid state which, besides establishing the predominance of the aromatic limiting resonance form in the molecular ground state, enables us to prove the preference for a "pyridinium-like" structure not only for the alkylated derivatives **22** but also for this protonated compound, containing a mobile hydrogen. This is particularly interesting for **21** because represents a structural evidence of the elevated acidity of the tetrazole ring. The equilibrium reported in **Figure. 15**, therefore privileges the tetrazolate tautomer, as expected comparing the acidity of the tetrazole ring ( $pK_a[\text{H}_2\text{O}] = 4.89$ ) to that of the pyridine conjugated acid ( $pK_a[\text{H}_2\text{O}] = 5.17$ ).<sup>85</sup>

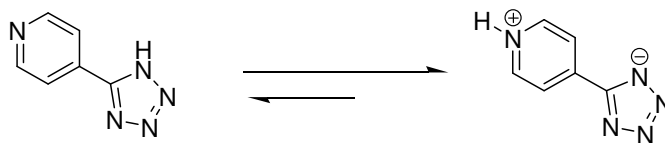


**Figure. 15:** The existing equilibrium for system 21 privileges the occurrence of the zwitterionic form in the solid state, due to the tetrazole intrinsic acidity

Considering the reported crystal structures, both compounds features an almost complete coplanarity between the tetrazole and the pyridine rings, reaching a torsion angle between the two of  $3.5^\circ$  for the methylated derivative **22**.

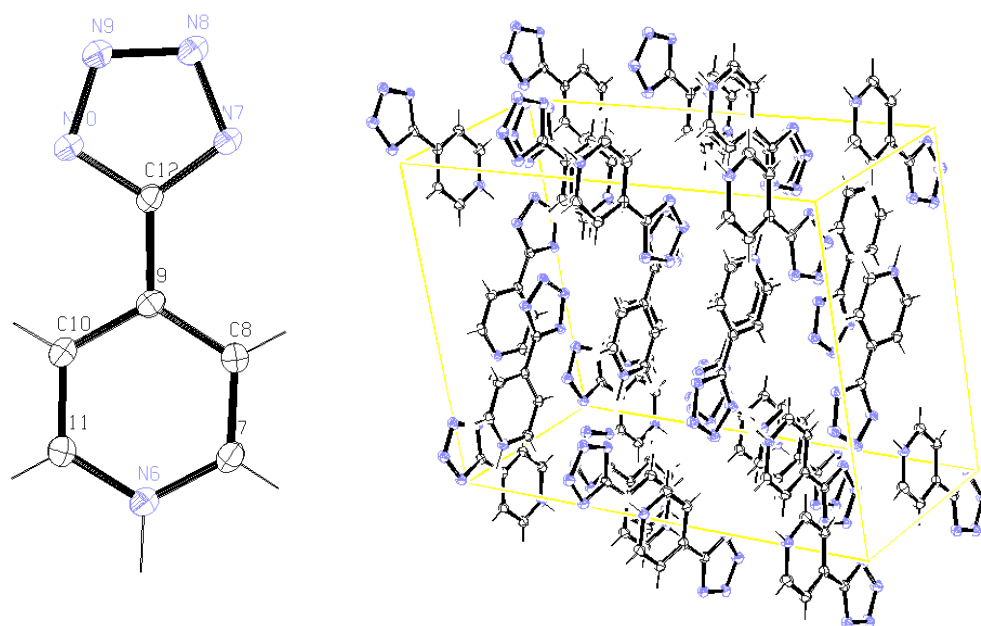


Figure. 16: Single crystal x-ray analysis for compound 21

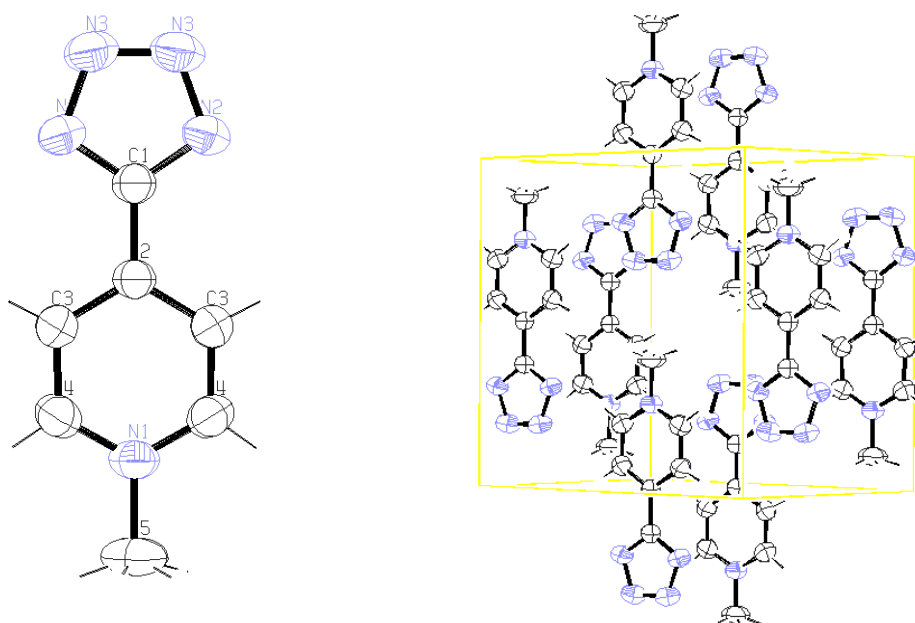
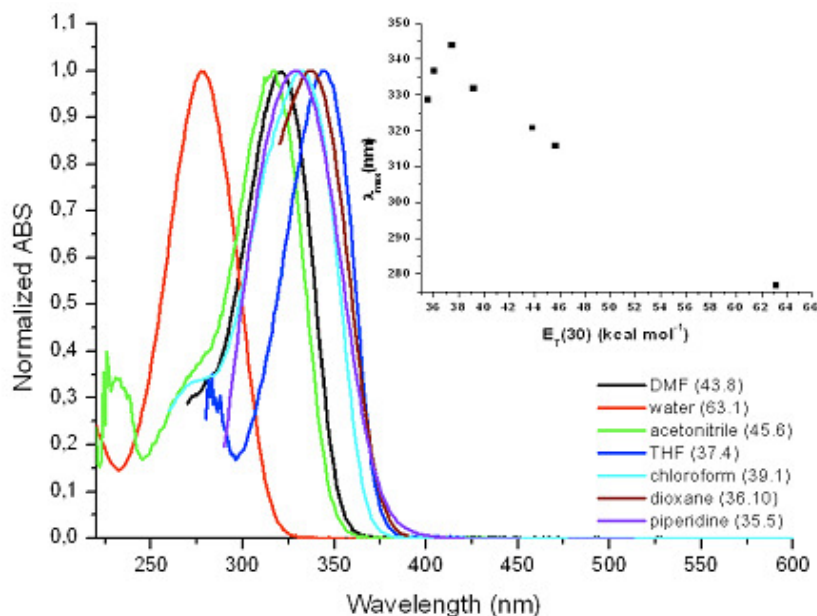


Figure. 17: Single crystal x-ray analysis for compound 22

The solid state packing diagram shows for **21** a crystallization in almost perpendicular couple in alternated layers inside the unit cell, whilst **22** crystallizes in antiparallel pairs within a monoclinic  $C2/c$  space group. The inter-ring distance C1–C2 (1.455(2) Å) for the latter is significantly shorter than that observed in typical biaryls (~1.487 Å), an evident sign of a very strong conjugation between donating and accepting rings. Nonetheless, the atomic distances of the tetrazolate portion are very similar to those reported for a series of tetrazolate salts.<sup>86</sup> In short, the crystal structure shows that the donating and accepting portions of **22** are very strongly conjugated, and that the charge-separated structure is stabilized by the cofacial intramolecular pyridinium-tetrazolate interaction.

In solution the contribution of the zwitterionic structure depends upon the specific solvent polarity, according to the well-known  $E_T(30)$  Reichardt's polarity scale.<sup>87,88</sup> Interestingly, **22** solvatochromism is not monotonous, as shown in **Figure. 18**, with a transition between a positive and a negative regime for  $E_T(30)$  values around 38 kcal mol<sup>-1</sup>.



**Figure. 18:** UV-Vis absorption spectra for system 22 in selected solvents. Inset: correlation between  $\lambda_{max}$  and  $E_T(30)$  empirical parameter (reported under brackets) for the employed solvents

This result can be rationalized assuming a dominant zwitterionic ground state in polar solvents and a quinoid structure in very low  $E_T(30)$  ones, passing through a cyanine-like form for  $E_T(30)$  values close to that of THF. In particular in DMF and  $\text{CH}_3\text{CN}$ , the structure still behaves as a zwitterion as it is also confirmed by cyclic voltammetry. The CV plot of **22** in  $\text{CH}_3\text{CN}$  (**Figure. 19**) shows in fact one strong irreversible reduction peak at  $-1.34$  eV vs. Fc/Fc+ coherently with the reduction of a pyridinium salt having an electron donating substituent (no additional electrochemical process was observed at more positive potentials).

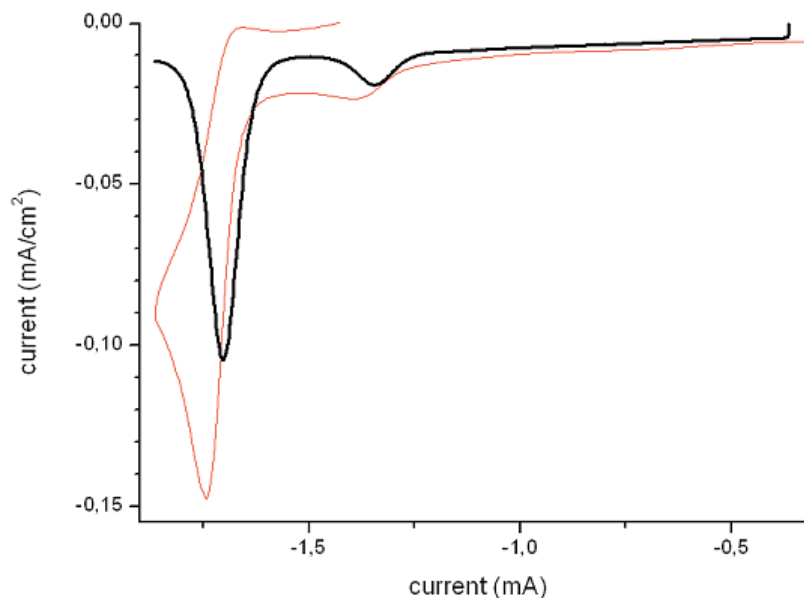


**Figure. 19:** Cyclic Voltammetry (red curve) and Differential Pulse Voltammetry (black) curves for a 0.1 M solution of tetrabutylammonium p-toluenesulfonate in  $\text{CH}_3\text{CN}$  of derivative **22**.

The above reported solvatochromic results suggested the possibility to access the whole BLA plot, thus reaching the highest hyperpolarizability limit in solvents possessing an  $E_T(30)$  value intermediate between that of THF (cyanine limit) and water (zwitterionic limit). Derivative **22** displayed the surprisingly large  $\mu\beta_{1.907}$  value of  $-2010 \times 10^{-48}$  esu as determined by the EFISH technique in DMF, with a non-resonant incident  $1.907$   $\mu\text{m}$  wavelength.



Although not particularly large in general, this value becomes really surprising once referred to the very large optical gap of our molecule; complete transparency in the visible range of the spectrum was in fact detected with the absorption band cut-off that barely reached 400 nm. Moreover **22** showed excellent photochemical and chemical stabilities along with remarkable thermal stability up to 250 °C. In this regard it is confirmed once again here how the use of a nitranionic donor center stabilizes the zwitterionic system towards ambient oxidation which represents the main drawback of the common carbanion-based zwitterionic derivatives present in the literature.

The exceptional transparency/optical nonlinearity trade-off of our high-gap UV-absorbing system **22** earned the maximum exposure and recognition within scientific community as it recently deserved to be published in the 'Emerging Investigator' themed issue in Chem. Comm. as issue 1, 2011.<sup>89</sup>

Tetrazolate **25**, preserves the same outstanding optical characteristic of the previous systems as exemplified by the linear sorption spectrum in **Figure. 20**.

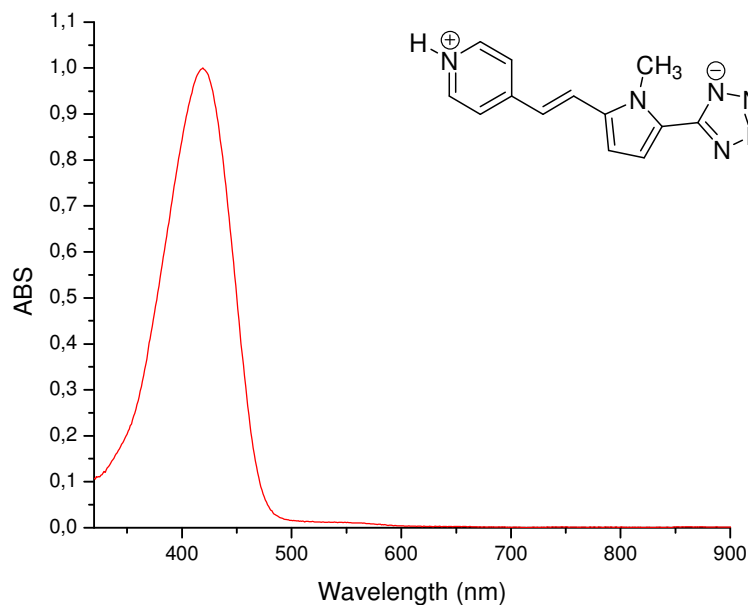


Figure. 20: Linear absorption spectrum of compound 25 in CH<sub>2</sub>Cl<sub>2</sub>

The optical transparency is preserved in the visible, only an absorption tail is in fact present above 450 nm which confers a light yellow color to the chromophore, and the thermal stability is maintained up to 275 °C, as determined by DSC analysis. The nonlinear optical response is notably enhanced with respect to compound **22**, the  $\mu\beta_{1.907}$  value of  $-3500 \times 10^{-48}$  esu in DMF, demonstrates the combined effects on the molecular electronic structure of both the elongation in the  $\pi$ -conjugation path and the introduction of the electron-rich heterocyclic donor.

The simpler acridinium derivative **29b** manifests in the optical responses the annelation effect preannounced in the previous section. The linear absorption behavior (**Figure. 21**) demonstrates complete transparency in the visible also for this class of compounds, whilst the solvatochromic response results drastically reduced compared to the pyridinic analogue. This is due to the different nature of the ground state level in the two situations: while for the pyridinium tetrazolates it is the zwitterionic/aromatic limiting form the predominant one describing the fundamental energy state, in the acridinic derivative the quinoid structure contribution is significantly present as well.

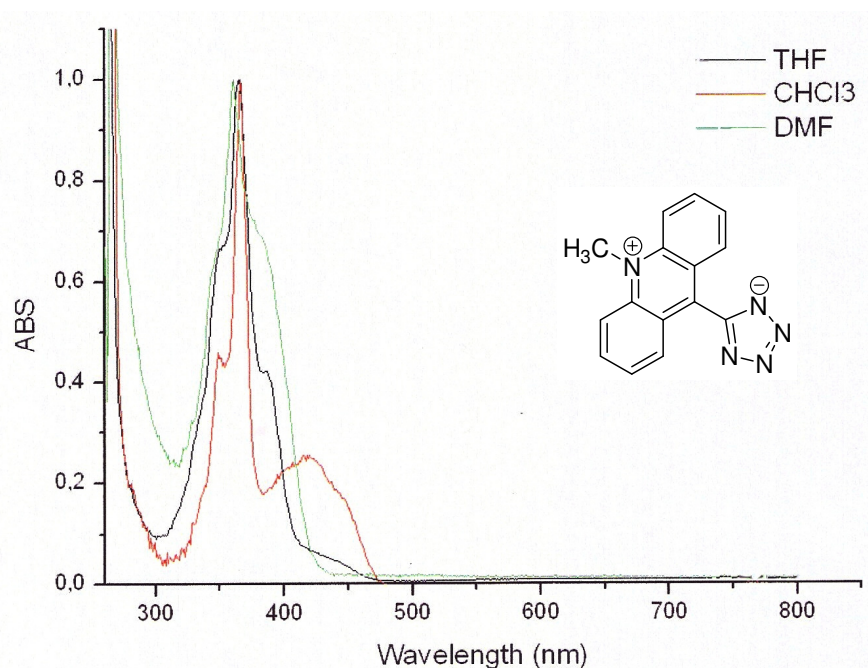


Figure. 21: UV-Vis absorption spectra for system **29b** in selected solvents

Besides the above reported linear absorption features, system **29b** manifest also a clear emission response (**Figure. 22**) with the excellent fluorescence quantum yield of 10% in water, which represents an extraordinary behavior in this solvent, also considering the possible applications of such system in biological applications.

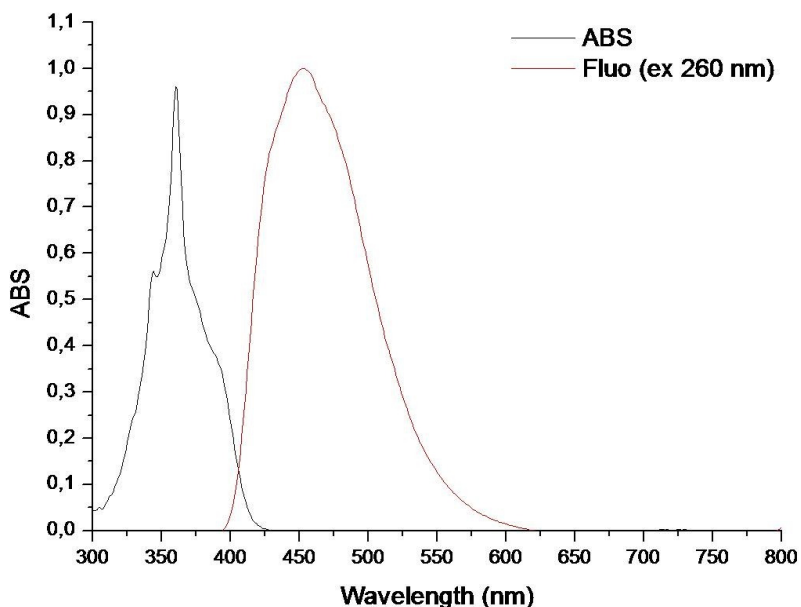


Figure. 22: Linear Absorption and emission spectra for compound 29b in H<sub>2</sub>O

The NLO response for acridinyl tetrazolate **29b** reflects all the structural considerations stated above with the final  $\mu\beta_{1.907}$  value in DMF of  $-1615 \times 10^{-48}$  esu demonstrating in any case the substantial predominance of a zwitterionic structure in this polar solvent.

System **30** introduced, which embodies all the previously reported theoretical-based NLO strategies, manifests an enhanced second-order optical response compared to the aforementioned acridinic derivative. In this case, a  $\mu\beta_{1.907}$  value of  $-1950 \times 10^{-48}$  esu in DMF was registered, confirming the reliability of the proposed design approach and the fundamental occurrence of a zwitterionic charge-separated resonance limiting structure in the ground state. Deeper analysis of the result anyway, do not evidence the tremendous enhancement in the NLO

response expected for a (TICT) twisted intramolecular charge transfer structure. The occurrence of a molecular twisting between the pyridine and pyrrole subunits is demonstrated by the structure of the UV-VIS linear absorption spectrum of **30**, which results in accordance with a sterically enforced reduction in D- $\pi$ -A conjugation.<sup>40</sup> The linear optical analysis in fact shows the presence of three different transitions: besides the low-energy intramolecular CT band (maximum at 600 nm in DMF), two other high-energy excitations occur in the UV region of the spectrum (peak at 275 nm and 360 nm in DMF). It is possible to rationalize such an optical behavior for the present molecular structure only considering the simultaneously occurrence of intra- (high-energy) and inter- (low-energy) subfragment excitations inside the molecule, thus demonstrating the effective twisted configuration. The low NLO response confirms that the tilt angle magnitude does not fall in the range requested to yield the large characteristic second-order enhancement; structure analysis (single crystal x-ray diffraction) are in course to confirm this justification.

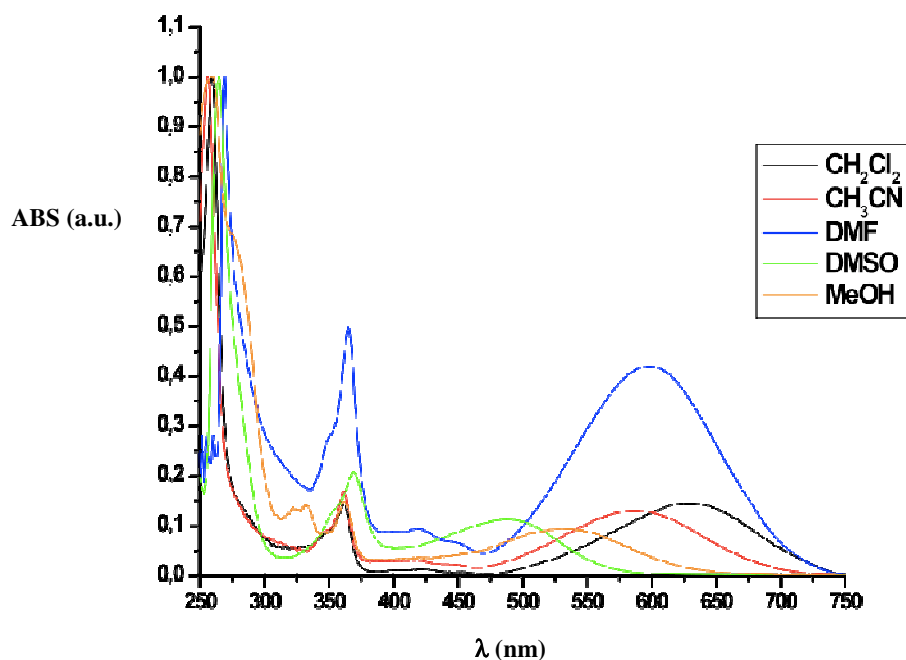


Figure. 23: UV-Vis absorption spectra for system 30 in selected solvents demonstrating the occurrence of high-energy intra- subfragment and low-energy inter- subfragment excitations

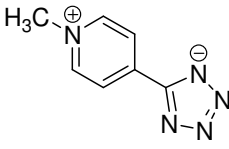
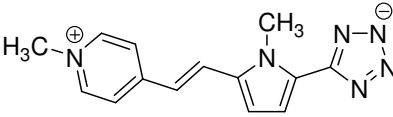
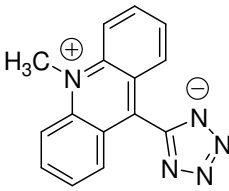
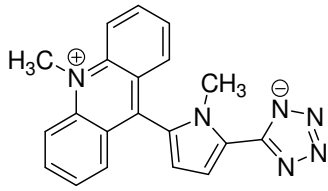
Molecule	$\mu\beta$ @ 1907 nm in DMF ( $\times 10^{-48}$ esu)
	- 2010
	- 3500
	- 1615
	- 1950

Table. 4:  $\mu\beta$  responses for the studied azinium tetrazolates as obtained by EFISH @ 1907 nm

## II.3 TOWARD ELECTRO-OPTIC MATERIALS

Electrons and photons form the practical basis of modern information technology for data- creating, processing, transporting and detecting. Transmitting signals by using infrared light through optical fiber is the most effective way to move large amounts of data rapidly over long distances. Consequently, optical communications form the backbone of the Internet and telephone networks, and they are envisioned to carry real-time multimedia content in the future. Approaches to increase optical bandwidth are being pursued to accommodate such a growth in data traffic. At present, high-speed optical networks use bandwidths of 10 GHz per channel, and 40-GHz products are being introduced,<sup>90</sup> whilst basic research efforts are aiming to push bandwidths even up to 160 GHz. Greater bandwidth request is driven by the desire for high capacity local area networks (LANs), for video transmission, for optical detection of radar and phased-array radar, for radiofrequency (and microwave to millimeter wave) distribution, and for ultrafast information processing such as analog-to-digital conversion. Expanding bandwidth beyond 100 GHz involves many scientific and engineering challenges, among which is the encoding of electronic data signals onto a lightwave carrier by modulating the light in phase or amplitude. This is usually done through second-order NLO materials exploiting their electro-optic (EO) effect in high-speed modulators, where a signal voltage changes the refractive index of an EO dielectric optical waveguide, modulating the phase of a guided lightwave. In the typical Mach-Zehnder electro-optic modulator geometry (**Figure. 24**), a uniform laser light pulse is split into two identical beams, one propagating in a simple non dispersing medium, the second travelling through an electro-optically active material. The application of an electric field on the active channel leads to a local refractive index variation, which causes a phase mismatch (variation of the speed of light) between the two propagating lightwaves.

Once the two beams are combined back into the same optical fiber, the intensity of the resulting lightwave is modulated according to the phase mismatch conditions, ultimately dependent on the frequency of the electric field.<sup>5</sup> An EO device produces the strongest modulation when the entity of phase-shifting is  $\Delta\Phi = \pi$  radians. For an input voltage  $V_{in}$ , it is possible to express  $\Delta\Phi \propto \pi (V_{in}/V_{\pi})$ , where  $V_{\pi}$  is the “half-wave voltage” that makes  $\Delta\Phi = \pi$  near zero frequency, and it is defined as:

$$\text{Eq 6} \quad V_{\pi} = \frac{\lambda_0 d}{2n^3 r_{33} L \Gamma}$$

where  $\lambda_0$  is the carrier wavelength,  $d$  is the gap between voltage electrodes,  $n$  is the optical refractive index,  $r_{33}$  is the EO coefficient of the dielectric material,  $L$  is the device length and  $\Gamma$  is defined as the signal electric field that would be there if air were the dielectric.<sup>91</sup>

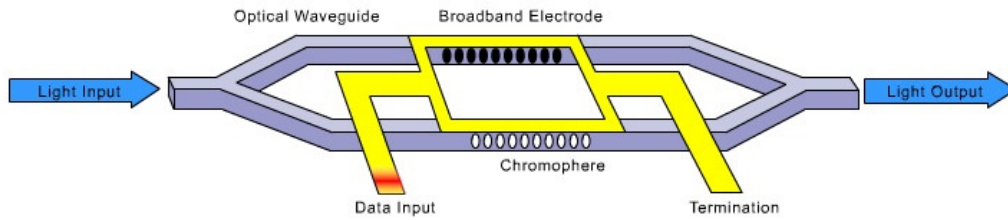


Figure. 24: Structure of a Mach-Zehnder Electro-Optic modulator

Today the whole optical information transmission industry is based on such laser codification, electro-optic therefore lies at the interface of the electronic and photonic technology, providing the means of converting information from the electronic domain to the photonic domain and vice versa. Besides the above reported application, modulators can indeed be configured to perform a variety of functions in both fiber and wireless communications systems (from optical switching, to millimeter wave signal generation, to optical beam steering, to radiofrequency detection, to phase control, to power

splitting, to wavelength division multiplexing WDM),<sup>92</sup> thus effectively improving the overall structure bandwidth. For each of these applications, electro-optic modulators must compete with established alternative technologies and the preparation of cheap, small, high performing and ultra high-speed (large bandwidth) modulators represents a major task to achieve. However, as drive voltage requirements and loss characteristics of modulators improve, and as the bandwidth requirements of various applications increase, modulators are more likely to become the technological choice; signal transduction, for example, was initially accomplished for telecommunication applications by use of modulated lasers, but as the need for higher bandwidth became evident in the late 1980s, attention turned to faster response electro-optic technologies, including: inorganic crystalline electro-optic materials (such as the standard  $\text{LiNbO}_3$ ), semiconductor electro-absorptive materials, and finally organic electro-optic materials.

Focusing on the current materials for state-of-the-art applications, lithium niobate is still the best inorganic crystal for high-speed modulation (being capable of routine operation at 40 Gbit/s), even though relatively high drive voltages are needed to change the refractive index enough to cause the required phase shifting. Among the various alternative material technologies, organic electro-optic materials characterized by extended  $\pi$ -electron conjugation afford in this regard the potential for the greatest bandwidth, the fundamental response time of such materials (responding to a time-varying electric field) being the phase-relaxation time of the  $\pi$ -electron system and thus in the order of tens of femtoseconds (which can translate to potential bandwidths of terahertz). High bandwidth ( $> 300$  GHz) is readily obtained in the literature with polymeric electro-optic modulators<sup>92</sup> due to low relative permittivities and relatively frequency-independent refractive indices and relative permittivities (permitting radiofrequency and optical waves to co-propagate significant distances without dephasing), whilst commercial Mach-Zehnder modulators showing



switching speed as fast as 100 Gbit/s and drive voltage as low as 2.5 V have recently been introduced on the market by the American company GigOptix Inc.,<sup>93</sup> demonstrating the efficiency and reliability of such high-performances polymeric thin film-based technology.

Of course, bandwidth by itself is not enough to ensure a wide-scale commercial utilization of organic electro-optic modulators; other crucial material characteristics include: the magnitude of electro-optic activity (which translates into drive voltage requirements), optical loss, stability (including thermal, mechanical, chemical and photochemical stability), and ease of integration with silica optical fibers and very large scale integration (VLSI) semiconductor electronic circuitry. Comparing again to lithium niobate (a material that secured its place as the dominant electro-optic material with refinements in crystal growth and device fabrication), whose electro-optic activity remained below the 30 pm/V value, the efficiency of the best organic electro-optic materials (in the form of poled-polymeric systems) is now a factor of 15 higher (Figure. 25).

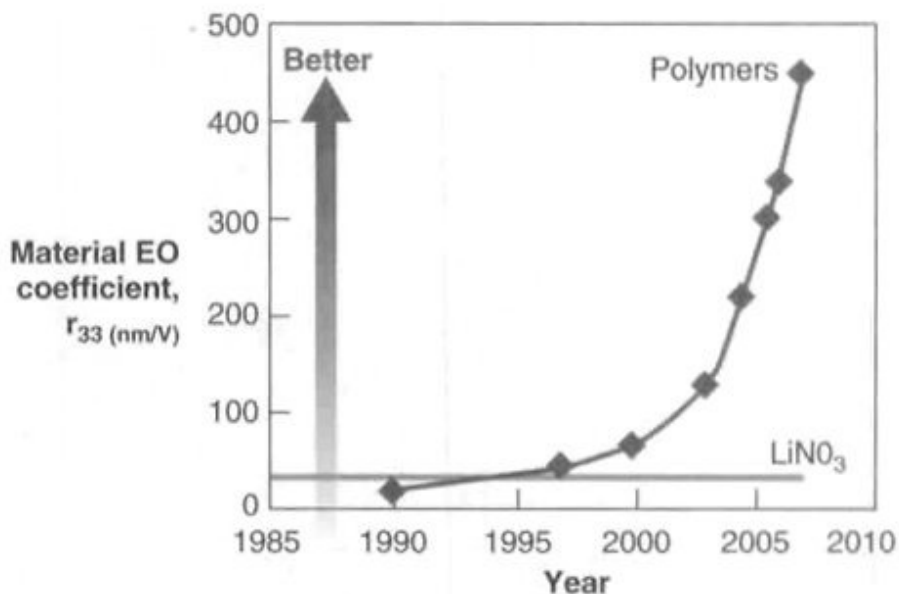


Figure. 25: The electro-optic efficiency of polymer devices, measured as the  $r_{33}$  coefficient, has more than tripled since 2003, and is now more than 15 times the value for  $\text{LiNbO}_3$ .

The core strategy for achieving high-performance organic electro-optic materials relates on transferring at the supramolecular level the high second-order NLO response of individual molecular entities, which can only be accomplished through an ordered antiparallel alignment. Investigation of the relationship between molecular  $\beta$  response and material EO coefficient, led to the following expression for  $r_{33}$ :<sup>94</sup>

$$\text{Eq 7} \quad r_{33}(\omega) = \frac{-2\chi_{zzz}^{(2)}(\omega)}{\eta^4} = \frac{N\beta_{zzz}(\omega, \epsilon) \langle \cos^3 \theta \rangle g(\omega)}{\eta^4}$$

where  $\chi_{zzz}$  is the principal element of the nonlinear susceptibility tensor at frequency  $\omega$ ,  $\eta$  is the refractive index of the EO material,  $N$  is the density of molecules in the material,  $\beta_{zzz}$  is the hyperpolarizability tensor element coincident with the molecular symmetry axis,  $\epsilon$  is the dielectric permittivity of the EO material,  $\langle \cos^3 \theta \rangle$  is the average molecular acentric order parameter denoting the extent of chromophore alignment, and  $g(\omega)$  is the local field factor.

While many outstanding research groups contributed to the foundations of electro-optics, the research since 2000 deviated substantially in terms of material and device focus from the earlier work. Anyway a few academic research programs focused on organic electro-optics did survive and were able to identify in the late 1990s and early 2000s structure-function relationships that led to dramatically improved electro-optic materials (in term of improved molecular first hyperpolarizability, improved supramolecular acentric order leading to improved macroscopic EO coefficients, and improved auxiliary properties such as optical loss and thermal and photochemical stability). With respect to the improvement of molecular and macroscopic optical nonlinearity, the research efforts of the Jen and Dalton group at the University of Washington<sup>95,96,97</sup> and the Marks group at Northwestern University<sup>98,99</sup> are particularly noteworthy.

The temporal evolution of device-relevant molecular first hyperpolarizability and macroscopic electro-optic activity for organic materials is shown in **Figure 26**.

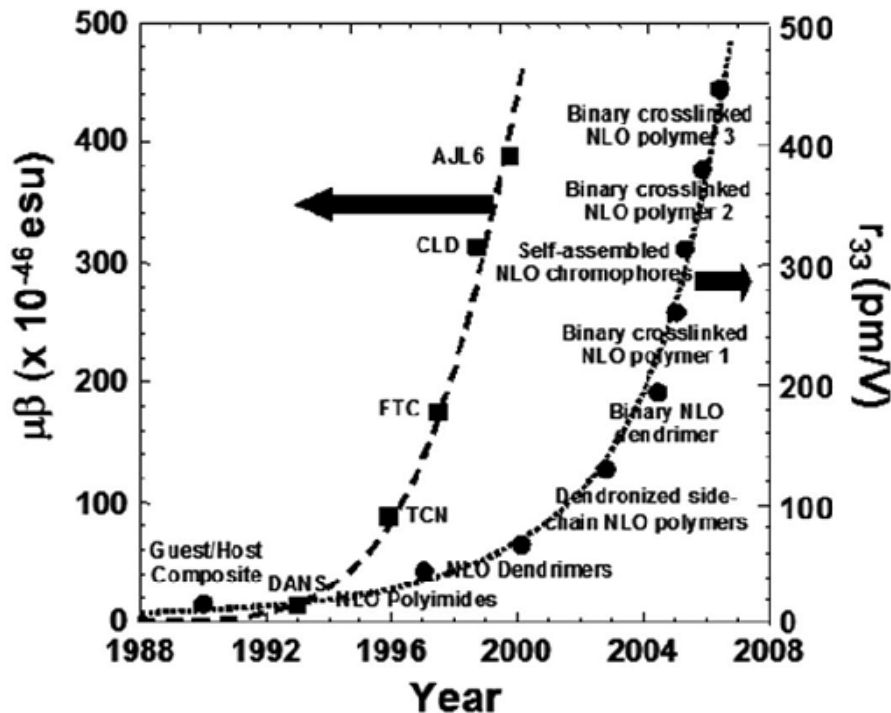


**Figure. 26:** Temporal evolution of microscopic and macroscopic second-order nonlinear optical activity in poled organic materials.

The best laboratory results so far are around 450 pm/V but a target as high as 1200 pm/V has been set in ambitious development programs.<sup>100</sup>

The recent resurgence of interest in organic electro-optic materials has also been motivated by a number of additional factors; among these is a growing interest in photonic and electronic integration, including chip-scale integration. Electronic integration following Moore's Law and exploiting silicon complementary metal oxide semiconductor materials technology has afforded dramatic improvement in size, weight, and power (SWAP) requirements as well as cost, reliability, and performance of modern electronics. Realization of comparable advantages for photonic (and photonic/electronic) integration remains a grand challenge that could have a comparable impact if successful.

SWAP requirements are obviously of critical importance for advanced applications, such as airborne and space defense systems, sensing, and telecommunications. Another motivator for chip-scale integration is the realization of increasing advantages with respect to power requirements, cable density, areal density and cost by using photonics rather than electronics for moving information, the latter choose is moving to ever shorter distances with time, reflecting the advantages that can be realized for these parameters by using photonics. Further essentially unique advantages of organic EO materials are the ease of fabricating conformal and flexible devices and in fabricating devices by a variety of processing methods (solution, vapor-phase...) including soft and nanoimprint lithography and various printing techniques. Other motivations of the resurgence of interest in new electro-optic materials are application requirements that cannot be met with conventional electro-optic materials and energy consumption. Finally, it can be noted that with video-on-demand, etc., bandwidth is again becoming an issue in telecommunications inspiring a revisiting of the use of organic materials. Indeed, the disparate SWAP, performance, cost, and reliability requirements of different applications are stimulating a broader search for new electro-optic materials to fulfill unsatisfied requirements.<sup>94</sup>

In the following our most recent affords in this context are reported; the realization of supramolecular ordered structures were achieved exploiting three of the main strategies reported in the literature for realizing EO materials, i.e., host-guest poled polymers, self-assembled monolayers, vapor-deposited thin films.

### 3.1 HOST-GUEST POLYMERIC SYSTEMS

One of the most widely-spread approach for the realization of organic EO materials is that of incorporating NLO active molecules into a polymeric matrix. For polymer-based EO materials, the crucial synthetic problem, beyond optimizing the individual response of the constituent chromophores, is to maximize the chromophore number density, while achieving and preserving maximum acentricity of the microstructure. The various proposed strategies to achieve these ends are reported in **Figure. 27** according to the approximate order in which they have been investigated.<sup>101</sup>

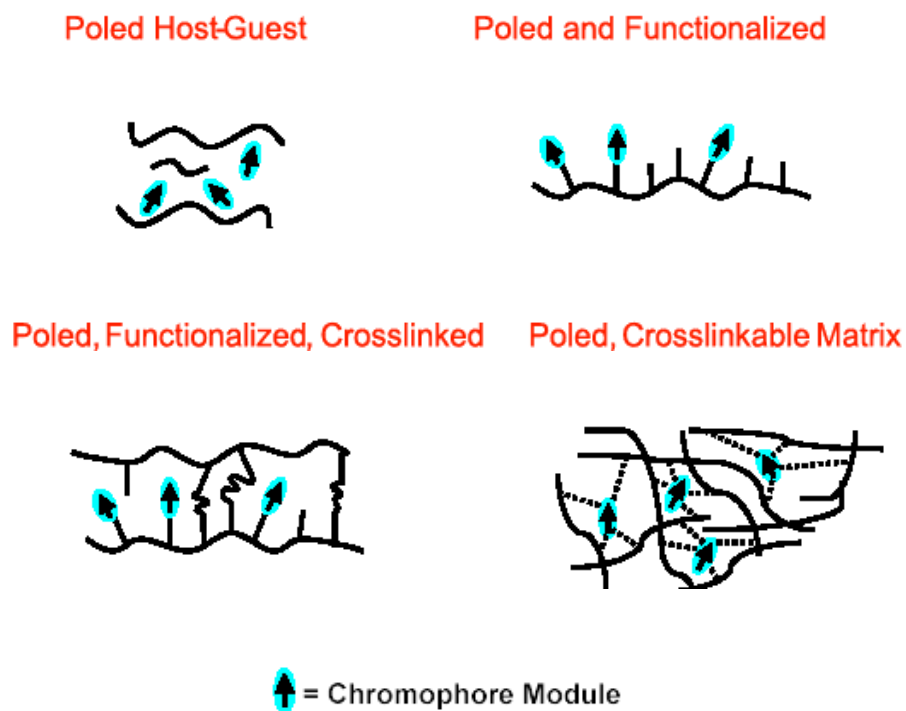


Figure. 27: Design motifs for molecular/polymers NLO materials

The first pioneering approach was to dissolve NLO chromophores in glassy polymers and then to align the dipolar chromophore molecules with a strong external orienting electric field (poling technique), while heating near the matrix glass transition temperature  $T_g$ .

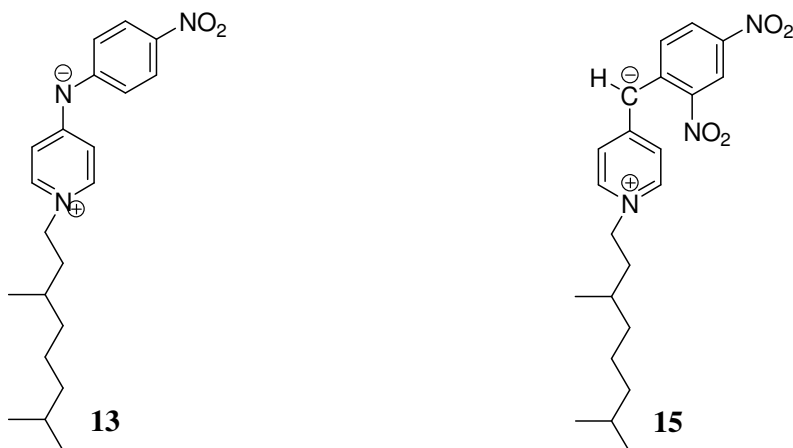
The obvious advantage of such an approach is its relatively simplicity, whilst the major drawback is the fact that the chromophore constituents are not strongly bound to the matrix. This phenomena causes in fact detrimental effects, such as: structural relaxation and lack of orientation after cooling and removal of the electric field, phase separation/aggregation, chromophore sublimation during poling at higher temperatures and dielectric breakdown.

Covalently linking selected high- $\beta$  chromophores to the backbones of high- $T_g$  glassy polymers potentially offer several advantages over poled host-guest systems, including: possibility of higher chromophore density without chromophore phase separation, greater thermal and chemical stability of the chromophore-polymer structure, impeded acentricity-degrading reorientation processes. Nevertheless, the active molecules must be finely designed to insert proper groups able of anchoring them onto the polymeric backbone, thus introducing a certain degree of complexity and supplemental molecular reactivity; moreover all poled chromophore – glassy polymer ensembles remains kinetically unstable with respect to relaxation to the thermodynamic equilibrium state of globally random orientation. The need for complete immobilization therefore stimulated efforts to achieve even greater chemical control over polymer chains dynamic, leading to the introduction of crosslinkable systems, capable of being aligned in the electric field and simultaneously locked in such an orientation. Also in this case the initial chromophoric design strategy is fundamental and a synergic work need to be done when choosing the polymeric matrixes.<sup>102</sup>

Herein is reported our contribution to the theme through an explorative study of the electro-optic properties of host-guest polymeric systems based on the pyridonemethide and pyridoneimine derivatives previously presented. As previously introduced, the active molecules were functionalized with proper branched alkyl chains in order to increase the compatibility with the polymeric matrix and contemporarily prevent reorientation phenomena after poling process.

The linear optical absorption characteristics of the NLO-phores were determined by us together with their thermal and photochemical stability, whilst the realization and optical characterization of the final host-guest polymeric EO material were performed by Dr. Fabio de Matteis and co-workers at the University of Roma Tor Vergata, Department of Physic.

The molecules tested for the achievement of EO materials were systems **13** and **15**:



The linear absorption spectra for systems **13** and **15** are reported in **Figure. 28** showing for both systems only one broad band in the visible, imputable to the main intramolecular CT transition; their molar extinction coefficients and linear optical characteristics, as obtained from the plots, are reported in **Table. 5**.

Chromophore	$\epsilon$ (L mol <sup>-1</sup> cm <sup>-1</sup> )	Absorption maximum in DMSO (nm)
<b>13</b>	<b>17000</b>	<b>457</b>
<b>15</b>	<b>45000</b>	<b>497</b>

Table. 5

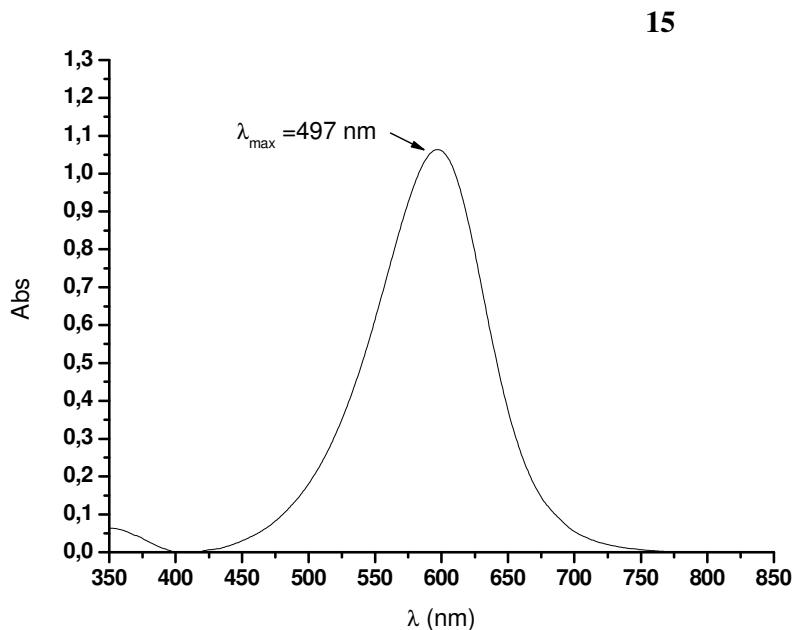
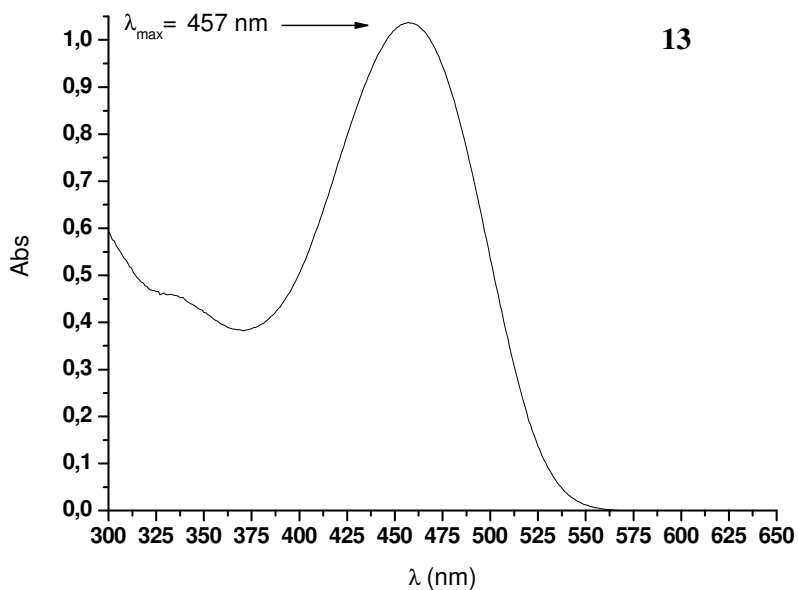


Figure. 28: Linear absorption spectra for 13 and 15 in DMSO

Thermal behavior and stability were investigated by means of differential scanning calorimetry (DSC) demonstrating, as expected, a substantial higher stability for the nitranionic derivate **13**.



Besides the melting transition, the molecule presents in fact only a single exothermic peak at 350 °C without any sensible variation of the stability up to this temperature value (**Figure. 29**).

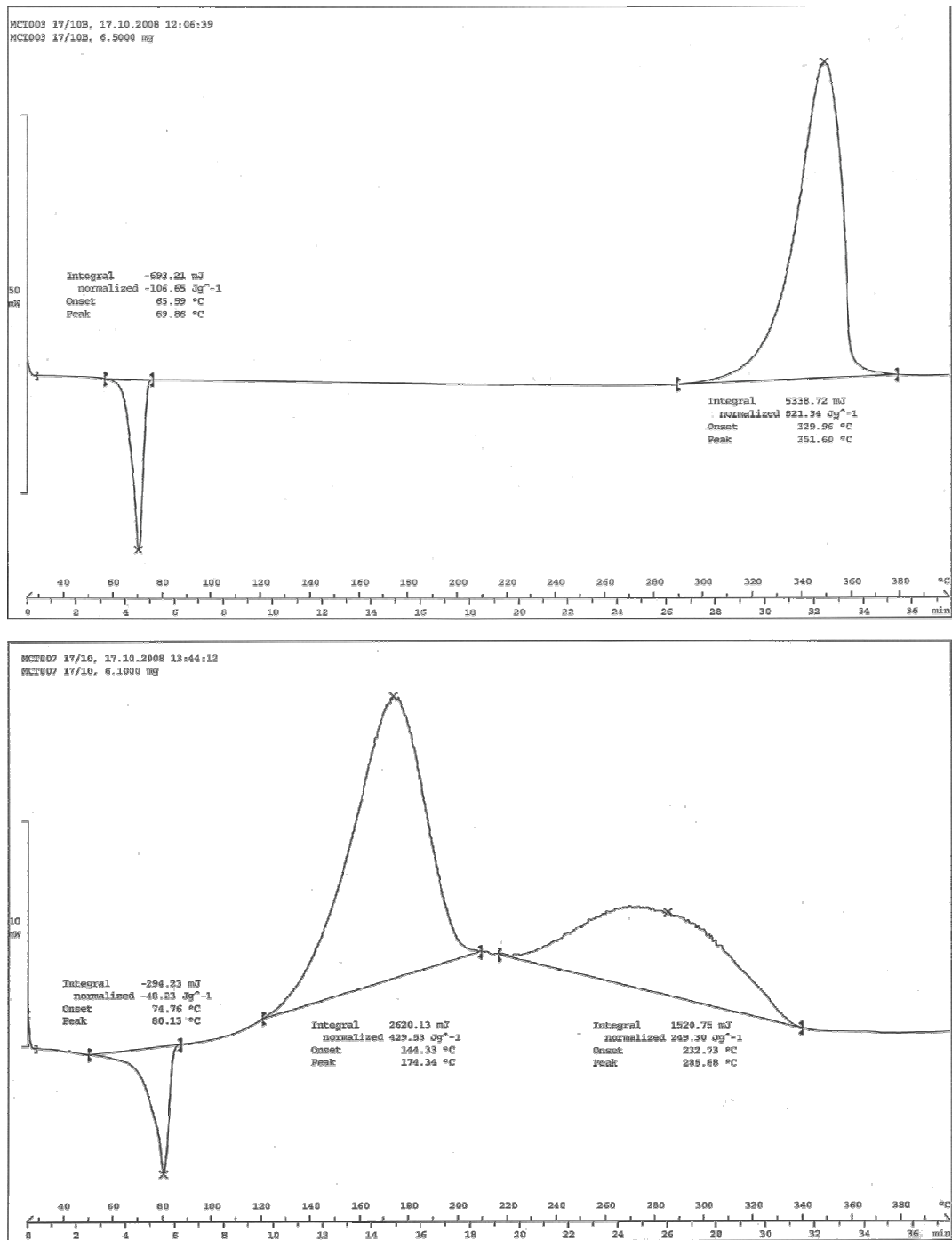


Figure. 29: Thermal behavior for system 13 (up) and 15 (down)

On the other hand the spectra for pyridonemethide compound **15** evidences decreased stability after melting, showing the presence of two subsequent exothermic transitions at 174 °C and 285 °C.

Starting from the above reported results, we conducted a few preliminary trials to investigate the possible maximum loading capacity of our NLO-phores into the polymeric matrix, and to estimate the thermal stability of the final host-guest materials. Three different polymers were chosen depending on their chemical and physical characteristic (mainly their glass transition temperature and their backbone structure): polymethylmethacrylate (PMMA), polycarbonate (PC), polysulphone (PSU).  $\text{CH}_2\text{Cl}_2$  solutions (dichloromethane was the only solvent capable of dissolving all the introduced polymers and chromophores) containing the chosen polymer with different loading of the examined chromophores (percentage by weight), were deposited through casting mode on a sodium-lime glass slide, heating the substrate at 35 °C, in order to facilitate the solvent evaporation and the film homogeneity. Linear absorption analysis were registered on the obtained polymeric films at room temperature first and then after subsequent treatments at different increasing temperatures in the oven (keeping the film at the imposed temperature value for 15 minutes), both in air and under nitrogen atmosphere. Also these analysis demonstrated the higher thermal stability of NLO-phores **13** compared to **15**; polymeric films containing the latter molecule (for every loading percentage), in fact, demonstrated a severe decreasing of the characteristic optical absorption band even for treatment at temperatures as low as 50 °C. Attempts to augment the stability performing thermal treatments under nitrogen or by adding to the solution 1,4-diazabicyclo-[2.2.2]octane (DABCO), in order to avoid photochemical degradation of dye by singlet oxygen,<sup>103</sup> resulted to fail.

The successive preliminary analysis and the final EO material preparation where therefore conducted focusing on the pyridoneimine compound **13** only. In this case, optimal stability were recorded through the above method for loading up to 50%; different host-guest

films were prepared for the three reported polymeric matrixes with increasing NLO-phore loadings from 10% to 50%, and in all such cases a very good thermal stability after thermal treatments were established, even for temperature next to the polymeric  $T_g$ . No significant alterations were detectable in the films, it was therefore demonstrated for these systems the capacity of retaining the original optical characteristics in the thermal conditions usually adopted during the poling process.

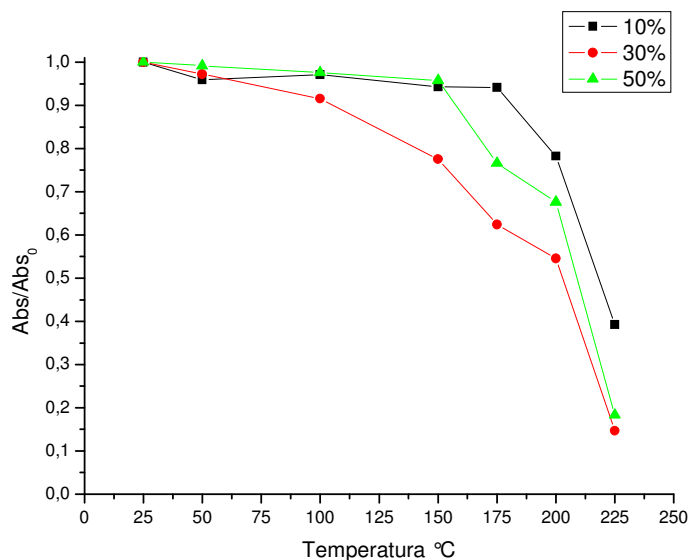


**Figure. 30:** Thermal stability for chromophore 13 in PMMA ( $T_g = 120$  °C) at different loadings

Host-guest system of **13** in PMMA demonstrated a maximum 10% optical loss, with respect to the system at room temperature conditions, for temperature treatments up to 120 °C, and such behavior even increased for loading up to 50% (**Figure. 30**).

Considering the material based on PC, an analogous behavior was detected, as reported in **Figure. 31** where minimum optical loss at the absorption maximum was registered at all the loading percentages, for treatment up to 120 °C. In this case at temperature next to the polymer glass transition (150 °C), the optical loss was somehow higher, reaching 15-20%, depending on the loading,

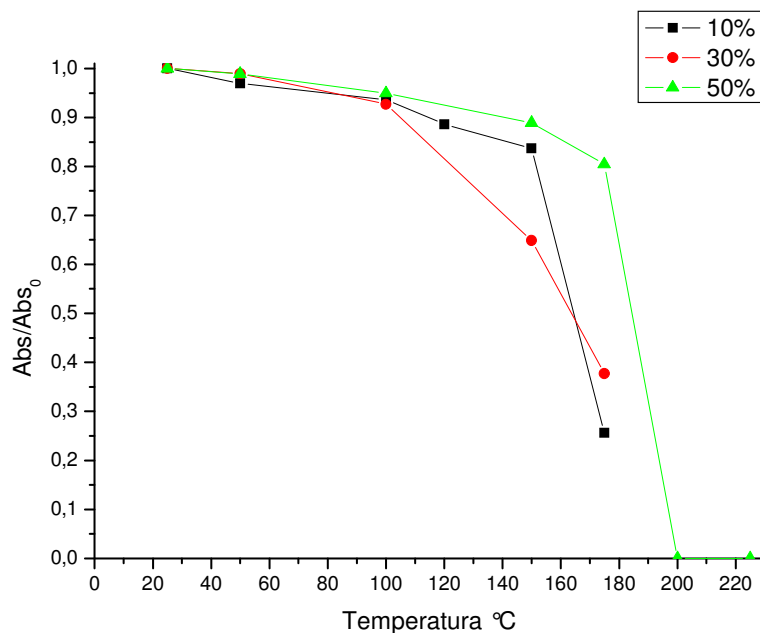


Figure. 31: Thermal stability for chromophore 13 in PC ( $T_g = 150$  °C) at different loadings

The optical loss is evidently lower (Figure. 32) for host-guest films of **13** in PSU. In this case, for temperatures as high as the polymer  $T_g$ , the reduction of the absorption in correspondence of the NLO-phore CT peak was as low as 15% for all the loadings except 50% where a 20% value was reached.

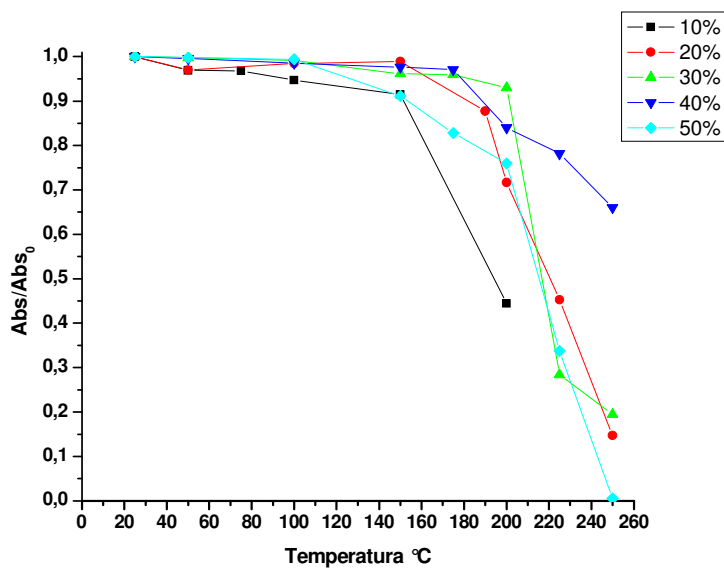


Figure. 32: Thermal stability for chromophore 13 in PSU ( $T_g = 190$  °C) at different loadings

The preliminary qualitative analysis above reported, were the basis for optimizing deposition, loading and corona poling processes during the realization of active electro-optic host-guest polymeric materials.

Solutions of compound **13** and chosen polymer (100 mg) in dichloromethane (3 mL) were deposited on BK7 glass substrates filtering through a 0.2  $\mu\text{m}$  filter, then spin-coating at 1100 rpm for 30 seconds and finally annealing 10 minutes at 60  $^{\circ}\text{C}$ . SHG measurements on the poled films were conducted 24 hours after depositions, during this time samples were stored in dry atmosphere in a dark room. Thermal treatments and poling conditions are reported together with the obtained EO responses in **Table. 6**.

**Table. 6:** Host-guest mixture compositions, poling conditions and electro-optic responses for compound 13-based thin polymeric EO films

Sample	Polymer	% Dye	Poling Field (KV)	Poling Temperature ( $^{\circ}\text{C}$ )	Poling Time (min)	$d_{33}$ (pm/V)
1	PMMA	10%	11	120	15	0.77
2	PMMA	10%	9.5	120	15	0.94
3	PMMA	10%	9.5	85	15	1.31
4	PC	10%	11	150	20	0.30
5	PC	10%	11	130	12	1.24
6	PC	10%	11	120	12	1.13
7	PC	10%	9.5	150	20	0.61
8	PC	10%	9.5	130	20	0.90
9	PSU	10%	11	190	20	1.35
10	PSU	10%	9.5	190	20	0.65
11	PSU	10%	9.5	165	20	1.95

From the above reported results it is worth noting how, for all the considered polymeric matrixes, the best results in term of EO responses were obtained for poling temperature well below the polymeric  $T_g$  (at least 20 °C lower) and for reduced poling fields. The film appearances and the linear optical characterizations, registered prior and after the poling process (not reported here), demonstrated in all the cases the substantial stability of the EO material using these latter processing conditions while showing noticeable degradation effects (film whitening and chromophore segregation) for higher poling temperature and more intense applied electric fields. This deterioration of the film optical quality, is imputable to NLO-phore sublimation and dielectric breakdown both due to the increased current inside the material, owing to the enhanced ionic conductivity in these more severe conditions.<sup>104</sup>

### 3.2 SELF-ASSEMBLED STRUCTURES

Of the diverse synthetic approaches to acentric chromophore matrices, self-assembly is one of the most intensely investigated alternative to polymer poling. This totally different strategy for the synthesis of supramolecular chromophoric structures is based on a layer-by-layer construction of artificial superlattices, using subsequent covalent connections between the constituent components. In principle such an approach could achieve far higher degrees of net chromophore alignment and number densities than electric field poling, and far greater structural control and temporal stability than a typical glassy polymer which is subject to physical aging.<sup>100,105</sup> In the simplest geometry, this approach exploits chemisorption of alkyl- or benzyl-halide-containing trichlorosilane coupling agents onto flat, highly hydroxyl-terminated surfaces (e.g. glass, silicon, polymers), which provides functionalized surfaces for the polar anchoring of bifunctional chromophore precursors. A nucleophilic NLO-phore, usually a stilbazole derivative, is thus reacted with the electrophilic surface, through quaternization of the pyridinic nitrogen leading to an almost

perpendicularly orientation of the molecules on the surface. The subsequent deposition step involves the introduction of a so-called capping-layer used to "lock in" the polar structure *via* three-dimensional siloxane-network formation. This capping reaction planarizes the structure, exposes silanol functionalities mimicking the original SiO<sub>2</sub> interface, and thus allows the whole process to be iterated to give a final multilayered superlattices. This chemically driven orientation is thermodynamically stable and give rise to robust, high quality ordered acentric electro-optic films (**Figure. 33**).<sup>106</sup>

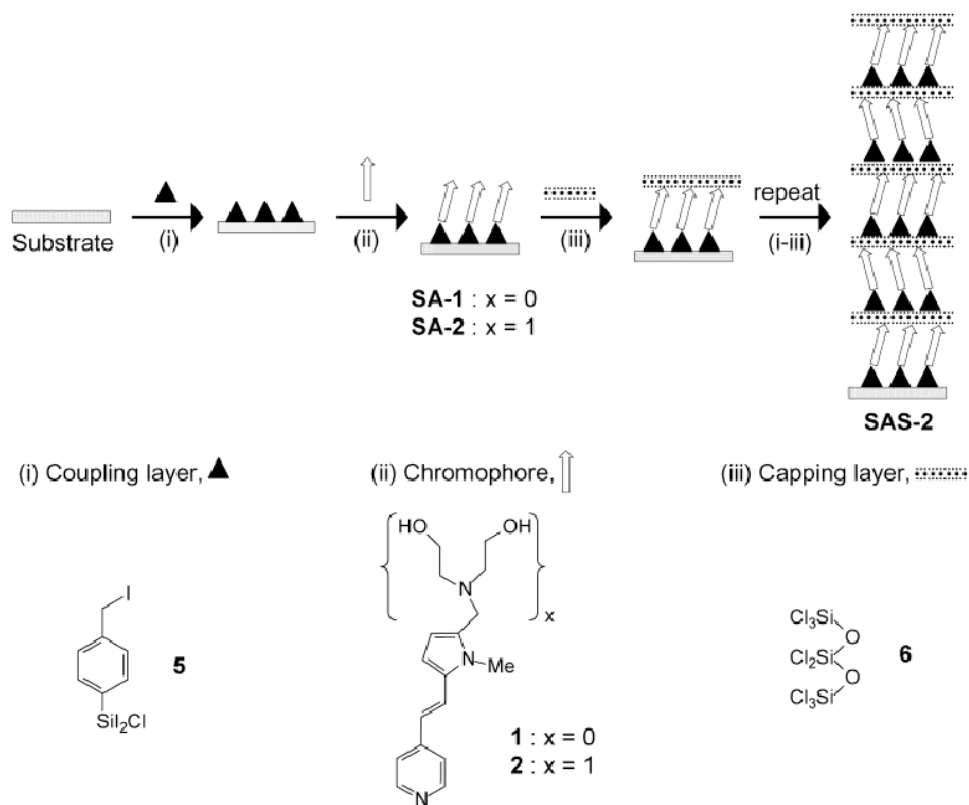


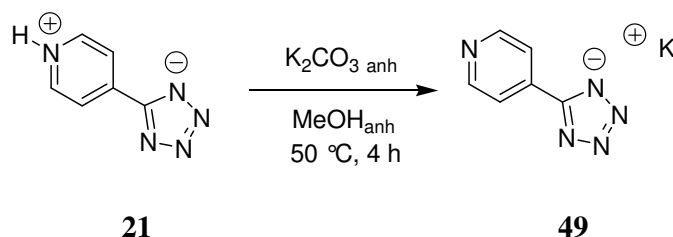
**Figure. 33:** Self-assembly of chromophoric superlattices by an iterative covalent steps

The above reported method was followed by us to build up zwitterionic NLO-phore containing self-assembled monolayers (SAM) based on our main pyridinium tetrazolate system **21**. This work was conducted at Northwestern University thanks to the ten-year collaboration between our group and the Marks group.

The first step consisted in the preparation of the substrates; different materials were used depending on the final techniques needed for analyzing the resulting films. Therefore, besides silicon and sodium lime glass, quartz slides were introduced due to the linear optical characteristics of compound **21**, which only absorbs in the UV region of the spectrum. The substrates cleaning step followed a standard literature procedure already reported by us:<sup>107</sup> immersion in a "piranha" solution ( $\text{H}_2\text{SO}_4$ :30%  $\text{H}_2\text{O}_2$  = 70:30 v/v) at 80 °C for 1 h, subsequently rinsing with deionized (DI) water and then sonication in a "standard cleaning 1" SC-1 solution (DI  $\text{H}_2\text{O}$ : 30%  $\text{H}_2\text{O}_2$ :  $\text{NH}_3$  = 5:1:1 v/v/v) for 45 min, final washing with copious amounts of Millipore  $\text{H}_2\text{O}$  and drying at 115 °C overnight before deposition of the coupling agent.

The extremely air-sensitive anchoring layer agent dichloriodo-(4-iodomethyl)phenylsilane was synthesized in anhydrous conditions from precursors p-(iodomethyl)phenyldiiodochlorosilane following the standard method reported by the Marks group.<sup>108</sup> The obtained white solid was deposited onto the cleaned substrates according to literature,<sup>109</sup> leading to highly hydrophobic surfaces, as confirmed by the registered elevated contact angle values (silicon  $72^\circ \pm 4^\circ$ , quartz  $85^\circ \pm 4^\circ$ ), indicative of dense coupling layer surface coverage.<sup>110</sup>

Tetrazole **21** was deposited from solution after deprotonation of the pyridinic nitrogen to give the corresponding potassium salt **49**, in a similar fashion to the one already reported in the previous synthetic section (**Scheme. 20**).



Scheme. 20



The first employed method for the deposition process focused on spin-coating, according to the reported procedures for our widely investigated dicyanomethanide zwitterionic systems.<sup>103,107</sup> Various conditions were tried (the main one consisting in spinning a 20mM solution of **49** in anhydrous MeOH at 2000 rpm for 30 sec + 1200 rpm for 30 sec, followed by treatment under vacuum for 30 min at 120 °C and with final acetone rinsing and double sonication in MeOH), but all the conducted attempts resulted to fail. No chromophoric film was in fact detectable on the surface, except for few white spots, after deposition, whilst profilometric as well as UV-VIS absorption analysis verified the complete absence of the desired film.

The explanation for such a result was found in the very low reactivity of the pyridinic nitrogen in compound **49**. The presence of the tetrazole ring in fact strongly depresses the nucleophilicity of the heterocyclic six-membered ring, which resulted very difficult to quaternize. To circumnavigate this major drawback, a different approach was introduced which focused on a "standard solution method".<sup>101</sup> Under nitrogen atmosphere, the previously functionalized substrates were therefore transferred into a **49** solution (by means of a teflon substrate holder) and refluxed (**Figure. 34**).



Figure. 34: Self-assembly reactor

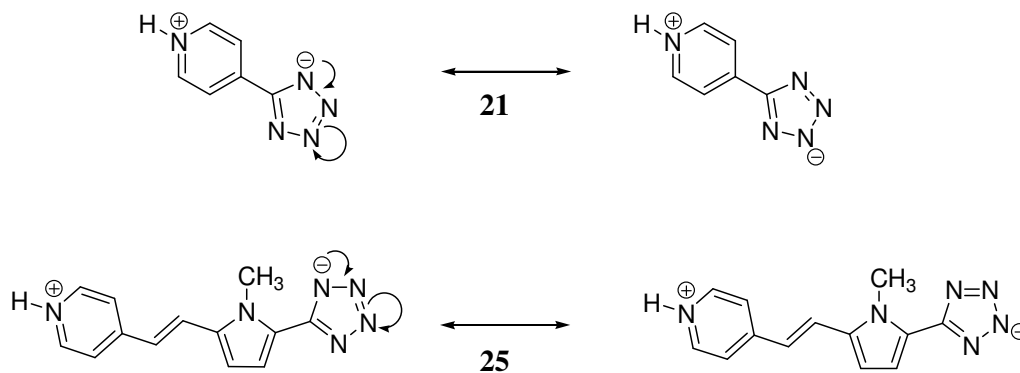


Compound **51** presenting an hydroxyl functionality was therefore introduced following the two synthetic pathways reported in the above **Scheme 21**. The first strategy starts from the zwitterionic NLO-phore **21** and involves alkylation of the pyridine moiety with 3-bromopropanol under microwave irradiation. The second route consider in the first step the alkylation of 4-cyanopyridine with the same alkylating agent leading to the hydroxypropyl derivative **50**, which was subsequently converted into the corresponding tetrazolate using standard literature methods. The desired product was successfully obtained by both methods and the anchoring process on the surface is currently under investigation.

### 3.3 VAPOR-DEPOSED THIN FILMS

In the search for a substitutive method to achieve highly ordered NLO thin films, the unconventional approach of obtaining self-assembled structures from the gas phase was taken into account. Small-molecule physical vapor deposition (PVD) processes are in fact widely used in the growth of organic thin films for organic light-emitting diodes (OLEDs) and field-effect transistors (OFETs) where they provide precise control of the film thickness, smoothness, and crystallinity with high chemical purity and in situ monitoring of the film growth and growth rate.<sup>111</sup> Supramolecular self-organization achieved through PVD method is based on weak supramolecular interactions and a precise control of the deposition parameters (deposition rate, substrate nature and temperature, presence of specific functionalities on the depositing molecules) is therefore required to optimize the film growth (a deeper analysis of the various factors influencing the film growth is reported in the second part of this thesis, concerning organic thin film transistors, *vide infra*). Considering the involved molecules, from a structural point of view, the presence of proper sites capable of giving H-bonding interactions has recently been used in fabricating EO nanoscopically acentric active thin films by process of PVD.<sup>112,113</sup>

Our efforts to realize ordered supramolecular structures exploiting the PVD process were focused on pyridinium tetrazolates **21** and **25**; the presence of the negative charged tetrazolate nitrogen and of the pyridinium hydrogen atom represented in our opinion the appropriate basis for the instauration of suitable H-bonding between the individual molecular entities during deposition. Considering in fact the different resonance limiting forms for the above NLO-phores, it is possible to recognize for the two a mesomeric structure having the H-bonding donating and accepting sites residing on the molecular axis opposite positions (**Scheme. 22**), thus conferring the correct molecular shape and functionality position for proper supramolecular interactions.



Scheme. 22

Various attempts were conducted with both chromophores, only the most significant ones are reported in the following, enabling us to elucidate the diverse encountered situations. It is worth noting that for all the performed depositions, the instrument was calibrated on the selected NLO-phore density prior to its utilization, and the lowest possible growth rate was always used (0.1-0.2 Å/s).

Zwitterion **21** was firstly deposited on bare substrates (silicon and quartz) maintained at room temperature. The profilometric measurements conducted on the evaporated film (**Figure. 35**) evidence a thickness in accordance with the nominal one read on the evaporator, with an acceptable film homogeneity.

In the UV-VIS absorption spectrum (**Figure. 36**) it is to emphasize the presence of a low-energy shoulder besides the characteristic molecular ICT band at 287 nm the presence, imputable to the occurrence of aggregation in the film solid state.<sup>114</sup>

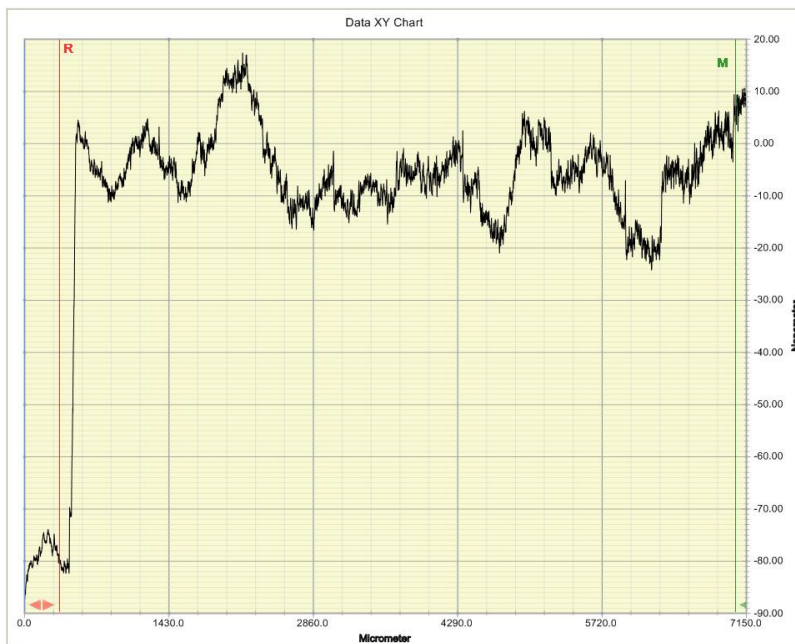


Figure. 35: Profilometer analysis

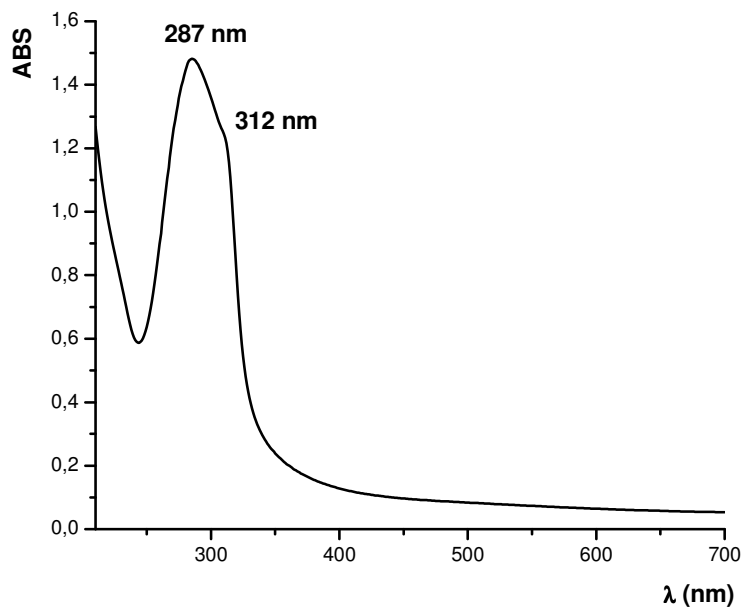
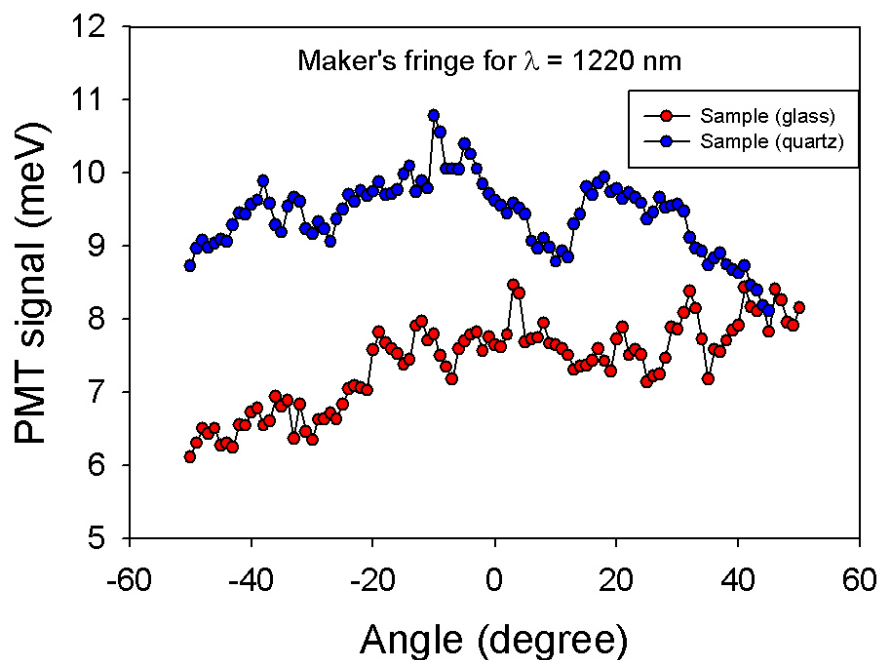
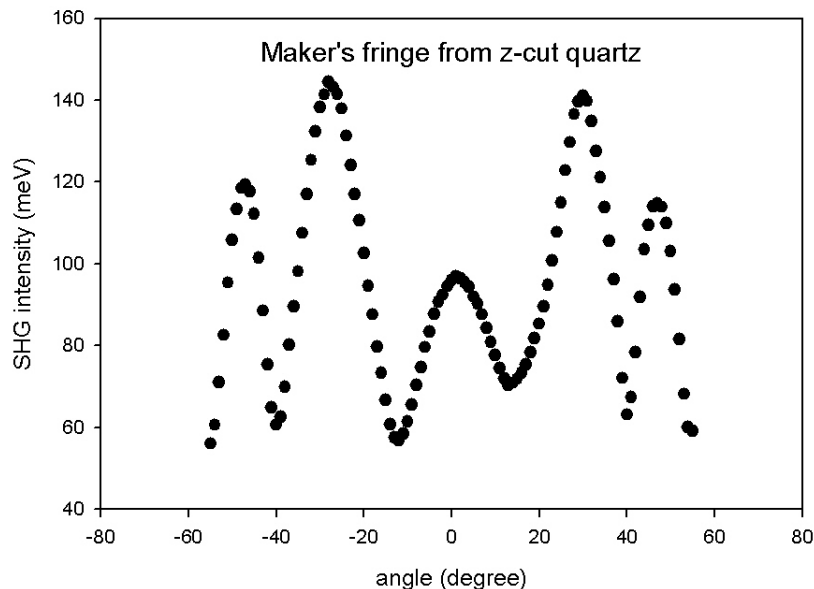


Figure. 36: UV-VIS absorption spectrum for thin film of 21 on bare quartz ( $T_d = r. t.$ )

The NLO characterization of films deposited both on glass and quartz substrates is reported in **Figure. 37**, which shows in the Maker's fringe analysis the complete absence of the typical expected interference pattern.<sup>115</sup> In **Figure. 38** the Maker's fringe analysis for standard z-cut quartz sample is reported for comparison.



**Figure. 37:** Maker's fringe analysis for film of 21 on bare quartz ( $T_d = r. t.$ )



**Figure. 38**

The above obtained results are consistent with a disordered orientation of the chromophore inside the film and substantially not homogeneously grown layers.

With the aim of obtaining a more homogeneous film, the substrate temperature was increased during deposition as it is usually done for organic semiconductor thin film deposition. Depositing at 80 °C surprisingly did not result in the formation of any film on the bare substrates and the same result was obtained for depositing temperature as low as 40°C. These outcomes evidence the high volatility of **21**, which sublimates from the substrates in the evaporator chamber.

Another approach to obtain a more ordered film was therefore introduced, supports functionalized with the previously shown anchoring layer were used in place of bare substrates, depositing the NLO-phore at room temperature. **Figure 39** shows the UV-VIS characterization for films deposited on one side (black line) and on both sides (blue line) of a quartz slide pre-functionalized with a benzyl iodide anchoring layer.

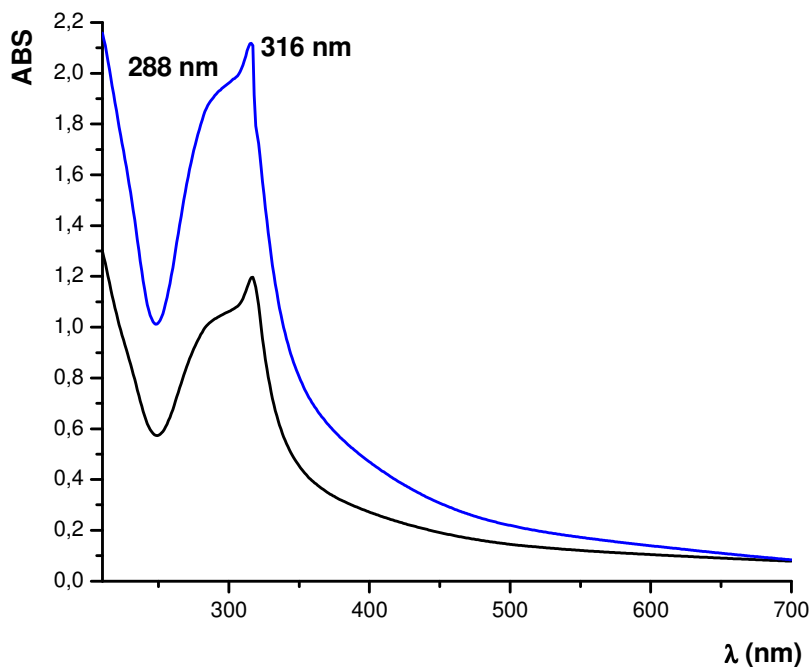


**Figure. 39:** UV-VIS absorption spectrum for thin film of 21 on functionalized quartz ( $T_d = r.t.$ )

It is evident from the spectrum the formation of aggregates in the solid state also in this evaporation conditions, the nonlinear response (**Figure. 40**) evidences again the complete absence of the required supramolecular alignment and ordering inside the thin film.

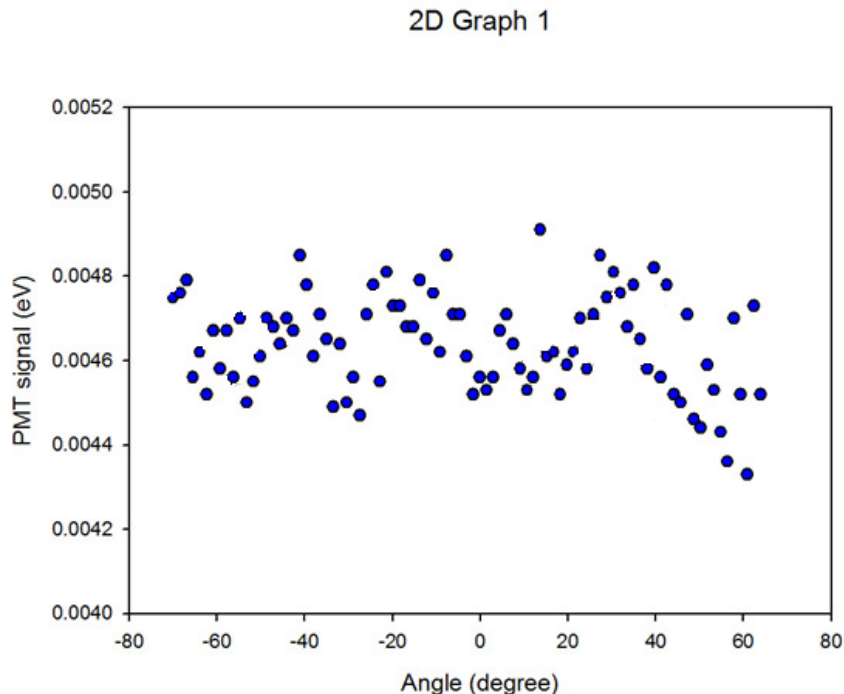


**Figure. 40:** Maker's fringe (1220 nm) analysis for thin film of **21** on functionalized quartz ( $T_d = r.t.$ )

We move on from trying to conduct further deposition attempts concerning NLO-phore **21**, transferring our investigation on system **25**. The first deposition was conducted on bare substrates at room temperature; the final film resulted far much thicker than expected, considering the nominal thickness measured during deposition by means of the integrated microbalance, also the surface morphology resulted very rough, thus demonstrating an inhomogeneous island-growth of the film on the substrate (**Figure. 41**). The linear absorption spectrum (**Figure. 42**) evidences the occurrence of aggregation in the solid state for this system as well, as expected due to the large dipolar molecular moment characteristic of the charge-separated structure.



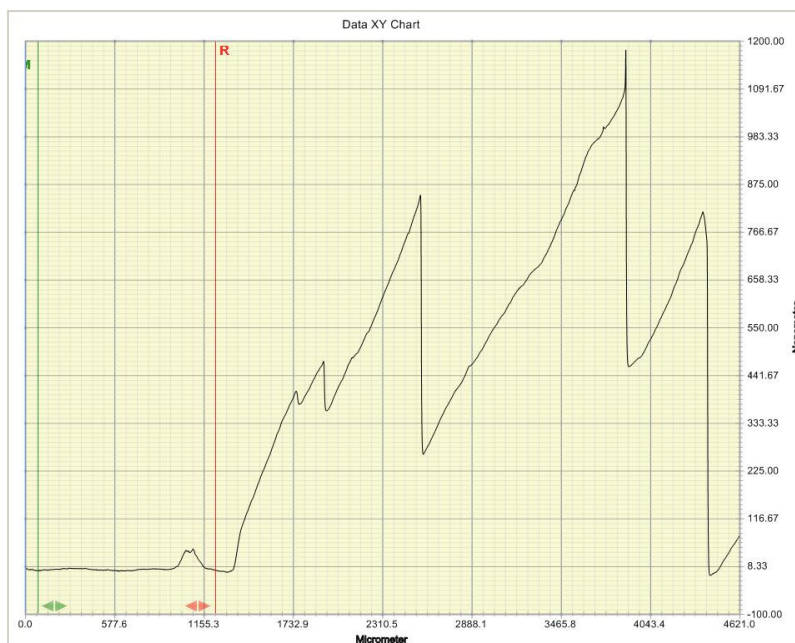


Figure. 41: Profilometer analysis

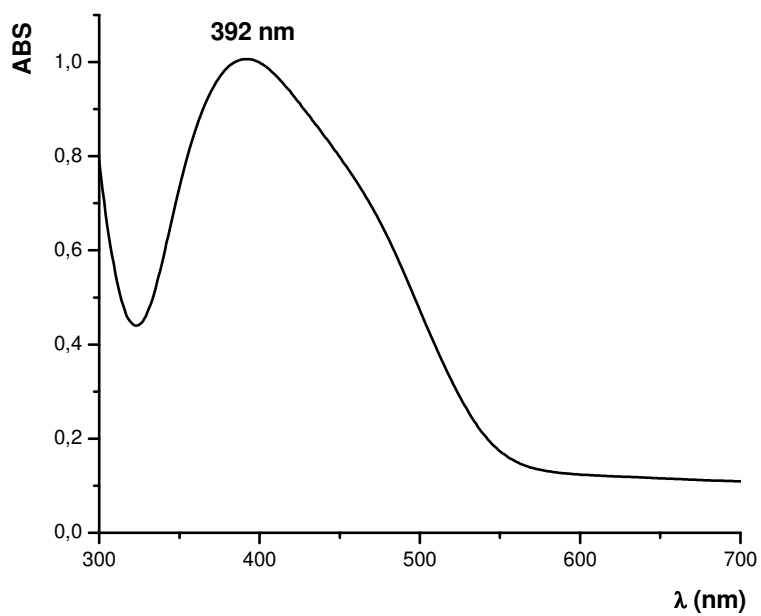


Figure. 42: UV-VIS absorption spectrum for thin film of 25 on bare quartz ( $T_d = r. t.$ )

Also for chromophore **25** we proceeded as previously done for zwitterion **21**, in order to obtain a more uniform film and a better molecular alignment in the deposited layers. We therefore increased the temperature of the substrates first, and this time we were able to obtain a film for  $T_d=40$  °C; UV-VIS spectrum confirmed the presence of the aggregated species and the profilometer analysis demonstrated only a little improvement in the surface morphology which remain highly irregular. The final suggested attempt exploited again the possibility of inducing a supramolecular ordering by means of a templating effect on the first depositing layer, induced by the presence of pre-assembled anchoring layer; the nonlinear (**Figure. 43**) analysis demonstrated also in this case the same results obtained for the previous NLO-phore, with the complete absence of any interference fringe in the Maker's fringe analysis and thus a lack of alignment inside the deposited film.

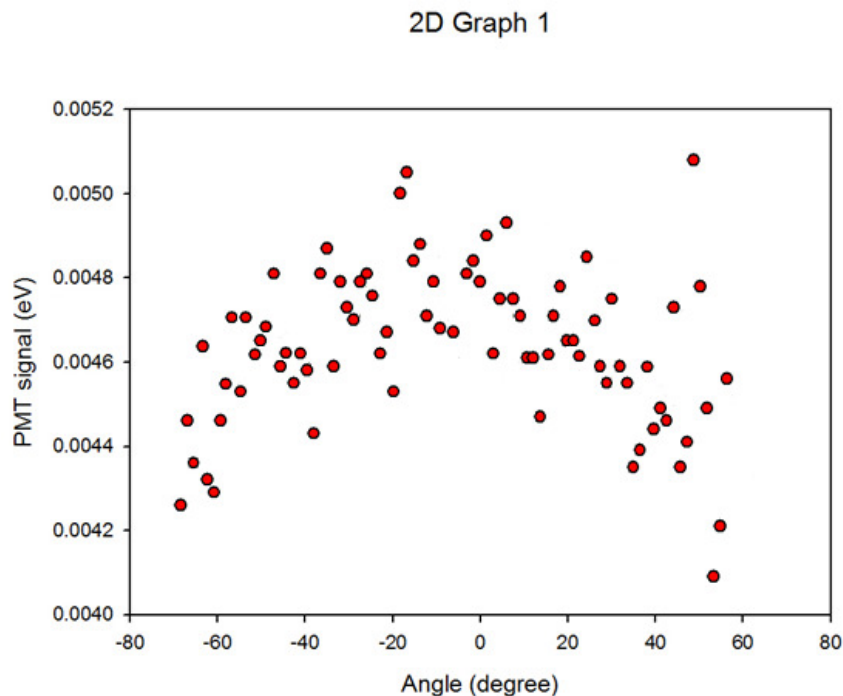


Figure. 43: Maker's fringe (1220 nm) analysis for thin film of **25** on functionalized quartz ( $T_d = r.t.$ )

### III. CONCLUSIONS

A detailed analysis of a wide class of heteroaromatic conjugated systems for NLO applications was reported. The most challenging design strategies for obtaining high second-order responses were described, showing the evolution from the common archetypal dipolar push-pull structures to the ultimate state-of-the-art systems, based upon highly polarizable charge-separated zwitterionic NLO-phores. Starting from the BLA theory it was first demonstrated the possibility of correlating the molecular structure to the final linear and nonlinear molecular optical behavior, thus enabling the exploration and manipulation of a whole range of different design approaches, capable of finely tailoring the intrinsic molecular characteristics on specific requests. End capping the  $\pi$ -conjugated system with stronger donor and acceptor groups represents in this sense only the very first effort, whilst subsequent strategies for enhancing  $\beta$  exploited the peculiar characteristics of heteroaromatic six-membered electron-poor rings and electron-rich five-membered heterocycles to accomplish innovative structural concepts. This was the case for the auxiliary- donor/acceptor theory we focused on to obtain the totally new systems **3**, **4**, **5** which presented other remarkable peculiarities, as for example the presence of the rarely encountered strong donating hydrazono moiety. Besides the latter, the concept of charged molecular ground state was here introduced, which found its highest expression in the zwitterionic systems. Moving apart from the common literature approach, we followed the innovative design strategies leading to a charge-separated aromatic molecular fundamental state, thus overturning the standard chromophore motif and allowing the accessibility to distinctive characteristics never met before, such as the possibility of finely span the entire BLA plot by simply choosing medium with the most suitable polarities. We deeply investigated these phenomena with all the subsequent introduced structures from pyridonemethides **12** and **15** to

the more stable pyridoneimines **13** and **15**, where the highly reactive and easily oxidizable carbanionic donating center was substituted with the more electronegative nitranionic bridge, capable of better sustain the negative charge. We demonstrated the possibility of realizing stable host-guest polymeric electro-optic materials, dispersing the structurally engineered molecules in the polymeric matrix and aligning them by means of electric poling techniques. The extreme consequence of the nitranionic-zwitterionic theme was achieved with the introduction of the azinyl tetrazolates class, where we exploited the synergic effect of the azinium ring (pyridinium and acridinium) electron withdrawing capacitance together with the donating behavior of the five-membered tetrazolate heterocycle. Pyridyl tetrazolate **22** in this regard represents an outstanding contribution to the field, due to the extraordinary transparency/nonlinearity tradeoff united with both the exceptional thermal and chemical stability and the interesting solvatochromism. Further developments in this regard led to the introduction of the more conjugated compound **25**, based on our literature benchmark dipolar dye, which enabled us to obtain the unprecedented nonlinear  $\mu\beta_{1.907}$  value of  $-3500 \times 10^{-48}$  esu (DMF). We conducted several different attempts to realize supramolecular ordered EO structures with the above two derivatives, but both self-assembly technique and physical vapor deposition resulted to fail mainly due to the depressed reactivity of the pyridinic nitrogen and to the lack of acentric order in the final deposited thin films. Acridinyl tetrazolates were finally introduced to study the effect of annelation on the relative contribution of the two resonance limiting forms in describing the ground state, thus investigating the possibility of affecting the molecular linear and nonlinear optical behavior through a simple benzofusion. Various synthetic strategies were pursued to obtain compound **29** and **30**, ultimately leading to the desired products. Compound **30** was particularly interesting as it embodies our approach to the novel paradigm for enhancing  $\beta$ , overtaking the classical two-state model by pioneering the concept of twisted charge transfer structures.

## EXPERIMENTAL SECTION

Solvents and reagents were provided by Sigma-Aldrich, Alpha Aesar and used without further purifications (except where specified). Compounds **1** and **2**,<sup>47</sup> **8**,<sup>51</sup> **21**,<sup>70</sup> and reagents 3,7-dimethyloctyl triflate<sup>22</sup> and 9-methylacridine,<sup>81</sup> were synthesized according to known literature procedures. Chromatography separations were conducted on silica 9385, 230-400 mesh provided by Sigma-Aldrich or alumina Merck 90 active, neutral (activity grade I), 70-230 mesh. The methodology followed for chromatographic purifications is reported in the literature.<sup>116</sup> Prime grade *p*-doped silicon wafers <100> used as substrates were provided by Montco Inc.

<sup>1</sup>H-NMR and <sup>13</sup>C-NMR spectra were recorded on an AMX-500 FT Bruker spectrometer. UV-Vis spectra were recorded on a JASCO V-57 spectrophotometer, both for solution sample and vapor-deposited films. Microwave reactions were conducted with a CEM Discover SP instrument. DSC traces were acquired on a Mettler-Toledo STARe instrument under nitrogen atmosphere. Melting points were collected with an Electrothermal instrument model 9100 and are incorrect. The values of  $\mu\beta_\lambda$  have been directly obtained from the EFISH measurements considering negligible the  $\gamma_0$  contribution to  $\gamma_{\text{EFISH}}$ . The EFISH measurements were carried out in DMF solutions at the same concentration ( $10^{-5}$  M) working at a nonresonant incident wavelength of 1.907  $\mu\text{m}$ , using a Q-switched, mode-locked Nd<sup>3+</sup>:YAG laser, equipped with a Raman shifter. All experimental EFISH  $\beta_\lambda$  values are defined according to the "phenomenological" convention.<sup>117</sup> Maker's fringe analysis were performed by the Ketterson research group at Northwestern University using the experimental setup reported in the literature.<sup>118</sup>

**1-(2,4-dinitrophenyl)-4-(2-(*N*-methylpyrrol-2-yl)vinyl)pyridinium chloride (3)**

A solution of 1-chloro-2,4-dinitrobenzene (1.970 g, 9.73 mmol) in dry  $\text{CH}_3\text{NO}_2$  (5 mL) is added dropwise to a solution of **1** (0.320 g, 1.74 mmol) in the same solvent (10 mL); the solution turns progressively red. After 48 hours reacting at room temperature, the reaction mixture is poured into  $\text{Et}_2\text{O}$  (100 mL) and a dark-red solid separates, which is the desired product (0.550 g, 1.42 mmol, 82%).

M.p. 242 °C.  $^1\text{H}$  NMR (500 MHz,  $\text{DMSO}-d_6$ )  $\delta$ [ppm]: 9.11 (d, 1H,  $J=2.2$ ), 8.97 (d, 2H,  $J=6.6$ ), 8.95 (dd, 1H,  $J=10.1, 2.3$ ), 8.39 (d, 1H,  $J=8.7$ ), 8.31 (d, 2H,  $J=6.7$ ), 8.18 (d, 1H,  $J=15.6$ ), 7.25 (s, 1H), 7.23 (d, 1H,  $J=15.7$ ), 7.06 (d, 1H,  $J=3.4$ ), 6.32 (t, 1H,  $J=2.66$ ), 3.86 (s, 3H).

**2-(*N,N*-dimethylhydrazonomethyl)-*N*-methyl-5-[2-(*N*-methylpyrid-4-yl)-vinyl] pyrrole triflate (4)**

1,4-dimethylpyridinium triflate (1.770 g, 6.88 mmol) and catalytic piperidine are added to a solution of **7** (0.990 mg, 5.52 mmol) in EtOH (15 mL); the solution changes color. The reaction mixture is let react at reflux temperature 2 hours, the solvent is then removed under reduce pressure and the residual is taken up with  $\text{CH}_2\text{Cl}_2$  (50 mL) and washed with water (3x50 mL). The organic phase is separated and the solvent removed, leaving the crude product which is purified by crystallization in EtOH (0.450 g, 1.08 mmol, 20%).

M.p. 151 °C.  $^1\text{H}$  NMR (200 MHz,  $\text{DMSO}-d_6$ )  $\delta$ [ppm]: 8.62 (d, 2H,  $J=6.9$ ), 8.23 (d, 1H,  $J=15.8$ ), 7.97 (d, 2H,  $J=6.9$ ), 7.56 (s, 1H), 6.94 (d, 1H,  $J=15.8$ ), 6.88 (d, 1H,  $J=3.0$ ), 6.54 (d, 1H,  $J=3.0$ ), 4.15 (s, 3H), 3.75 (s, 3H), 3.00 (s, 6H).

**2-(*N,N*-dimethylhydrazonomethyl)-*N*-methyl-5-[2-(*N*-(2,4-dinitrophenyl)pyrid-4-yl)-vinyl] pyrrole chloride (5)**

A solution of **9** (105 mg, 0.41 mmol) in dry  $\text{CH}_3\text{CN}$  (5 mL) is added dropwise to a solution of 1-chloro-2,4-dinitrobenzene (440 mg, 2.17 mmol) in the same solvent (10 mL). The reaction mixture turns

progressively green, after 48 hours reacting at room temperature, Et<sub>2</sub>O is added (150 mL) and the precipitate dark solid is filtered, which is the pure product (100 mg, 0.22, 53%).

M.p. 190 °C. <sup>1</sup>H NMR (500 MHz, DMSO-*d*<sub>6</sub>)δ[ppm]: 9.10 (d, 1H, *J*=2.5), 8.92 (dd, 1H, *J*=8.7, 2.5), 8.76 (d, 2H, *J*=7.1), 8.34 (d, 1H, *J*=8.7), 8.16 (d, 1H, *J*=15.3), 8.12 (d, 2H, *J*=6.8), 7.27 (s, 1H), 7.20 (d, 1H, *J*=4.4), 7.14 (d, 1H, *J*=15.2), 6.60 (d, 1H, *J*=4.4), 3.93 (s, 3H), 3.03 (s, 6H).

#### ***N*-Methyl-2-(*N,N*-dimethylhydrazonomethyl)pyrrole (6)**

A solution of *N*-methylpyrrole-2-carboxyaldehyde (1.016 g, 9.31 mmol) and *N,N*-dimethylhydrazine (0.770 g, 12.82 mmol) in EtOH (4 mL) is let react under microwave irradiation at 50 W, 25 min. The obtained dark yellow solution is reduced under vacuum and purified by filtration through a short silica plug (AcOEt/Petroleum ether 6:1) to give the pure product as a yellow oil (1.250 g, 8.53 mmol, 91%).

<sup>1</sup>H NMR (200 MHz, DMSO-*d*<sub>6</sub>)δ[ppm]: 7.32 (s, 1H), 6.70 (t, 1H, *J*=2.0), 6.18 (dd, 1H, *J*=3.7, 1.9), 5.98 (t, 1H, *J*=3.7), 3.73 (s, 3H), 2.78 (s, 6H).

#### ***N*-Methyl-5-(*N,N*-dimethylhydrazonomethyl)pyrrole-2-carboxaldehyde (7)**

Freshly distilled POCl<sub>3</sub> (1.930 g, 12.56 mmol) is added dropwise to a solution of anhydrous DMF (0.903 mg, 12.35 mmol) at 0 °C; the Vilsmeier adduct forms as a white solid. After 30 min the ice-bath is removed and dry DCE is added (20 mL). After complete dissolution of the adduct, a solution of **6** (1.290 g, 8.53 mmol) in the same solvent is added, the solution turns progressively dark. The mixture is let react overnight at room temperature. The obtained suspension is diluted with dry DCE (20 mL) and is treated with a saturated K<sub>2</sub>CO<sub>3</sub> solution (200 mL) for 1 hour till basic pH is reached. The organic phase is separated and the aqueous phase extracted with CH<sub>2</sub>Cl<sub>2</sub> (2x100 mL). The organic phases are collected and concentrated obtaining a brownish oil which is purified by chromatography (silica,

AcOEt/Petroleum ether 6:4) to give the desired product, as a yellow oil, in the form of two non-separable isomers (1.480 g, 8.27 mmol, 97%).

$^1\text{H}$  NMR (200 MHz, DMSO- $d_6$ ) $\delta$ [ppm]: isomer 1: 9.97 (s, 1H), 7.59 (s, 1H), 6.80 (d, 1H,  $J=3.0$ ), 6.41 (d, 1H,  $J=3.0$ ), 3.75 (s, 3H), 2.96 (s, 6H); isomer 2: 9.41 (s, 1H), 7.19 (s, 1H), 6.94 (d, 1H,  $J=4.2$ ), 6.39 (d, 1H, 4.3), 4.01 (s, 3H), 2.96 (s, 6H).

#### 2-(*N,N*-dimethylhydrazonomethyl)-*N*-methyl-5-[2-(pyrid-4-yl)-vinyl]pyrrole (**9**)

A mixture of **8** (165 mg, 0.777 mmol), *N,N*-dimethylhydrazine (55 mg, 0.920 mmol) and anhydrous *p*-toluenesulfonic acid (155 mg, 0.900 mmol) is dissolved in EtOH (20 mL) and refluxed 4 hours. The red-colored reaction mixture is poured into a saturated  $\text{K}_2\text{CO}_3$  solution and stirred 1 hour, till basic pH is reached. The solution is extracted with  $\text{CH}_2\text{Cl}_2$  (3x50 mL) and the organic solvent is removed under vacuum to give the desired product as a yellow solid (120 mg, 0.472 mmol, 61%).

$^1\text{H}$  NMR (200 MHz, DMSO- $d_6$ ) $\delta$ [ppm]: 8.47 (d, 2H,  $J=5.9$ ), 7.51 (d, 2H,  $J=6.1$ ), 7.50 (d, 1H,  $J=16.0$ ), 6.88 (d, 1H,  $J=16.0$ ), 6.67 (d, 1H,  $J=4.0$ ), 6.32 (d, 1H,  $J=4.0$ ), 3.87 (s, 3H), 2.85 (s, 6H).

#### *N*-(3,7-dimethyloctyl)-4-(4-nitrobenzylidene)-1,4-dihydropyridine (**12**)

A solution of **16** (965 mg, 1.91 mmol) in  $\text{CH}_2\text{Cl}_2$  (15 mL) is treated under stirring 3 h with the ion exchange resin AMBERLIST IRA-400 BASIC, the color turns immediately deep blue-violet.

The resin is filtered off and the solvent removed under reduce pressure leading to the desired product as a sticky blue-violet solid (650 mg, 1.83 mmol, 96%).

$^1\text{H}$  NMR (500 MHz, DMSO- $d_6$ ) $\delta$ [ppm]: 7.93 (d, 2H,  $J=9.1$ ), 7.20 (d, 2H,  $J=9.1$ ), 7.20 (d, 1H,  $J=$  Not readable), 6.79 (d, 1H,  $J=6.6$ ), 6.20 (d, 1H,  $J=6.3$ ), 5.37 (s, 1H), 3.72-3.62 (m, 2H), 1.69-1.63 (m, 1H), 1.54-1.36 (m, 3H), 1.32-1.08 (m, 6H) 0.90 (d, 3H,  $J=6.3$ ), 0.84 (d, 6H,  $J=6.5$ );  $^{13}\text{C}$  NMR (125.7 MHz, DMSO- $d_6$ ) $\delta$ [ppm]: 148.81 (1C), 142.06 (1C), 139.08 (1C), 138.09 (1C), 135.34 (1C), 124.84 (2C), 123.82 (2C), 117.43 (1C), 108.69 (1C), 100.87 (1C), 53.27 (1C),



39.07 (1C), 37.62 (1C), 36.86 (1C), 29.94 (1C), 27.82 (1C), 24.47 (1C), 23.04 (1C), 22.95 (1C), 19.69 (1C).

***N*-(1-(3,7-dimethyloctyl)-1*H*-pyridin-4-ylidene)-4-nitroaniline (13)**

Potassium *tert*-butoxide (0.458 g, 4.08 mmol) is added to a solution of **17** (1.50 g, 3.90 mmol) in DMSO (15 mL), the mixture is stirred 15 min and turns light yellow. A solution of fluoro-4-nitrobenzene (0.568 g, 4.03 mmol) in the same solvent (15 mL) is then added dropwise to the mixture. After 24 h the reddish reaction mixture is poured into ice, and the resulting orange precipitate is collected by filtration. The obtained crude sticky solid is purified by trituration with petroleum ether to give the desired pure product as a bright orange solid (0.450 g, 1.27 mmol, 32%).

M.p. 65 °C. <sup>1</sup>H NMR (500 MHz, DMSO-*d*<sub>6</sub>) δ [ppm]: 8.08 (dd, 2H, *J*=7.1, 2.0), 7.54 (d, 2H, *J*=7.6), 6.91 (dd, 2H, *J*=7.0, 2.0), 6.31 (d, 2H, *J*=7.6), 3.87-3.78 (m, 2H), 1.71-1.67 (m, 1H), 1.54-1.44 (m, 2H), 1.40-1.36 (m, 1H), 1.29-1.18 (m, 4H) 1.14-1.08 (m, 2H), 0.90 (d, 3H, *J*=6.5), 0.85 (d, 6H, *J*=6.6); <sup>13</sup>C NMR (125.7 MHz, DMSO-*d*<sub>6</sub>) δ [ppm]: 160.85 (1C), 157.52 (1C), 140.14 (2C), 140.00 (1C), 125.92 (2C), 121.62 (2C), 111.92 (2C), 53.92 (1C), 39.06 (1C), 37.78 (1C), 36.83 (1C), 29.95 (1C), 27.82 (1C), 24.45 (1C), 23.04 (1C), 22.95 (1C), 19.67 (1C).

***N*-(1-(2-ethylheptyl)-1*H*-pyridin-4-ylidene)-2,4-dinitroaniline (14)**

A solution of **18** (170 mg, 0.509 mmol) in dry CH<sub>3</sub>CN (3 mL) is heated at 50 °C under stirring, a solution of fluoro-2,4-dinitrobenzene (95 mg, 0.510 mmol) in the same solvent (2 mL) is then added dropwise and the mixture is refluxed 3 h. AcOEt (30 mL) is added to the reaction mixture and the organic phase is washed with an aqueous 20% NaOH basic solution (3x50 mL). The organic solvent is removed and the residual is taken up with dichloromethane; the desired product contained in the organic phase is purified by filtration through a short

alumina plug giving the desired adduct as a bright red solid (120 mg, 0.322 mmol, 63%).

$^1\text{H}$  NMR (500 MHz,  $\text{DMSO-}d_6$ )  $\delta$ [ppm]: 8.60 (d, 1H,  $J=3.0$ ), 8.17 (dd, 1H,  $J=9.2, 2.8$ ), 7.76 (d, 2H,  $J=7.5$ ), 7.19 (d, 1H,  $J=9.2$ ), 6.51 (d, 2H,  $J=7.5$ ), 3.85 (d, 2H,  $J=7.4$ ), 1.77-1.74 (m, 1H), 1.28-1.18 (m, 8H), 0.89-0.85 (m, 6H);  $^{13}\text{C}$  NMR (125.7 MHz,  $\text{DMSO-}d_6$ )  $\delta$ [ppm]: 159.19 (1C), 153.30 (1C), 141.61 (3C), 137.41 (1C), 128.12 (1C), 122.72 (1C), 122.09 (1C), 112.98 (2C), 59.75 (1C), Covered by DMSO signal(1C), 29.66 (1C), 28.16 (1C), 23.08 (1C), 22.88 (1C), 14.34 (1C), 10.62 (1C).

#### ***N*-(3,7-dimethyloctyl)-4-(2,4-dinitrobenzilydene)-1,4-dihydropyridine (15)**

A solution of **20** (1.775 g, 6.11 mmol) in  $\text{CH}_2\text{Cl}_2$  (15 mL) is treated under stirring 5 h with the ion exchange resin AMBERLIST IRA-400 BASIC, the color turns immediately dark blue. The resin is filtered off and the solvent removed under reduce pressure leading to the desired product as a dark blue-green solid (1.880 mg, 4.70 mmol, 90%).

M.p. 87 °C.  $^1\text{H}$  NMR (500 MHz,  $\text{DMSO-}d_6$ )  $\delta$ [ppm]: 8.63 (d, 1H,  $J=2.6$ ), 7.85 (dd, 1H,  $J=9.4, 2.4$ ), 7.76 (d, 2H,  $J=7.3$ ), 7.72 (d, 1H,  $J=9.5$ ), 7.05 (d, 2H,  $J=7.3$ ), 6.37 (s, 1H), 4.04-3.92 (m, 2H), 1.78-1.71 (m, 1H), 1.57-1.47 (m, 2H), 1.45-1.33 (m, 1H), 1.32-1.19 (m, 3H), 1.18-1.09 (m, 3H), 0.91 (d, 3H,  $J=6.4$ ), 0.85 (d, 6H,  $J=6.6$ );  $^{13}\text{C}$  NMR (125.7 MHz,  $\text{DMSO-}d_6$ )  $\delta$ [ppm]: 149.01 (1C), 140.78 (1C), 139.48 (2C), 139.03 (1C), 135.72 (1C), 125.99 (1C), 124.42 (1C), 124.16 (1C), 117.27 (2C), 97.79 (1C), 54.93 (1C), 39.07 (1C), 37.83 (1C), 36.81 (1C), 30.05 (1C), 27.82 (1C), 24.44 (1C), 23.04 (1C), 22.95 (1C), 19.65 (1C).

#### ***N*-(3,7-dimethyloctyl)-4-(4-nitrobenzyl)pyridinium triflate (16)**

A solution of 3,7-dimethyloctyl trifluoromethanesulfonate (3.000 g, 10.33 mmol) in dry toluene (10 mL) is added dropwise to a suspension of 4-(4-nitrobenzyl)pyridine (2.010 g, 9.38 mmol) in the same solvent (30 mL). The mixture is let react 48 h at room temperature, a light

brown oil separates from the reaction environment, which is the desired product. The oil is taken up with MeOH (10 mL) and washed several times with cyclohexane to yield the desired product as a light yellow oil (4.700 g, 9.31 mmol, 99%).

$^1\text{H}$  NMR (200 MHz,  $\text{DMSO-}d_6$ )  $\delta$ [ppm]: 9.05 (d, 2H,  $J=6.5$ ), 8.24 (d, 2H,  $J=8.8$ ), 8.07 (d, 2H,  $J=6.6$ ), 7.66 (d, 2H,  $J=8.7$ ), 4.62-4.47 (m, 2H), 4.45 (s, 2H), 2.04-1.82 (m, 1H), 1.80-1.58 (m, 1H), 1.58-1.35 (m, 2H), 1.34-1.00 (m, 6H) 0.92 (d, 3H,  $J=6.4$ ), 0.82 (d, 6H,  $J=6.5$ ).

#### **4-amino-1-(3,7-dimethyloctyl)pyridinium triflate (17)**

A solution of 3,7-dimethyloctyl trifluoromethanesulfonate (3.018 g, 10.39 mmol) in dry  $\text{CH}_3\text{CN}$  (10 mL) is added dropwise to a solution of 4-aminopyridine (0.970 g, 10.30 mmol) in the same solvent (15 mL). The mixture is let react 18 h at room temperature and then poured into AcOEt (50 mL) and washed with brine till neutral pH is reached. The organic solvent is removed in vacuum leaving the desired product as a waxy white solid (3.360 g, 8.74 mmol, 85%).

M.p. 182 °C.  $^1\text{H}$  NMR (200 MHz,  $\text{DMSO-}d_6$ )  $\delta$ [ppm]: 8.21 (d, 2H,  $J=7.1$ ), 8.07 (s, 2H), 6.82 (d, 2H,  $J=7.1$ ), 4.21-4.05 (m, 2H), 1.84-1.63 (m, 1H), 1.59-1.40 (m, 1H), 1.25-1.08 (m, 8H), 0.89 (d, 3H,  $J=6.3$ ), 0.84 (d, 6H,  $J=6.6$ ).

#### **4-amino-1-(2-ethylhexyl)pyridinium iodide (18)**

A solution of 3-(iodomethyl)heptane (2.591 g, 10.79 mmol) in dry  $\text{CH}_3\text{CN}$  (10 mL) is added dropwise to a solution of 4-aminopyridine (1.015 g, 10.78 mmol) in the same solvent (25 mL). The mixture is let react refluxing 3 h, the white precipitate solid is removed by filtration and washed several times with cyclohexane to give the desired clean product (2.220 g, 6.64 mmol, 62%).

M.p. 124 °C.  $^1\text{H}$  NMR (200 MHz,  $\text{DMSO-}d_6$ )  $\delta$ [ppm]: 8.19 (d, 2H,  $J=7.3$ ), 8.08 (s, 2H), 6.83 (d, 2H,  $J=7.4$ ), 4.03 (d, 2H,  $J=7.5$ ), 1.80-1.74 (m, 1H), 1.40-1.00 (m, 8H), 0.92-0.79 (m, 6H).

**4-(2,4-dinitrobenzyl)pyridine (19)**

4-(4-nitrobenzyl)pyridine (3.00 g, 14.00 mmol) is added at 0 °C to a sulfonitric solution of H<sub>2</sub>SO<sub>4</sub> 96% (5.9 mL, 105.00 mmol) and HNO<sub>3</sub> 65% (1.2 mL, 17.20 mmol), the mixture is let react at 0 °C 1h, than at room temperature 3 h and finally heated up at 85 °C 3 h. The solution is poured into ice and neutralized with a solution of NH<sub>3</sub> 33% obtaining a dark yellow suspension which is extracted with Et<sub>2</sub>O (2x100 ml) and AcoEt (1x 50 mL). The solvent is removed in vacuum leading to the desired product as a dark green solid (2.87 g, 11.07 mmol, 80%).

<sup>1</sup>H NMR (200 MHz, DMSO-*d*<sub>6</sub>) δ[ppm]: 8.78 (d, 1H, *J*=2.3), 8.55 (dd, 1H, *J*=8.5, 2.4), 8.49 (d, 2H, *J*= 6.0), 7.83 (d, 1H, *J*=8.5), 7.17 (d, 2H, *J*=5.7), 4.42 (s, 2H).

**N-(3,7-dimethyloctyl)-4-(2,4-dinitrobenzyl)pyridinium triflate (20)**

A solution of 3,7-dimethyloctyl trifluoromethanesulfonate (1.83 g, 6.30 mmol) in dry toluene (5 mL) is added dropwise to a solution of **19** (1.49 g, 5.70 mmol) in the same solvent (15 mL). The mixture is let react overnight at room temperature. A yellow oil separates from the reaction environment, which is removed. The oil is dissolved in MeOH (25 mL) and washed with cyclohexane (3x25 mL). The solvent is removed in vacuum leaving the desired product as a yellow oil (2.89 g, 5.25 mmol, 92%).

<sup>1</sup>H NMR (200 MHz, DMSO-*d*<sub>6</sub>) δ[ppm]: 9.02 (d, 2H, *J*=6.4), 8.85 (d, 1H, *J*=2.4), 8.63 (dd, 1H, *J*=8.5, 2.3), 7.98-7.87 (m, 3H), 4.75 (s, 2H), 4.68-4.53 (m, 2H), 2.00-1.81 (m, 1H), 1.77-1.63 (m, 1H), 1.56-1.38 (m, 2H), 1.35-1.00 (m, 6H), 0.92 (d, 3H, *J*=6.4), 0.84 (d, 6H, *J*=6.6).

**1-methyl-4-(tetrazole-5-ate)pyridinium (22)**

A suspension of derivative **2** (238 mg, 1.62 mmol) and anhydrous K<sub>2</sub>CO<sub>3</sub> (112 mg, 0.81 mmol) in MeOH (3 ml) is warmed at 40 °C and stirred till complete dissolution of the precipitate. CH<sub>3</sub>I (312 mg, 2.20 mmol) is added to the colorless solution and the reaction mixture is

heated under microwave irradiation at 130 °C for 90 min at a maximum irradiation power of 80 W. After the irradiation, the mixture is slowly cooled without removing the septum observing the slow precipitation of a light brown solid (flakes). After 4 h at room temperature, the brown precipitate is filtered under reduced pressure to give a light brown crystalline powder that is washed on the filter with 10 ml of MeOH (180 mg, 1.13 mmol, 70%).

M.p. 238-239 °C.  $^1\text{H}$  NMR (500 MHz,  $\text{D}_2\text{O}$ ) $\delta$ [ppm]: 8.62 (d, 2H,  $J=6.7$ ), 8.20 (d, 2H,  $J=6.8$ ), 4.28 (s, 3H). Anal. Calcd for  $\text{C}_7\text{H}_7\text{N}_5$ : C, 52.17; H, 4.38; N, 43.45. Found: C, 51.89; H, 4.53; N, 43.05.

#### 1-methyl-5-(2-(pyridin-4-yl)vinyl)pyrrole-2-carbonitrile (24)

**23** (1.600 g, 7.00 mmol) is dissolved in a freshly distilled acetic anhydride (20 mL) and refluxed 3 h. The reaction mixture is cooled and  $\text{CH}_2\text{Cl}_2$  (100 mL) is added, the solution is poured into ice and basified with a saturated  $\text{Na}_2\text{CO}_3$  solution. The organic phase is washed several times with fresh water and is separated. The solvent is removed in vacuum leading to the crude product as a brown solid which is crystallized in EtOH affording the desired product as a yellow solid (0.880 g, 4.21 mmol, 60%).

M.p. 167 °C.  $^1\text{H}$  NMR (500 MHz,  $\text{DMSO}-d_6$ ) $\delta$ [ppm]: 8.56 (d, 2H,  $J=6.0$ ), 7.61 (d, 2H,  $J=6.0$ ), 7.53 (d, 1H,  $J=16.3$ ), 7.18 (d, 1H,  $J=16.3$ ), 7.01 (d, 1H,  $J=4.2$ ), 6.78 (d, 1H,  $J=4.2$ ), 3.85 (s, 3H);  $^{13}\text{C}$  NMR (125.7 MHz,  $\text{DMSO}-d_6$ ) $\delta$ [ppm]: 150.51 (2C), 144.30 (1C), 137.23 (1C), 128.41 (1C), 121.34 (2C), 120.82 (1C), 120.43 (1C), 114.49 (1C), 108.80 (1C), 105.31 (1C), 33.13 (1C).

#### 5-(1-methyl-5-(2-(pyridinium-4-yl)vinyl)-1-pyrrol-2-yl)tetrazolate (25)

**24** (600 mg, 2.860 mmol) is loaded in a screw-capped Schlenk flask with tetrabutylammonium fluoride (454 mg, 1.440 mmol) and trimethylsilyl azide (495 g, 4.300 mmol), and heated at 120 °C for 7 h under vigorous stirring. HCl 1 M is then added to the cooled reaction mixture and stirred, a reddish solid precipitates which is filtered and

washed with water and Et<sub>2</sub>O. The desired product is obtained as a red solid (210 mg, 0.833 mmol, 30%).

M.p. No melting. <sup>1</sup>H NMR (500 MHz, DMSO-*d*<sub>6</sub>) δ[ppm]: 8.59 (d, 2H, J=4.2), 7.73 (d, 2H, J=5.8), 7.70 (d, 1H, J=16.2), 7.16 (d, 1H, J=16.1), 6.94 (d, 1H, J=4.2), 6.90 (d, 1H, J=4.2), 4.14 (s, 3H); <sup>13</sup>C NMR (125.7 MHz, DMSO-*d*<sub>6</sub>) δ[ppm]: 150.01, 148.57, 147.07, 136.35, 125.33, 121.70, 120.22, 114.09, 109.90, 33.45.

#### 1-(*tert*-butyldimethylsilyl)tetrazole (26)

In rigorously anhydrous conditions, freshly distilled triethylamine (4.72 g, 46.63 mmol) is added to a solution of 1*H*-tetrazole (3.12 g, 44.54 mmol) in anhydrous toluene (35 mL) and the mixture is cooled to 10 °C. *tert*-butyldimethylsilyl chloride (7.05 g, 46.78 mmol) is then added in 15 min and the reaction environment is cooled at 0 °C. After reacting 24 h at 0 °C the solvent is removed by distillation, anhydrous *n*-hexane is added (60 mL) and the reaction mixture at 0 °C overnight. The white suspension is filtered under nitrogen atmosphere leading to a colorless solution, the solvent is removed in vacuum at room temperature leading to a white waxy solid. After trituration with CH<sub>2</sub>Cl<sub>2</sub> the solvent is filtered off and the desired product is obtained as a white solid after removing the solvent at reduced pressure (0.950 g, 5.15 mmol, 12%).

<sup>1</sup>H NMR (500 MHz, CD<sub>3</sub>CN) δ[ppm]: 0.90 (s, 9H), 0.06 (s, 3H).

#### 2,3,5,6-tetrafluoro-4-(1*H*-tetrazol-5-yl)pyridine (27)

&

#### 2,3,5,6-tetrafluoro-4-(1*H*-tetrazol-1-yl)pyridine (28)

In rigorously anhydrous conditions, **26** (0.950 g, 5.15 mmol) is dissolved in anhydrous THF (10 mL) and cooled to -98 °C by means of a MeOH/liquid N<sub>2</sub> bath. TMEDA (1 mL) is added under inert atmosphere and after a few minutes *n*-Butyllithium (3.22 mL, 1.6 M in hexane, 5.15 mmol) is added dropwise. After 5 min the solution is added dropwise to a solution of pentafluoropyridine (1.306 g, 7.72 mmol) in the same solvent keeping both flasks at -98 °C. The solution turns

slowly yellow and a fine precipitate is formed. The mixture is let react overnight allowing the cooling bath to slowly reach room temperature. The solvent is removed from the reaction environment and the solid mixture is washed with Et<sub>2</sub>O, the residual is then taken up with AcOEt and washed with HCl 10%. The organic phase is separated and the solvent removed under reduce pressure leading to a yellow solid that crystallizes in vacuum (0.600 g, 2.73 mmol, 53%). Compound **28** is separated by sublimation at 40 °C (10<sup>-3</sup> torr).

M.p. 65-67 °C. <sup>1</sup>H NMR (500 MHz, DMSO-*d*<sub>6</sub>) δ[ppm]: **27**: No signal; **28**: 9.47 (s, 1H); <sup>13</sup>C NMR (125.7 MHz, DMSO-*d*<sub>6</sub>) δ[ppm]: 144.00 (dm, <sup>1</sup>J<sub>CF</sub>=243), 136.51 (dm, <sup>1</sup>J<sub>CF</sub>=269). Anal. Calcd for C<sub>6</sub>HF<sub>4</sub>N<sub>4</sub>: C, 32.89; H, 0.46; N, 31.96. Found: C, 33.36; H, 1.07; N, 31.75.

#### 1-*H*-4-(tetrazole-5-ate)acridinium (29a)

**34** (230 mg, 1.126 mmol) is loaded in a screw-capped Schlenk flask with tetrabutylammonium fluoride (178 mg, 0.563 mmol) and trimethylsilyl azide (195 g, 1.689 mmol), the mixture is heated 7 h under vigorous stirring at 90 °C. CH<sub>2</sub>Cl<sub>2</sub> (50 mL) is then added to the cooled reaction mixture and extracted with HCl 1 M (50 mL). At the interlayer between the two phases a yellow solid is formed which is filtered, affording the desired product (150 mg, 0.607, 54%).

M.p. 209 °C. <sup>1</sup>H NMR (500 MHz, DMSO-*d*<sub>6</sub>) δ[ppm]: 8.33 (d, 2H, J=8.7), 7.99 (ddd, 2H, J=8.1, J=5.9, J=1.9), 7.74-7.70 (m, 4H); <sup>13</sup>C NMR (125.7 MHz, DMSO-*d*<sub>6</sub>) δ[ppm]: 148.29, 131.72, 129.92, 128.51, 125.83, 124.87. Anal. Calcd for C<sub>14</sub>H<sub>9</sub>N<sub>5</sub>·1/4H<sub>2</sub>O: C, 67.39; H, 3.74; N, 28.07. Found: C, 67.75; H, 3.62; N, 27.65.

#### 1-methyl-4-(tetrazole-5-ate)acridinium (29b)

**29a** (285 mg, 1.150 mmol) is treated with a basic K<sub>2</sub>CO<sub>3</sub> solution (80 mg, 0.570 mmol) in MeOH at room temperature for 1 h. Excess MeI (821 mg, 5,783 mmol) is added to the colorless solution and let react under stirring for 48 hours. A light yellow solid precipitates which is the by-product **36**, the solvent is reduced in vacuum and the residual is

treated in water at 40 °C for 45 min, the suspended solid is filtered off and the solvent is removed from the solution leading to crude product that is purified by trituration in acetone (47 mg, 0.180 mmol, 17%).

M.p. No melting.  $^1\text{H}$  NMR (500 MHz,  $\text{D}_2\text{O}$ ) $\delta$ [ppm]: 8.18 (d, 2H,  $J=9.4$ ), 7.97 (t, 2H,  $J=7.4$ ), 7.79 (d, 2H,  $J=9.2$ ), 7.61 (t, 2H,  $J=7.4$ ). Anal. Calcd for  $\text{C}_{15}\text{H}_{11}\text{N}_5\cdot\text{H}_2\text{O}$ : C, 64.51; H, 4.69; N, 25.07. Found: C, 64.73; H, 4.92; N, 24.61.

### 5-(1-methyl-5-(10-methylacridinium-9-yl)pyrrol-2-yl)tetrazolate (30)

Acridinium methosulfate **42** (1.060 g, 3.480 mmol) and **47** (0.235 g, 1.700 mmol) are suspended in 2-propanol. *N,N*-Diisopropylethylamine (0.173 g, 1.34 mmol) is added and the mixture refluxed. The color immediately changes turning violet, the mixture is refluxed till almost all of the starting acridinium salt is consumed (2 h). Solvent is removed and the residue purified by chromatography (Alumina, AcOEt/MeOH 5:1) to give the pure title product as a deep purple solid (0.360 g, 1.058, 62%).

M.p. 208 °C.  $^1\text{H}$  NMR (500 MHz,  $\text{DMSO-}d_6$ ) $\delta$ [ppm]: 8.78 (d, 2H,  $J=9.0$ ), 8.41 (t, 2H,  $J=7.5$ ), 8.29 (d, 2H,  $J=8.5$ ), 7.99 (t, 2H,  $J=7.8$ ), 6.98 (d, 1H,  $J=4.0$ ), 6.82 (d, 1H,  $J=3.5$ ), 4.84 (s, 3H), 3.67 (s, 3H);  $^{13}\text{C}$  NMR (125.7 MHz,  $\text{DMSO-}d_6$ ) $\delta$ [ppm]: 155.61, 151.14, 142.02, 138.43, 134.43, 130.72, 128.45, 126.49, 119.68, 118.71, 110.65, 108.62, 39.23, 35.97. Anal. Calcd for  $\text{C}_{20}\text{H}_{16}\text{N}_6\cdot\text{H}_2\text{O}$ : C, 67.02; H, 5.06; N, 23.45. Found: C, 67.35; H, 4.62; N, 22.91.

### Acridine-9-carboxaldehyde (32)

9-Methylacridine (5.00 g, 25.88 mmol) and 4-Nitroso-*N,N*-dimethylaniline (5.00 g, 33.29 mmol) are suspended in EtOH (50 mL) and refluxed for 8 h. The dark red precipitate is filtered and washed with hot EtOH leading to the pure nitron compound **31** (6.120 g, 17.22 mmol, 67%) which is used without any further purification. **31** is refluxed 10 h in HCl 6M (200 mL), the reaction environment is then cooled in an ice bath and a dark yellow precipitated is progressively



formed which is filtered and stirred in a saturated  $\text{Na}_2\text{CO}_3$  solution till reaching a basic pH. The pure aldehyde is thus obtained by filtration (3.070 g, 15.16 mmol, 88%).

M.p. 145.5-147 °C.  $^1\text{H}$  NMR (500 MHz,  $\text{DMSO}-d_6$ ) $\delta$ [ppm]: 11.51 (s, 1H), 8.85 (d, 2H,  $J=8.8$ ), 8.28 (d, 2H,  $J=8.7$ ), 7.93 (t, 2H,  $J=7.1$ ), 7.80 (t, 2H,  $J=7.1$ ).

#### Acridine-9-carbaldehyde oxime (33)

A solution of **32** (3.070 g, 15.16 mmol) in EtOH (30 ML) is added to a suspension of sodium acetate (1.865g, 22,74 mmol) and hydroxylamine hydrochloride (1.180 g, 16.98 mmol) in the same solvent (170 mL). The mixture is refluxed 4 h and then cooled to room temperature, affording the desired product as a yellow solid which is filtered and washed with water (2.870 g, 12.92, 85%)

$^1\text{H}$  NMR (500 MHz,  $\text{DMSO}-d_6$ ) $\delta$ [ppm]: 9.32 (s, 1H), 8.54 (d, 2H,  $J=8.8$ ), 8.20 (d, 2H,  $J=8.8$ ), 7.89 (t, 2H,  $J=7.6$ ), 7.68 (t, 2H,  $J=7.7$ ).

#### Acridine-9-carbonitrile (34)

**33** (2.870 g, 12.92 mmol) is dissolved in acetic anhydride (60 mL) and refluxed 8h assisting at the progressive solution darkening and the precipitation of a yellow solid which is filtered and washed with water to obtain the pure product (2.380 g, 11.65 mmol, 90%).

M.p. 180-182 °C.  $^1\text{H}$  NMR (500 MHz,  $\text{DMSO}-d_6$ ) $\delta$ [ppm]: 8.30 (t, 4H,  $J=9.6$ ), 8.02 (ddd, 2H,  $J=9.0$ ,  $J=6.7$ ,  $J=1.3$ ), 7.91 (ddd, 2H,  $J=8.4$ ,  $J=6.7$ ,  $J=1.0$ ).

#### 9-cyano-10-methylacridinium triflate (35)

Under anhydrous conditions **34** (1.490 g, 7.30 mmol) is dissolved in dry toluene (30 mL), dimethyl sulfate (3.710 g, 29.41 mmol) is added and the reaction mixture refluxed for 11 h. A dark yellow solid separates which is filtered and washed several times with toluene leading to the desired product (0.940 g, 2.906 mmol, 39%).

$^1\text{H}$  NMR (500 MHz,  $\text{DMSO-}d_6$ ) $\delta$ [ppm]: 9.00 (d, 4H,  $J=9.2$ ), 8.28 (t, 4H,  $J=7.6$ ), 3.36 (s, 3H).

### 9-(1*H*-pyrrol-2-yl)acridine (37)

Acridine (3.00 g, 16.74 mmol) and pyrrole (2.90 g, 43.24 mmol) are loaded in a microwave test tube in dry toluene (15 mL) and the reaction mixture is heated under microwave irradiation at 140 °C, 8 h at a maximum irradiation power of 270 W. After the irradiation, the mixture is slowly cooled, the precipitated is filtered and washed with petroleum ether and cyclohexane leading to the desired pure product as a yellow solid (0.750 g, 3.070 mmol, 18%).

M.p. 228 °C.  $^1\text{H}$  NMR (500 MHz,  $\text{DMSO-}d_6$ ) $\delta$ [ppm]: 11.63 (s, 1H), 8.19 (d, 2H,  $J=8.7$ ), 8.06 (d, 2H,  $J=8.7$ ), 7.86 (ddd, 2H,  $J=8.0$ ,  $J=6.5$ ,  $J=1.3$ ), 7.59 (ddd, 2H,  $J=7.9$ ,  $J=6.5$ ,  $J=1.2$ ), 7.20 (s, 1H), 6.53 (s, 1H), 6.44 (s, 1H).

### 9-(1-methyl-pyrrol-2-yl)acridine (38)

In anhydrous conditions, NaH (0.440 g, 11.00 mmol) is washed with dry hexane (3x10 mL) under stirring, the solvent is removed and anhydrous DMF (10 mL) is added. An ice bath is placed under the reaction flask. **37** (2.180 g, 8.820 mmol) is suspended in anhydrous DMF (150 mL) and the solution is added dropwise to the reaction mixture. The solution turns violet. After 30 min at 0 °C, iodomethane (1.660 g, 11.73 mmol) is added and the reaction mixture turns dark yellow. The ice bath is removed allowing the solution to slowly reach room temperature. Water is added (600 mL) and a yellow precipitates is formed, after 1 h under stirring the solid is filtered and washed several times with water, leading to the desired pure product (2.148 g, 8.320 mmol, 93%)

M.p. 148 °C.  $^1\text{H}$  NMR (500 MHz,  $\text{DMSO-}d_6$ ) $\delta$ [ppm]: 8.23 (d, 2H,  $J=8.7$ ), 7.88 (t, 2H,  $J=7.9$ ), 7.73 (d, 2H,  $J=8.5$ ), 7.61 (t, 2H,  $J=7.6$ ), 7.19 (t, 2H,  $J=2.1$ ), 6.39-6.37 (m, 2H), 3.23 (s, 3H);  $^{13}\text{C}$  NMR (125.7

MHz, DMSO- $d_6$ ) $\delta$ [ppm]: 148.80, 138.46, 130.82, 129.88, 126.99, 126.89, 126.47, 126.11, 124.82, 112.48, 108.44, 34.70.

#### 5-(acridin-9-yl)-1-methyl-pyrrole-2-carbaldehyde (39)

In anhydrous conditions, **38** (2.148 g, 8.32 mmol) is dissolved in anhydrous DMF (25 mL) and the solution is cooled to 0 °C. POCl<sub>3</sub> (2.680 g, 17.48 mmol) is added dropwise and the solution turns immediately red. After 30 min at 0 °C, the reaction is stirred 2 h at room temperature and finally heated 3 h at 50 °C. The solution is thrown into a Na<sub>2</sub>CO<sub>3</sub> saturated aqueous solution and stirred till a basic pH is reached. A dark yellow solid precipitates which is filtered leading to the desired product (2.020 g, 7.050 mmol, 85%).

M.p. 194 °C. <sup>1</sup>H NMR (500 MHz, DMSO- $d_6$ ) $\delta$ [ppm]: 9.77 (s, 1H) 8.29 (d, 2H, J=8.7), 7.94-7.90 (m, 2H), 7.70-7.62 (m, 4H), 7.41 (d, 1H, J=4.0), 6.63 (d, 1H, J=4.0), 3.49 (s, 3H); <sup>13</sup>C NMR (125.7 MHz, DMSO- $d_6$ ) $\delta$ [ppm]: 180.82, 148.73, 136.50, 135.65, 133.59, 131.17, 130.20, 127.90, 126.16, 125.84, 123.88, 113.84, 33.97. Anal. Calcd for C<sub>19</sub>H<sub>14</sub>N<sub>2</sub>O: C, 79.70; H, 4.93; N, 9.78. Found: C, 79.56; H, 4.66; N, 9.76.

#### 5-(acridin-9-yl)-1-methyl-pyrrole-2-carbaldehyde oxime (40)

Sodium acetate (0.463 mg, 5.640 mmol) and hydroxylamine hydrochloride (0.549 g, 7.900 mmol) are suspended in EtOH (30 mL). A solution of **38** (2.020 g, 7.050 mmol) in the same solvent (90 mL) is added to the reaction mixture, which is then refluxed 17 h. A precipitate is formed which is filtered, the solution is poured into water (600 mL) and filtered again leading to the product as a yellow solid (1.880 g, 6.240 mmol, 80%).

<sup>1</sup>H NMR (500 MHz, DMSO- $d_6$ ) $\delta$ [ppm]: 10.97 (s, 1H) 8.27 (s, 1H), 8.25 (d, 2H, J=8.8), 7.90 (t, 2H, J=7.7), 7.73 (d, 2H, J=8.7), 7.64 (t, 2H, J=7.6), 6.75 (d, 1H, J=3.7), 6.45 (d, 1H, J=3.7), 3.35 (s, 3H).

**5-(acridin-9-yl)-1-methyl-pyrrole-2-carbonitrile (41)**

**40** (2.230 g, 7.400 mmol) is dissolved in acetic anhydride (50 mL) and refluxed 7 h. The reaction solution is poured into water (300 mL) and a yellow solid precipitates which is filtered and purified by chromatography (silica, *n*-hexane/AcOEt 1:1), leading to the desired product as a yellow solid (0.860 g, 3.035 mmol, 41%).

M.p. 186-187 °C. <sup>1</sup>H NMR (500 MHz, DMSO-*d*<sub>6</sub>) δ[ppm]: 8.28 (d, 2H, J=8.8), 7.94-7.90 (m, 2H), 7.68-7.64 (m, 4H), 7.34 (d, 1H, J=4.0), 6.59 (d, 1H, J=4.0), 3.34 (s, 3H); <sup>13</sup>C NMR (125.7 MHz, DMSO-*d*<sub>6</sub>) δ[ppm]: 148.73, 135.57, 133.01, 131.09, 129.99, 127.77, 126.25, 126.01, 120.28, 114.28, 113.24, 105.99, 33.97. Anal. Calcd for C<sub>19</sub>H<sub>13</sub>N<sub>3</sub>: C, 80.54; H, 4.62; N, 14.83. Found: C, 80.25; H, 4.31; N, 14.75.

**10-methylacridinium methosulfate (42)**

Acridine (5.000 g, 27.90 mmol) is dissolved in dry toluene (50 mL), dimethyl sulfate (5.300 g, 42.01 mmol) is added to the solution and the reaction mixture is refluxed 13 h. A yellow solid precipitates which is filtered and washed with petroleum ether and *n*-hexane leading to the desired pure product (8.100 g, 26.70 mmol, 95%)

M.p. 217 °C. <sup>1</sup>H NMR (500 MHz, DMSO-*d*<sub>6</sub>) δ[ppm]: 10.20 (s, 1H), 8.81 (d, 2H, J=9.2), 8.65 (dd, 2H, J=8.4, J=0.9), 8.48 (t, 2H, J=8.4), 8.05 (t, 2H, J=7.7), 4.87 (s, 3H), 3.38 (s, 3H).

**10-methyl-9-(1-methylpyrrol-2-yl)-9,10-dihydroacridine (43)**

**42** (2.000 g, 6.590 mmol) and 1-methyl-pyrrole (0.546 g, 0.910 mmol) are dissolved in CH<sub>3</sub>CN (50 mL) and refluxed 12 h. The reaction solution turns progressively dark red. The reaction environment is poured into Et<sub>2</sub>O (500 mL) and stirred 30 min, a red suspension is formed which is filtered and subsequently washed with AcOEt, Et<sub>2</sub>O, petroleum ether and *n*-hexane leading to 10-methyl-9-(1-methylpyrrol-2-yl)acridinium intermediate which is isolated, dissolved in MeOH (20 mL) and cooled to 0 °C. A solution of NaBH<sub>4</sub> (0.100 g, 2.643 mmol) in

water (5 mL) is then added dropwise to the solution, copious gas is emitted. The mixture is let react under stirring at 0 °C 30 min and then 45 min at room temperature. Water is added till a yellowish suspension is formed; the reaction suspension is extracted with AcOEt (3x50 mL), the organic phase is separated and the solvent eliminated under reduced pressure leading to the desired product as a light yellow solid (0.740 g, 2.700 mmol, 41%).

<sup>1</sup>H NMR (500 MHz, DMSO-*d*<sub>6</sub>) δ[ppm]: 7.21-7.18 (m, 4H), 7.00 (d, 2H, J=8.0), 6.91 (t, 2H, J=8.2), 6.55 (s, 1H), 6.46 (t, 1H, J=2.4), 6.06 (s, 1H), 5.63 (t, 1H, J=2.2), 4.98 (s, 1H), 3.43 (s, 3H), 3.33 (s, 3H, partially covered by water).

**1-methyl-5-(10-methyl-9,10-dihydroacridin-9-yl)pyrrole-2-carboxaldehyde (44)**

**43** (0.730 g, 2.660 mmol) is dissolved in anhydrous DMF (15 mL) and cooled to 0 °C. After 15 min POCl<sub>3</sub> (0.871 g, 5.680 mmol) is added dropwise and the mixture is allowed to slowly reach room temperature. The reaction is let under stirring 3 days at room temperature 48 h. The yellowish solution is poured into an aqueous Na<sub>2</sub>CO<sub>3</sub> and a light brown solid precipitates which is filtered and washed leading to the desired product (0.680 g, 2.250 mmol, 84%).

<sup>1</sup>H NMR (500 MHz, DMSO-*d*<sub>6</sub>) δ[ppm]: 9.35 (s, 1H), 7.28 (d, 2H, J=7.1), 7.24 (t, 2H, J=7.3), 7.15 (d, 2H, J=8.1), 6.96 (t, 2H, J=7.2), 6.67 (s, 1H), 6.49 (s, 1H), 5.12 (s, 1H), 3.71 (s, 3H), 3.35 (s, 3H, partially covered by water).

**1-methyl-5-(10-methyl-9,10-dihydroacridin-9-yl)pyrrole-2-carbaldehyde oxime (45)**

Sodium acetate (0.175 mg, 2.130 mmol) and hydroxylamine hydrochloride (0.161 g, 2.320 mmol) are suspended in EtOH (10 mL). A solution of **44** (0.600 g, 1.980 mmol) in the same solvent (20 mL) is added to the reaction mixture, which is then refluxed 17 h. The solution gets darker, the solution is poured into water (800 mL) and a

precipitate is formed which is filtered and washed leading to the desired product (0.360 g, 1.130 mmol, 57%).

$^1\text{H}$  NMR (500 MHz,  $\text{DMSO-}d_6$ )  $\delta$ [ppm]: 10.65 (s, 1H), 7.89 (s, 1H), 7.23 (t, 2H,  $J=7.2$ ), 7.02 (d, 2H,  $J=8.1$ ), 6.93 (t, 2H,  $J=7.3$ ), 6.24 (d, 1H,  $J=1.4$ ), 5.94 (d, 1H,  $J=1.6$ ), 5.01 (s, 1H), 3.56 (s, 3H), 3.35 (s, 3H, partially covered by water).

#### 1-methyl-pyrrole-2-carbonitrile (46)

Finely triturated  $\text{K}_2\text{CO}_3$  (5.000 g, 108.53 mmol) is suspended in dry acetone (50 mL) and stirred 30 min. 1H-pyrrole-2-carbonitrile (5.000 g, 54.79 mmol) is added to the suspension and let react 1 h at room temperature. Iodomethane (15.500 g, 109.20 mmol) is added to the mixture and let stir 1 h at room temperature. The reaction mixture is then refluxed 13 h. The solid is filtered off and the solvent is removed from the solution leaving a white solid which is sonicated in  $\text{CH}_2\text{Cl}_2$ . The solid is filtered off and the solvent is removed from the organic phase leading to desired product as a dark yellow oil (5.140 g, 48.43 mmol, 88%).

$^1\text{H}$  NMR (500 MHz,  $\text{DMSO-}d_6$ )  $\delta$ [ppm]: 7.70 (t, 1H,  $J=1.9$ ), 6.89 (dd, 1H,  $J=3.9$ ,  $J=1.5$ ), 6.17 (dd, 1H,  $J=3.9$ ,  $J=2.6$ ), 3.75 (s, 3H).

#### 1-methyl-pyrrole-2-carbonitrile (47)

**46** (0.507 g, 4.777 mmol), tetrabutylammonium fluoride (0.757 mg, 2.400 mmol) and trimethylsilyl azide (0.816 g, 7.082 mmol) are stirred at 90 °C for 9 h. AcOEt (20 mL) is added and the organic phase is washed with HCl 1M (3x5 mL). The organic phase is separated and the solvent is eliminated in vacuum leaving the crude product as a white solid. The product is purified by trituration in  $\text{Et}_2\text{O}/n$ -hexane 1:1 (0.320 g, 2.145 mmol, 45%).

$^1\text{H}$  NMR (500 MHz,  $\text{DMSO-}d_6$ )  $\delta$ [ppm]: 16.41 (bs, 1H), 7.10 (t, 1H,  $J=1.9$ ), 6.83 (dd, 1H,  $J=3.8$ ,  $J=1.5$ ), 6.21 (t, 1H,  $J=3.9$ ), 3.98 (s, 3H).

**1-(3-hydroxypropyl)-4-methylpyridinium bromide (50)**

4-cyanopyridine (420 mg, 4.030 mmol) and 3-bromopropanol (590 mg, 4.240 mmol) are dissolved in  $\text{CH}_3\text{CN}$  (4 mL) and heated under microwave irradiation at 120 °C for 2 h at a maximum irradiation power of 80 W. After the irradiation, water is added to the mixture; the aqueous phase is extracted with  $\text{Et}_2\text{O}$  (3x50 mL) leading to a yellow solution. The organic phase is separated and the solvent removed under reduced pressure leading to a yellow oil which is dried in vacuum affording the product as a yellow solid (680 mg, 2.800 mmol, 69%).

$^1\text{H}$  NMR (200 MHz,  $\text{DMSO}-d_6$ )  $\delta$ [ppm]: 9.43 (d, 2H,  $J=6.5$ ), 8.73 (d, 2H,  $J=6.3$ ), 4.81 (s, 1H), 4.76 (d, 2H,  $J=6.9$ ), 3.51-3.43 (m, 2H), 2.17-2.04 (m, 2H).

**1-(3-hydroxypropyl)-4-methylpyridinium bromide (51)**

ROUTE 1) **50** (255 mg, 1.050 mmol) and sodium azide (92 mg, 1.420 mmol) are dissolved in  $\text{H}_2\text{O}$  (3 mL) and heated under microwave irradiation 30 min at 100°C, at a maximum irradiation power of 80 W. After the irradiation, a light orange solution is obtained; water is removed in vacuum leaving a white/pink solid which is washed with MeOH sonicating and filtered. The residual impurities are eliminated by treatment with activated carbon in water at 50 °C for 45 min, affording the desired product as a white solid (50 mg, 0.244 mmol, 23%).

ROUTE 2) **21** (305 mg, 2.070 mmol) is suspended in  $\text{CHCl}_3$  (3 mL) and diisopropylethylamine (290 mg, 2.24 mmol) is added dropwise till complete dissolution of the reagent. 3-bromopropanol is added to the mixture which is then heated under microwave irradiation at 65 °C for 2 h 30 min at a maximum irradiation power of 80 W. The pure product precipitates as a white solid (80 mg, 0.390 mmol, 20%).

M.p. degradation at 232 °C.  $^1\text{H}$  NMR (500 MHz,  $\text{D}_2\text{O}$ )  $\delta$ [ppm]: 8.71 (d, 2H,  $J=6.8$ ), 8.21 (d, 2H,  $J=6.9$ ), 4.58 (t, 2H,  $J=7.2$ ), 3.59 (t, 2H,  $J=5.9$ ), 2.18-2.12 (m, 2H);  $^{13}\text{C}$  NMR (125.7 MHz,  $\text{DMSO}-d_6$ )  $\delta$ [ppm]: 157.74, 144.94, 144.32, 124.04, 58.67, 57.76, 32.62.

## REFERENCES

- <sup>1</sup> Burland, D. M. *Chem. Rev.* **1994**, *94*, 1.
- <sup>2</sup> Born, M.; Wolf, E. *Principles of Optic*, Pergamon Press, Oxford, **1989**.
- <sup>3</sup> Kanis, D. R.; Ratner, M. A.; Marks, T. J. *Chem. Rev.* **1994**, *94*, 195.
- <sup>4</sup> Beverina, L. *Multiphoton processes in heterocycles-based organics*, Tesi di Dottorato, Facoltà di scienze MM. FF. NN., Dottorato di ricerca in Scienza dei Materiali, Relatore Chiar.mo Prof. Pagani G. A., XV ciclo-A.A. **1998-2000-2001-2002**.
- <sup>5</sup> Abbotto, A.; Beverina, L. "Molecular Organic Materials for Nonlinear Optics: How to Interact with Laser Beams and Exploit Molecular Structural Properties to Make Advanced Technology", *Seminars in Organic Chemistry XXXI Summer School "A. Corbella"*, June 19-23 **2006**, Palazzo Feltrinelli, Gargnano (Bs).
- <sup>6</sup> Abbotto, A.; Beverina, L.; Bozio, R.; Bradamante, S.; Ferrante, C.; Pagani, G. A.; Signorini, R. *Adv. Mater.* **2000**, *12*, 1963.
- <sup>7</sup> Rumi, M.; Ehrlich, E. J.; Heikal, A. A.; Perry, J. W.; Barlow, S.; Hu, Z.; McCord-Maughon, D.; Parker, T. C.; Röckel, H.; Thayumanavan, S.; Marder, S. R.; Beljonne, D.; Brédas, J. L. *J. Am. Chem. Soc.* **2000**, *112*, 9500.
- <sup>8</sup> Brédas, J. L.; Adant, C.; Tackx, P.; Persoons, A. *Chem. Rev.* **1994**, *94*, 243.
- <sup>9</sup> Verbiest, T.; Houbrechts, S.; Kauranen, M.; Clays, K.; Parsoons, A. *J Mater. Chem.* **1997**, *7*, 2175.
- <sup>10</sup> Ma, H. et al. *Adv. Funct. Mater.* **2002**, *12*, 9, 567.
- <sup>11</sup> Abotto, A.; Beverina, L.; Bradamante, S.; Facchetti, A.; Klein, C.; Pagani, G. A.; Redi-Abshiro, M.; Wortmann, R. *Chem. Eur.* **2003**, *9*, 1991.
- <sup>12</sup> Marder, S.; Cai, Y.; Bedworth, P. V.; Jen, A. K. Y. *Adv. Mater.* **1997**, *9*, 2, 132.
- <sup>13</sup> Levine, B. F.; Bethea, C. G. *J. Chem. Phys.* **1975**, *63*, 2666.
- <sup>14</sup> Williams, D. J. *Angew. Chem. Int. Ed. Engl.* **1983**, *23*, 690.
- <sup>15</sup> Oudar, J. L.; Chemla, D. S. *J. Chem. Phys.* **1977**, *66*, 2664.
- <sup>16</sup> Marder, S. R. et al. *Science* **1991**, *252*, 103.
- <sup>17</sup> Marder, S. R. et al. *J. Am. Chem. Soc.* **1994**, *116*, 10703.
- <sup>18</sup> Marder, S. R. et al. *Nature* **1997**, *388*, 845.
- <sup>19</sup> Blanchard-Desc, M. et al. *Chem. Eur. J.* **1997**, *3*, 1092.
- <sup>20</sup> Marder, S. R. et al. *J. Am. Chem. Soc.* **1997**, *119*, 2311.
- <sup>21</sup> Albert, I. D. L.; Marks, T. J.; Ratner, M. A. *Chem. Mater.* **1998**, *10*, 753.
- <sup>22</sup> Abbotto, A.; Bradamante, S.; Facchetti, A.; Pagani, G. A. *JOC* **1997**, *62*, 5755.



- <sup>23</sup> Kannan, R.; He, G. S.; Yuan, L. X.; Xu, F. M.; Prasad, P. N.; Dombroskie, A. G.; Reinhardt, B. A.; Baur, J. W.; Vaia, R. A.; Tan, L. S. *Chem. Mater.* **2001**, *13*, 1896.
- <sup>24</sup> Kang, H.; Facchetti, A.; Zhu, P.; Jiang, H.; Yang, Y.; Cariati, E.; Righetto, S.; Ugo, R.; Zuccaccia, C.; Macchioni, A.; Stern, C. L.; Liu, Z.; Ho, S. T.; Marks, T. J. *Angew. Chem. Int. Ed.* **2005**, *44*, 7922.
- <sup>25</sup> Beverina, L.; Fu, J.; Leclercq, A.; Zojer, E.; Pacher, P.; Barlow, S.; Van Stryland, E. W.; Hagan, D. J.; Bredas, J. -L.; Marder, S. R. *J. Am. Chem. Soc.* **2005**, *127*, 7282.
- <sup>26</sup> Abbotto, A.; Beverina, L.; Bozio, R.; Facchetti, A.; Ferrante, C.; Pagani, G. A.; Pedron, D.; Signorini, R. *Org. Lett.* **2002**, *4*, 1495.
- <sup>27</sup> Varanasi, P. R.; Jen, A. K. Y.; Chandrasekhar, J.; Namboothiri, I. N. N.; Rathna, A. *JACS* **1996**, *118*, 12443.
- <sup>28</sup> Wang, Y. K.; Shu, C. F. *J. Mater. Chem.* **1998**, *8*, 833.
- <sup>29</sup> Quist, F.; Vande Velde, C. M. L.; Didier, D.; Teshome, A.; Asselbeerghs, I.; Clays, K.; sergeyev, S. *Dyes and Pigments* **2009**, *81*, 203.
- <sup>30</sup> Albert, I. D. L.; Marks, T. J.; Ratner, M. A. *JACS* **1997**, *119*, 6575.
- <sup>31</sup> Breitung, E. M.; Shu, C. F.; McMahon, R. J. *JACS* **2000**, *122*, 1154.
- <sup>32</sup> Zhano, J. et al. *JACS* **2010**, *20*, 2359.
- <sup>33</sup> Moylan, C. R. et al. *JOC* **2004**, *69*, 8239.
- <sup>34</sup> Kuzyk, M. G. *Phys. Rev.Lett.* **2000**, *85*, 1218.
- <sup>35</sup> Kang, H.; Facchetti, A.; Jiang, H.; Cariati, E.; Righetto, S.; Ugo, R.; Zuccaccia, C.; Macchioni, A.; Stern, C.; Liu, Z.; Ho, S. T.; Brown, E. C.; Ratner, M. A.; Marks, T. J. *JACS* **2007**, *129*, 3267.
- <sup>36</sup> Albert, I. D. L.; Marks, T. J.; Ratner, M. A. *JACS* **1997**, *119*, 3155.
- <sup>37</sup> Albert, I. D. L.; Marks, T. J.; Ratner, M. A. *JACS* **1998**, *120*, 11174.
- <sup>38</sup> Keinan, S.; Zojer, E.; Bredas, J. L.; Ratner, M. A.; Marks, T. J. *THEOCHEM* **2003**, *633*, 227.
- <sup>39</sup> Kang, H.; Facchetti, A.; Stern, C.; Rheingold, L.; Kassel, W. S.; Marks, T. J. *Org. Lett.* **2005**, *7*, 3721.
- <sup>40</sup> Kang, H.; Facchetti, A.; Zhu, P.; Jiang, H.; Yang, Y.; Cariati, E.; Righetto, S.; Ugo, R.; Zuccaccia, C.; Macchioni, A.; Stern, C.; Liu, Z.; Ho, S. T.; Marks, T. J. *Angew. Chem. Int. Ed.* **2005**, *44*, 7922.
- <sup>41</sup> Abbotto, A.; Alanzo, V.; Bradamante, S.; Pagani, G. A. *J. Chem. Soc., Perkin Trans. 2*, **1991**, 481.

- 
- <sup>42</sup> Bradamante S.; Pagani G. A. *Pure Appl. Chem.*, **1989**, *61*, 709.
- <sup>43</sup> Berlin, A.; Bradamante, S.; Pagani, G. A. *J. Chem. Soc., Perkin Trans. 2*, **1988**, 1525.
- <sup>44</sup> Abbotto, A.; Bradamante, S.; Pagani, G. A. *JOC*, **1996**, *61*, 1761.
- <sup>45</sup> Abbotto, A.; Alanzo, V.; Bradamante, S.; Pagani, G. A.; Rizzoli, C.; Calestani, G. *Gazz. Chim. Ital.* **1991**, *121*, 365.
- <sup>46</sup> Abbotto, A.; Bradamante, S.; Pagani, G. A. *Gazz. Chim. Ital.* **1994**, *124*, 301.
- <sup>47</sup> Bradamante, S.; Facchetti, A.; Pagani, G. A. *J. Phys. Org. Chem.* **1997**, *10*, 514.
- <sup>48</sup> Hutchings, M. G.; Ferguson, I.; McGeekin, D. J.; Morley, J. O.; Zyss, J.; Ledoux, I. *J. Chem. Soc. Perkin Trans. 2* **1995**, 171.
- <sup>49</sup> Boldt, P.; Eisentraeger, T.; Glania, C.; Goeldenitz, J.; Kraemer, P.; Matschiner, R.; Rase, J.; Schwesinger, R.; Wichern, J.; Wortmann, R. *Adv. Mater.* **1996**, *8*, 672.
- <sup>50</sup> Facchetti, A.; Annoni, E.; Beverina, L.; Morone, M.; Zhu, P.; Marks, T. J.; Pagani, G. *A. Nat. Mater.* **2004**, *3*, 910.
- <sup>51</sup> Abbotto, A.; Beverina, L.; Manfredi, N.; Pagani, G. A.; Archetti, G.; Kuball, H. G. ; Wittemburg, C.; Heck, J.; Holtmann, J. *Chem. Eur. J.* **2009**, *15*, 6175.
- <sup>52</sup> Facchetti, A.; Beverina, L.; Van der Boom, M.; Dutta, P.; Evmenenko, G.; Shukla, A. D.; Stern, C.; Marks, T. J.; Pagani, G.A. *JACS* **2006**, *128*, 2142.
- <sup>53</sup> He, G. S.; Yuan, L.; Prasad, P. N.; Abbotto, A.; Facchetti, A.; Pagani, G. A. *Optics Communications* **1997**, *140*, 49.
- <sup>54</sup> Abbotto, A.; Bellotto, L.; Bozio, R.; Ferrante, C.; Fortunati, I.; Garbin, E.; Marinzi, C.; Painelli, A.; Sissa, C.; Terenziani, F. "One- and two-photon absorption and emission properties of heteroaromatic bichromophores", *Proc. SPIE, Int. Soc. Opt. Eng.* **2008** 6999.
- <sup>55</sup> Abbotto, A.; Bradamante, S.; Facchetti, A.; Pagani, G. A. *JOC* **1997**, *62*, 5755.
- <sup>56</sup> Abbotto, A.; Bradamante, S.; Pagani, G. A. *JOC* **2001**, *66*, 8883.
- <sup>57</sup> Abbotto, A.; Bradamante, S.; Pagani, G. A. *JOC* **1993**, *58*, 444.
- <sup>58</sup> Abbotto, A.; Bradamante, S.; Pagani, G. A. *JOC* **1993**, *58*, 449.
- <sup>59</sup> Preussmann, R. et al *Justus Liebigs Annalen der Chemie* **1965**, *684*, 57.
- <sup>60</sup> Hiroaka, H. *Bull. Chem. Soc. Jpn.* **1966**, *39*, 380.
- <sup>61</sup> Abe, J.; Shirai, Y. *JACS* **1996**, *118*, 4705.
- <sup>62</sup> Alcade, E.; Dinares, I.; Fayet, J. P.; Vertut, M. C.; Elguero, J. *J. Chem. Soc. Chem. Commun.* **1986**, 734.

- <sup>63</sup> Czyznikowska, Z.; Kurzawa, J.; Zalesny, R.; Lipkowski, P.; Bartkowiaklcade, W. *Chem. Phys. Lett.* **2009**, *480*, 37.
- <sup>64</sup> Alcade, E.; Dinares, I.; Fayet, J. P.; Vertut, M. C.; Elguero, J.; Miravitlles, C.; Molins, E. *JOC* **1987**, *52*, 5009.
- <sup>65</sup> Alcade, E.; Dinares, I.; Pons, J. M.; Roca, T. *JOC* **1994**, *59*, 639.
- <sup>66</sup> Alcade, E.; Dinares, I.; Pons, J. M.; Roca, T. *JOC* **1994**, *59*, 644.
- <sup>67</sup> Harvill, E. K.; Schreiner, E. C.; Roberts, C. W.; Herbst, R. M. *JOC* **1950**, *15*, 662.
- <sup>68</sup> Koldobskii, G. I.; Ostrovskii, V. A.; Popavskii, V. S. *Khimiya Geterotsiklicheskikh Soedinenii* **1981**, *10*, 1299.
- <sup>69</sup> Koldobskii, G. I.; Ostrovskii, V. A. *Russian Chemical Reviews* **1994**, *63*, 797.
- <sup>70</sup> McManus, J.M.; Herbst, R. M. *JOC* **1959**, *24*, 1462.
- <sup>71</sup> Sharpless, K. B. et al. *JACS* **2003**, *125*, 9983.
- <sup>72</sup> Holzer, W.; Jäger, C. *Monatsh. Chem.* **1992**, *123*, 1027.
- <sup>73</sup> Koguro, K. et al. *Synthesis* **1998**, 910.
- <sup>74</sup> Amantini, D. et al. *JOC* **2004**, *69*, 2896.
- <sup>75</sup> Ma, H.; Jen, A. K. Y.; Dalton, L. *Adv. Mater.* **2002**, *14*, 1339.
- <sup>76</sup> Kradjel, C. *Fresenius J. Anal. Chem.* **1991**, *339*, 65.
- <sup>77</sup> Wann, D. A.; Gronde, I.; Foerster, T.; Hayes, S. A.; Masters, S. L.; Robertson, H. E.; Mitzel, N. W.; Rankin, D. W. H. *Dalton Trans.* **2008**, *29*, 3817.
- <sup>78</sup> Satoh, Y.; Marcopulos, N. *Tetrahedron Letters.* **1995**, *36*, 1759.
- <sup>79</sup> Wuts, P. G. M.; Greene, T. W. *Greene's protective groups in organic synthesis*, 5th ed., John Wiley & Sons, Inc., New York, **2007**.
- <sup>80</sup> Abbotto, A.; Beverina, L.; Bradamante, S.; Facchetti, A.; Klein, C.; Pagani, G. A.; Redi-Abshiro, M.; Wortmann, R. *Chem. Eur. J.* **2003**, *9*, 1991.
- <sup>81</sup> Bernthsen, A. *Justus Liebigs Annalen der Chemie* **1884**, *224*, 45.
- <sup>82</sup> Alterman, M.; Hallberg, A. *JOC* **2000**, *65*, 7984.
- <sup>83</sup> Demko, Z. P.; Sharpless, K. B. *JOC* **2001**, *66*, 7945.
- <sup>84</sup> Treibs, A.; Fligge, M. *Justus Liebigs Annalen der Chemie* **1962**, *652*, 176.
- <sup>85</sup> Brown, H. C.; Mihn, X. R. *JACS* **1955**, *77*, 1723.
- <sup>86</sup> Allen, F. H.; Kennard, O.; Watson, D. G.; Brammer, L.; Orpen, A. G.; Taylor, R. *J. Chem. Soc., Perkin Trans. 2* **1987**, SI.
- <sup>87</sup> Reichardt, C. *Chem. Soc. Rev.* **1992**, *21*, 147.
- <sup>88</sup> Reichardt, C. *Chem. Rev.* **1994**, *94*, 2319.

- <sup>89</sup> Beverina, L.; Sanguineti, A.; Battagliarin, G.; Ruffo, R.; Roberto, D.; Righetto, S.; Soave, R.; Lo Presti, L.; Ugo, R.; Pagani, G. A. *Chem. Commun.* **2011**, 47, 292.
- <sup>90</sup> Lee, M.; Katz, H. E.; Erben, C.; Gill, D. M.; Gopalan, P.; Heber, J. D.; McGee, D. J. *Science* **2002**, 298, 1401.
- <sup>91</sup> Shi, Y.; Zhang, C.; Zhang, H.; Bechtel, J. H.; Dalton, L. R.; Robinson, B. H.; Steier, W. H. *Science* **2000**, 288, 119.
- <sup>92</sup> Dalton, L. R.; Steier, W. H.; Robinson, B. H.; Zhang, C.; Ren, A.; Garner, S.; Chen, A.; Londergan, T.; Irwin, L.; Crlson, B.; Fifield, L.; Phelan, G.; Kincaid, C.; Amend, J.; Jen, A. *J. Mater. Chem.* **1999**, 9, 1905.
- <sup>93</sup> For more informations please visit [www.gigoptix.com](http://www.gigoptix.com).
- <sup>94</sup> Dalton, L. R.; Sullivan, P.; Bale, D. H. *Chem. Rev.* **2010**, 110, 25.
- <sup>95</sup> Dalton, L. R. *Thin Solid Films* **2009**, 518, 429.
- <sup>96</sup> Dalton, L. R. et al. *J. Phys. Chem.* **2008**, 112, 8091.
- <sup>97</sup> Dalton, L. R. et al. *Chem. mater* **2007**, 19, 1154.
- <sup>98</sup> Marks, T. J. et al. *JACS* **1995**, 118, 8034.
- <sup>99</sup> Marks, T. J. et al. *Chem. Mater.* **2002**, 14, 4982.
- <sup>100</sup> Hecht, J. *Laser Focus World* **2008**, 44, 123.
- <sup>101</sup> Marks, T. J.; Ratner, M. A. *Angew. Chem. Int. Ed.* **1995**, 34, 155.
- <sup>102</sup> Haller, M.; Luo, J.; Li, H.; Kim, T. D.; Liao, Y.; Robinson, B. H.; Dalton, L. R.; Je, A. K. Y. *Macromolecules* **2004**, 37, 688.
- <sup>103</sup> Facchetti, A.; Van der Boom, M. E.; Abbotto, A.; Beverina, L.; Marks, T. J.; Pagani, G. A. *Langmuir* **2001**, 17, 5939.
- <sup>104</sup> Herminghaus, S.; Smith, B. A.; Swalen, J. D. *J. Opt. Soc. Am. B* **1991**, 11, 2311.
- <sup>105</sup> Van der Boom, M. E. *Angew. Chem. Int. Ed.* **2002**, 41, 3363.
- <sup>106</sup> Yitzchaik, S. Marks, T. J. *Acc. Chem. Res.* **1996**, 29, 197.
- <sup>107</sup> Facchetti, A.; Van der Boom, M. E.; Abbotto, A.; Beverina, L.; Dutta, P.; Evmenenko, G.; Marks, T. J.; Pagani, G. A. *Chem. Mater.* **2003**, 15, 1064.
- <sup>108</sup> Zhu, P.; Van der Boom, M. E.; Kang, H.; Dutta, P.; Evmenenko, G.; Marks, T. J. *Chem. Mater.* **2002**, 14, 4982.
- <sup>109</sup> Lin, W.; Lin, W.; Wong, G. K.; Marks, T. J. *JACS* **1996**, 118, 8034.
- <sup>110</sup> Facchetti, A.; Van der Boom, M. E.; Abbotto, A.; Beverina, L.; Dutta, P.; Evmenenko, G.; Marks, T. J.; Pagani, G. A. *Chem. Mater.* **2002**, 14, 4996.

- 
- <sup>111</sup> Frattarelli, D.; Schiavo, M.; Facchetti, A.; Ratner, M. A.; Marks, T. J. *JACS* **2007**, *131*, 12595.
- <sup>112</sup> Facchetti, A.; Annoni, E.; A.; Beverina, L.; Morone, M.; Zhu, P.; Marks, T. J.; Pagani, G. A. *Nature Materials* **2004**, *3*, 810.
- <sup>113</sup> Rashid, A. N.; Erny, C.; Gunter, P. *Adv. Mater.* **2003**, *15*, 2024.
- <sup>114</sup> Nunzi, F.; Fantacci, S.; De Angelis, F.; Sgamellotti, A.; Cariati, E.; Ugo, R.; Macchi, P. *J. Phys. Chem. C* **2008**, *112*, 1213.
- <sup>115</sup> Jerphagnon, J.; Kurtz, S. K. *J. Appl. Phys.* **1970**, *41*, 1667.
- <sup>116</sup> Still, W. C.; Kahn, M.; Mitra, A., *J. Org. Chem.*, **1978**, *43*, 2923.
- <sup>117</sup> Willetts, A.; Rice, J. E.; Burland, D. M.; Shelton, D. P. *J. Chem. Phys.* **1992**, *97*, 7590.
- <sup>118</sup> Wang, G.; Zhu, P.; Marks, T. J.; Ketterson, J. B. *Appl. Phys. Lett.* **2002**, *81*, 2169.

---

# PART TWO

## HETEROAROMATIC CONJUGATED MATERIALS FOR TRANSISTOR APPLICATIONS

## I. INTRODUCTION

### **I.1 FIELD EFFECT TRANSISTORS (FETs)**

Modern information technology is based on integrated semiconductor circuits (IC) used for data processing (logic), data storage (memory) and data transfer in networks. Besides all the opto-electronic devices, such as detectors and optical emitters (e.g. lasers, LEDs), transistors can be reasonably defined as the most important core element employed for telecommunication applications, being the fundamental component of all the active devices for both the aforementioned fields of data processing in logic and memory circuits, as well as for power electronics.

The first introduction of the field effect phenomenon in an electronic device dates back to the early 30's with the separate works of Lilienfeld and Heil, practical applications of field-effect transistors (FETs) however were not exploited until the 60's when the growth and processing of semiconductors (silicon technology) became sufficiently reliable and clean for large-scale development.

Engineering control of semiconductor materials and devices has grown tremendously since the original concept of FET was introduced: nowadays it is commonplace to fabricate ICs containing several million FETs with minimum feature size in the range of 0.35 – 0.50  $\mu\text{m}$ ,<sup>1</sup> while metal-oxide-semiconductor field-effect transistors (MOSFETs) based on inorganic materials are the crucial building blocks in the electronic industry, proven to be reliable, highly efficient and with performances increasing regularly according to the Moore's law.<sup>2</sup>

The enormous development in computing, telecommunications, consumer electronics, and other areas most using ICs containing MOSFETs as their main active elements, has led the global scientific community and the semiconducting industry to invest increasing efforts and resources in the research field of FET, with the main aims

of enhancing the performances (e.g. higher transistor density per unit IC, lower power consumption, faster switching process, ease of integration, miniaturization) as well as reducing the costs (manufacturing, fabrication technology) and broaden the applicability to novel requests.

### 1.1 BASIC CONCEPTS AND PROCESSES

A field-effect transistor can structurally be classified as a three-port device (in contrast to diodes that are two-port devices) in which an input signal at one contact controls the resistance between two other contacts; thus, in a common view, FET behaves as a resistor, controlled by an external bias voltage. FET simultaneously presents amplifying properties both for current and/or voltage.<sup>5</sup>

The architecture is rather simple: it consists of a current channel (SEMICONDUCTOR MATERIAL) with two contacts (namely SOURCE and DRAIN), and a third contact (GATE) which is separated from the current channel by an insulating layer (DIELECTRIC). The current ( $I_{DS}$ ) of carriers injected by an external applied voltage ( $V_{DS}$ ) from the source contact into the semiconductor toward the drain contact, is controlled by the polarity and magnitude of another external voltage (named gate voltage  $V_G$ ), which affects the size and shape of the conductive channel, thus modifying its conductance.

Three main types of FET can be considered, MOSFET (Metal-Oxide Semiconductor FET), MESFET (Metal Semiconductor FET) and HEMT (High Electron Mobility Transistor) (**Figure 1**), the most important of which being the MOSFET, because of its role as the basic element in all silicon-based ICs. For this reason, in the following only this type will be completely described in its working operation.



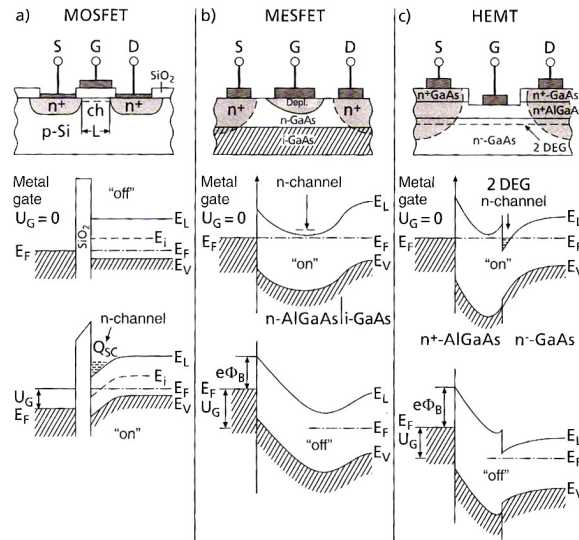


Figure 1: Schematic layout and band schemes for: (a) MOSFET, (b) MESFET, (c) HEMT

The schematic cross-sections (**Figure 2**) allow to display  $n$ MOSFET's\* essential features for the two different modes of operation: enhancement-mode and depletion-mode.

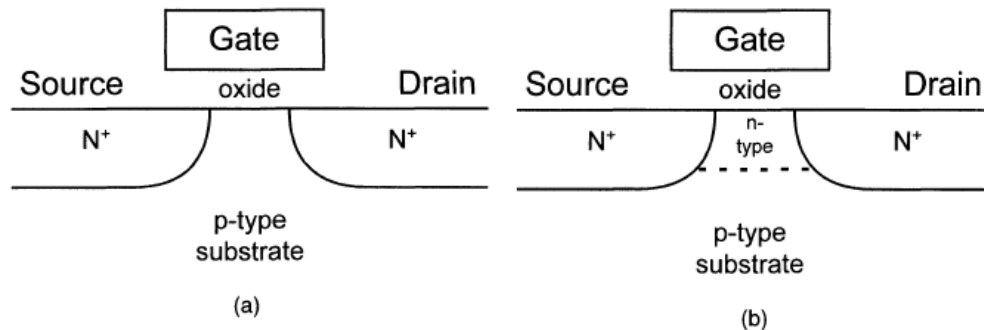


Figure 2: Cross-section of  $n$ MOSFET: (a) enhancement-mode, (b) depletion-mode

Considering the enhancement-mode device first, source and drain regions are constituted of highly  $n^+$ -doped wells generated by ion implantation in an underlying  $p$ -doped silicon wafer; the two  $n^+$ -doped wells are thus separated by a  $p$ -type region. It is possible to recognize here one of the most important building blocks of semiconductor

\*  $p$ MOSFET is analogous but with opposite polarities of charges and voltages.

devices: the  $p$ - $n$  junction. The  $p$ -type region between the  $n^+$ -source and drain is separated from the metallic gate (usually obtained by very highly doped silicon, that essentially acts as a metal) by a thin dielectric layer, traditionally made of  $\text{SiO}_2$ .

For any externally applied  $V_{\text{DS}}$ , one of the two  $p$ - $n$  junctions in the FET will be biased in the reverse direction allowing only a small current between source and drain. Since the gate contact is isolated from the semiconductor by the dielectric layer, a capacitor-like structure is formed: the external applied bias voltage  $V_{\text{G}}$  gives rise to a large electric field across the gate dielectric oxide layer that in turn causes a band-bending in the underlying semiconductor. If a sufficiently positive gate voltage is applied (greater than the so-called threshold voltage  $V_{\text{T}}$ , *vide infra*), the initial  $p$ -type region is inverted (the intrinsic energy level bends under the gate Fermi level) becoming an  $n$ -accumulation layer; the two  $n^+$ -doped wells thus become connected by the creation of this exceedingly thin (1-10 nm)<sup>1</sup> enhanced-conductivity layer, and the device shifts to the “ON” state.

In the depletion-mode device, the channel region between the heavily  $n^+$ -doped wells contacts consists of lightly  $n$ -doped semiconductor, and a conductive path therefore exists between source and drain, even without any external  $V_{\text{G}}$ : the device is thus normally in its “ON” state. When a negative  $V_{\text{G}}$  is applied, a region depleted of electrons forms under the gate, which increases as the external voltage becomes more negative. For large enough negative bias the conductive channel is closed and the device is turned “OFF”.

Focusing on the enhanced-mode  $n$ MOSFET only, it is now possible to delineate three different working regions for the device, depending on the magnitude of the voltages at the contacts with respect to the above mentioned threshold voltage ( $V_{\text{T}}$ ), which is usually defined as the minimum gate voltage needed to create the inversion layer at the interface between dielectric and semiconductor.

The three different regimes are denominated: subthreshold regime, linear regime and saturation regime.

- Subthreshold regime (also called Cutoff mode)

This regime occurs for  $V_G < V_T$ : the conduction between the source and drain contacts is very low, whatever  $V_{DS}$  may be, because one of the back-to-back  $p$ - $n$  junction is always reversed.<sup>4</sup>

A very small  $I_{DS}$  (leakage current) originates, due to diffusion of the more energetic carriers for statistical distribution reason rather than for Ohmic conduction; in this bias regime  $I_{DS}$  can be expressed as being exponentially dependent on  $V_G$  (Eq. 1)<sup>5</sup>:

$$\text{Eq. 1} \quad I_{DS} = I_0 \exp\left(\frac{V_G - V_T}{\eta V_{th}}\right)$$

where  $I_0$  is a process-dependent parameter (the current for  $V_G = V_T$ ),  $V_{th}$  is the thermal voltage ( $= k_B T/q$ ),  $V_G$  is the gate voltage,  $V_T$  is the threshold voltage and  $\eta$  is the subthreshold slope factor correlated to the capacitance of the depletion and dielectric layers.

In digital application a sharp subthreshold behavior is desired, since this provides an "ideal" switch, in addition it is important to note that poor subthreshold characteristic leads to higher currents in the "OFF" state and in turn to higher power consumption. A measurement of the device goodness in the subthreshold regime is given by the amount of gate voltage required to increase the  $I_{DS}$  by a decade (mV/decade), a parameter commonly known as "subthreshold swing".

- Linear regime (also called Ohmic mode)

In the region where  $V_G > V_T$  and  $V_{DS} < (V_G - V_T)$ , the FET device works in the so-called Ohmic mode, or linear regime as due to the linear proportionality between  $I_{DS}$  and  $V_{DS}$  (Eq. 2):

$$\text{Eq. 2} \quad I_{DS} = \frac{W}{L} \mu C_i \left( V_G - V_T - \frac{V_{DS}}{2} \right) V_{DS}$$

where  $W$  and  $L$  are the conductive channel width and length respectively,  $V_G$  is the gate voltage,  $V_T$  is the threshold voltage,  $V_{DS}$  is the drain-source voltage,  $\mu$  is the charge-carrier mobility and  $C_i$  is the dielectric capacitance. As can be easily noted from the equation, the drain-source current in the linear regime is strictly dependent on intrinsic as well as fabrication/process parameters which comprise all the FET components.

- Saturation regime (also called Active mode)

Starting from the linear regime (**Figure 3a**), so that ( $V_G > V_T$ ); as  $V_{DS}$  increases, the gate-to-channel potential, which gives rise to the inversion layer, decreases approaching the drain contact. For further increases of the source-drain voltage,  $V_{DS} > (V_G - V_T)$ , the depletion width grows near the drain junction (**Figure 3b**) and the gate-to-channel potential becomes sufficiently reduced so that the inversion can no longer be maintained: the inversion layer is said to be pinched-off at the drain end. The electron concentration in this region is greatly reduced compared to the inversion layer but it is sufficient to conduct the  $I_{DS}$ , which now becomes weakly dependent upon  $V_{DS}$  and mainly controlled by  $V_G$  (Eq. 3).<sup>6</sup>

Eq. 3

$$I_{DS} = \frac{1}{2} \frac{W}{L} \mu C_i (V_G - V_T)^2$$

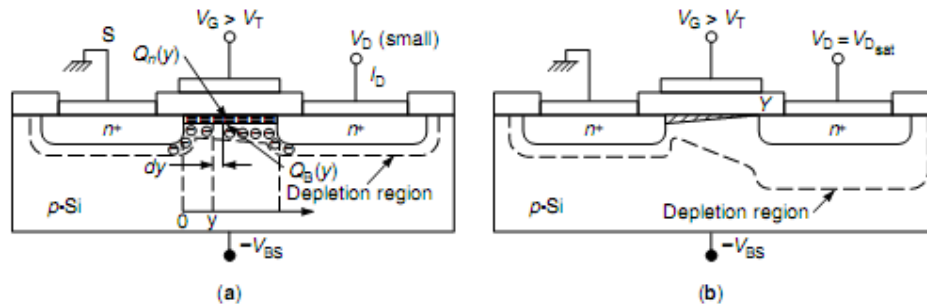


Figure 3:  $n$ MOSFET cross section operated in the (a) linear and (b) saturation regime

The performances of a MOSFET depends essentially on the perfection of the gate  $\text{SiO}_2$  layer and its interface with the underlying Si channel; any residual trap defect states in the oxide or at the Si/ $\text{SiO}_2$  interface would be detrimental to performances since the charge influenced by  $V_G$  would merely resides in the defects. Since only Si is able to form thin, but nevertheless tight and stoichiometrically almost ideal oxides, with atomically smooth interfaces to the Si substrate, MOSFETs can be fabricated on crystalline Si wafer only. Other traditional crystalline semiconductor materials such as III-V compounds (e.g. GaAs, InSb, InGaP) in fact, while being superior to silicon with regard to electron mobility (and thus device speed), do not form perfect oxide overlayer, rendering the device ineffective. The MESFET concept allows circumnavigating this major drawback and is therefore the most common FET exploiting III-V semiconductors. Moreover, since semiconductor heterostructure of high quality can be produced by modern epitaxy techniques (e.g. MBE, MOCVD) this approach can be further broadened to realize HEMTs.<sup>3</sup>

The transistor technology reported so far concerns established microelectronic and nanoelectronic systems where progress is driven primarily by reducing the critical dimensions of the functional elements (e.g. channel lengths and dielectric layer thickness), to reach higher integration scale (moving toward Very Large Scale Integration, VLSI), to increase the speed and computing capacity and to reduce the operating voltages.

A completely different approach is needed for those applications where the overall size of the systems, rather than the minimum feature size of the individual components, represents the primary scaling metric.<sup>7</sup> This type of electronics, referred to as macroelectronics, imply the introduction of a novel genre of transistors to enable classes of applications that lie outside those easily addressed with the wafer-based electronics; distribution over large areas and covering of flexible substrates can be achieved moving to Thin Film Transistors (TFTs).

## 1.2 THIN FILM TRANSISTORS (TFTs)

The first TFT, demonstrated by Weimer in 1962, was fabricated with a thin film of polycrystalline CdS in a structure similar to that of MESFET: the source and the drain contacts are directly deposited onto a semiconductor layer (the conductive channel), which is separated from the gate metal contact by a thin film of insulator. This simple and at the same time revolutionary geometry reached the necessary stability for fabrication processes and operation only with the introduction of amorphous silicon ( $a$ -Si:H) in the '70's; then on, the two stories became strictly bounded one to the other and still today  $a$ -Si:H represents the dominant semiconductor material for transistors in these systems. Large substrate size rather than device density is the driver for TFTs, in fact as a result of the different fabrication methods, the cost per unit area of TFTs is much lower than silicon ICs, the cost per FET is instead much higher. TFTs cannot therefore compete with silicon ICs for processing power, and conversely silicon ICs are never going to be made in square meter size arrays; thus the choice between one or the other technology is rather obvious, depending on the requested applications. Displays are by far the largest applications of TFTs, but they are also used in digital X-ray imagers, and have potential applications in radio-frequency identification (RFID) tags, sensors, medical devices and low-cost disposable-electronic.<sup>8</sup>

The emerging direction in the research field of TFTs is to develop alternative materials and patterning technique for these macroelectronic systems, with the goals of increasing their performances, decreasing their costs per unit area and enabling them to be formed on low-cost, high-scale, bendable substrates. Integration with plastic substrates, the most attractive type of flexible substrate, is in this contest a challenging theme to pursue, which requires ease of integration, low-temperature processing and final stability.

In the following, the most recent options regarding inorganic semiconductor TFTs are surveyed, empathizing their *pros* and *cons*.

### 1.2.1 SILICON

Hydrogenated amorphous silicon and nanocrystalline silicon are the two extremes of a wide range of silicon thin films structures presenting various degrees of crystallinity, different deposition methods, mobilities and ultimately properties (**Figure 4**).

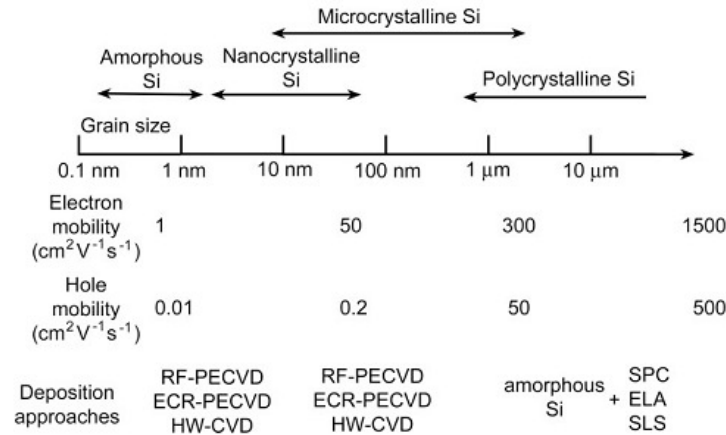


Figure 4: Grain size and carrier mobilities of Si films with various crystallinities

Today, 30 years after the first demonstration, hydrogenated amorphous silicon (*a*-Si:H) dominates the flat panel display allowing a 50 Km<sup>2</sup> annual output of display, with the possibility of uniformly depositing nearly 10 m<sup>2</sup> of semiconducting material on a single substrate, thanks to gas-phase deposition methods.

*a*-Si:H at the existing state of the art, presents mobility in the range of 0.5–1 cm<sup>2</sup>/Vs, current on/off ratio (i.e. the ratio between the measured currents for the device in the “ON” and “OFF” state) well in excess of 10<sup>6</sup>, and switching voltage within about 5–8 V, making it fall within the requests for LCD devices. Furthermore, if compared to the crystalline counterpart, amorphous silicon exhibit great advantages such as: possibility of readily control the electronic properties of films over a wide range, low-temperature (< 300 °C) for film deposition processes, usage of various kind of substrates (e.g. glass, stainless steel, flexible

polymers, even paper) and ease of deposition through various chemical vapor methods (e.g. CVDs, PECVD, RF-PECVD, HW-CVD).<sup>9,10</sup>

The major drawback of amorphous silicon, that stimulates researches toward alternative materials, is its electrical instability: continued application of a gate voltage causes a threshold voltage shift, which is essentially permanent at room temperature. Besides this, low mobilities and difficulties in solution processing are two other inconveniences which avoid its possible application in very small LCDs (where standard ICs driver circuits take up too much space and are relatively expensive) or OLED displays.

Polysilicon overcomes this problems allowing to obtain mobilities up to  $300 \text{ cm}^2/\text{Vs}$  (both *n*-channel and *p*-channel operations) and avoiding bias-stress instability. The reason why polysilicon has not replaced amorphous silicon yet in LCDs and other large-area applications is mainly the higher manufacturing cost due to the requirements of more process steps and lithography masks. Pursuing the goal of reducing such costs, with the final aim of flexible electronics and simplified production methods, novel materials are being introduced in the literature seeking opportunities for new functionality and applications.<sup>8</sup>

### 1.2.2 METAL OXIDES

Oxides of transition metals, such as ZnO and its derivatives (binary and ternary oxides with other materials such as  $\text{In}_2\text{O}_3$ ,  $\text{Ga}_2\text{O}_3$ ,  $\text{SnO}_2$ ), are an emerging class of inorganic semiconductor for large-area electronics, very interesting for their peculiar electrical and optical properties: the large optical gaps ( $> 3 \text{ eV}$ ) ensure transparency, whilst controlling the doping level (oxygen vacancies, hydrogen incorporation) and the deposition processes (gas-phase pulsed-laser deposition, spin-cast from colloidal solutions), it is possible to obtain amorphous or polycrystalline films with mobilities in the range between  $1\text{--}100 \text{ cm}^2/\text{Vs}$ .



When combined with transparent conductors and dielectrics, these materials allow unusual applications such as invisible electronics for heads-up display on windshield or cockpit enclosures, and integration with flexible substrate has also been demonstrated: devices based on amorphous  $\text{InGaO}_3(\text{ZNO})_5$  (*a*-IGZO) deposited on PET substrates continue to operate when bent to radii of curvature radius as small as 30 mm, with only slight reductions (<15%) in mobility<sup>11</sup>, while inorganic/organic hybrid TFTs using all-transparent components materials has been proved to be obtained by large-scale/large-area room temperature fabrication techniques.<sup>12</sup>

Although promising for a range of applications, then main issue of this systems is the electrical stability related to the oxygen bonding: creation of oxygen vacancies (which can be induced by the gate voltage), causes doping which results in a threshold voltage shift, thus giving a bias-stress effect; furthermore processing the metal oxide TFTs is not as easy to control as for silicon. Therefore this technology might only be competitive in term of low-temperature deposition and integration with flexible substrate since higher mobilities can be achieved.

### **1.2.3 NANOSTRUCTURES**

Single-crystalline nanostructures (e.g. nanowires, nanoribbons and nanotubes) formed from inorganic semiconductors are of great interest for TFTs because they provide monocrystalline transport pathways (and thus high mobility), and an associated potential for gaining high performances; the hope in ICs applications is the challenging goal of positioning individual nanowires precisely for device processing, moving to single nanowire-FETs, thus shrinking the device size below the limit imposed by conventional silicon processing.

The small size allows nanostructures to be held in solution, and so inexpensive wet-deposition method are available; a wide range of chemical synthetic approaches, basically bottom-up techniques,

including both gas-phase methods (known as vapor-liquid-solid processes) and liquid-phase method (known as solution-liquid-solid processes), are available to generate nanowires of various materials (Silicon, Germanium, III-V compounds, II-VI compounds and oxides).<sup>7</sup>

Typically, chemically synthesized nanowires/nanoribbons are dispersed in appropriate solvents prior to the device integration, thus requiring external forces (e.g. shear forces, mechanical pressures, electrical and magnetic field) to introduce well-defined order: increased alignment generally comes at a cost of more complex processing. Current research is focused of this ordering process and on the difficult task of scaling it up for large-area manufacturing.

The growth temperature does not limit the type of substrate that can be used, so nanowires TFTs can be readily integrated with plastic. Prototype flexible display based on TFTs made from silicon, carbon nanotubes and various oxides nanowires (including previously reported  $\text{In}_2\text{O}_3$ , ZnO,  $\text{SnO}_2$ ) have been demonstrated<sup>13</sup> even though contacts in such devices tend to be difficult to form, because of the small size of the wire. Since several nanowires materials work well, the formation of contacts and fabrication process may determine which material ultimately proves most successful.

2010 Physic Nobel Prize was awarded to physicists Andre Geim and Konstantin Novoselov, both of the University Of Manchester (UK), for their research on graphene, whose remarkable electronic properties made it a promising candidate for future nanoelectronics and a particularly attractive case of study also for TFTs applications. In this regard, the work group of Avouris at IBM Thomas J. Watson Research Center (NY) recently reported an example of bilayer graphene FETs with high on/off current ratio, demonstrating the great potential of this system in applications such as digital electronics, terahertz technology and infrared nanophotonic.<sup>14</sup>

## I.2 ORGANIC THIN FILM TRANSISTORS (OTFTs)

Organic thin films have been widely investigated as active layers in optoelectronic devices, possessing many unique advantages compared to their inorganic counterpart: their low elastic modulus is consistent with bending and flexibility, the low-temperature solution-deposition enables easy and low cost fabrications (making them suitable for printing systems and inexpensive manufacturing), large-area integration is possible due to the good compatibility with different substrates, structural tailoring and light weight are other characteristics important for real-world applications.

During the past decade, the field known as "organic" or "plastic" electronics, in which the active (semi)conducting material as well as dielectrics and other passive components are ideally composed of organic small molecules or polymers, has developed dramatically, involving many academic and industrial research groups, leading in some cases to commercialized products.<sup>15</sup> Despite this success and the potential applications, organic semiconductors have historically failed to have a significant practical impact, mainly due to their significant low mobility. Recently, however the latest progresses in the field of OTFTs have demonstrated a dramatic improvement, opening the door to the possibility of challenging amorphous silicon TFT for many different low-performance applications (where high speed is not a central issue, or where standard inorganic cannot compete): printed radio-frequency technologies, electronic sensors, light emissions, pixel drivers and switching elements in active matrix flat panel display (AMFPDs) based on liquid crystals (AMLCDs) and organic light emitting diodes (AMOLEDs) or "electronic papers" displays, based on pixels comprising electrophoretic ink-containing particles.<sup>2,16</sup>

## 2.1 DEVICE ARCHITECTURES & PRINCIPLES

Differently from inorganic materials, where extrinsic doping determines the nature of charge carriers, organic semiconductors can allow both hole and electron transport, and are classified as *p*-type or *n*-type according to which type of carrier is more efficiently transported through the material. The organic semiconductor category is thus determined by the operation model of corresponding devices; in OFETs both the carrier transport and the carrier injection influence the device operation model. This means that, aside from the intrinsic properties of the organic semiconductor, both the work function of the source and drain metal electrodes and the dielectric properties of the insulating layer could influence the device operation model. It is therefore more appropriate to think in term of *p*- or *n*-channel transistors.<sup>17</sup>

If only one kind of carrier is preferentially injected and transported into the semiconducting channel, the device exhibits unipolar characteristics, whilst when both carrier types can be injected and transported in the same device, this shows ambipolar characteristics.

Schematically it is possible to define OTFTs as a special kind of OFETs made by depositing thin film materials on top of one another in a stacked layer configuration. According to different preparation sequences of the source and drain contacts and organic semiconductor layer, OTFTs can be fabricated in different configurations and geometries (**Figure 5**). Two basic structures for OTFTs can be recognized, depending on the relative position of the gate electrode layer: the bottom-gate and the top-gate. The bottom-gate scheme can be divided further in two more geometries, considering the position of the source and drain metal contacts, namely top-contact (whether the metal contacts are the outer most layer, deposited upon all the others), or bottom-contact (when the semiconductor layer is deposited over the metal contacts)\*.

---

\* It would be possible to have also a top-gate/top-contact structure but it is less largely diffused so it will not be reported here.

Each configuration presents *pros* and *cons* and the choice of one or the others has consequences on the final performances.

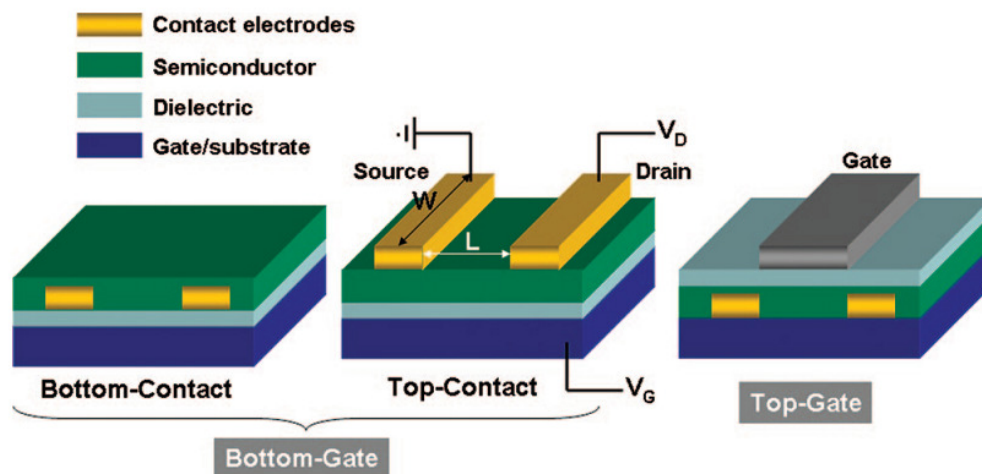


Figure 5: Different structures of OTFTs.  $L$ , channel length;  $W$ , channel width

- Top-gate/bottom-contact (TG/BC) configuration

This is the OTFT geometry that historically ensures good dielectric/semiconductor contact in single crystal FETs. It appears to be an ideal configuration for low-cost, large-area fabrication on flexible substrates, furthermore the organic layer results protected against environmental influences; however it is also the most challenging, since it requires successive semiconductor/dielectric top gate electrode depositions and good contact between the bottom source/drain electrodes and the organic semiconductor. To enable top-gate devices, the first prerequisite is the semiconducting layer to remain intact during deposition (spin coating) of the overlaying dielectric layer; this goal is usually achieved by choosing specific dielectric/solvent combination such that the solvent only dissolves the dielectric material but not the underlying semiconducting layer.<sup>18</sup>

- Bottom-gate/bottom-contact (BG/BC) (Coplanar) configuration

The bottom-gate/bottom-contact geometry is the most used device structure where all the components' layers (i.e., the dielectric layer,

the gate electrode, the source and drain contacts) are fabricated before the organic layer deposition. This aspect is particularly attractive due to the sensitivity of the organic semiconductors toward solvents/chemicals used in the photolithographic patterning or printing of the source and drain electrodes. The BG/BC configuration thus results in a more feasible geometry for many practical applications and it is notable that the highest mobility values reported in literature with single-crystal OFETs have been obtained by using this approach. Despite this, OTFT bottom-contact devices usually suffer from lower performance due to the poor contact and poor semiconductor morphology: in the case of a thin film device in fact, compared to the top-contact geometry, a higher contact resistance is encountered due to a higher density of trap states at the semiconductor/contact interface (especially at the edge of the contacts where a large number of grain boundaries resides), a more difficult charge-carrier injection/retrieval also occurs.<sup>19</sup>

- Bottom-gate/top-contact (BG/TC) (Staggered) configuration

For devices with top-contact geometry, the structure can be easily realized through subsequent deposition of the organic layer and patterning of the metal contacts on it by shadow masking. Excellent electrode/organic layer contact can thus be obtained: the staggered configuration is recognized to offer a lower contact resistance because of metal penetrations into the film and intermixing between the two components. Most high-performance organic semiconductor TFTs reported in the literature show the top-contact configuration<sup>20</sup>, but disadvantages exist also for this geometry, the most important being: the need for semiconducting layer protection (against environmental/chemical attacks) and for alternatives patterning of the source and drain electrodes (for using in manufacturing), the presence of access resistance deriving from the high resistive semiconductor region located between the contacts and the conductive channel itself.

TFTs are based on a common working process that will be illustrated in the following, exploiting the TC/BG configuration (**Figure 6**).

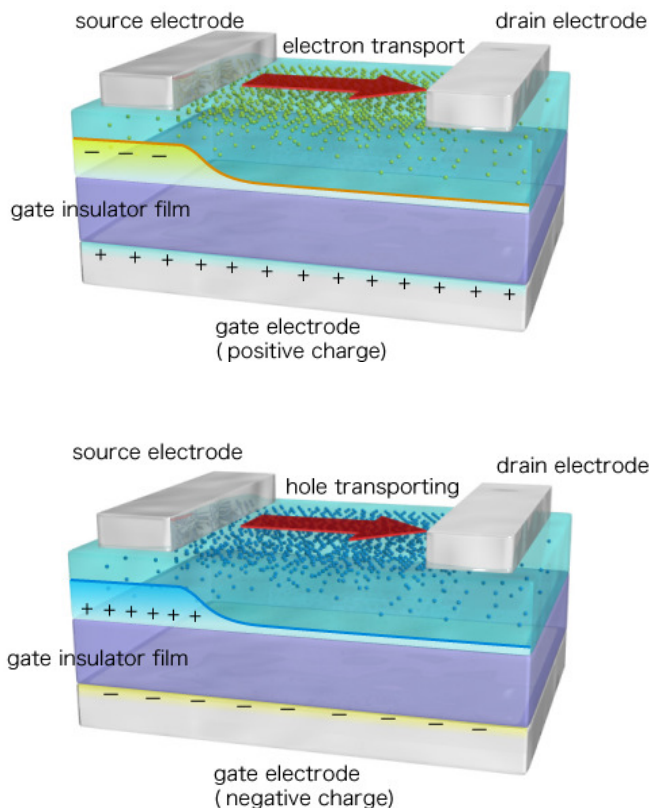


**Figure 6:** C cross-section scheme for TC/BG OTFT showing the working process for (a) *n*-channel and (b) *p*-channel devices

The accumulation model is the most frequently applied method to describe OTFTs, which can be viewed as a modified capacitor where the gate electrode and the semiconductor layer, enclosing the dielectric film, embody the role of the metal plates of the latter. Commonly, in a capacitor where good conductors form the plates, charges are localized close to the interface with the dielectric. In a traditional semiconductor, like silicon, these localized charges form a thin conducting layer (as previously discussed): when no voltage is applied between source and drain ( $V_{DS}=0$ ), the density of charge carrier is uniform along this layer. On the contrary, electrically speaking, an organic semiconductor behaves essentially like an insulator; that is, its density of charge carriers (usually thermally induced and not due to chemical doping) is very low, orders of magnitude lower than what is encountered in conventional inorganic semiconductors.

As a consequence, when an external  $V_{DS}$  is applied there is no conduction of intrinsic charges, but rather an injection of charges from the electrodes (an *intrinsic* ohmic conduction however can be measured when a low voltage is applied to a two terminal device, due to small non-intentional doping). When (for  $V_{DS} \neq 0$ ) the applied gate voltage ( $V_G$ ) goes beyond a given threshold voltage ( $V_T$ ), an equal amount of charge, but opposite in sign, appears at both sides of the dielectric, which results in the formation of the conduction channel. The sign of the gate voltage is opposite to that of the majority charges in the conducting channel, that is positive for an *n*-channel (**Figure 6a**) and negative for a *p*-channel (**Figure 6b**).<sup>21</sup>

The origin of the  $V_T$  has several explanations, one of them is the presence of non-intentional shallow traps in the semiconductor that must be filled before mobile charges can flow in the channel, another important one is the result of charge states or dipoles at the dielectric/semiconductor interface.

It is therefore clear from the above explanation how the performances of OTFTs not only rely on the nature of the organic semiconductor but also on injecting electrodes (source and drain), gate dielectric and eventually other factors (e.g. device architecture, deposition methods); all of that must be taken into account to optimize the device response and for comparing characteristics form different devices.

The main characteristic which allows to estimate the quality of the organic transistor, is the semiconductor field-effect mobility ( $\mu$ ), that can be extracted from the expression for  $I_{DS}$  (Eq. 3) noting that plotting the square root of the saturation current against  $V_G$  would result in a straight line; the mobility can be obtained from the slope of this line to zero current (Eq. 4)<sup>19</sup>:

$$\text{Eq. 4} \quad \sqrt{I_{DS}} = \sqrt{\frac{1}{2} \frac{W}{L} C_i \mu (V_G - V_T)}$$



In the saturation regime however the density of charge varies considerably along the conductive channel, from a maximum near the source to practically zero at the drain. The mobility in organic semiconductors is not constant, rather it largely depends on various parameters including the density of charge carriers, with the consequence that in the saturation regime the mobility is not constant along the channel, and the above extracted value only represents a mean value. For this reason, it is often more prudent to extract the mobility in the linear regime, where the density of charge is more uniform. The evaluation of the mobility in this region is usually done through the so-called transconductance ( $g_m$ ) which follows from the first derivative of the expression for  $I_{DS}$  in the linear regime (Eq. 5):

$$\text{Eq. 5} \quad g_m = \frac{\partial I_D}{\partial V_G} = \frac{W}{L} C_i \mu V_D$$

It is to be noted that also this method present limitations, in fact the above equation is valid for the limited cases where the mobility is slowly varying with  $V_G$  (i.e., the mobility is gate voltage independent) but this is not always the case in non-ideal devices, furthermore other factors such as contact resistances should be considered.

Other important figures of merit that must be optimized for TFTs are the threshold voltage ( $V_T$ ), the subthreshold slope (S), which is related to how efficiently the gate field modulates the OFF an ON current and how abruptly the device turns ON (Eq. 6), and the  $I_{ON}/I_{OFF}$  ratio (Eq. 7):

$$\text{Eq. 6} \quad S = \frac{\partial V_G}{\partial \log I_D} = \frac{k_B T}{e} \ln(10) \left( 1 + \frac{C_{IT}}{C_i} \right)$$

where  $C_{IT}$  is the capacitance due to interfaces traps.

The importance of this parameter can be summarized by saying that the steeper the slope the faster will be the device switching on and interface trap filling.<sup>22</sup>

$$\text{Eq. 7} \quad \frac{I_{ON}}{I_{OFF}} = \frac{C_i \mu V_G}{2\mu_R q N_A t}$$

where  $\mu_R$  is the semiconductor mobility and  $N_A$  the carrier concentration in the OFF state,  $t$  is semiconductor film thickness and  $q$  is the electron charge.<sup>23</sup>

All the above parameters, combined with the necessity of stability and low-cost production drive the search toward new active materials. Even if a correlation between structural properties and device performance has already been demonstrated, after several decades of intensive research the basic understanding of charge transport in organic semiconductors still remains unclear, being much more limited than that of their inorganic counterparts. In the latter case the atoms are held together with very strong covalent bonds (76 kcal/mol for Silicon)<sup>20</sup> and charge carriers move as highly delocalized plane waves in wide bands. Considering the organic semiconductor, the weak Van der Waals interactions between organic molecules are responsible for the carrier transport, therefore different conducting mechanisms are proposed. The complexity of transport phenomena in these systems is due to the polaronic nature of charge carriers and the strong interaction of small polarons with each other and with defects.<sup>24</sup> Furthermore the transport of field-induced carriers in OTFTs is consistent with a surface mechanism, thus differing significantly from bulk phenomena. Single-crystal OFET is often used to better understand the charge transport at the surface of an organic semiconductor and to explore the upper limit of the mobility for OTFTs. Contributions from different groups using different experimental techniques (field-effect data measurements, Hall effect results, Seebeck coefficient analysis) confirms a band-like mechanism in the highly ordered bulk of the crystal, but this mechanism is not applicable to disordered films, where carrier transport take place between localized states, and charge carriers are scattered every step.

Thermally-activated polaron hopping and multiple trapping and release (MTR) mechanism, which assumes that charge transport occurs in a delocalized band while it is limited by the distribution of traps near the band (for polycrystalline films the trap could exist in grain boundaries), have been proposed to describe transport in such systems.

Regardless of what the ultimate transport mechanism is, it is clear that strengthened intermolecular interaction and overlap are preferable for effective carrier transport; additionally the energy levels and gaps, which influence carrier injection and semiconductor stability, play important roles in determining the device performances.<sup>17</sup>

As a unique characteristic of the organic semiconductors, molecular packing, energy level and physical properties can be finely controlled by the molecular design, as it is shown in the next section.

### I.3 ORGANIC SEMICONDUCTORS

The organic semiconductor is the core element of OFETs and its development represents therefore a key issue for the fabrication of high-performance devices. Exploiting the potential of synthetic organic chemistry in this field, made it possible to generate a large number of organic semiconductor classes, that in turn allowed the organic electronic solid state community to draw important relations between molecular structure and structural organization in the solid state, film morphology, and ultimately, electrical performance.

$\pi$ -Conjugated organic materials have shown a unique blend of charge-transport properties with convenient processing characteristics, which made them the ideal systems for such a kind of application;<sup>25</sup> an exciting library of systems has been developing in the literature following these guideline and the resulting structure-property rationalizations can be used to delineate general criteria (relating both the injection and current-carrying characteristics) that must be satisfied in designing novel semiconducting organic materials<sup>2</sup>:

- The HOMO/LUMO energies of the individual molecules (perturbed by their placement in a crystalline solid) must be at levels where holes/electrons can be induced at accessible applied voltage (i.e., a fine matching with the metal contacts work function is required).
- The crystal structure of the material must provide sufficient overlap of frontier orbitals to allow efficient charge migration between neighboring molecules.
- The molecules should be preferentially oriented with their long axes parallel to the substrate normal, since the most efficient charge transport occurs along the directions of intermolecular  $\pi$ - $\pi$  stacking.
- The crystalline domains of the semiconductor must cover the area between the source and drain contacts uniformly.
- Extremely high purity is required in order to avoid presence of charge traps in the conductive channel.

### 3.1 *p*-CHANNEL SEMICONDUCTORS

At the present time many dozens of research groups are devoted to the synthesis of new organic semiconductors; hundreds of compounds have been demonstrated being hole-transporting systems (*p*-channel) in OTFTs, and new ones are reported almost every month. The preferences for holes transport is determined by the position of the HOMO energy levels relative to the metal contact work function: systems involving high HOMO level and electro-donating properties are good candidate for *p*-channel semiconductors.

Different classes of compounds show this electronic behavior and it is a common approach dividing these systems into two main categories: small molecules and polymers.

#### 3.1.1 SMALL MOLECULES

Typical *p*-channel semiconductors involve molecular electron-rich structures as aromatic and heteroaromatic fused ring (acenes), heterocyclic oligomers, and macrocycle derivatives (**Figure 7**).<sup>26</sup> In the following a brief overview of these systems will be given, empathizing the correlation between molecular design and final device behavior.

- Acenes

Pentacene (**P5**) is perhaps the most important exponent of this class of compounds, and one of the most extensively studied organic semiconductor, displaying: the highest mobility in OTFTs ( $3.0 \text{ cm}^2/\text{Vs}$ ), current ratio  $I_{\text{ON}}/I_{\text{OFF}} > 10^8$ , near-zero threshold voltages and subthreshold slope as low as 1.2 V per decade. Besides these remarkable performances, the major disadvantages of this system are represented by its instability toward oxygen/light and its low solubility, which represents an obstacle for solution methods and large-area applications. Generally, skeletal modifications, such as replacement of benzene with thiophene rings, modification of the conjugation length

and insertion of alkyl and aromatic substituent, dramatically affect the molecular electronic characteristics (mainly modifying the frontier orbitals energies), the packing behavior and the supramolecular ordering, the solubility and the environmental stability, thus modifying the final semiconducting performances.

Rubrene is a clear example of the above mentioned molecular engineering: mobility value as high as  $40 \text{ cm}^2/\text{Vs}$  has been reported for OFETs based on rubrene single crystals<sup>27</sup>, whilst analogous devices based upon 5,11-dichlorotetracene single crystals<sup>26</sup> (which mainly presents the same molecular core) exhibit a more modest mobility value of  $1.6 \text{ cm}^2/\text{Vs}$ .

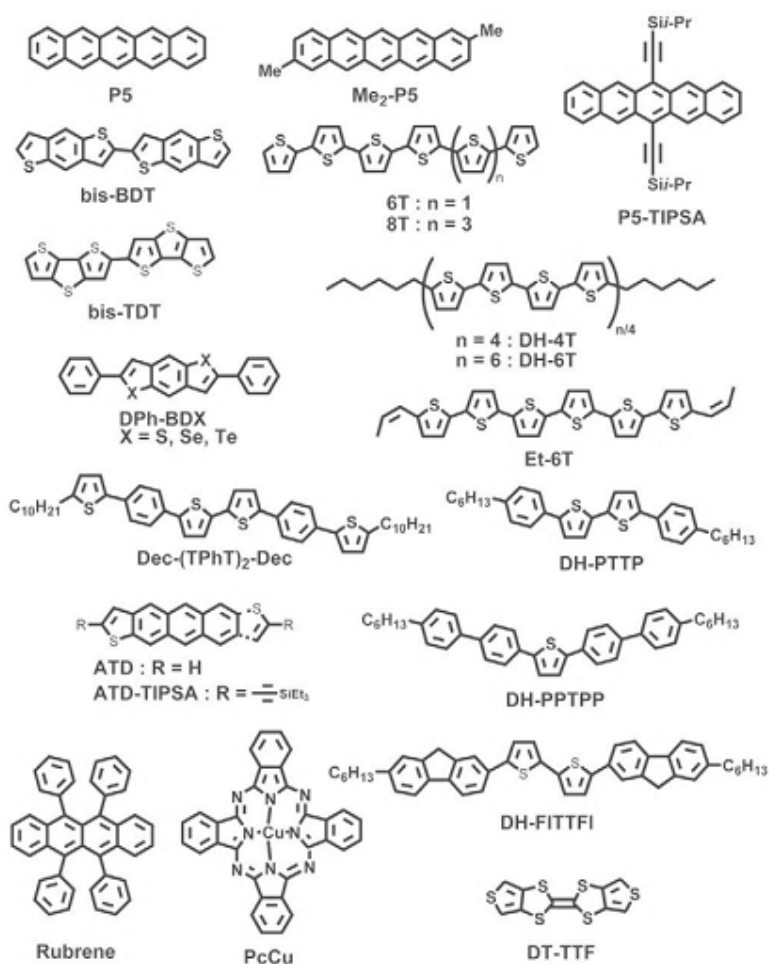


Figure 7: Chemical structures of some molecular *p*-channel semiconductors

- Heterocyclic oligomers

Another important class of molecular semiconductor is based on heteroaromatic electron-excessive rings, mainly thiophene derivatives. Thiophene oligomers have been extensively studied, and the effects of ring numbers and alkyl chain substituent lengths on OFETs characteristics have been investigated<sup>28,29</sup>: four to six thiophene rings and 2-6 carbon numbers of alkyl chain are necessary for obtaining high mobilities. Common best mobility values for these systems are in the range between 0.1–0.3 cm<sup>2</sup>/Vs. Further, development of the starting structures in term of performances and stability is based on the following strategies: employing rigid, rod-like molecules, extending the  $\pi$ -conjugation lengths along the molecular principal axis, enhancing the  $\pi$ -stacking to obtain close packed structures, improving the environmental stability by lowering the HOMO level, favoring crystalline structures and solubility through fine regioregular synthesis and functionalization. These approaches led to the introductions of thiophene-phenylene oligomers, linearly condensed heterocycles, and electron-acceptor substituted units. An interesting example of this accurate design is that of anthradithiophene (**ADT**)<sup>28</sup> where the molecular shape of pentacene (which leads to favorable crystal packing geometry and orientation) is combined with thiophene end groups (which should increase stability and favor the attachment of solubilizing substituents) in order to incorporate the peculiar properties of the parental compounds.

- Macrocyclic derivatives

Phthalocyanines (**Pc**) are a class of planar aromatic macrocycles consisting on four isoindole units, presenting 18  $\pi$ -electrons; different metal elements, one or two depending on the size and the oxidation state, can replace the hydrogen atom of the central cavity leading to supramolecular complexes. The major drawback of these systems is the poor solubility due to the strong intermolecular interactions in the solid state, thus requiring the introduction of substituents for solution

processability, a method that dramatically would reduce the fabrication costs. The strong intermolecular interactions leading to  $\pi$  -  $\pi$  stacking is however the responsible for their conducting behavior, which results in high mobilities of 0.2–0.6 cm<sup>2</sup>/Vs for tris(phthalocyaninato) rare earth tripledecker complexes.<sup>30</sup>

Other macrocyclic structures reported in the literature comprise triarylamine-based systems, where the cyclic structure could allow the formation of a crystalline structure. This can be achieved thanks to a restriction of the rotation of phenyl groups, which in turn leads to a planar structure and an orderly molecular packing. As a consequence both the mobility and the ON/OFF ratio of the cyclic triphenylamine are an order of magnitude larger than those of linear analogues.

### 3.1.2 POLYMERIC SYSTEMS

Polymeric semiconductors typically comprise coupled aromatic monomer units, with extended  $\pi$  orbital conjugation along the length of the backbone (**Figure 8**). These materials offer advantages of easy processing from solution and good film forming properties, the main reason to use such kind of materials in fact is that they can be solution coated into cohesive and conformal thin films. Control of film thickness and morphology can be achieved by optimization of solubility, solution rheology and thermal properties. Solubility is induced through the attachment of aliphatic side units, while both polymer molecular weight and poly-dispersity are important properties to optimize that influence the formulation rheology, as well as the thin film formation and morphology from solution printing or casting.

Thiophene-containing polymers have exhibited amongst the highest charge carrier mobilities from OFETs fabricated by solution deposition. When thiophenes are coupled together in their 2<sup>nd</sup> and 5<sup>th</sup> positions, an extended delocalized electronic orbital system can be achieved, in which the electron-rich rings are conjugated together and exhibit a coplanar conformation.



This conformation provides the molecular template for achieving a highly crystalline thin-film microstructure, which plays a role in their excellent charge transport properties.

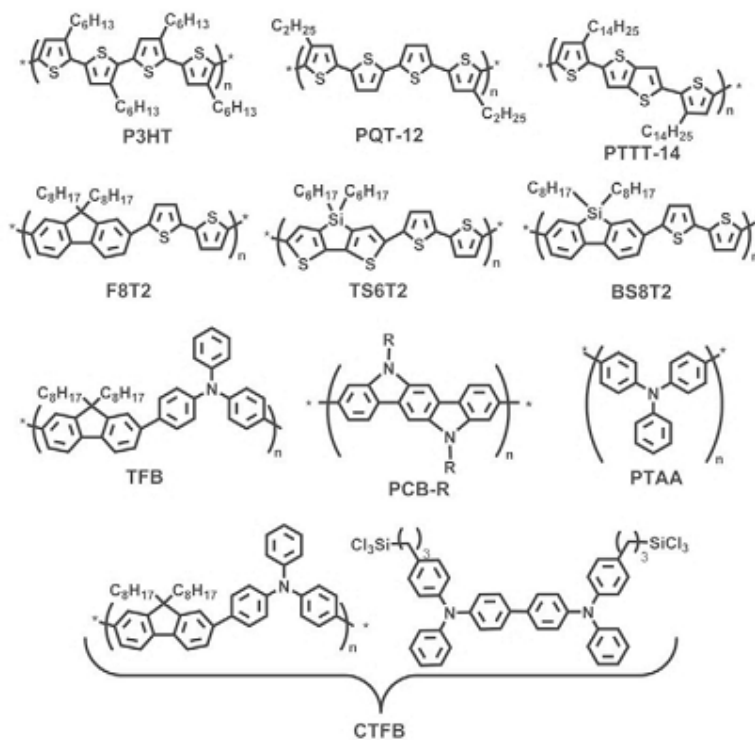


Figure 8: Chemical structure of some polymeric *p*-channel organic semiconductors.

The first solution-processed semiconducting polymer to exhibit charge carrier mobilities in the range of  $0.1 \text{ cm}^2/\text{Vs}$  has been regioregular **P3HT**; its head-to-tail regioregular molecular structure was found to be essential to achieve highly crystallinity in the solid state, improve microstructural ordering, decrease band gap and substantially improve field-effect mobilities.<sup>31</sup> P3HT emerged as a benchmark semiconducting polymer, and provided critical guidance for the design of new polymers that can replicate or even improve such electrical performances. Fundamental weakness in the alkythiophene polymers have to be resolved for developing such new high-performance derivatives: firstly, the monomer is non-centrosymmetric which limits the range of

polymerization techniques that can be used to construct highly regular repeat units, and also introduces batch-to-batch variability; secondly, the highly electron richness of the delocalized systems is susceptible of oxidation and doping degradation; finally, high side-chain density prevents alkyl substituents interdigitation and thus ordering (the nature of the side chains has a critical impact on the self-assembly, crystallization and semiconducting properties). To address these problems new polythiophenes systems have been introduced, such as regioregular polyquaterthiophenes (**PQTs**) and a class of alternating copolymers of thieno[3,2-b]thiophene and 4,4'-dialkyl 2,2'-bithiophene monomers (**PTTT**)<sup>32</sup>, which shows highly organized morphology, large crystal domain and finally good transistor response (mobilities in the range between 0.2-0.7 cm<sup>2</sup>/Vs) and stability.

Other families of *p*-channel polymers are based on various core units (e.g. fluorene, siloles, carbazole, triarylamine) or exploit cross-linking approaches.<sup>18</sup>

### 3.2 *n*-CHANNEL SEMICONDUCTORS

The literature on *n*-channel OTFTs takes us back only twenty years, in fact despite the latest impressive results, electron-transporting organic semiconductor are, compared to *p*-channel, far less developed in terms of our understanding of the fundamental structure-charge transport property relationships and carrier activation-deactivation mechanism<sup>2</sup>. However, *n*-channel semiconductors are important components of bipolar transistors, *p-n* junction diodes and are essential for the fabrication of organic complementary circuits. The latter devices (organic counterpart of the complementary metal-oxide-semiconductor, CMOS, technology used for constructing ICs and other digital logic circuits), have emerged as a promising circuit technology for organic semiconductors due to low power consumption/dissipation and high noise margins.<sup>33,34</sup>

There are several reasons why only limited numbers of high-performance *n*-channel semiconductors have been introduced so far: first, most organic materials tend to transport holes better than electrons, lower field-effect mobilities are thus usually obtained for OTTFs and less organic *n*-channel systems are available; second, the performances of *n*-channel semiconductors are easily degraded due to their environmental instability<sup>35</sup>. The majority of the existing *n*-channel semiconductors are sensitive to air and moisture, this is because *n*-type charge carriers are susceptible of trapping by the most common reactive species in an ambient atmosphere, H<sub>2</sub>O and O<sub>2</sub>. This inherent instability is thus not due to intrinsic chemical degradation resulting in material decomposition, but rather depends on the vulnerability of the charge carriers to trapping in ambient conditions, which seriously degrades effective field-effect mobility.<sup>33</sup>

Two main strategies can be followed to address this problem: from a kinetic point of view it is useful to isolate the active semiconductor from the environmental agents through encapsulation method, thus inhibiting the red-ox processes. Thermodynamic stability instead is more complex to achieve, involving a careful tuning of the molecular electron affinity; through a precise molecular tailoring, the LUMO energy should in fact be lowered below that of most atmospheric trapping species, and contemporarily be matched with respect to the Fermi level of the source and drain electrodes, in order not to limit the electron injection.<sup>20</sup> There are two main strategies to gain the required stability and achieve efficient FET electron conductivity: introduction of substituents capable of both creating a denser molecular packing and reducing the frontier orbital energies, or modification of the insulator surface properties to eliminate electron-trapping sites.

The most investigated air-stable *n*-type organic semiconductors can be prepared by introducing electron acceptor groups to *p*-channel semiconductors, this common approach can be rationalized in term of HOMO-LUMO levels, noting that the introduction of such moieties decreases the LUMO level.

Common systems are thus perfluorinated metallophthalocyanines, fluoroacyl oligothiophenes, *N-N'*-fluorocarbon-substituted naphthalene and perylene diimides (**Figure 9**).

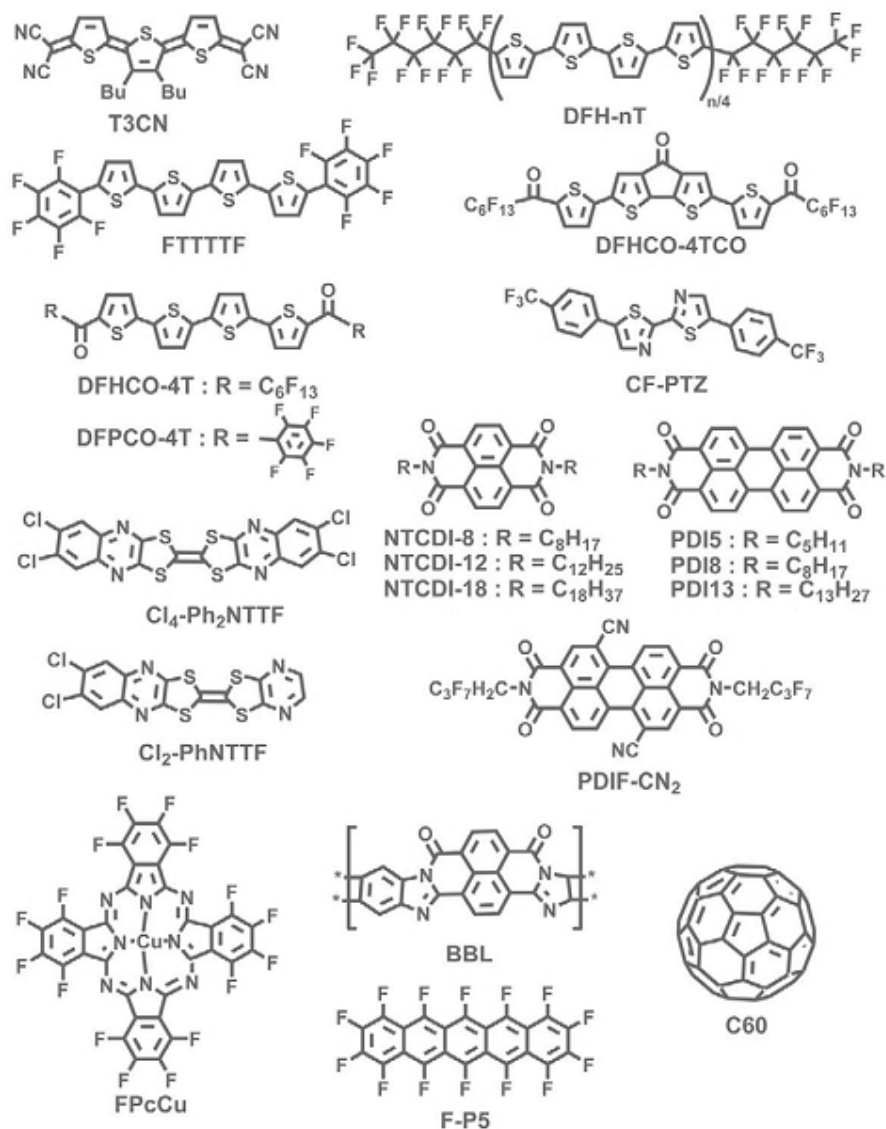


Figure 9: Chemical structure of some *n*-channel organic semiconductors.

- Perfluorinated metallophthalocyanines

The energy levels of phthalocyanines derivatives can be tuned by substitution with ewg group, leading to air stable systems easily purified by vacuum sublimation. The best reported transistor performance has been reported for copper complex (**FPcCu**).<sup>36</sup>

- Fluoroacyl oligothiophenes

Many *n*-channel semiconductors are based on oligothiophenes in which the molecular energy levels have been tuned by substitution with cyano, perfluoroalkyl/aryl, and alkyl/arylcarbonyl. The relatively minor change in the substituent of DH-6T that leads to DHF-6T is sufficient to dramatically alter the thin film semiconducting properties from *p*-type to *n*-type; it is worth noting that in this case, perfluoroalkyl chain exhibit only strong  $\sigma$ -inductive electron-withdrawing effect (-I) as fluorine atoms are not directly connected to the  $\pi$  system.<sup>37</sup> Mobilities as high as 0.01 cm<sup>2</sup>/Vs have been measured for this molecule. Other studies demonstrate the possibility of regiochemically inducing modulation of major carrier sign, exhibiting both *p*- and *n*-channel behavior within the same series, having the same core structure and prepared under identical film growth, device configuration and environmental measurement conditions, by manipulating relative positions of perfluoroalkyl substituent<sup>38</sup>, or perfluoroarene building blocks in mixed perfluoroarene-thiophene oligomers (**FTTTTF**).<sup>39</sup> Higher mobilities have been obtained with air-stable *n*-channel oligothiophenes containing or substituted with carbonyl groups (**DFHCO-4T**,  $\mu = 1.7$  cm<sup>2</sup>/Vs) as vapor-deposited film.<sup>15</sup>

- Fused acenes

Important electron conductors are based on fused acenes such as naphthalene and perylene<sup>40</sup>. Unsubstituted naphthalene carbodiimide (**NTCDI**) derivatives exhibit relatively low mobilities, introducing alkyl substituent leads to *N-N'*-dialkyl-substituted NTCDIs which behave much better (**NTCDI-8**,  $\mu = 0.16$  cm<sup>2</sup>/Vs) but are still relatively instable in air; incorporation of fluoroalkyl groups stabilizes the system allowing electron transport in air.<sup>41</sup> *N-N'*-substituted perylene diimides (**PDI**) have been recently intensively studied<sup>41,42</sup> demonstrating air stability, minimal hysteresis and the record mobility of 2.1 cm<sup>2</sup>/Vs.

## I.4 ENHANCING THE DEVICE PERFORMANCES

Analysis on the recent literature on OTFTs indicates that this new technology will succeed if dramatic, understanding-based increases of performance, compatible with low-cost materials processing and device manufacturability, are achieved. To reach sufficient low operating voltages and high source-drain currents at relatively high operation speeds it is clear, from the intrinsic characteristic of these systems, that a whole sum of elements have to be taken into account besides the mere search for the highest mobility organic semiconductor. Considering that the greatest organic field effect mobility reported to date was obtained for a single-crystal organic semiconductor, it seems increasingly unlikely that solution-processed amorphous/polycrystalline semiconductors films alone will ever achieve the desired performances.<sup>23</sup> In this regard it should be emphasized that OTFTs are truly interface devices in which the semiconductor properties are strongly linked to those of the dielectric; thus, for device performances to have a major impact, a quantum jump in dielectric materials is needed over what is currently achievable. At the same time, OTFTs responses are directly connected to the device structure and the deposition methods, which therefore represent a severe issue to be considered in order to pursue advantageous low-cost/large-area fabrications, compared to the inorganic counterpart. In the following sections the attention will be focused directly on these issues; the role of the dielectric materials will be addressed firstly illustrating their characteristics and requisites through the various classes entered in the literature, then the importance of the interfaces and of a proper chemical surface engineering will be addressed, both together with the relevance embodied by the deposition methods.

#### 4.1 THE DIELECTRIC LAYER

The substantial improvements on OTFT performances (in term of field-effect response, environmental stability and even processability) can be achieved by modifying the active interfaces and taking into account the importance of both the insulating dielectric material and the metal contacts. The dielectric definitely plays a leading role in the characteristics of the device, and the motion of carriers is critically determined by the intrinsic properties of the semiconductor-insulator couple; one fundamental task is therefore to understand in what way the presence of the insulator layer influences the motion of the mobile carriers in the channel and thus developing components able to address the desired requests.

Generally speaking, a high-performance transistor comprises a surface-smooth dielectric layer in which charge injection from the gate does not occur, and which is free of static charges that might disturb the threshold voltage of the device<sup>19</sup>. A true breakthrough approach in dielectric materials must therefore achieve: very large increases in gate capacitance, high dielectric strength, very low leakage currents, low hysteresis ( $C_i$ -V), conformal coverage, high thermal and chemical stability and simple solution-phase fabrication. These dielectric features should in turn result in OTFTs presenting: very low operation voltages, large breakdown fields, crisp saturation behavior in current-voltage characteristics, generality with both  $p$ - and  $n$ -channel semiconductors, amenability to relatively large area devices and high fabrication yields over practical TFT area.<sup>23</sup>

Before considering the different classes of dielectric materials introduced, it is important to briefly overview the involved parameters we have to manage when dealing with a dielectric. An important parameter is the maximum possible electric displacement ( $D_{\max}$ ) the gate insulator can sustain (Eq. 8):

$$\text{Eq. 8} \quad D_{\max} = \epsilon_0 \kappa E_B$$

where  $E_B$  is the dielectric breakdown field,  $\epsilon_0$  is the permittivity of vacuum and  $\kappa$  is the relative static permittivity of the material (dielectric constant). For a planar structure, the capacitance (i.e., the proportionality constant between the applied voltage and the charge created) can be expressed as (Eq. 9):

$$\text{Eq. 9} \quad C_i = \epsilon_0 \frac{\kappa}{d} A$$

where  $A$  is the area of the electrodes and  $d$  is the dielectric thickness.

A viable approach to significantly reduce the OTFT operating voltage and simultaneously enhance the  $I_{DS}$  is to increase the capacitance of the dielectric; this can be done in two principal ways according to Eq. 9: reducing the dielectric film thickness and exploiting high- $\kappa$  dielectric materials. This second approach is what led to the current chemical researches on innovative dielectric materials for OFETs. Several classes of new dielectric materials have been investigated for OTFTs and novel approaches to modify the surface of the final insulating film have been recently discussed.<sup>43</sup> The large majority of devices has been historically made on silicon dioxide thermally grown on single-crystal silicon wafer; this dielectric is readily accessible and extremely important when comparing the properties of newly synthesized organic semiconductors, but it possesses a relatively low dielectric constant ( $\kappa=3.9$ ) and presents a large density of electron-trapping site at the semiconductor interface due to the existence of surface hydroxyl groups. Considering that the key to low voltage application resides in the reduction of the threshold voltage and the inverse subthreshold slope, which are both controlled by the gate insulator, it is mandatory to search for thin, high- $\kappa$  gate dielectrics to achieve the requirements needed for new technologies (such as reducing the device size). In this sense  $\text{SiO}_2$  has reached its scaling limit, directing the study toward alternative inorganic insulators.<sup>44</sup> Anyway, generally conventional inorganic materials, must be very thick to avoid leakage, cannot be



deposited from solution, result difficult to deposit as smooth films on plastic substrates and in many cases do not yield flexible devices due to cohesion, delamination or cracking. Also new high- $\kappa$  metal oxides ( $\text{HfO}_2$ ,  $\text{Ta}_2\text{O}_5$ ,  $\text{Y}_2\text{O}_3$ ,  $\text{CeO}_2$ ,  $\text{TiO}_2$ ) present limitations concerning processability, mechanical flexibility, compatibility with organic semiconductors and, even though solution-based methodologies are possible, these materials must usually be surfaced-modified to enhance semiconductor film growth.

Polymeric dielectrics offer a great potential to overcome these limitations due to their capability of leading to films with good characteristics through simple solution-processes as spin-coating and printing methods. Polymers having different chemical structures and chemical and physical properties are readily available (e.g. polymethylmethacrylate PMMA, polystyrene PS, polyvinylchloride PVC, polyvinylalcohol PVA, polyvinylphenol PVP, polyimides) but the corresponding TFTs still operate at relatively high voltage. This reflects the substantial insulator thicknesses ( $\gg 0.3 \mu\text{m}$ ) required to reduce gate leakage currents to acceptable levels, thereby affording low capacitance metric ( $\ll 20 \text{ nF/cm}^2$ ). Latest results however demonstrate the possibility of achieving high dielectric constant, robustness, easy processability, low current leakages and operating bias using crosslinked polymer blends (CPB)<sup>45</sup> which also allow reducing the dielectric thickness. Capacitances in the order of  $300 \text{ nF/cm}^2$  have been reported for a 20 nm-thick film, which result far greater than those of 300 nm-thick  $\text{SiO}_2$  gate dielectric ( $\sim 20 \text{ c}$ ). By controlling and optimizing the cross-linking conditions, employing moderately reactive cross-linkers, appropriate solvents and polymer/cross-linker concentration ratios it is possible to readily deposit from solution (spin-coating or gravure printing) adherent, pinhole-free and smooth gate dielectric with tunable thickness and capacitance.<sup>46</sup> Besides these features, the cross-linking (insolubility) ensures subsequent device layers to be deposited on top without dissolution of the dielectric and to covalently graft the insulator layer on typical gate materials.

These ultrathin 10-20 nm gate insulators, moreover, exhibit among the largest reported  $\kappa/d$  ratios (which is essential for efficient device scalability), result electrically uniform over large areas, are compatible with both bottom and top contact TFT geometries and can be readily patterned for vertical interconnects using conventional microelectronic lithography, reactive ion etching or liquid-phase buffer oxide etching. Finally, this approach is applicable to diverse gate and semiconductor materials: flexible inorganic/organic hybrid TFTs using all-transparent component materials have been demonstrated using this approach.<sup>12</sup>

Dielectric materials composed of molecular components are ideal candidates for OFETs, because small molecules have nanometer length scales, tunable electronic structures, processability on flexible substrates, and are compatible with organic semiconductors. Thus one class that obviously received great interest is that of self-assembled monolayers (SAMs) and self-assembled multilayers (SAMTs). Here the strategy is that of increasing the capacitance of the dielectric layer by decreasing its thickness to a few nanometers, without incurring leakage currents. If we compare layers of SiO<sub>2</sub> in this thickness range, very poor insulating behavior is found, with leakage currents as high as 10<sup>-3</sup>-10<sup>-1</sup> A/cm<sup>2</sup>, in contrast, leakage currents on the order of 10<sup>-8</sup> A/cm<sup>2</sup> are usual for SAMs and SAMTs.<sup>44</sup>

Only a brief summary of the latest reported example in the literature concerning this approach are shown in the following, a more exhaustive description of SAMs as surface-modifying agents will be given in the next section.

The notion of high capacitance SAMs and their use as the gate dielectric in OTFTs was pioneered by Vuillaume et al in 1996 when it was established that SAMs of *n*-octadecyltrichlorosilane (*n*-ODTS) grafted on the native oxide of Si wafer were good insulators, despite a thickness of only 2.8 nm.<sup>47</sup> In the last ten years new concepts related to the preparation of SAMs for electronic applications emerged; the initial idea of exploiting SAMs made by alkyl chains, thanks to their behavior as very thin insulator with very high electric breakdown fields (mainly

due to the large HOMO-LUMO gap), fostered the fabrication of new nanostructures extending to dipolar molecules, to increase the film dielectric constant. The Northwestern group investigated self-assembled nanodielectrics (SANDs), fabricated either via a layer-by-layer solution phase self-assembly or via a vapor-phase processing (v-SAND), based upon alternating  $\sigma$ - $\pi$  organosilane precursors to yield 3D-crosslinked hybrid organic-inorganic dielectric multilayers.<sup>48,49</sup> The systems were grown by sequential deposition of polarizable  $\pi$ -conjugated components as the stilbazolium group (**Stb**), and crosslinkable  $\sigma$  building-blocks such as  $\alpha,\omega$ -difunctionalized hydrocarbon chains (**Alk**) and octachlorotrisiloxane capping layer (**Cap**) (**Figure 10**):

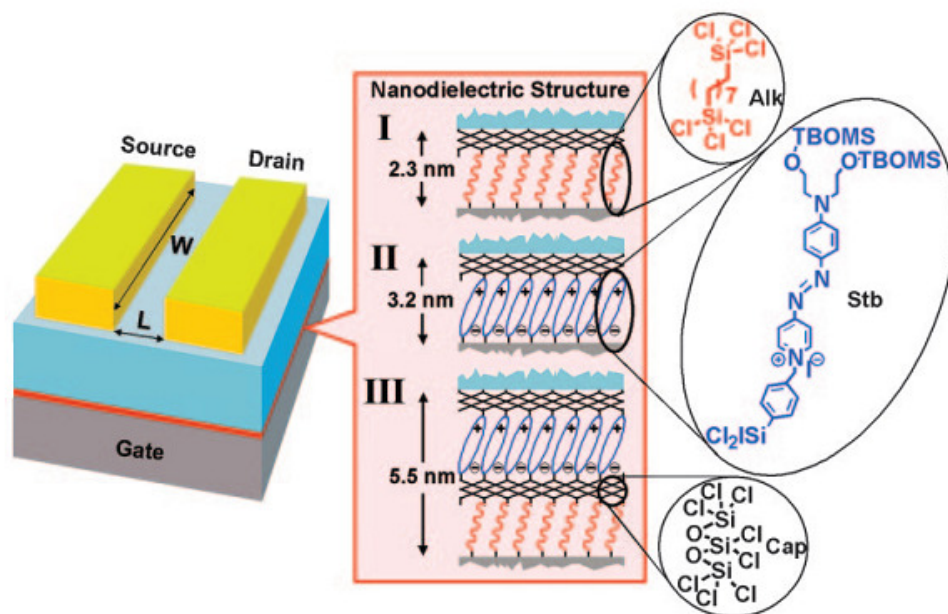


Figure 10: Schematic representation of the OTFT components showing the molecular structures of self-assembled nanodielectrics I-III.

Depending on the constituent molecules used, type-I, type-II, and type-III SANDs were fabricated with maximum capacitances as high as  $400 \text{ nF/cm}^2$  (type-I),  $710 \text{ nF/cm}^2$  (type-II) and  $390$  (type-III) at  $10^2 \text{ Hz}$ . Further development on this research reported the excellent SANDs compatibility with single-wall carbon nanotubes semiconductors.<sup>50</sup>

## 4.2 THE ROLE OF INTERFACES

So far, due to the interest in new materials with higher intrinsic charge-carrier mobility, the work of chemists in OFETs was centered on the synthesis of novel organic semiconductors for the active layer and not on the chemistry of surfaces, even though most phenomena occur at the interface rather than in the bulk. It is in fact nowadays clear that injection, accumulation and flow of carriers in an operating field-effect device are surface processes, as the charge transport occurs only in the first few layers of the semiconductor, next to the dielectric.<sup>51</sup> Within this frame, the preparation of SAMs and SAMTs represents the most convenient chemical way to modify a surface, and therefore an interface between different materials, enabling us to go beyond the present limits of organic electronics. SAMs are getting introduced to improve the performances of the most critical OTFT interfaces (dielectric/semiconductor and metal/semiconductor) providing a flexible tool to prepare artificial surface and to finely tune their morphology and energetics.

- Semiconductor/Dielectric Interface

The first major problem related to the gate dielectric is the presence of trap sites on the surface which dramatically interfere with the charge conduction through the semiconducting channel. Considering the common literature benchmark  $\text{SiO}_2$ , even though its growth has been optimized to form a defect-free interface with Si, its top surface can contain Si-OH defects and  $\text{H}_2\text{O}$  which create surface states. Such energy states at the interface on inorganic oxides and dielectrics are particularly important as they can lead to carrier trapping and hysteresis. Besides influencing the mobility of the charge carriers, even the sign of the charge carriers is strongly affected by the presence of defects at the surface; furthermore, great attention has to be given to the dielectric surface energy as it influences the morphology of the semiconductor thin film, and in turn the device performances.

In spite of the fact that SAMs allow a direct control of these key parameters, a clear picture of the effects of dielectric surface modification on device performances is still lacking, due to the complexity of the problem and a full interpretation is therefore not yet available in the literature. Among the accounted effects, the modification of the dielectric/semiconductor interface influences: surface morphology, surface smoothness, surface polarity, on the one hand, and semiconductor crystallinity, ordering and molecular packing<sup>53</sup> on the other hand. Introduction of SAMs as modifying agents lead to overall device performance enhancement, such as: reduction of the subthreshold slope, increase of mobility, increase of  $I_{ON}/I_{OFF}$  ratio, change of polarity of the major charge-carrier type, modulation of carriers density in the channel, shift of the threshold voltage.

SAMs can be fabricated basically with three methods: vapor deposition, solution-casting, spin-coating. Vapor deposition generally gives rise to a smoother surface compared to solution immersion, solution-casting is the most common method because of its easy implementation and acceptable quality, spin-coating is faster than the other two methods but not optimal due to lack of uniformity.

Whatever the involved method, the driving force for functionalization of dielectric oxides resides in the chemistry of the reactive species involved, which usually comprise organosilicon derivatives (formation of polysiloxane, which is connected to surface silanol groups via Si-O-Si bonds to the incoming silane) and carboxylic or phosphonic acid derivatives (acid-base reaction with the separation of salts).

- **Metal/Semiconductor Interface**

Much effort is still to be made to fully understand the injection processes from a metal into an organic semiconductor, and the requirements for an ohmic contact is the basis for the downscaling of an organic device, in which the charge carriers are essentially supplied by the injecting electrodes.<sup>55</sup> As charge transport within the conductive channel of the transistor improve, the injection and collection of the

charges at the source and drain electrodes, respectively, become a crucial issue to be solved. Two different aspects essentially govern these phenomena: the energy-level alignment at both sides of the interface (molecular HOMO-LUMO and metal work function), and the morphology of the active layer in the contact region. A useful way to improve both these mechanisms and to get better molecule-electrode contacts is to prepare SAMs on the surface of the metal electrodes. It is clear that such a solution is not always applicable, as it is only compatible with devices based on a bottom-contact (BC) architecture; in this case in fact the metal electrodes are defined before the deposition of the organic layer. The benchmark for SAMs on metal surfaces is represented by alkanethiols on gold, one of the most used metals for the preparation of the electric contacts in OFETs. The introduction of thiol SAMs has proven to have a double effect: the dipole moment associated with the monolayer modifies the effective metal work function, while introducing hydrophobic SAMs can enhance the metal surface wettability of aliphatic and aromatic compounds, thus improving the organic semiconductor adhesion, increasing the grain size and enhancing the molecular orientation relative to the metal.

All these effects reduce the contact resistance, thanks to a finely tuning of the energy levels matching and an increased charge mobility within the layer close to the contacts, which improves the charge injection.

From a chemical point of view, the first choice for SAMs is between aliphatic and aromatic thiols; alkanethiols have a large energy gap HOMO-LUMO (8 eV) and hence are good insulators. Thus in principle, one cannot expect an alignment of the HOMO or the LUMO levels of thiols respect to the metal Fermi energy, and therefore cannot anticipate an efficient charge injection through such an insulating layer. The conduction mechanism through SAMs is generally ascribed to pure tunnelling<sup>54</sup>; within this framework, aromatic or polyconjugated molecules are a better choice thanks to their smaller gaps (2 to 4 eV).

Morphological effects and templating behavior also play a role in determining the interaction with the semiconductor organic layer.

In summary, the use of structurally and electronically similar compounds to modify the electrodes leads to an improved electronic coupling between the metal contacts and the organic semiconductor and dramatically decreases the contact resistance in nanoscale OFETs.

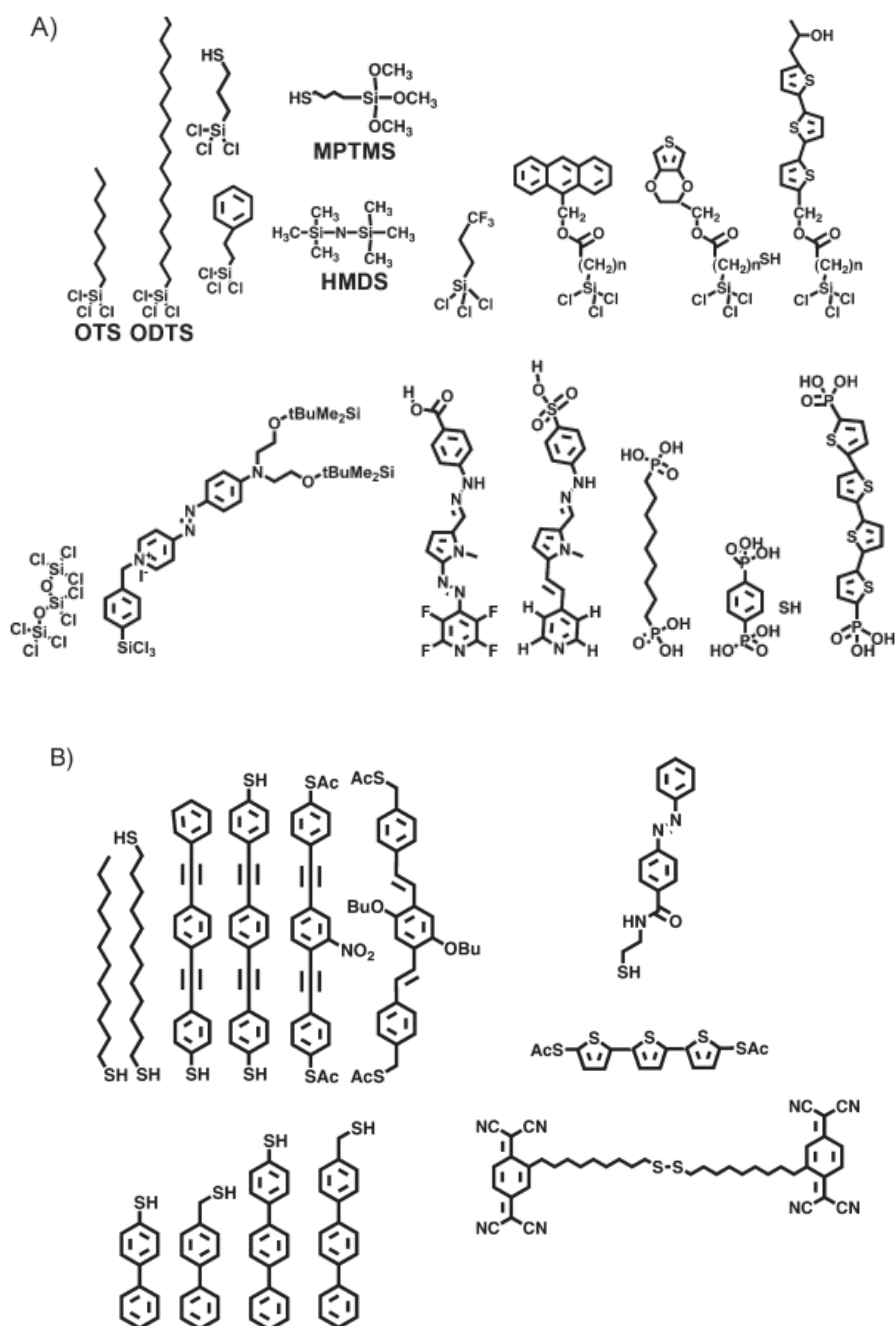


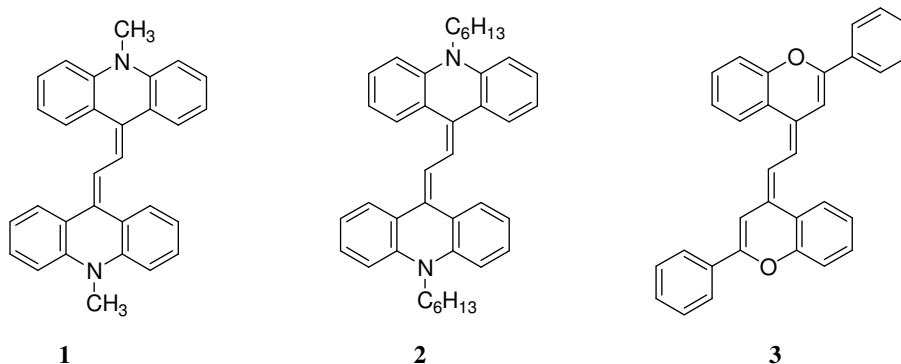
Figure 11: Examples of molecular structures used for self-assembly on (A) oxide dielectric surfaces, (B) gold electrodes.

## II. RESULTS & DISCUSSION

### II.1 SYNTHESIS OF THE ORGANIC SEMICONDUCTORS

The systems introduced for OTFTs applications embody our first explorative contribute to this field of research; the reported study in fact, represents the results of an early investigation born during the personal international experience in professor Marks research group at Northwestern University. Thus, considering the limited time to play around with, just few compounds have been synthesized and analyzed for testing their behavior as organic semiconducting materials, whilst the major efforts in this work were focused on the optimization of the subsequent device realization process (*vide infra*).

The structural feature common to all the introduced systems (Scheme 1) is the presence of a highly  $\pi$ -delocalized electronic system framed into a flat heteroaromatic core; this characteristic should guarantee a fine supramolecular cofacial arrangement thanks to favorable  $\pi$ - $\pi$  stacking interactions, thus enabling a satisfactory alignment for charge-carrier intermolecular hopping into the device semiconducting channel.



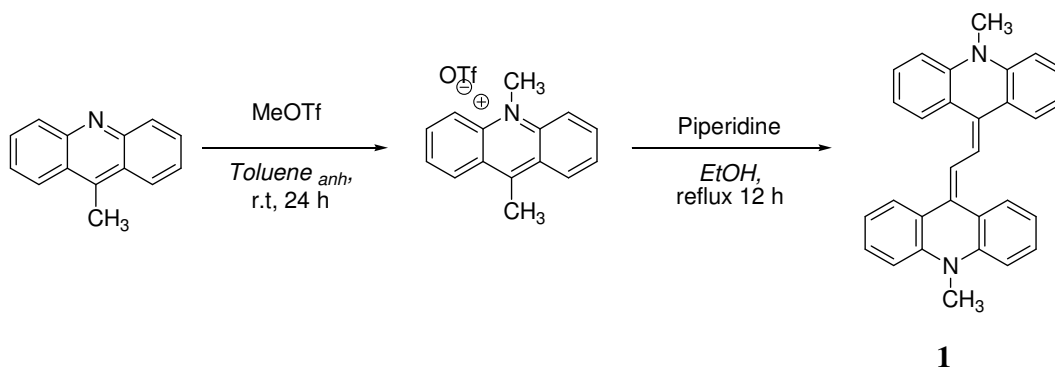
Scheme 1

System 1 consists of a high molecular weight donor already introduced in the literature by our research group as a Weitz-type electrochromic system for electron injection interlayers on metal electrodes.<sup>55</sup>



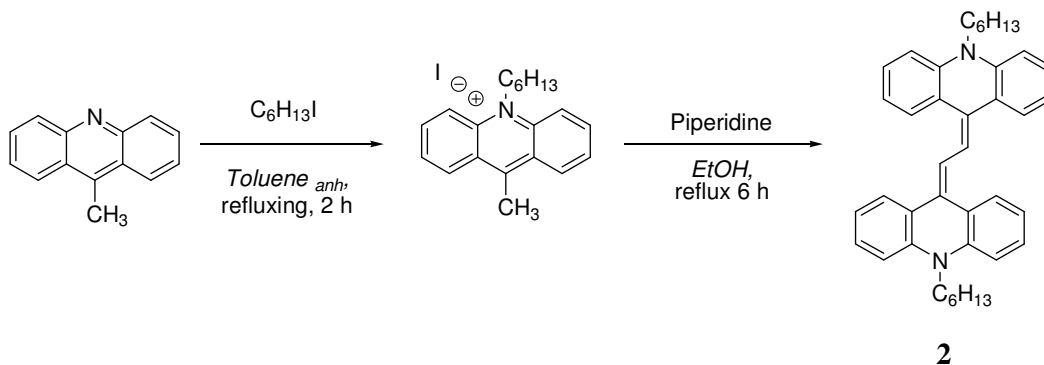
Derivative 2 was also introduced, which presents a C-6 alkyl chain on the acridinic nitrogens, in order to investigate the effect of the substituents on the supramolecular organization<sup>28,31</sup>, thus analyzing its impact on the film morphology and crystallinity, and finally on the transistor response. The last system introduced is flavene compound 3 which represents a synthetic analogue of natural flavylum salts of anthocyanidin type.<sup>56</sup>

Compound 1 was synthesized in a two-step process following the original synthetic pathway already reported in the literature by our group: in the first step, 9-methylacridine is methylated with methyltrifluoromethane sulphonate in anhydrous toluene at room temperature, leading to the desired methyl-acridinium salt as a yellow powder. The obtained product is suspended in absolute ethanol and refluxed; piperidine is then added to the reaction mixture observing a gradual turning of the color from yellow to deep red, corresponding to the formation of the carbanionic reactive species. After 12 hours refluxing, the suspension is cooled to room temperature and the red precipitate is collected by filtration. The crude product, after purification by means of filtration through a silica plug, leads to the desired product as a crystalline red solid.



Scheme 2

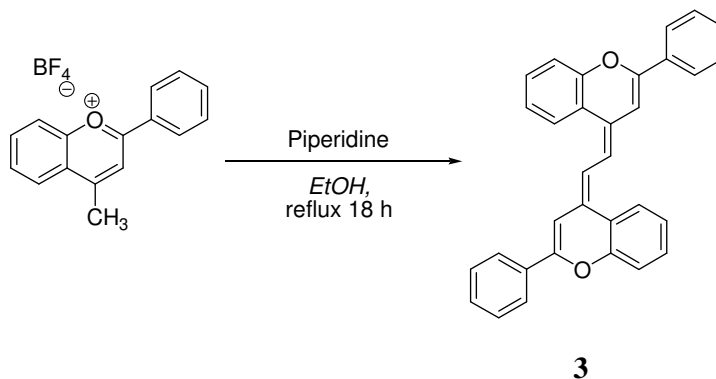
System **2** was obtained in a similar way (Scheme 3):



Scheme 3

Alkylation of 9-methylacridine with 1-iodohexane, leads to the expected acridinium salt, which is not isolated and used without further purification for the successive step. Treatment with piperidine in refluxing ethanol and purification by chromatography ( $\text{SiO}_2$ , Toluene) lead to the desired red product.

Flavene derivative **3** can be considered as the oxygenated analogue of the previous compounds, its synthesis is therefore similar to the already reported ones (Scheme 4):



Scheme 4

Starting from the commercial available precursor 4-methyl-2-phenylchromenium tetrafluoroborate salt, the desired product is easily obtained as a red solid totally insoluble in EtOH, after refluxing for 18 hours in the same solvent with excess piperidine.

Crystals of the final product were successfully grown by layering techniques from a solution of Toluene/Et<sub>2</sub>O and *n*-hexane; pictures from the single crystal X-ray analysis are reported in the following which show a peculiar herringbone arrangements of the individual molecules inside the unit cell (Figure 12).

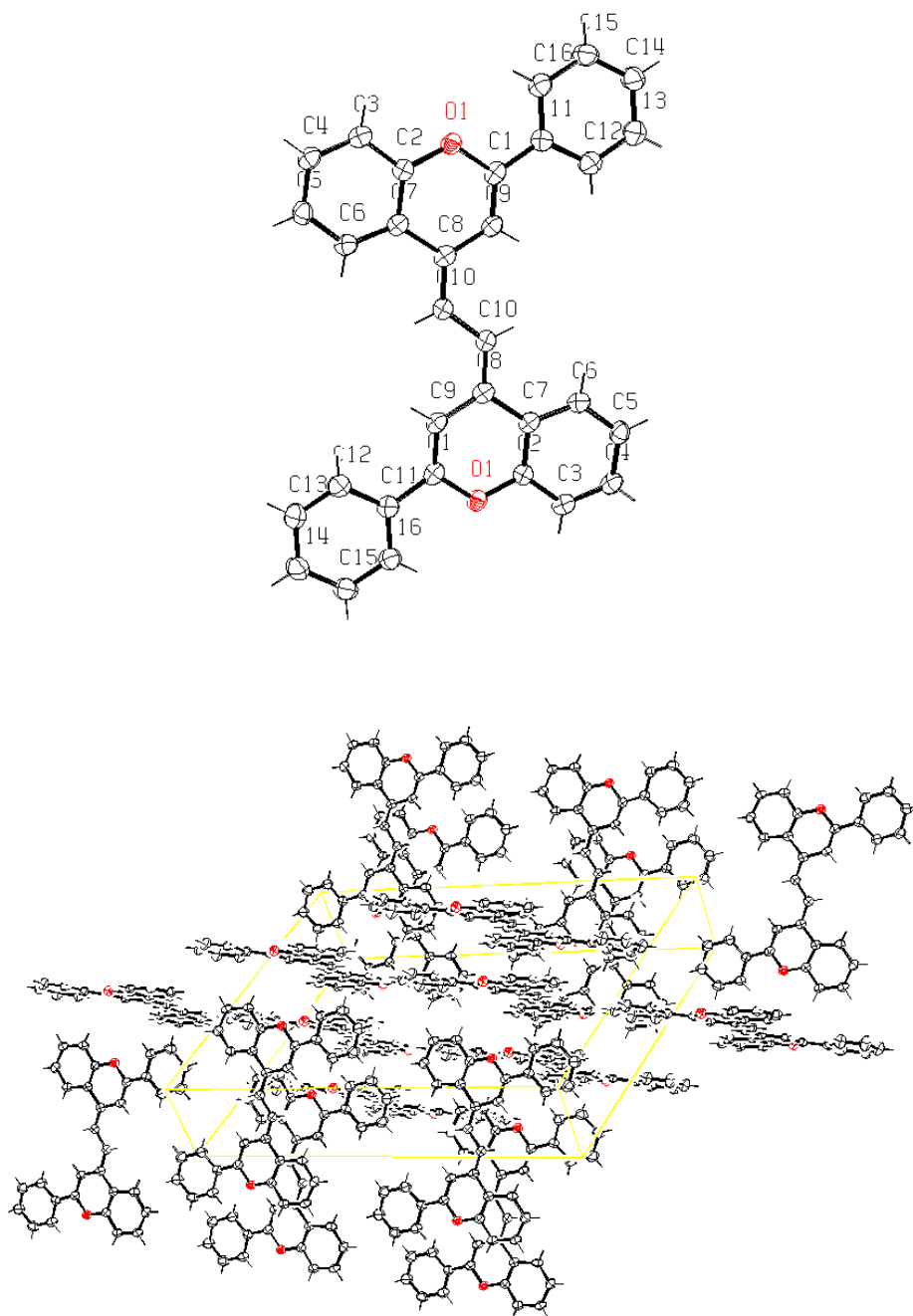


Figure 12: Single crystal x-ray analysis for compound 3

## II.2 OTFT DEVICES

When testing new organic systems as possible component of the active semiconductor layer in OTFTs it is important to underline once again the various parameters that influence the final performances of the device, enabling us to compare the obtained results. As already reported in the previous section, the choice of the insulating dielectric layer, as well as the interface treatment, strongly affects the principal figures of merit of the device; besides this, also the architecture geometry and the film deposition method deeply affect the reliability of the transistor behavior. Keeping that in mind, it is obvious how a complete optimization of the above variables was not possible to achieve in a very short period of time, therefore this part of the PhD research work represents just an explorative approach to the OTFTs theme.

All the introduced compounds were tested as semiconductors in OTFTs devices realized in the Bottom-Gate/Top-Contact (BG/TC) configuration. The choice of this particular geometry derives from the already mentioned characteristics of this configuration, which basically allows: ease of layers deposition through vapor-phase methods and very good electrode/semiconductor contact. Minor importance is instead given at this stage of research to the major drawbacks of this structure, represented by the necessity of an alternative way of contact patterning for device miniaturization and manufacturing, and of a semiconductor protecting agents, which become important in more advanced production steps concerning real-market applications.

The gate electrode, as usual for standard explorative and comparative measurements reported in the literature<sup>15</sup>, is constituted by prime grade highly boron *p*-doped <100> silicon wafer with 300 nm of thermally grown oxide as basic dielectric layer. The cleaning process of such a substrate was accomplished in two steps: the first part consisted of a double washing with ethanol solutions sonicating, followed by a final oxygen plasma cleaning treatment.

The cleaned substrates thus obtained were subsequently functionalized with a SAM of the organosilicon derivative hexamethyldisilazane (HMDS), deposited from the vapor phase under inert nitrogen atmosphere. This method, consisting in evaporating the pure molecule on the highly hydroxylated substrates surface in a controlled confined space, is particularly suitable for this kind of volatile silanes presenting short chain lengths and high vapor pressure, therefore avoiding solution processing which suffers from low reproducibility and high sensitivity to the detrimental water presence.<sup>57</sup> Humidity and deposition time are important parameters to balance also in the vapor-phase method, determining the final surface coverage, mainly due to the hygroscopic nature of the HMDS molecules: a one week deposition-time under inert nitrogen atmosphere at room temperature gave the best results in term of reproducibility and level of hydrophobicity, as proved by the high value obtained in contact angle surface measurements ( $> 95^\circ$ ).

The two following steps consisted in the vapor-phase deposition of the organic semiconductor (first) and the metal contacts (on top).

### **2.1 SEMICONDUCTOR & CONTACTS DEPOSITION**

The organic layer was deposited by vapor-phase method (PVD) in a high-vacuum chamber, directly on the pre-treated substrates mounted on an appropriate substrate holder. Diverse parameters have to be taken into account during the PVD process in order to obtain a uniform, homogeneous film with a high degree of crystallinity; the latter aspect being fundamental because involves a highly ordered supramolecular packing and a suitable molecular alignment, which are the main factors enabling the efficient intermolecular charge hopping needed to obtain a high carrier mobility inside the semiconducting channel. The base-pressure of the deposition system is the primary parameter since it determines, among other things, the mean free path of the sublimed organic semiconductor molecules, and the presence of

unwanted atoms and molecules in the vicinity of the substrate surface during film formation.<sup>20</sup> The machinery used for the present depositions was based on a common high vacuum bell-jar system, so a vacuum as high as  $10^{-6}$  torr could always be achieved for our purpose. Another important parameter to be considered is the deposition rate: lower rates allow a more uniform deposition of the evaporating molecules, avoiding an irregular island-growth and favoring an ordered edification of the supramolecular architecture upon the first monolayers, which can also act as a templating agent for the oncoming molecular beam. The lowest possible rate allowed by the organic evaporator in use, which determines the quantity of the depositing material by means of a microbalance, was set during all the depositions process ( 0.1-0.2 Å/s).

A third aspect which strongly influences the organic film morphology and, in a polycrystalline film, the dimension of the grains size (whose density and extension determine the amount of charge-trapping sites inside the semiconductor layer), is the substrate temperature; it is in fact been demonstrated<sup>15,41,58</sup> that higher substrate temperatures during deposition favor a re-ordering of the molecules on the substrate, thus leading to the development of a structurally more conform organization and enhancing the growth of higher crystalline grains, with a substantial increase of the field effect mobility and the  $I_{ON}/I_{OFF}$  ratio.

The nominal film thickness for all the depositions of our organic compounds was set to 50 nm and verified by means of profilometer analysis after film formation; thicker films are considered to be deleterious since the conductive channel involves the first few monolayers of deposited organic materials only, whilst the remaining bulk material acts as further insulating layer between the gate and the metal contacts. Dealing with metal contacts, the source and drain electrodes were deposited on top of the organic layer through a patterning mask by means of a metal evaporator analogous to the that use for the organics; the metal being gold due to a fine matching between its work-function and the energy levels of the organic molecules' frontier orbitals.

## 2.2 DEVICE CHARACTERIZATION

The OTFTs for each one of the synthesized organic semiconductors were stored under nitrogen atmosphere once obtained, and their performances tested no longer 3 days after the organic layer deposition. All the measurements were conducted at room temperature under vacuum ( $10^{-6}$  torr) at the probe station system reported in the Figure 13.

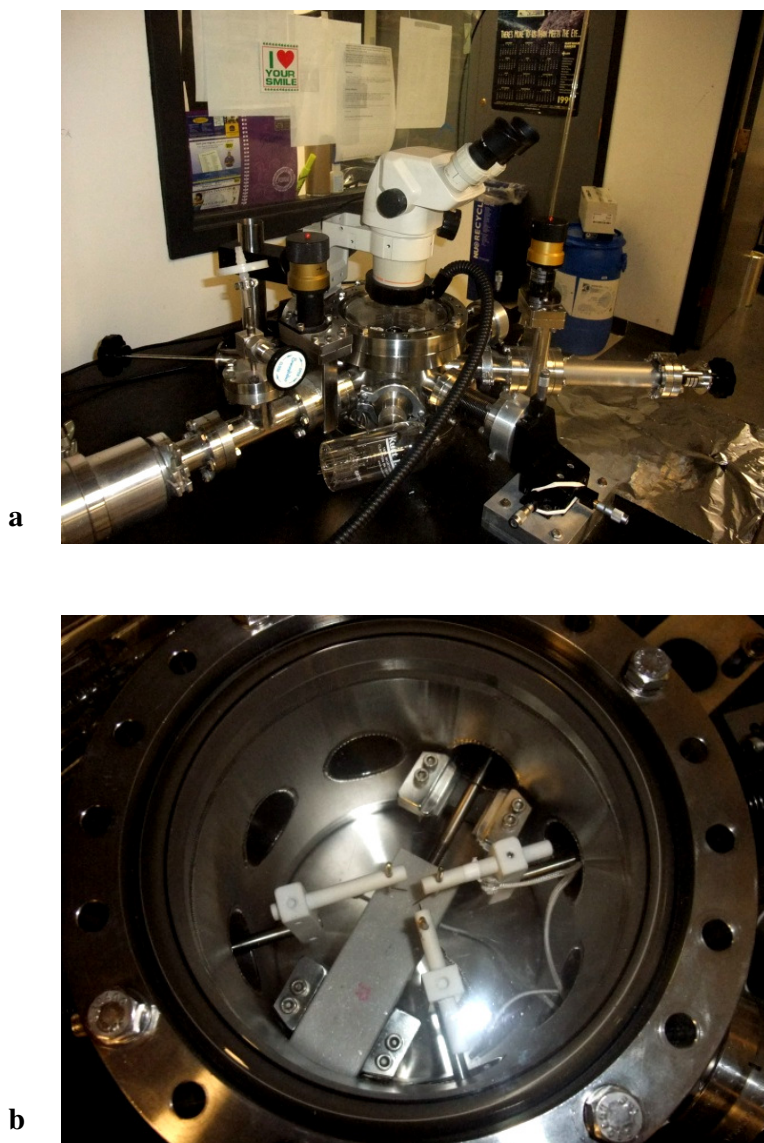


**Figure 13: Picture of the (a) probe station for the OTFTs performances measurements and (b) particular of the vacuum chamber with the contact electrodes.**

The system allows conducting two different kinds of measurements, giving the so-called OFET "transfer plots" and "output characteristics". The former is performed in the imposing an external fixed large  $V_{DS}$  and monitoring the  $I_{DS}$  response while changing the applied  $V_G$  at fixed step; by this method it is also possible to gain informations regarding the device stability, analyzing the presence/absence of hysteresis in a bi-directional transfer measurement. The second type of measurement is instead conducted by varying the  $V_{DS}$ : the  $I_{DS}$  is thus detected for different fixed external  $V_G$ , obtaining an output plot of the OFET in all its working regimes (namely, subthreshold, linear and saturation).

All the reported  $I_{DS}/V_G$  semilogarithmic transfer plots, whose analysis enables us to obtain the principal OTFT figures of merit (i.e. field-effect mobility, gate threshold voltage and current ON/OFF ratio), were obtained as the average of three different measurements on various points of the same device. To compare the electrical properties across the organic semiconductors series, all the above parameters were calculated for a high enough  $V_{DS}$ , ensuring that the device was operating in the saturation regime.

Considering system 1, the following graphs show the OTFT response for the first trial with the organic layer deposited at room temperature.

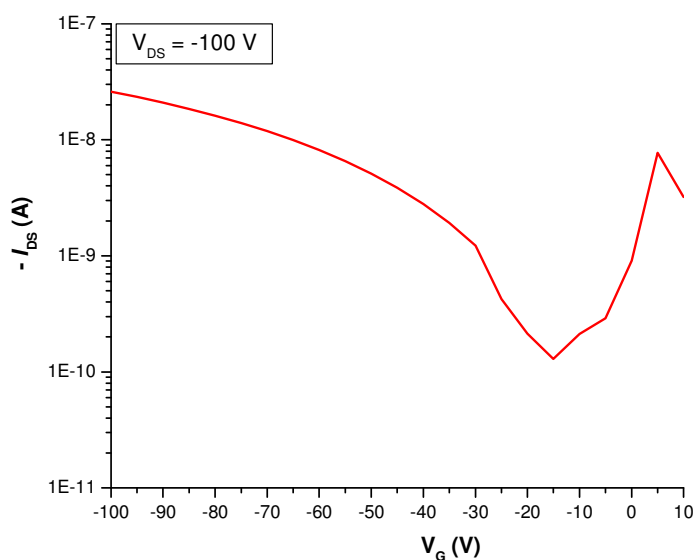


Figure 14: Transfer plot for compound 1-based OTFT ( $T_d = r. t.$ )



The investigation of the semiconducting activity of **1** (Figure 14) demonstrates a substantial *p*-channel behavior, excluding *n*-channel or ambipolar character for such a device.

Considering the expression for  $I_{DS}$  in the saturation regime introduced in the previous section (Eq. 4):

$$\sqrt{I_{DS}} = \sqrt{\frac{1}{2} \frac{W}{L} C_i \mu (V_G - V_T)}$$

knowing the channel length (100  $\mu\text{m}$ ), the channel width (5000  $\mu\text{m}$ ) and the dielectric layer capacitance ( $1 \times 10^{-8}$ ), from the fitting of the linear part of the plot for  $(-I_{DS})^{-1/2}$  (Figure 15) it is possible to extrapolate for **1** a mobility value of  $1.3 \times 10^{-5} \text{ cm}^2/\text{Vs}$  and a threshold gate voltage of -11 V; the  $I_{ON}/I_{OFF}$  obtained directly from the transfer plot is  $\sim 10^2$ .

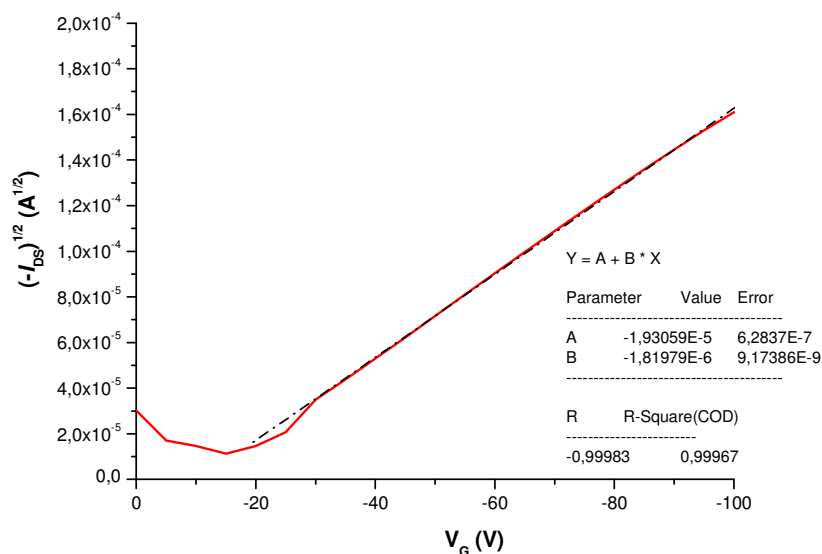


Figure 15:  $(-I_{DS})^{1/2}$  plot versus  $V_G$  for compound **1**-based OTFT ( $T_d = r. t.$ )

The bi-directional transfer plot, which permits to evidence the device operating stress and stability, is reported in Figure 17. The graph clearly evidence the presence of hysteresis, as common for organic semiconductors, corresponding to 10-20 v shifts in the gate voltage, indicating substantial charge injection into device trapping sites.

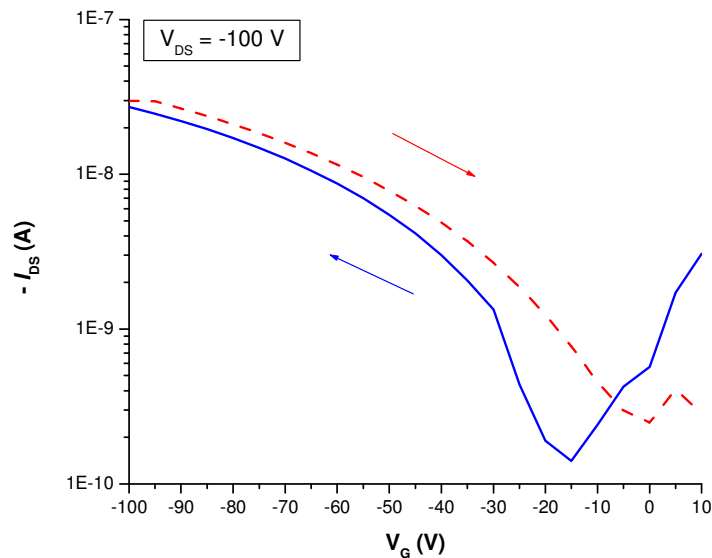


Figure 16: Bi-directional transfer plot for compound 1-based OTFT ( $T_d = r.t.$ )

The Drain-Source current/voltage output reported in Figure 18 reveals well-defined linear and saturation regimes:

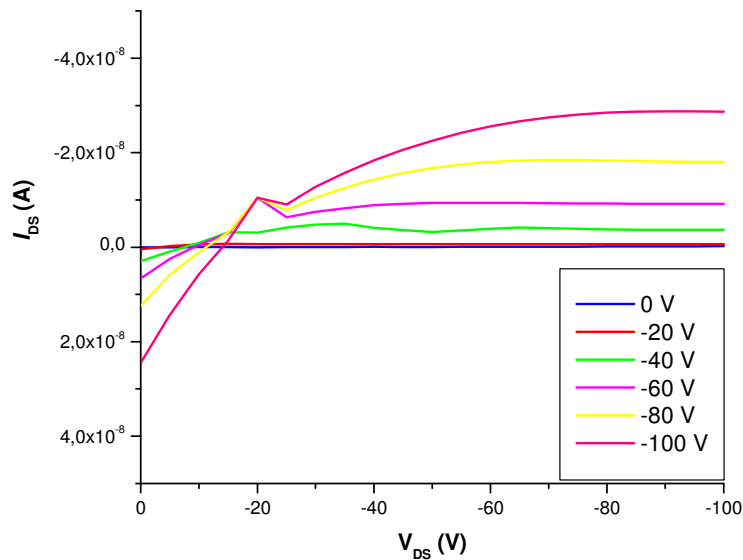


Figure 17: Drain-Source current/voltage output plot for compound 1-based OTFT ( $T_d = r.t.$ )

The analysis of the above results permits to infer that this first experiment for compound 1-based OTFT need further improvement to meet the requests for stability-performance tradeoff.

X-ray analysis of the organic layer (Figure 18) demonstrated a complete amorphous film without a single diffraction peak, which encouraged us to push further the exploration on the **1**-based OFET, seeking the possibility of inducing a certain degree of crystallinity by increasing the deposition temperature. This approach was also pursued with the aim of obtaining better interface contacts between the OFET components, and finally enhancing the overall OFET response.

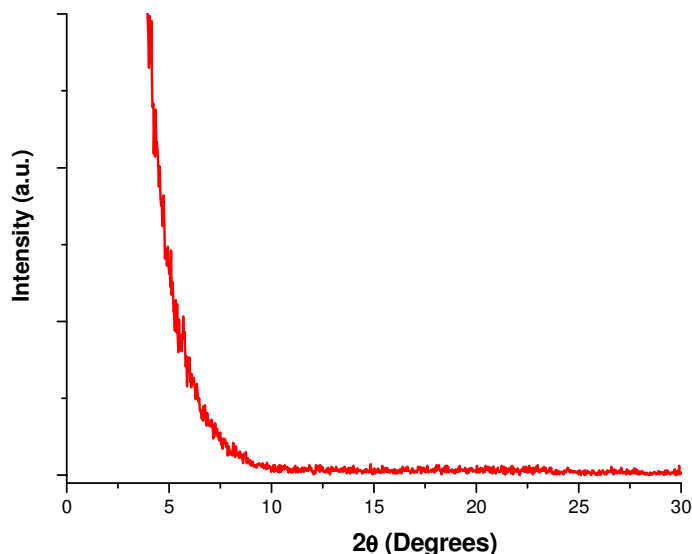


Figure 18: X-ray diffraction  $\theta$ - $2\theta$  scans of compound **1** thin film deposited at  $T_d = r.t.$

Deposition of **1** at 70 °C led to films completely different from the previous ones, both in the color and in the superficial homogeneity; moreover, the profilometer analysis did not allow to measure any sensible thickness. Once again the X-ray analysis demonstrated a complete amorphous material and, not surprisingly with these preliminary remarks, the final OFET response resulted meaningless. The approach of enhancing the OFET performances through an augmented  $T_d$  resulted to fail, even though no degradation of the organic semiconductor material was detectable (as ascertained from UV-VIS analysis in solution of the deposited material).

The most probable reason for this result is an incoherently film growth, which strongly alters the film morphology, therefore avoiding fine phases matching and intermolecular charge hopping.

Compound **2** was introduced to enhance the OFET response using a different approach, that is modifying the starting molecular design through the introduction of alkyl substituents on the  $\pi$ -conjugated core which should help achieving better molecular packing and alignments.

The OTFT device preparation was carried in the same way as it was done for derivative **1**, thus the first deposition was conducted again at room temperature; also in this case, X-ray analysis conducted on the organic film showed a completely amorphous phase (Figure 19).

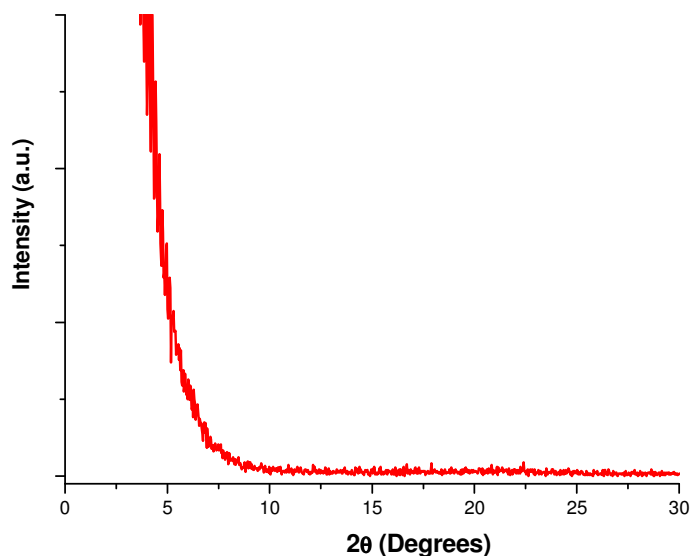


Figure 19: X-ray diffraction  $\theta$ - $2\theta$  scans of compound **2** thin film deposited at  $T_d = r.t.$

The OTFT parameters were extracted from the transfer plot (Figure 21) and the  $(-I_{DS})^{-1/2}$  graph (Figure 22) as already stated.

A field-effect mobility of  $1.7 \times 10^{-6} \text{ cm}^2/\text{Vs}$  an order of magnitude lower than that of *N*-methyl analogue **1**, demonstrates the deleterious effect of the longer alkyl chain on the molecular ordering inside the film, this phenomenon affect also the threshold voltage, whose shift toward a positive value (8 V) clearly evidence the impossibility of completely

turning the device off, due to the presence of residual charge carriers in the semiconducting channel, an aspect confirmed by the very low  $I_{ON}/I_{OFF}$  ratio which barely reach a  $10^1$  value.

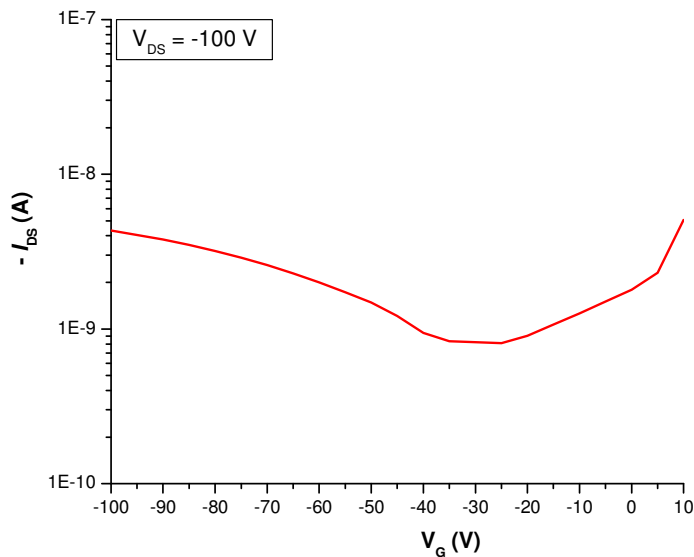


Figure 20: Transfer plot for compound 2-based OTFT ( $T_d = r. t.$ )

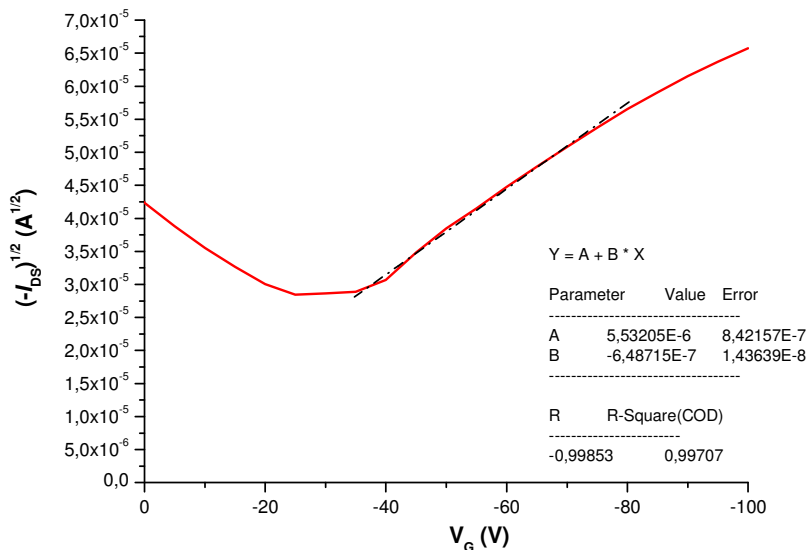


Figure 21:  $(-I_{DS})^{1/2}$  plot versus  $V_G$  for compound 2-based OTFT ( $T_d = r. t.$ )

The bi-directional transfer plot (Figure 22) however reveals a minimal hysteresis thus confirming a substantial device stability, whilst the output characteristic (Figure 23) confirms the very poor OTFT device response.

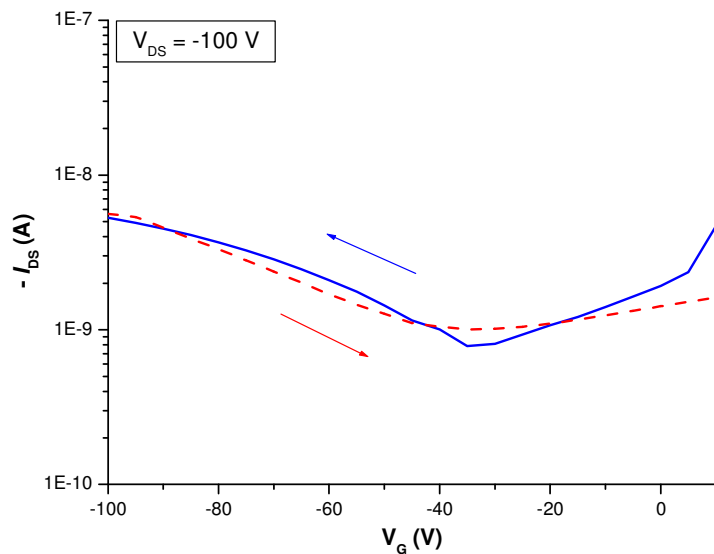


Figure 22: Bi-directional transfer plot for compound 2-based OTFT ( $T_d = \text{r.t.}$ )

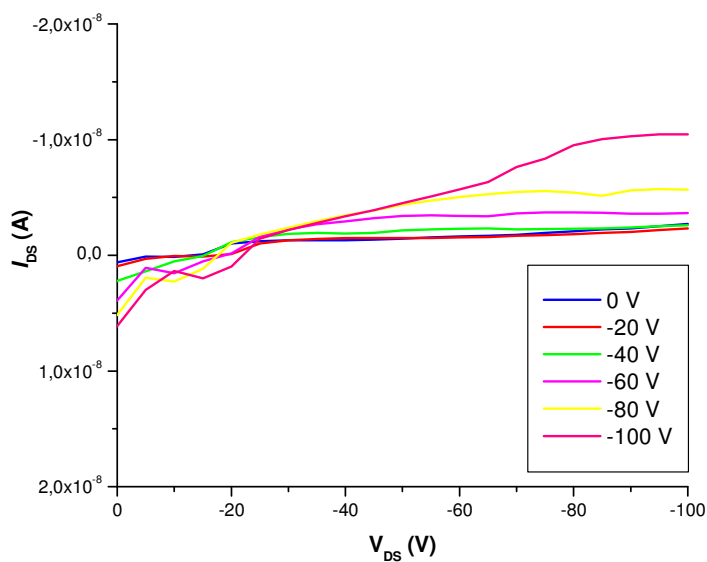


Figure 23: Drain-Source current/voltage output plot for compound 2-based OTFT ( $T_d = \text{r.t.}$ )

The attempt of enhancing the molecular ordering inside the film through an increase of the deposition temperature failed, giving a completely incoherent organic layer which rapidly degrades, as evidenced by the formation of highly colored spots on the surface. OTFTs response also in this case resulted meaningless and are not reported in the following.

Flavene derivative **3**, deposited in the same initial conditions used for the other two compounds, manifests a significant improvement in the OTFT response, which also in this case is coherent with a *p*-type device.

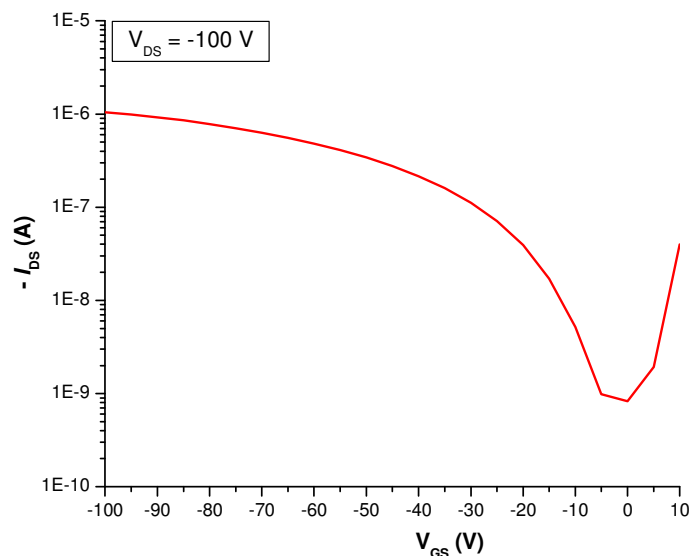


Figure 24: Transfer plot for compound 3-based OTFT ( $T_d = r. t.$ )

The transfer plot (Figure 24) demonstrates an appreciable increase of the device  $I_{ON}/I_{OFF}$  ratio which reaches a value as high as  $1 \times 10^3$ , with apparently very low residual charges in the OFF state. The analysis of the  $(-I_{DS})^{-1/2}$  graph (Figure 26) permits to evaluate a field-effect mobility of  $6.5 \times 10^{-4} \text{ cm}^2/\text{Vs}$  with an interesting minimal  $V_T$  of just -4 V.

Very minimal hysteresis is detectable from the bi-directional transfer plot in the saturation regime (Figure 27) confirming the electrical stability of the semiconducting layer under bias stress.

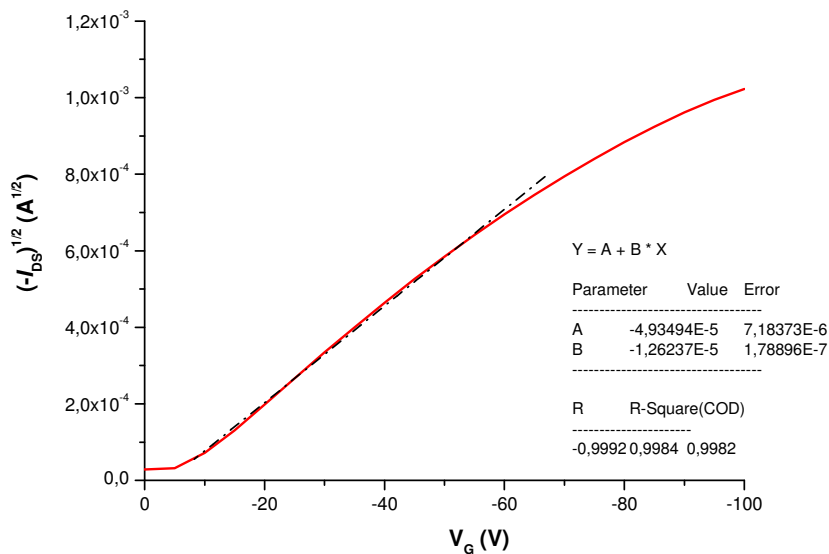


Figure 25:  $(-I_{DS})^{1/2}$  plot versus  $V_G$  for compound 3-based OTFT ( $T_d = r. t.$ )

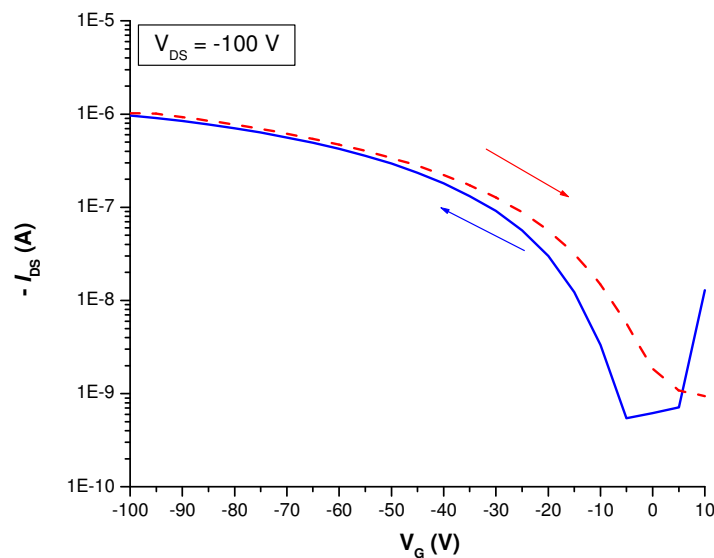


Figure 26: Bi-directional transfer plot for compound 3-based OTFT ( $T_d = r. t.$ )

Finally the output plot (Figure 28) underlines this effective stability/performance tradeoff for the entire OTFT working regime.



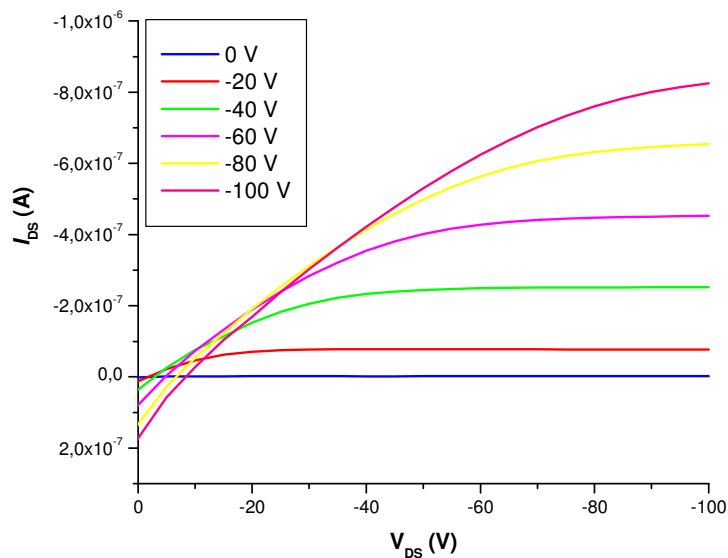


Figure 27: Drain-Source current/voltage output plot for compound 3-based OTFT ( $T_d = r.t.$ )

X-ray analysis on the organic film as deposited, shows also for compound **3** a complete amorphous phase when physically deposited on room temperature substrates (Figure 28).

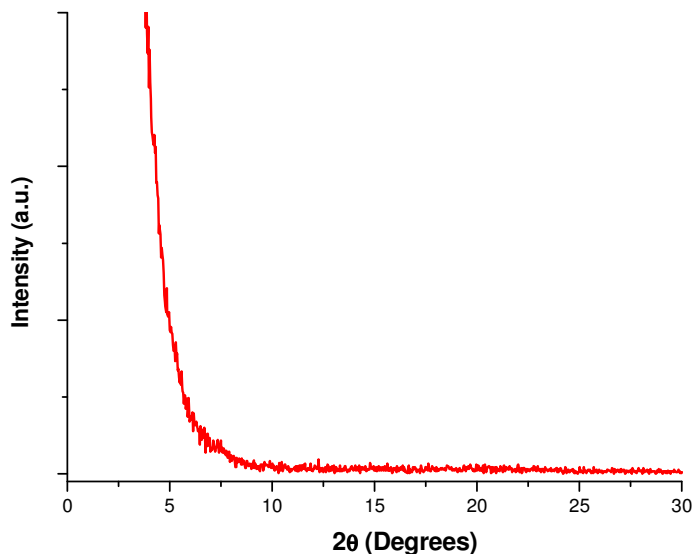


Figure 28: X-ray diffraction  $\theta$ - $2\theta$  scans of compound 3 thin film deposited at  $T_d = r.t.$

The strategy of enhancing the OTFT response by increasing the deposition temperature was followed also for this system given the starting favorable conditions. In the first trial  $T_d$  was set to 70 °C, the film appearance was analogous to that of the room temperature deposited one and the profilometer analysis demonstrated a thickness values comparable to the nominal one read on the evaporator display. X-ray analysis of the film (Figure 29) evidences the appearance of a diffraction peak at 7.50 degrees, thus proving the occurrence of crystalline domains into the organic layer which in turn causes, as expected, an OTFT performances enhancement as will be shown.

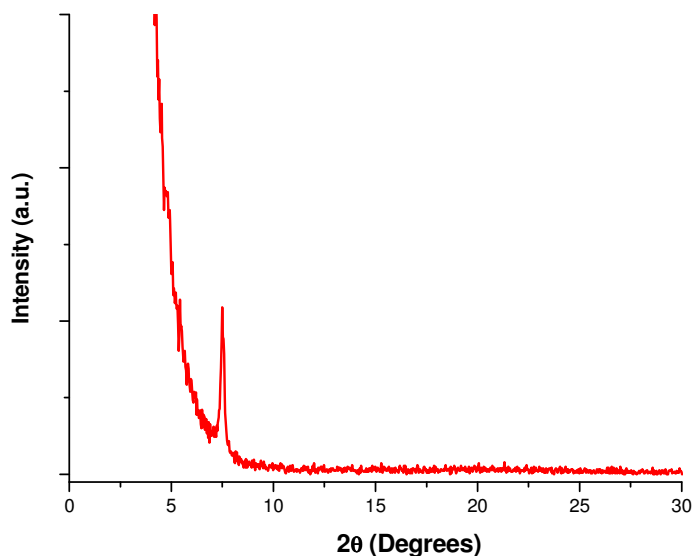


Figure 29: X-ray diffraction  $\theta$ - $2\theta$  scans of compound 3 thin film deposited at  $T_d = 70$  °C

The transfer plot (Figure 30) for compound-**3** OTFT deposited at 70 °C shows a slightly decrease of the  $I_{OFF}$  initial current contemporary revealing a two-fold increase of the maximum current in the ON state, thus leading to an enhancement of the final OTFT current ratio. This value rises in fact to  $5 \times 10^{-3}$ , with a five-fold increase respect to the sample deposited at room temperature. The extrapolated holes mobility (Figure 31) also increases, reaching a top value of  $1.5 \times 10^{-3} \text{ cm}^2/\text{Vs}$  with a global more than two-fold enhancement. The threshold voltage changes very little from the previous value, moving to -5 V.

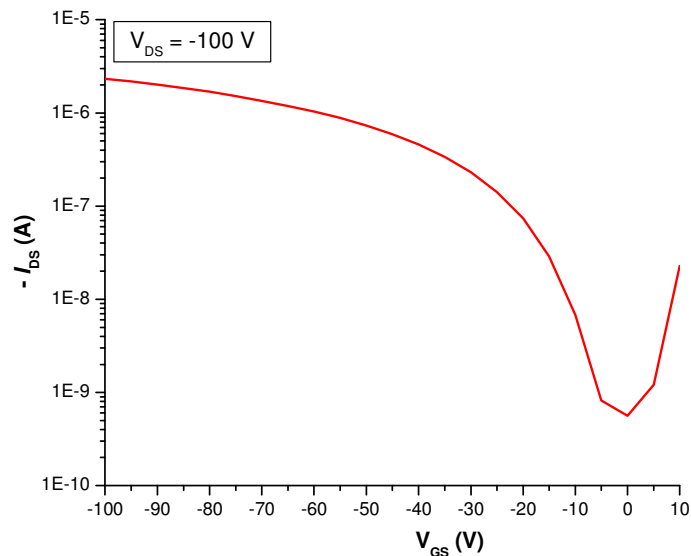


Figure 30: Transfer plot for compound 3-based OTFT ( $T_d = 70\text{ }^\circ\text{C}$ )

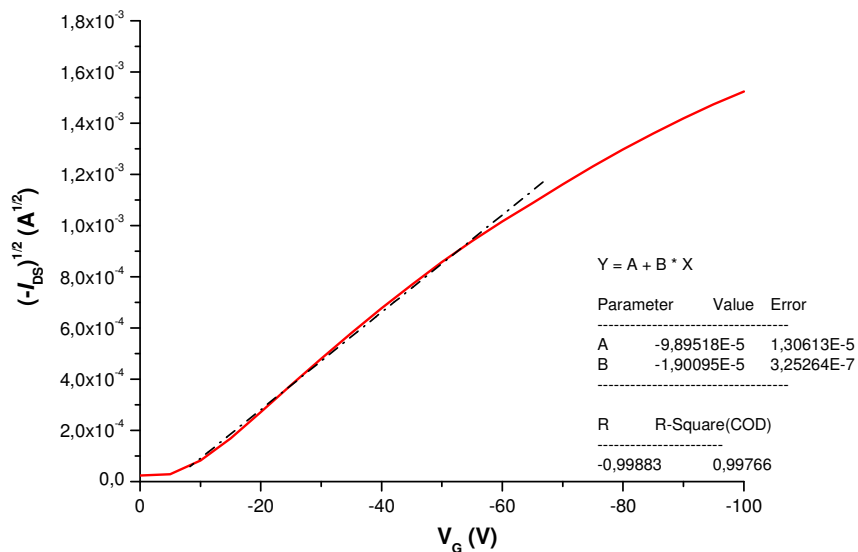


Figure 31:  $(-I_{DS})^{1/2}$  plot versus  $V_G$  for compound 3-based OTFT ( $T_d = 70\text{ }^\circ\text{C}$ )

The OTFT response picture is completed by the bi-directional transfer plot (Figure 32) and the device output characteristics (Figure 33) which confirm the system stability and the absence of trapping/recovery phenomena.

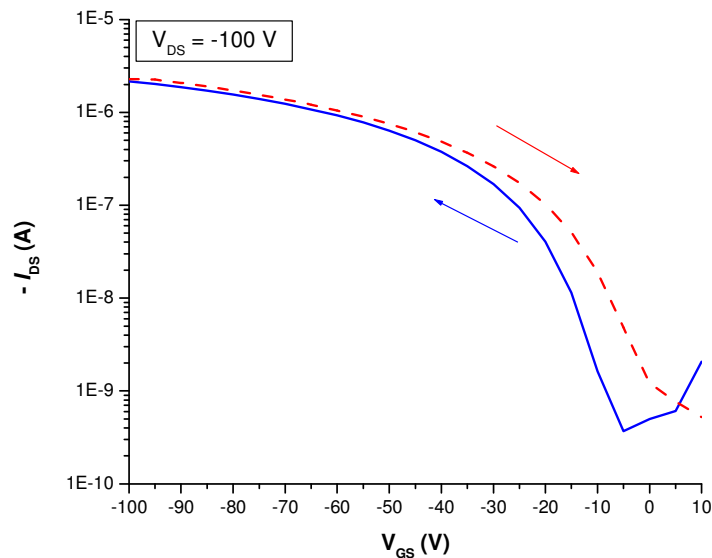


Figure 32: Bi-directional transfer plot for compound 3-based OTFT ( $T_d = 70\text{ }^\circ\text{C}$ )

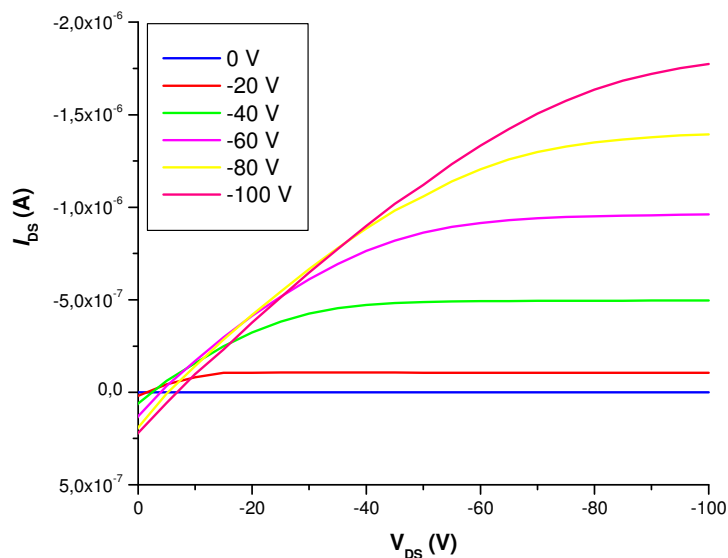


Figure 33: Drain-Source current/voltage output plot for compound 3-based OTFT ( $T_d = 70\text{ }^\circ\text{C}$ )

Considering the above results other experiments were conducted in the same directions further increasing the  $T_d$ . The first experiment was conducted increasing the substrate temperature to  $100\text{ }^\circ\text{C}$  but at the end of the deposition no film was formed on the surface (as confirmed by thickness measurements and UV-VIS absorption analysis).

This is due to the sublimation of the depositing materials from the substrate surface directly in the high vacuum chamber during the process. The second experiments were conducted using conditions in between the two previous ones, a  $T_d$  as high as 85 °C was used but also in this case no organic film was deposited on the substrate confirming the 70 °C temperature as the higher limit for the deposition of this molecule.

Table 1 reports the main OTFT parameters obtained for the tested compounds in the different deposition conditions.

Film	$T_d = 30\text{ °C}$			$T_d = 70\text{ °C}$		
	$\mu$	$I_{ON}/I_{OFF}$	$V_T$	$\mu$	$I_{ON}/I_{OFF}$	$V_T$
1	$1.3 \times 10^{-5}$	$10^3$	-11	-	-	-
2	$1.7 \times 10^{-6}$	$10^1$	8	-	-	-
3	$6.5 \times 10^{-4}$	$10^{-3}$	-4	$1.5 \times 10^{-3}$	$5 \times 10^{-3}$	-5

**Table 1: FET Mobilities ( $\mu$ ,  $\text{cm}^2/\text{Vs}$ ),  $I_{ON}/I_{OFF}$  Ratios and Threshold Voltage ( $V_T$ , V) for semiconductor film of series 1 – 3**

### III. CONCLUSIONS

The series of planar highly conjugated heteroaromatic systems **1 – 3** have been studied as a promising new class of vapor-phase processable active semiconducting layer for organic thin film transistor devices.

The structural characteristics of the molecules result clearly compatible with their applications in the field-effect electronic device: highly conjugated  $\pi$ -electronic systems, planar configurations, presence of heteroaromatic moieties and the possibility of an easy functionalization, in fact constitute a summary of favorable features which enable a finely tuning of the electronic properties at the molecular level, and lead in turn to a viable manipulation of the final supramolecular arrangements in the solid states.

The introduced molecules were straightforwardly synthesized following a common pathway, thus leading to the desired products in good yields after reacting in refluxing EtOH with a piperidine excess. The energy of the frontier HOMO level matched properly with the work function of the gold metal-contacts favoring charge-carriers injection from the electrodes and enabling their insertions in a BG/TC configuration OTFT device. Exploiting their volatile nature, the organic compounds were adequately sublimated onto a gate/dielectric couple constituted of the common literature benchmark Si/SiO<sub>2</sub>, pre-functionalized with a hexamethyldisilazane (HMDS) self-assembled monolayer. Metal contacts were finally vapor-deposited on top without affecting the molecular stability. All the systems manifested *p*-channel activity into the assembled device structure with remarkable stability and encouraging field-effect responses. Optimization of the organic layer properties were explored depositing the film at various temperatures: the evaluation of the OTFT response as a consequence of the resulting changes in film morphology and molecular solid-state packing, also considering the effect on the film crystallinity, mainly shows opposite behavior for the two types of introduced compounds.

Whilst the Weitz-type donor compounds **1** and **2** manifest semiconducting behavior into the thin film staggered structure only when deposited at room temperature, the oxygenated flavene derivate **3** shows an overall higher device compatibility, resulting in an enhancement of the OTFT characteristic response when deposited at a temperature as high as 70 °C ( $\mu = 1.5 \times 10^{-3} \text{ cm}^2/\text{Vs}$ ,  $I_{\text{ON}}/I_{\text{OFF}} = 5 \times 10^3$ , Threshold Voltage = -5 V), the film being partially crystalline in this latter case.

The presented study therefore represents an encouraging contribute to this research field considering both its essentially explorative nature, and the interesting results obtained for organic systems originally not designed for such an application. Optimization of both the molecular design and the transistor components/processes is a stimulating challenge to pursue for the future.

## EXPERIMENTAL SECTION

Solvents, piperidine, methyl trifluoromethanesulfonate, 1-iodohexane and 4-methyl-2-phenylchromenium tetrafluoroborate were provided by Sigma-Aldrich and used without further purifications. 9-methylacridine was synthesized according to known literature procedure.<sup>69</sup> Chromatography separations were conducted on silica 9385, 230-400 mesh, provided by Sigma-Aldrich. Prime grade *p*-doped silicon wafers <100> with 300 nm of thermally grown oxide used as device substrates were provided by Montco Inc.; the substrates were cleaned by rinsing and sonicating twice in EtOH and plasma cleaning with a Harrick Plasma Cleaner/Sterilizer PDC-32G. X-ray diffraction ( $\Theta$  -  $2\Theta$  and  $\omega$  scans) was performed on a Rigaku ATXG thin film diffractometer in slit-configuration with a monochromated Cu K $\alpha$  radiation source. OTFT electrical measurements were performed with a Keithley 6430 subfemtoammeter and a Keithley 2400 source meter in vacuum probe station. <sup>1</sup>H-NMR and <sup>13</sup>C-NMR spectra were recorded in benzene and acetone on an AMX-500 FT Bruker spectrometer. UV-Vis spectra were recorded on a JASCO V-57 spectrophotometer, both for solution sample and vapor-deposited films. Melting points were collected with an Electrothermal instrument model 9100 and are incorrect.

### **1,2-bis-(10-methylacridin-9(10*H*)-ylidene)ethane (1)**

A suspension of 9,10-dimethylacridinium trifluoromethane sulphonate (6.454 g, 18.00 mmol) in EtOH (100 mL) is refluxed till complete dissolution of the suspended material. Piperidine (6 mL) is added dropwise to the refluxing mixture observing a gradual turning of the color from yellow to deep red. After 12 h at reflux temperature, the red suspension is cooled to room temperature and the red precipitate is collected by filtration under reduced pressure. The crude product is dissolved in toluene (70 mL) and filtered through a short silica plug.



The solvent is removed under reduced pressure from the collected solution affording the desired product as a red crystalline solid (1.561 g, 3.79 mmol)\*.

M.p. 190 °C (dec).  $^1\text{H}$  NMR (500 MHz,  $\text{C}_6\text{D}_6$ )  $\delta$ [ppm]: 8.18 (dd,  $J=7.7\text{Hz}$ ,  $J=1.4\text{Hz}$ , 2H), 7.88 (dd,  $J=7.7\text{Hz}$ ,  $J=1.2\text{Hz}$ , 2H), 7.50 (s, 2H), 7.29-7.26 (m, 2H), 7.19-7.14 (m, 4H), 7.01 (t,  $J=7.8\text{Hz}$ , 2H), 6.74 (d,  $J=8.3\text{Hz}$ , 2H), 6.66 (d,  $J=8.2\text{Hz}$ , 2H), 2.86 (s, 6H);  $^{13}\text{C}$  NMR (125.7 MHz,  $\text{C}_6\text{D}_6$ )  $\delta$ [ppm]: 142.83, 141.16, 132.03, 129.19, 128.24, 127.40, 124.71, 123.54, 122.02, 121.47, 120.34, 112.67, 112.60, 32.92; Anal. Calcd for  $\text{C}_{30}\text{H}_{24}\text{N}_2 \cdot 2\text{H}_2\text{O}$ : C, 80.33; H, 6.29; N, 6.25. Found: C, 80.27; H, 5.75; N, 6.82.

### 1,2-bis-(10-hexylacridin-9(10H)-ylidene)ethane (2)

A suspension of 10-hexyl-9-methylacridinium iodide (0.384 g, 0.95 mmol) in EtOH (15 mL) is refluxed till complete dissolution of the suspended material. Piperidine (0.3 mL) is added dropwise to the refluxing mixture observing a gradual turning of the color from yellow to deep red. The mixture is refluxed for 6 h, the solvent is removed under reduced pressure and the residue purified by chromatography (silica, toluene) to give the desired product as a red powder (0.200 g, 0.36 mmol)\*.

M.p. 183 °C (dec).  $^1\text{H}$  NMR (500 MHz,  $\text{C}_6\text{D}_6$ )  $\delta$ [ppm]: 8.12 (dd,  $J=7.7\text{Hz}$ ,  $J=1.4\text{Hz}$ , 2H), 7.81 (dd,  $J=7.8\text{Hz}$ ,  $J=1.3\text{Hz}$ , 2H), 7.36 (s, 2H), 7.21 (t,  $J=8.5\text{Hz}$ , 2H), 7.10 (t,  $J=8.5\text{Hz}$ , 2H), 7.05 (t,  $J=7.8\text{Hz}$ , 2H), 6.91 (t,  $J=7.2\text{Hz}$ , 2H), 6.90 (d,  $J=7.1\text{Hz}$ , 2H), 6.80 (d,  $J=8.2\text{Hz}$ , 2H), 3.53 (t,  $J=8.1\text{Hz}$ , 2H), 1.54-1.51 (m, 4H), 1.18-1.05 (m, 12H), 0.84-0.80 (t,  $J=7.2\text{Hz}$ , 6H);  $^{13}\text{C}$  NMR (125.7 MHz,  $\text{C}_6\text{D}_6$ )  $\delta$ [ppm]: 141.66, 140.11, 131.75, 129.62, 128.62, 128.06, 124.53, 123.85, 122.19, 121.50, 120.15, 112.85, 112.83, 46.34, 31.44, 26.55, 25.67, 22.71, 13.93.

\* The yields are not reported because the exact reaction mechanism is still under investigation. It has in fact been ascertained that the synthetic pathways undoubtedly involve RedOx processes which clearly influence and determine the final reaction stoichiometry.

**1,2-bis-(2-phenyl-4*H*-chromen-4-ylidene)ethane (3)**

4-methyl-2-phenylchromenium tetrafluoroborate (2.000 g, 6.49 mmol) is suspended in EtOH (20 mL) and heated till complete dissolution of the suspended material. Piperidine (2 mL) is added and the mixture is refluxed for 18 h. A red precipitate is formed which is totally insoluble in EtOH, after separation the desired product is obtained as a red powder (0.500 g, 1.15 mmol)\*.

M.p. 251°C (dec). <sup>1</sup>H NMR (500 MHz, DMSO-d<sub>6</sub>) δ[ppm]: 8.26 (d, *J*=8.2Hz, 2H), 8.08 (d, *J*=7.5Hz, 4H), 7.53 (t, *J*=7.3Hz 4H), 7.46 (t, *J*=7.2Hz, 2H), 7.38 (s, 2H), 7.37 (t, *J*=8.0Hz, 2H), 7.26 (d, *J*=7.6Hz, 2H), 7.25 (t, *J*=7.1Hz, 2H), 7.20 (s, 2H); <sup>13</sup>C NMR (125.7 MHz, DMSO-d<sub>6</sub>) δ[ppm]: 151.59, 149.00, 133.34, 132.05, 129.72, 129.19, 125.34, 125.13, 124.89, 123.96, 123.33, 117.87, 111.82, 101.91.

## REFERENCES

- <sup>1</sup> Faricelli, J. "Transistors, Field-Effect", *Encyclopedia of Applied Physics*, Wiley-VCH, New York, **2003**.
- <sup>2</sup> Facchetti, A. *Materials Today* **2007**, *10*, 28.
- <sup>3</sup> Ibach, L.; Lüth, H. *Solid-State Physics*, Springer, New York, **2003**.
- <sup>4</sup> Kirk-Othmer *Kirk-Othmer Encyclopedia of Chemical Technology*, Vol 22, 5th ed., John Wiley & Sons, Inc., New York, **2006**.
- <sup>5</sup> Hirose, T. et al *IEEJ Trans*, **2009**, *4*, 278.
- <sup>6</sup> Sze, S. M.; Ng, Kwok K. *Physics os Semiconductor Devices*, John Wiley & Sons, New York, **2007**.
- <sup>7</sup> Rogers, J. A.; Sun, Y. *Adv. Mater.* **2007**, *19*, 1897.
- <sup>8</sup> Street, R. A. *Adv. Mater.* **2009**, *21*, 2007.
- <sup>9</sup> Wagner, S. *Phys. Status Solidi A* **2010**, *3*, 501.
- <sup>10</sup> Shimada, T.; Takahashi, K.; Sato, T.; Okazaki, Y. "Properties and applications of amorphous materials", *Encyclopedia of Applied Physics*, Wiley-VCH, New York, **2003**
- <sup>11</sup> Nomura, K. et al. *Nature* **2004**, *432*, 488.
- <sup>12</sup> Wang, L.; Yoon, M.; Facchetti, A.; Marks, T. J. *Adv. Mater.* **2007**, *19*, 3252.
- <sup>13</sup> Rogers, J. A. et al. *Nature* **2008**, *454*, 495.
- <sup>14</sup> Avouris, P. and co-workers *Nano Lett.* **2010**, *10*, 715.
- <sup>15</sup> Yoon, M.; DiBenedetto, S. A.; Russel, M. T.; Facchetti, A.; Marks, T. J. *Chem. Mater.* **2007**, *19*, 4864.
- <sup>16</sup> Wisnieff, R. *Nature* **1998**, *394*, 225.
- <sup>17</sup> Di, C.; Yu, G.; Liu, Y.; Zhu, D. *J. Phys. Chem. B* **2007**, *111*, 14083.
- <sup>18</sup> Yan, H.; Yoon, M.; Facchetti, A.; Marks, T. J. *Appl. Phys. Lett*, **2005**, *87*, 183501.
- <sup>19</sup> Braga, D.; Horowitz, G. *Adv. Mater.* **2009**, *21*, 1473.
- <sup>20</sup> Dimitrakopoulos, C. D.; Malenfant, P. R. L. *Adv. Mater.* **2002**, *14*, 99.
- <sup>21</sup> Miozzo, L.; Yassar, A.; Horowitz, G. *J. Mater. Chem.* **2010**, *20*, 2513.
- <sup>22</sup> Unni, K. N. N.; Pandey, A. K.; Nunzi, J. M. *Chem. Phys. Lett.* **2005**, *407*, 95.
- <sup>23</sup> Facchetti, A.; Yoon, M.; Marks, T. J. *Adv. Mater.* **2005**, *17*, 1705.
- <sup>24</sup> Gershenson, M. E.; Podzorov, P.; Morpurgo, A. F. *Rev. Mod. Phys.* **2006**, *78*, 973.
- <sup>25</sup> Roberts, M. E.; Sokolov, A. N.; Bao, Z. *J. Mater. Chem.* **2009**, *19*, 3351.
- <sup>26</sup> Yamashita, Y. *Sci. Technol. Adv. Mater.* **2009**, *10*, 024313.
- <sup>27</sup> Takeya, J. et al *Appl. Phys. Chem* **2007**, *90*, 102120.

- 
- <sup>28</sup> Katz, H. E.; Bao, Z.; Gilat, S. L. *Acc. Chem. Res.* **2001**, *34*, 359.
- <sup>29</sup> Roncali, J. et al *Adv. Mater.* **2003**, *15*, 306.
- <sup>30</sup> Cheng, Y. L. et al *JACS* **2005**, *127*, 15700.
- <sup>31</sup> McCollough, I. et al *Adv. Mater.* **2009**, *21*, 1091.
- <sup>32</sup> McCollough, I. et al *Nat. Mater.* **2006**, *5*, 328.
- <sup>33</sup> Jones, B. A.; Facchetti, A.; Wasielewski, M. R.; Marks, T. J. *Appl. Phys. Lett.* **2006**, *88*, 183102.
- <sup>34</sup> Sirringhaus, H. *Nat. Mater.* **2003**, *2*, 641.
- <sup>35</sup> Bao, Z. *Adv. Mater.* **2000**, *12*, 227.
- <sup>36</sup> Bao, Z. et al *JACS* **1998**, *120*, 207.
- <sup>37</sup> Facchetti, A. et al *Angew. Chem. Int. Ed.* **2000**, *39*, 4547.
- <sup>38</sup> Facchetti, A. et al *JACS* **2004**, *126*, 13859.
- <sup>39</sup> Facchetti, A. et al *Angew. Chem. Int. Ed.* **2003**, *42*, 3900.
- <sup>40</sup> Jones, B. A.; Ahrens, M. J.; Yoon, M.; Facchetti, A.; Wasielewski, M. R.; Marks, T.J. *Angew. Chem. Int. Ed.* **2004**, *43*, 6363.
- <sup>41</sup> Jones, B. A.; Facchetti, A.; Wasielewski, M. R.; Marks, T.J. *JACS* **2007**, *129*, 15259.
- <sup>42</sup> Jones, B. A.; Facchetti, A.; Wasielewski, M. R.; Marks, T.J. *Adv. Funct. Mater.* **2008**, *18*, 1329.
- <sup>43</sup> DiBenedetto, S. A.; Facchetti, A.; Ratner, M, A.; Marks, T.J. *Adv. Mater.* **2009**, *21*, 1407.
- <sup>44</sup> Ponce Ortiz, R.; Facchetti, A.; Marks, T. J. *Chem. Rev.* **2010**, *110*, 205.
- <sup>45</sup> Yoon, M.; Facchetti, A.; Marks, T. J. *JACS* **2005**, *127*, 10338.
- <sup>46</sup> Kim, C.; Wang, Z.; Choi, H.; Ha, Y.; Facchetti, A.; Marks, T. J. *JACS* **2008**, *130*, 6867.
- <sup>47</sup> Vuillame, D. et al *Appl. Phys. Lett.* **1996**, *69*, 1646.
- <sup>48</sup> Yoon, M.; Facchetti, A.; Marks, T. J. *PNAS* **2005**, *102*, 4678.
- <sup>49</sup> DiBenedetto, S. A.; Frattarelli, D.; Facchetti, A.; Ratner, M, A.; Marks, T.J. *JACS* **2008**, *130*, 7528.
- <sup>50</sup> Hur, S.; Yoon, M.; Gaur, A.; Shim, M.; Facchetti, A.; Marks, T. J.; Rogers, J. A. *JACS* **2005**, *127*, 13808.
- <sup>51</sup> Daraktchiev, M. et al *New J. Phys.* **2005**, *7*, 133.

- <sup>52</sup> Todescato, F.; Capelli, R.; Dinelli, F.; Murgia, M.; Camaioni, N.; Yang, M.; Bozio, R.; Muccini, M. *J. Phys. Chem. B* **2008**, *112*, 10130.
- <sup>53</sup> Shen, Y. et al *Chem. Phys. Chem.* **2004**, *5*, 16.
- <sup>54</sup> Kreuter, C. et al *New J. Phys.* **2008**, *10*, 075001.
- <sup>55</sup> Bröker, B.; Blum, R.; Beverina, L.; Hofmann, O. T.; Sassi, M.; Ruffo, R.; Pagani, G. A.; Heimel, G.; Vollmer, A.; Frisch, J.; Rabe, J. P.; Zojer, E.; Koch, N. *Chem. Phys. Chem.* **2009**, *10*, 2947.
- <sup>56</sup> Chen, C. H.; Doney, J. J.; Reynolds, G. A.; Saeva, F. D. *JOCS* **1983**, *48*, 2757.
- <sup>57</sup> Spori, D. M.; Venkatarman, N. V.; Tosatti, S. G. P.; Durmaz, F.; Spencer, N. D. *Langmuir* **2007**, *23*, 8053.
- <sup>58</sup> Dimitrakopoulos, C. D.; Brown, A. R. *J. Appl. Phys.* **1996**, *80*, 2501.
- <sup>59</sup> Bernthsen, A. *Justus Liebigs Annalen der Chemie* **1884**, *224*, 45.

